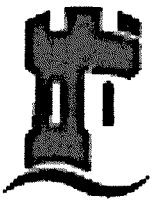

The University of Nottingham

A HERMITE RADIAL BASIS FUNCTIONS CONTROL VOLUME NUMERICAL METHOD TO SIMULATE TRANSPORT PROBLEMS

Paolo Orsini

GEORGE GREEN LIBRARY OF
SCIENCE AND ENGINEERING

Thesis Submitted to the University of Nottingham for degree of Doctor of Philosophy

December 2009

To Mum and Dad and my girlfriend Emily

LIST OF CONTENTS

ABSTRACT

This thesis presents a Control Volume (CV) method for transient transport problems where the cell surface fluxes are reconstructed using local interpolation functions that besides interpolating the nodal values of the field variable, also satisfies the governing equation at some auxiliary points in the interpolation stencils. The interpolation function relies on a Hermitian Radial Basis Function (HRBF) meshless collocation approach to find the solution of auxiliary local boundary/initial value problems, which are solved using the same time integration scheme adopted to update the global control volume solution. By the use of interpolation functions that approximate the governing equation, a form of analytical upwinding scheme is achieved without the need of using predefined interpolation stencils according to the magnitude and direction of the local advective velocity. In this way, the interpolation formula retains the desired information about the advective velocity field, allowing the use of centrally defined stencils even in the case of advective dominant problems. This new CV approach, which is referred to as the CV-HRBF method, is applied to a series of transport problems characterised by high Peclet number.

This method is also more flexible than the classical CV formulations because the boundary conditions are explicitly imposed in the interpolation formula, without the need for artificial schemes (e.g. utilising dummy cells). The flexibility of the local meshless character of the CV-HRBF is shown in the modelling of the saturated zone of the unconfined aquifer where a mesh adapting algorithm is needed to track the phreatic surface (moving boundary). Due to the use of a local RBF interpolation, the dynamic boundary condition can be applied in an arbitrary number of points on the phreatic surface, independently from the mesh element.

The robustness of the Hermite interpolation is exploited to formulate a non-overlapping non-iterative multi-domain scheme where physical matching conditions are satisfied locally, i.e. imposing the continuity of the function and flux at the sub-domain interface.

List of articles resulting from this work

Journal Article

Orsini P.; Power H.; Morvan H. (2008): Improving Volume Element Method by Meshless Radial Basis Function, *CMES: Computer Modeling in Engineering and Sciences,* **23**(3), 187-207.

Orsini P.; Power H.; Lees M.; Morvan H. (2009): A Control Volume Radial Basis Function Techniques for the Numerical Simulation of Saturated Flows in Semi-confined Aquifer, *Transport in Porous Media,* **79**(2), 171-196.

Orsini P.; Power H.; Morvan H.; Lees M. (2009): An implicit upwinding volume element method based on meshless radial basis function techniques for modelling transport phenomena, *International Journal for Numerical Methods in Engineering.* In press.

Orsini P.; Power H.; Morvan H.; Lees M. (2009): Non-overlapping domain decomposition algorithm for the Hermite Radial Basis Function Control Volume method (To be submitted).

Orsini P.; Power H.; Morvan H.; Lees M. (2009): A Multi Speciecs Reactive Transport Software based on the Hermite Radial Basis Function Control Volume method (To be submitted).

Chapters in Books

Orsini P.; Power H.; Lees M.; Morvan H. (2009). Improving the convergence of the Hermite CVRBF method for unstructured meshes. *Advances on the Meshless Local Petrov-Galerkin (MLPG) Method.* S. N. Atluri. To appear.

ACKNOWLEDGEMENT

First of all I would like to thank my first supervisor Prof. Henry Power for his constant support, encouragement and open approach to any new ideas I had during this research. No matter what the question, he always had the time to hear it, and the knowledge to answer it.

I acknowledge my associate supervisor Dr. Hervé Morvan for his valuable feedback throughout the course of this research programme.

I acknowledge the University of Nottingham for the use of the facilities in the School of Mechanical Material and Manufacturing Engineering.

The European Commission for the 'European research and innovation activity' is acknowledged for its financial contribution to the GABARDINE project that sponsored this research (Contract no: 518118, sixth framework program, priority 1.1.6.3, Global change and Ecosystems).

LIST OF FIGURES

LIST OF TABLES

LIST OF SYMBOLS

Alphabetic Symbols

$[a]$	wave amplitude vector
$[A]$	local system matrix
$[A_{GLB}]$	global system matrix
$B[]$	boundary operator
$[b]$	local system right hand side
c	generic chemical species
c_S	absolute value of the RBF free parameter
c_S^*	length fraction used for the computation of the RBF free parameter
D	diffusion coefficient
D_{ij}	(i,j)-component of the diffusion tensor
D_{ij}^S	(i,j)-component of the dispersitity tensor
$E\%$	relative percentage error
$F(\ )$	flux operator
F^S	implicit function that describes the phreatic surface
f_s	source function (known term of the governing equation)
f_B	boundary condition known term
g	gravity acceleration
h	phreatic surface elevation
I	infiltration rate
$[Ir]$	integration reconstruction vector
K_r	reactive coefficient
K_{MgCO_3}	magnesite dissociation equilibrium constant
K_{ij}	(i,j)-term of the hydraulic conductivity tensor
$L[]$	PDE operator

L_a^m, L_b^m, L_c^m, L_d^m	natural coordinate of the integration point m
L_{MIX}	characteristic length scale of the of the well mixed portion of space
Lst_{max}	maximum distance found between the local interpolation centres
L_R	characteristic length scale of the problem
$L^t_{2residual}$	L_2 -norm of the residual at the interval t
L_E	characteristic length of the element edge
L_{2error}	L_2 -norm error
L^t_{2error}	L_2 -norm at the interval t
$L^t_{2residual}$	L_2 -norm of the nodal residual at the time t (global residual at the time t)
M	RBF integer exponent
N	number of test points in the local interpolation
N_{bc}	number of boundary points in the local interpolation
$Nele$	total number of elements
Nst	total number of interpolation stencils
N_{sp}	number of chemical species
N_{tr}	number of trial centres (or RBF function) in the local interpolation
$Nnodes$	total number of mesh nodes
$Nsint$	number of integration point for a control volume face
$Nsurf$	number of cell faces
$Nsurf_{Si}$	number of sub-volume faces that define the node-control volume
$Nvint$	number of integration point in the control volume
nd	number of dimensions
n_i	normal component in i-direction
n_i^{Int}	component i of the sub-domain interface normal
n_i^l	outward normal in the i-direction of the cell cafe l
n_i^S	i-component of phreatic surface normal vector
ns	number of sub-volumes
Pe	Peclet Number
P^n	sinks point strenght (Pumping point)
P_{M-1}	polynomial of order M-1

p	pressure
Q	volumetric rate (pumping or injecting)
q_i	*i*-component of specific discharge or seepage velocity or infiltration velocity
U_i	i-component of the velocity
U	module of the velocity
R_n	reaction term for the species *n*
R_n^0	reaction term for the species *n* not depending on the concentration c_n
r	radial distance
res_i	residual in the node *i*
S_l	area of the cell face-*l*
S_0	storativity
t	time
V_P	volume of the control volume p (central control volume)
V_{Si}	volume of the subvolume *i*
v_i	*i*-component of darcy flux, or net average velocity
W^m	source point strenght (Injecting point)
w^m	integration weight for the point *m*

Greek Symbols

α_j	RBF interpolation coefficients
ε_{tol}	numerical tolerance for the non-linear iteration converging criteria
ϕ	generic field variable (e.g. concentration, temperature, piezometric head)
ϕ_{ana}	analytical solution
Γ	source points in the aquifer
η	soil porosity
$[\lambda]$	eigenvalue vector
θ	Crank-Nicholson time-stepping scheme weighting parameter
ρ	density
τ_D	dispersion time scale
Ω	internal domain

Ω^{IA}	ion activity product
$\partial\Omega$	domain boundaries
Ψ	generic RBF function

1 INTRODUCTION

1.1 Literature review

1.1.1 Control volume method (CV)

The control volume (CV) method is one of the most popular numerical techniques in Computational Fluid Dynamics (CFD) due to its robustness, simplicity and mass conservation capability. Originally the method was applied only to structured meshes, but with the incredible computer development of the last twenty years there has been a large increase of engineering applications that benefit from numerical modelling, and the use of unstructured grids to discretise complex geometries became necessary to simplify the mesh generation process. However, when unstructured meshes are employed instead of structured ones, both cell stencil selection and flux computation become more difficult. Although significant works have been carried out in this field, methods that aim to high order convergence solution with unstructured meshes are still a subject of active research.

In the literature, two different approaches are reported when unstructured control volume schemes are considered: Cell-centred (CC) and vertex-centred (VC) schemes. The second scheme is usually called the Control Volume Finite Element (CV-FEM) scheme. In the cell-centred configuration the CVs used to integrate the governing equation are the elements of the mesh that discretises the problem, and pertinent information concerning the system variables are stored at the centre of these elements. The main ideas behind this scheme, widely used in computational fluid dynamic (CFD), are reported in Versteeg and Malalasekera (2007); for some practical applications see also Date (2005). In the vertex-centred scheme, system variable information is stored at the vertices of the mesh elements, and the CVs are constructed around these vertices. The field variable within each element is defined in terms of the element nodal values using FE shape functions (polynomial functions), and the corresponding gradient is obtained by differentiation of the same shape functions. Since the first publication by Baliga and Patankar (1980) the CV-FEM has been successfully used as a numerical tool in a wide range of application (for more details see Rousse (2000); Liu et al. (2002); Ben Salah et al. (2005); Grissa et al. (2007)).

Regardless of the type of scheme implemented, the accuracy of the CV method discretisation is strongly dependent on the flux approximation which is adopted. This is usually computed considering two contributions; the advective flux and the diffusive flux. Generally each of these terms requires a different method of approximation that suits its physical nature.

In the vertex-centred schemes, the gradient at the CV faces found in the diffusive flux is obtained by differentiation of the shape functions. A different strategy is reported in literature for cell-centred CV methods. In this case the diffusive flux is usually decomposed in terms of appropriately chosen orthonormal vectors, Versteeg and Malalasekera (2007). In two-dimensional (2D) problems, the scheme takes account of two different contributions to compute the gradient vector of the field variable at the cell faces: along the line which joins the two cell centres and along the cell face tangential direction. The normal component is finally expressed in terms of these two gradient projections. The first term is obtained by a central finite difference (FD) formula, which is of second order of accuracy only when the adjoining control volumes are of equal length in the normal direction. The second term, the tangential component, is still computed with a second order central FD formula which is a function of the cell face end points. As in the cell-centred scheme the values of the function at the face end points are generally unknown, these values are usually obtained by simple averaging over neighbouring cell centres. The evaluation of the gradient using the approach explained above brings a computational error which increases with skewness and the degradation of the element aspect ratio. To avoid this discretisation error, Turner and Ferguson (1995) proposed the use of a four-node formula, instead of a two-node one. This approach captures both the normal and tangential components of the gradient vector and consequently reduces the error associated with the domain discretisation.

In general, the computation of the advective flux requires a different approach, since this type of flux is characterised by the flow direction of the carrying fluid. It is well known that for advective dominant problems featuring function discontinuities, spurious oscillations (instabilities) are frequently observed when using numerical techniques based on centrally defined interpolation functions. Such instabilities are due to the dispersive errors in the evaluation of the advective flux. In central schemes, as for the case of centrally defined CV methods, the interpolation stencil includes points from the upstream and downstream directions of the advective velocity field using similar weighting functions. In such numerical schemes the spurious oscillations are controlled introducing upwinding interpolation techniques where the upstream points are heavily weighted compared to the downstream ones. This method it often combined with gradient limiters and Reimann solvers to guarantee mass conservation (see Versteeg and Malalasekera (2007) for a comprehensive review of the most commonly available upwind schemes).

CV schemes based on upwind strategy are characterised by a typical artificial diffusivity that, controlling the dispersive error, helps to improve their stability at the expense of the accuracy. These methods are limited to the first order in regions characterised by discontinuities. In the last twenty years, there have been many attempts to overcome, or at least mitigate, this problem. Among these the most popular are the essentially non-oscillatory (ENO); Shu and Oshert (1989), and the weighted essentially non-oscillatory (WENO); Jiang and Shu (1996), schemes. High accuracy schemes such as flux limiting or (WENO) methods aim to improve the accuracy of upwinding schemes by including some downstream information in the interpolation without increasing dispersive errors or instability. Unfortunately, the selection of upwind stencils is completely ad hoc and their implementation for unstructured meshes dealing with complex three-dimensional problems is not a trivial task.

More recently, Nessyahu and Tadmor (1990) and Kurganov and Lin (2007) have reported on how to reduce the diffusivity error in central upwind CV schemes by utilising one-sided local propagation speeds in term of a Godunov-type projection evolution method to locally capture the shock evolution. Although these works have achieved significant contributions to improve the evaluation of advective fluxes without inducing instabilities, the use of one-dimensional polynomials can be considered an evident limitation for applications to complex three-dimensional unstructured meshes.

In an attempt to increase the accuracy of unstructured CV schemes, innovative ideas regarding the flux reconstruction have been proposed in the last few years. Abgrall (1994) revisited the possibility of performing the flux reconstruction in triangular meshes through the use of local two-dimensional polynomial functions. The same idea has been extended to three-dimensional problems in the WENO scheme presented by Dumbser and Kaser (2007). Large attention has also been given to the least squares function reconstruction technique (LSRT). This technique has been used in the computation of flux corrective terms, Jayantha and Turner (2003), (2005), to increase the spatial accuracy of CV schemes, and also, in a more direct approach, in the reconstruction of the fluxes at the cell faces of the control volume (Ollivier-Gooch and Van Altena (2002). Other researchers proposed the Gauss-Green gradient reconstruction technique (GGRT), which has been used in combination with the LSRT to compute the gradients at the cell faces of the CV (Truscott and Turner (2004) and Manzini and Putti (2007)). New ideas have been found also in the spectral volume (SV) developed by Liu et al. (2006) where the unstructured grid cells are partitioned into structured sub-cells. The main problem of this approach, recognised by the authors themselves, is that a good partitioning requires the set up of a large number of parameters, which becomes extremely difficult for 3D problems. Liu et al. consequently abandoned the SV idea in favour of a finite difference formulation in which the

mass conservation is locally guaranteed, imposing that the flux between two adjoined unstructured cells be the same (Liu et al. (2006)). The reconstruction schemes reported in the last paragraph also require the use of upwinding interpolation stencils in order to guarantee their stability when dealing with advective dominant problems.

One possible alternative to improve the accuracy of the evaluation of the flux is the use of radial basis functions (RBF). In the literature, the RBF interpolation method is considered as an optimal numerical technique for interpolating multidimensional scattered data. Although most work done so far on RBF relates to scattered data interpolation, there has recently been an increased interest in the use of RBF as the base of meshless collocation approaches for solving partial differential equations (PDEs) (see Kansa and Hon (2000), for the unsymmetric approach, and Jumarhon et al. (2000), for the symmetric approach). While the global formulation of these techniques becomes unpractical when the number of collocation points is relative large, their local implementation can be explored for the improvement of classical numerical methods.

The idea of introducing RBF interpolations to improve the accuracy of a classical numerical scheme has been recently employed by Wright and Fornberg (2006). In this work the authors utilise a Hermitian RBF interpolation to remove the symmetry constraint required to achieve high order approximation in the FD scheme. Cecil et al. (2004) use RBF as interpolants to reconstruct locally the gradients of the function in their numerical scheme for the Hamilton–Jacobi equation on unstructured data sets for arbitrary dimension. In this way they avoid the use of multidimensional polynomials that leads to ill-conditioning problems when solving the local linear systems necessary to find the interpolation coefficients.

The use of RBF interpolation to improve the Boundary Element Method (BEM) has been implemented amongst others by Sladek et al. (2005), using a local integral equation formulation, while May-Duy et al. (2006) used a global formulation. On the other hand, Nguyen-Van et al. (2007) incorporates the strain smoothing method for mesh-free conforming nodal integration into the Finite Element Method (FEM).

At the knowledge of the writer, the RBFs were used for the first time in the context of control volume methods in the 'optimal recover' approach of Sonar (1996) and Iske and Sonar (1996) for two-dimensional triangular grids. In these works the flux at the cell face integration points is 'recovered' from the cell average values evaluated in the cell being integrated and in its neighbours. In his optimal recovery, Sonar removes the poor approximation of locating the mean values in the cell centres, demonstrating that such constrain limits to the first order in space the accuracy of most of the classic control volume schemes. In Sonar's approach the

interpolants are integrals obtained by applying the cell average operator to the second argument of the RBFs, i.e. by using an Hermitian interpolation scheme with the average integral operators included in the expression (see section 1.1.2 for more details). The interpolation coefficients are found imposing that the average of the interpolants must be equal to the average of the unknown function in the control volumes of the prescribed stencil. Note that this is the same condition used in the works of Abgrall (1994) and Dumbser and Kaser (2007) mentioned above, in which polynomials are used rather than RBFs. In Sonar's CV method, originally developed for hyperbolic conservation laws, the ENO technique is employed to avoid instabilities rising from the advection flux computation.

More recently, Moroney and Turner (2006), (2007) improved Liu et al. (2002) CV approach, for 2D and 3D problems respectively, by using RBF interpolation functions instead of FE polynomial shape functions to reconstruct the field variables and their derivatives. Their approach relies on a local RBF interpolation of the field variable used to obtain the surface fluxes, where the CV centres of the considered stencil act as trial points. Moroney and Turner claim the ability of their CV-RBF scheme to achieve high order of convergence on relatively coarse meshes due to the accuracy of the RBF interpolation to evaluate derivatives (Madych (1992) and Fornberg and Flyer (2005)) and thus guarantee a very good approximation of the diffusive flux. In the case of advective dominant problems, Turner's et al. CV-RBF approach also requires the implementation of some kind of upwinding scheme in order to avoid spurious oscillations in their numerical results.

1.1.2 Radial basis function meshless collocation methods

In recent years the theory of radial basis functions has undergone intensive research and enjoyed considerable success as a technique for interpolating multivariable data and functions. A radial basis function $\Psi\left(\left\|x-\xi^j\right\|\right)$ depends upon the separation distances of a subset of trial centres $\left\{\xi^j \in \Re^n;\ j=1,2,...,N_{tr};\right\}$ and a field point $x \in \Re^n$, where N_{tr} is the number of trial centres. Due to the RBF spherical symmetry around the centres ξ^j (trial points), they are called radial. The distances $\left\|x-\xi^j\right\|$, are usually taken to be the Euclidean metric. The set of field points where the function is evaluated in the interpolation are known as test or collocation points. In RBF interpolation it is usual to select the trial and test points as the same set of points; however this is not necessary in principle.

The most popular RBFs are listed in Table 1.1 below:

Radial basis functions (RBFs)		
Generalized Thin Plate Spline	Generalized Multiquadric	Gaussian
$r^{2M-2}\log r$	$\left(r^2+c_S^2\right)^{M/2}$	$exp\left(-r^2/c_S^2\right)$
where M is an integer and $r=\left\|x-\xi^j\right\|$.		

Table 1.1 - Table of most popular Radial Basis Functions

The Gaussian and the inverse multiquadric, i.e. $M<0$ in the generalised multiquadric function, are positive definite functions. The thin-plate splines (TPS) and the multiquadric, i.e. $M>0$, are conditionally positive definite functions of order M, which require the addition of a polynomial term of order $M-1$ along with a homogeneous constraint condition (see equation (1.3) below) in order to obtain an invertible interpolation matrix. The multiquadric functions with values of $M=1$ and $c_S=0$ are often referred to as conical functions and with $M=3$ and $c_S=0$, as Duchon cubic.

Even though TPS have been considered optimal in interpolating multivariate functions, they only converge linearly, Powell (1994). On the other hand, the multiquadratic (MQ) functions converge exponentially as shown by Madych and Nelson (1990); however they contain a free parameter, c_S, often referred to as the shape parameter. When c_S is small the resulting interpolating surface is pulled tightly to the data points, forming cone-like basis functions and as c_S increases, the peak of the cone gradually flattens. It is worth noting that the set up of this parameter is not trivial and is still a matter of intensive research (see Wright and Fornberg (2006)).

In a typical interpolation problem, there are N pairs of data points $\{(x^i,\Phi(x^i))_{i=1,2,..N}\}$, which are assumed to be samples of the unknown function Φ that is to be interpolated by the function ϕ as

$$\phi(x)=\sum_{j=1}^{N}\alpha_j\Psi\left(\left\|x-\xi^j\right\|\right)+\sum_{j=1}^{NP}\alpha_{j+N}P_{M-1}^j(x) \tag{1.1}$$

in the sense that

$$\Phi\left(x^i\right)=\sum_{j=1}^{N}\alpha_j\Psi\left(\left\|x^i-\xi^j\right\|\right)+\sum_{j=1}^{NP}\alpha_{j+N}P_{M-1}^j\left(x^i\right) \tag{1.2}$$

along with the constraint condition

$$\sum_{j=1}^{N} \alpha_j P_{M-1}^k\left(x^j\right) = 0 \qquad k = 1,\ldots,NP \tag{1.3}$$

Here α_j, with $j = 1,\ldots,N,N+1,\ldots,N+NP$, are real coefficients to be found from the interpolation. Ψ is a radial basis function and NP is the total number of terms in the polynomial (determined by the polynomial order M and the number of spatial dimensions). In order to retain a simple notation the polynomial terms that appear in the second term of the right hand side of (1.1) will be indicated as P_{M-1}.

The matrix formulation of the above interpolation problem can be written as $[A][\alpha] = [b]$ with

$$[A] = \begin{pmatrix} [\Psi] & [P_{M-1}] \\ [P_{M-1}^T] & [0] \end{pmatrix}$$

$$[b]^T = \left(\left[\Phi\left(x^i\right)\right],[0]\right) \tag{1.4}$$

Micchelli (1986) proved that for a case where the test points are all distinct, the matrix resulting from the above radial basis function interpolation is always non singular. Although a matrix such as $[A]$ is always invertible in theory, i.e. well posed, numerical experiments show that the condition numbers of the matrix obtained with the use of RBFs like Gaussian or multiquadric are extremely large when compared with those resulting from the generalised thin-plate splines with low values of M, Schaback (1995). Similar condition number issues to those encountered with the use of the Gaussian or multiquadric functions are found when using the generalised thin-plate splines function with large values of M.

Consider now a boundary value problem defined by

$$L[\phi] = f_s(x) \quad \text{on} \quad \Omega \tag{1.5}$$

$$B[\phi] = f_B(x) \quad \text{on} \quad \partial\Omega \tag{1.6}$$

where the operators L and B are linear partial differential operators on the domain Ω and on the contour $\partial\Omega$ respectively. The unsymmetric RBF collocation method, also referred to as Kansa's method (KRBF), represents the solution of the above boundary value problem by the

interpolation (1.1). In the collocation scheme of the Kansa's method, a set of N test points are considered, these are divided in N_{bc} boundary points, where the boundary condition (1.6) is imposed, and $N - N_{bc}$ interior points, where the governing equation (1.5) is satisfied. The trial points are usually chosen to be the same set of the test points.

The above expansion for ϕ leads to a collocation matrix $[A]$ of the form:

$$[A] = \begin{pmatrix} B_x[\Psi] & B_x[P_{M-1}] \\ L_x[\Psi] & L_x[P_{M-1}] \\ P_{M-1}^T & 0 \end{pmatrix} \tag{1.7}$$

which is fully populated and non-symmetric.

The unsymmetric approach has been applied to a wide range of problems with great success. See for example Hon and Mao (1998) and Fedoseyev et al. (2002). However, no existence of solution and convergence analysis are available in the literature, and it has been reported that in some cases the resulting matrices were extremely ill-conditioned and even singular for some distribution of the nodal points, Dubal et al. (1993). In those cases where the matrix obtained is singular, it is possible that a small perturbation of the functional centre locations or the value of the shape parameter can result in a non-singular matrix Brown (2005). More recently, Ling et al. (2006) showed the feasibility of a generalised variant of the Kansa's method by using separated trial and test spaces. Under this condition, for a sufficiently dense set of N_{tr} linearly independent continuous trial functions and a set of N test points, whose locations are chosen to minimise the residual, the resulting interpolation matrix has full rank N_{tr}. Then it is possible to find a trial centres distribution for which the resulting Kansa's collocation matrix can be non-singular.

Fasshauer (1997) suggested an alternative approach to the unsymmetric method, based on the Hermite interpolation property of the radial basis functions. This states that the RBFs are not only able to interpolate a given function, but also any integral or partial differential operators. This method will be referred to as HRBF. The convergence proof for a RBF Hermite-Birkhoff interpolation was given by Wu (1992) who subsequently also proved the convergence of this approach when solving PDEs, Wu (1998) (see also Franke and Schaback (1998)). In this approach, the solution ϕ of the above boundary value problem is defined by

$$\phi(x)=\sum_{j=1}^{N_{bc}}\alpha_j B_\xi \Psi\left(\left\|x-\xi^j\right\|\right)+\sum_{j=N_{bc}+1}^{N}\alpha_j L_\xi \Psi\left(\left\|x-\xi^j\right\|\right)+\sum_{j=1}^{NP}\alpha_{j+N}P_{M-1}^j(x) \qquad (1.8)$$

In the above expression L_ξ and B_ξ are the differential operators used in (1.5) and (1.6) acting on Ψ viewed as a function of the second argument ξ. Applying the boundary condition (1.6) to the interpolation (1.8) in the N_{bc} boundary points, and the governing equation (1.5) in the $N-N_{bc}$ interior points, leads to a symmetric collocation matrix $[A]$, which is of the form

$$[A]=\begin{pmatrix} B_x B_\xi[\Psi] & B_x L_\xi[\Psi] & B_x[P_{M-1}] \\ L_x B_\xi[\Psi] & L_x L_\xi[\Psi] & L_x[P_{M-1}] \\ B_x\left[P_{M-1}^T\right] & L_x\left[P_{M-1}^T\right] & [0] \end{pmatrix} \qquad (1.9)$$

The matrix (1.9) is of the same type as the scattered Hermite interpolation matrices and thus non-singular as long as Ψ is chosen appropriately, i.e. provided that there are no collocation points that share linearly dependent operators, Wu (1992), Wu (1998). A major point in favour of the Hermite based approach is that the matrix resulting from the scheme is symmetric, as opposed to the completely unstructured matrix of the same size resulting from the unsymmetric scheme. For further details on the application of the above HRBF collocation approach see La Rocca et al. (2005).

Another flexibility of the Hermitian method consists of applying the PDE operator directly on top of boundary points without causing a singularity in the collocation matrix. This is an intrinsic feature of this method, in which the solution is constructed from operators applied to the basis functions rather than the basis functions themselves. This technique is known as 'double collocation', and was recently studied by La Rocca and Power (2008). They found that using double collocation at the boundary points offered great improvements in the accuracy of the solution near the domain boundary particularly in the approximation of derivatives. The improvement using double collocation is better than using an additional set of internal points and moving them closer to the boundary. It is worth noting that the requirement of satisfying simultaneously both the boundary condition and governing equation yields to a C^2 continuity of the approximation at the boundary points. In general, in a Hermite approach, the resulting matrix will be non-singular as long as the partial differential operators applied to each point are linearly independent; even if in a single node, more than two different differential operators are imposed.

In principle the double boundary collocation scheme can be implemented also in the unsymmetric approach (Kansa's method). However, due to lack of dependence on the differential operators in the interpolation formula, see equation (1.1), this alternative will return an over-determined system of algebraic equations that can be solved in the least square sense. Another alternative of imposing both internal and boundary operators on the domain boundary when using the Kansa's method, without obtaining an over-determined system, is offered by the use of two different set of collocation points at the boundary in which the differential conditions are required to be satisfied independently, Fedoseyev et al. (2002). But with this approach the two differential operators cannot be imposed simultaneously in the same set of boundary nodes.

From a series of simple steady state numerical examples, Fasshauer (1997) concluded that the Hermitian method performs slightly better than Kansa's method in most circumstances. More recently Power and Barraco (2002) found that the unsymmetric method faced some difficulties when solving convection-diffusion problems at high Péclet number, which do not occur when using the Hermitian approach. Jichun and Chen (2003) pointed out that such inconvenience can be removed by using higher-order radial basis functions and overlapping domain decomposition technique.

The computational costs of both the symmetric and unsymmetric methods are very high due to the use of global interpolation functions in the representation of the problem solution, resulting in fully populated coefficient matrices. Besides, the matrices obtained tend to become progressively more ill-conditioned as the number of trial and test points increase, and for interpolation functions featuring higher degree M. For cases where it is necessary to employ a large number of points (over a few thousands) the resulting systems are practically unsolvable with the use of standard algorithms.

Several techniques have been proposed to improve the conditioning of the coefficient matrix and the solution accuracy, such as the replacement of global solvers by block partitioning, LU decomposition schemes, matrix preconditioners, overlapping and non-overlapping domain decomposition amongst others (for an overview see Kansa and Hon (2000)).

One of the last efforts to improve the solution algorithms for such badly conditioned systems is found in Ling and Hon (2005). In this paper a method based on an affine space decomposition that decouples the influence between the interior and boundary collocations is proposed. Even though the results are encouraging, this method requires a singular value decomposition (SVD), resulting in a quite expensive solution procedure from a computational point of view.

Other research groups have been working on approaches based on domain decomposition methods. Between them Wong et al. (1999) developed a multizone algorithm for the mutiquadric scheme to reduce the matrix size. Zhou et al. (2003) tested the overlapping domain decomposition with both multiplicative and additive Schwarz iterative techniques for the Kansa's (unsymmetric) RBF collocation method, while Hernandez Rosales and Power (2007) proposed a non-overlapping domain decomposition algorithm for the Hermite radial basis function meshless collocation method.

Another alternative to the global interpolation is given by the use of the compactly supported RBFs. These type of functions return sparse interpolation matrices since only few terms have to be considered for the evaluation of the interpolants. Each function is defined by a centre and a compact support r

$$\Psi = \begin{cases} \Psi'(r) & 0 \le r \le 1 \\ 0 & r > 1 \end{cases} \tag{1.10}$$

Wendland (1995) derived positive definite functions for one, three, and five-dimensional problems of different degree of continuity starting from the truncated power functions. These functions are reported in Table 1.2 for three dimensional problems together with their degree of continuity

$nd = 3$	$\Psi' = (1-r)_+^2$	C^0	(1.11)
	$\Psi' = (1-r)_+^3 (3r+1)$	C^2	(1.12)
	$\Psi' = (1-r)_+^6 (35r^2+18r+3)$	C^4	(1.13)
	$\Psi' = (1-r)_+^8 (32r^3+25r^2+8r+1)$	C^6	(1.14)

Table 1.2 - Compact support functions

The choice of the support size is the critical point of those methods based on this type of functions. It has been found that the best solutions are obtained for a support of the same size of the computational domain, a situation that brings back all the problems encountered in a global formulation.

Although many attempts have been made to resolve these issues, solving practical engineering applications with meshless collocation methods based on the global RBF interpolation is still considered prohibitive. In recent years, special attention has been given to the use of local RBF interpolations which are assembled to obtain the global solution (see Lee et al. (2003), Shu et al.

(2003), Sarler and Vertnik (2006), Vertnik et al. (2006), Stevens et al. (2009)). The local strategy results in well-conditioned and banded systems improving the behaviour of this type of meshless methods.

1.2 Objective and motivations

The work carried out in the present thesis is devoted to develop a hybrid method between classical CV schemes and RBF mesheless collocation methods with the intent of exploiting at most the best features of these two numerical techniques. In the finite volume community there is evidence of a constant research to find more accurate and flexible interpolation algorithms to be used in the flux reconstruction step for the case of unstructured meshes. On the other hand, the mesheless collocation methods are among the best numerical schemes in dealing with scatter data points, and the RBF have been found to be the most accurate interpolations by many researchers. At the same time they suffer ill-conditioning problems that limit their use to relatively simple problems.

The main objective of this research is to develop a method that combines the RBF strong form formulation applied locally to each cell, with the CV weak form to solve the global problem. The new numerical scheme will benefit the mass conservation and the sparse matrix of the control volume scheme and the high accuracy of the RBF meshless methods in the local interpolations also in those cases of non uniform distribution of points. From a different point of view, it could be said that the new method aims to overcome the ill-conditioning problem typical of the RBF meshless collocation methods, and at the same time offers a valid alternative to the classical polynomial functions used in the flux reconstruction of CV schemes.

Although the meshless benefit is lost in the global formulation, due to the use of an element mesh, this feature is preserved locally, opening great opportunities in the selection of the stencil of points that support the local interpolation and in the boundary conditions implementation.

The problems solved in this work are focused on groundwater water applications since the present study was funded by the European Commission GABARDINE project (Contract no: 518118), sixth framework program, priority 1.1.6.3 (Global change and Ecosystems).

All the results are obtained using a in-house software written mainly in FORTRAN 95 by the author, while a commercial mesh generator (GAMBIT, Ansys) is employed in the construction of the computational grids needed for the domain discretisation.

1.3 Original contribution

In Moroney and Turner (2006) and (2007) , a local interpolation of the field variable based on equation (1.1) is used to construct the shape functions of the CV-FEM method. The centres of the control volumes belonging to the stencil are used as the corresponding trial and test points of the interpolation.

Following Moroney and Turner (2006); (2007), in this thesis it is proposed to use a RBF meshless technique to improve the accuracy of classical CV schemes. The method is based on a local RBF interpolation of the field variable at the control volume cell centres, as in the case of Moroney and Turner CV-RBF approach. In addition, in the present approach, the local interpolation is required to satisfy the partial differential equation (PDE) of the governing equation and the boundary condition operators at a set of auxiliary points in the interpolation stencils. The corresponding interpolation of the field variables, internal and boundary differential operators is equivalent to solve a local initial/boundary value problem, for which the solution is found by using the meshless collocation techniques recalled in section 1.1.2. Therefore, this approach combines the meshless strong form formulation applied to the local initial/boundary value problems with the CV weak form used to solve the global problem. In this way a high order CV scheme is obtained resolving the ill-conditioning issues encountered in the reconstruction step by Abgrall (1994) and Dumbser and Kaser (2007) for the computation of the polynomial coefficients. In fact, choosing the RBF type appropriately and limiting the number of collocation points used leads to an interpolation that is well posed in all dimensions. This method is also more flexible than the classical CV formulations because the boundary conditions are explicitly imposed in the interpolation formula, without the need for artificial schemes (e.g. utilising dummy cells).

The use of prescribed local interpolation functions (polynomials, RBFs etc.) that do not satisfy the original governing equation is a common approach used in all numerical techniques based on a weak formulation. These local approximations strongly limit the result of the obtained global solutions (including Turner et al. CV-RBF approach), independently of how robust is the integral representational formula used in the approach (even in those BEM cases when the exact integral representational formula is obtained from the Greens identities). For analytical functions the success of these weak formulations using this type of interpolation is a consequence of the theorems on analytical continuation, which guarantee the representation of the unknown function in terms of polynomial series in a neighbourhood around a collocation point (Taylor series), restricting these approaches to the use of small elements or cells.

In the new approach presented in this work, instead of using previously prescribed interpolation function, local approximate solutions of the original partial differential equations are used as interpolants, which also satisfy the boundary condition in those stencils enclosing boundary points. The use of interpolating functions that satisfy the boundary condition is a well-established scheme in numerical analysis and it has been the basis of some classical numerical approaches, as in the case of the Ritz method for the calculus of variations. However, in the hybrid control volume/meshless collocation method proposed in this thesis, local approximate solutions of the governing equation based on RBF collocation approaches are used as interpolation functions to improve the performance of a CV method for the first time, see Orsini et al. (2008).

Having an interpolation that satisfies locally the partial differential operator, including the advective terms, provides an implicit upwind formulation. In fact, the velocity field contained in the PDE operator is directly included in the local RBF interpolation, providing the required information about the flow direction on the evaluation of the advective fluxes. In this approach, it is not necessary to recourse to upwinding schemes in order to obtain the solution of advective dominant problems without spurious oscillations. Each local system is centrally defined, without the need of using interpolation stencils predefined according to the magnitude and direction of the local advective flow velocity.

1.4 Structure of the thesis

In chapter 2 the formulation of the CV scheme proposed is presented for the solution of general boundary value problems. Both the unsymmetric (Kansa's method) and symmetric (Hermitian method) RBF collocation methods can be used in the local solution and the method will be referred as CV-KRBF or CV-HRBF depending on which of the two approaches is adopted. The new numerical scheme is validated in a series of one- and three-dimensional steady test cases, giving particular attention to the comparison between the CV-KRBF and CV-HRBF. In addition, a convergence analysis is performed, analysing different stencil configurations for the local interpolation. The effect of using different types of RBFs functions is also investigated.

In chapter 3 the CV-HRBF is extended to study transient transport problems. The local interpolation function, which relies on a Hermitian Radial Basis Function (HRBF), is found solving a local boundary/initial value problem using the same time integration scheme adopted to update the global CV solution. Two time-stepping formulations are considered: a full implicit approach and the weighted Crank-Nicholson one. A fully kinetic formulation for the solution of

non-linear reactive transport systems typical of groundwater quality control problems is also developed. The implicit upwinding scheme, intrinsic to the proposed CV-HRBF, is tested by solving a travelling front problem at Péclet number equal to 500, 1000 and infinity; with the latter corresponding to a shock front. In addition, the accuracy of the numerical method is validated against one and three-dimensional reactive transport problems characterised by smooth solutions. Finally the process of magnesite dissociation in local non-equilibrium conditions is modelled in an experimental column domain to validate the kinetic formulation of the CV-HRBF.

In chapter 4 two alternatives to improve the convergence of the CV-HRBF method for unstructured meshes are investigated: increasing the order of the numerical integration schemes, and the use of vertex centred (VC) discretisation which guarantees a numerically conservative scheme. The convergence and the flux analysis of the two approaches implemented are carried out in a one-dimensional advection diffusion problem using three unstructured meshes progressively refined. In addition the second order integration and the VC discretization are also assessed for steady and unsteady three dimensional advection diffusion problems using unstructured meshes.

In chapter 5 the CV-HRBF scheme is adapted to solve ground water flow in the saturated zone of the semi-confined aquifer. The method is combined with a local re-meshing technique in order to track the phreatic surface, where the gradients required to satisfy the kinematic condition are computed by the same local RBF interpolations used for the flux computation. The proposed numerical approach is validated in a series of three-dimensional groundwater flow problems where the operations of recharging and extracting water from a semi-confined aquifer are modelled. Finally the injection into the saturated zone carried out from one of the GARBADINE project partners in the experimental test site of Campina De Faro (Portugal) is also modelled, and the result compared with the available experimental data.

In chapter 6 a non-overlapping non-iterative multi-domain formulation for the CV-HRBF is proposed, where the local Hermitian RBF meshless collocation method is used to satisfy a physical matching condition at the sub-domain boundaries. The algorithm is first validated in one-dimensional advection diffusion problems for which an analytical solution is known. More general applications in two and three dimensional domains are then considered. A heat transfer problem in strongly heterogeneous materials, and a groundwater flow problem in presence of geological layers characterised by different hydraulic conductivity are taken as engineering applications to test the capabilities of the CV-HRBF method to handle multizone problems. A final test is carried out for a one-dimensional unsteady transport problem for a single species in

a channel consisting of two adjacent zones that feature a different Peclet number. This is part of an on-going research that will be completed in the near future.

2 THE CV UNSYMMETRYC (Kansa), AND SYMMETRIC (Hermite) RBF FORMULATIONS (CV-K/HRBF) FOR BOUNDARY VALUE PROBLEMS

2.1 Introduction

To construct local interpolants as approximate solutions of the problem being solved, the most critical point is to couple the solution of the local boundary value problems, one for each cell, to the global control volume assembling procedure. With any RBFs, the local approximate solutions can be found using the KRBF or the HRBF methods introduced in section 1.1.2. The resulting interpolations can be linked to the control volume solution by expressing the global unknown values as Dirichlet conditions in the RBF collocation system. This way of coupling the finite volume equation with the strong RBF formulation is the most natural one, and it already has been used in Moroney and Turner (2006) (2007) and Orsini et al. (2008). In the works by Moroney and Turner a simple RBF interpolation is used, while in Orsini et. al. the K/HRBF approach is employed. In the case of the K/HRBF technique, applying the PDE and boundary operators to the local interpolation in a set of auxiliary points does not change the coupling algorithm, but instead increases the size of the local RBF collocation system. The additional information provided by the PDE and the boundary operator points transform the normal interpolation to a boundary value problem solution, and the increase in computational cost and complexity of implantation at local level is the price to be paid for such an improvement.

Both KRBF and HRBF methods can be used in the local solution. The method proposed in this thesis will be referred to as CV-KRBF or CV-HRBF, depending on which of the two approaches is adopted. It is worth mentioning that the KRBF can be considered as a sub-case of HRBF where neither the PDE nor boundary operators are considered as trial functions (see section 1.1.2). As a consequence, only the CV-HRBF will be comprehensively presented in the next section. Once this scheme is understood, the corresponding CV-KRBF can be obtained from the previous one by cancelling few terms in the interpolation and significantly simplifying the local system.

For the sake of simplicity in the presentation of the formulation, the schematic diagrams showing implementation details will be presented for two-dimensional cell centre structured volume elements. However, the proposed method is also valid for three-dimensional problems, for structured and unstructured meshes, as it is independent from cell shape and mesh type. This flexibility reflects one of the advantages of using an RBF interpolation rather than polynomial functions in the flux reconstruction algorithm. In this chapter only the cell centred discretisation scheme is considered, while the vertex centred formulation will be introduced in chapter 4.

2.2 The CV-K/HRBF formulation

Consider a steady boundary-value problem for which the governing equation features an advective term, a diffusion term, a reactive term and a general source

$$L(\phi)=\frac{\partial}{\partial x_i}\left(D_{ij}\frac{\partial \phi}{\partial x_j}\right)-\frac{\partial U_i\phi}{\partial x_i}+K_r\phi=f_s(x) \qquad i,j=1,nd \quad \text{on} \quad \Omega \tag{2.1}$$

$$B(\phi)=f_B(x) \qquad \text{on} \qquad \partial\Omega \tag{2.2}$$

where $x\in R^3$, ϕ is the unknown field variable, D_{ij} is the diffusivity tensor, U_j is the component of the advective velocity along the j-direction, K_r the reactive coefficient. In equation (2.2) $B(\ )$ is the corresponding partial differential operator defining the boundary conditions, i.e. equal to the value of the function when Dirichlet conditions are given, the normal derivative for Neumann conditions and a combination of the two in the case of Robin or mixed conditions.

Following the approach of the classical cell-centred CV scheme, equation (2.1) is integrated over the grid elements, leading to

$$\int_{V_P}\frac{\partial}{\partial x_i}\left(D_{ij}\frac{\partial \phi}{\partial x_j}\right)dV-\int_{V_P}\frac{\partial U_i\phi}{\partial x_i}dV+\int_{V_P}K_r\phi dV=\int_{V_P}f_s(x)dV \tag{2.3}$$

Applying the divergence and the mean value theorems, the following equation is obtained

$$\int_S\left(D_{ij}\frac{\partial \phi}{\partial x_j}-U_i\phi\right)n_i dS+K_rV_P\bar{\phi}_P=V_P\bar{f}_{sP} \tag{2.4}$$

where the bar indicates the cell average operator over the control volume, $\overline{(\bullet)} = 1/V_P \int_{V_P} (\bullet) dV$, and V_P is the volume of the cell over which the integration is performed. The volume integrals are evaluated using the midpoint integration formula, i.e. the mean values $\bar{\phi}_P$ and $\bar{f}_{sP}$ in equation (2.4) are considered to be located at the control volume centre. If *Nsurf* is the number of cell faces in the control volume, the integral over the control volume surface can be divided into *Nsurf* sub-integrals

$$\int_S \left(D_{ij} \frac{\partial \phi}{\partial x_j} - U_i \phi \right) n_i dS = \sum_{l=1}^{Nsurf} \int_{S_l} \left(D_{ij} \frac{\partial \phi}{\partial x_j} - U_i \phi \right)\Big|_l n_i^l dS \tag{2.5}$$

As done in equation (2.4) for the volume, the surface integrals are approximated by the midpoint integration formula. The surface mean values of the function ϕ and its gradient are assumed to be placed at the midpoint of the cell faces; this approximation leads to the following control volume discretisation equation

$$\sum_{l=1}^{Nsurf} \left(D_{ij} \frac{\partial \phi}{\partial x_j} - U_i \phi \right)\Big|_l n_i^l S_l + K_r V_P \bar{\phi}_P = V_P \bar{f}_{sP} \tag{2.6}$$

where n_i^l is the *i*-component of the outward pointing normal to the l^{th} face and S_l the area of the l^{th} face. In equation (2.6), the field variable ϕ and its gradient at the centre of the cell faces are given in terms of the cell average values found in the interpolation stencil. This is done by the use of a RBF interpolation as described in the next paragraphs. Different alternatives to improve the numerical integration are considered in chapter 4, where two approaches of increasing the order of the surface and volume integrations are investigated and tested.

The cell centres of the surrounding control volumes, along with a few scattered data points placed inside and nearby the neighbouring cells, are used as a set of trial points for the local RBF interpolation. In addition, if a stencil is close to a domain boundary, the points at the intersection between the boundary and the stencil are also included in the interpolation, Figure 2.1. Applying a Dirichlet condition at the cell centres, the boundary operator (2.2) at the boundary points, and the internal operator (2.1) at the auxiliary scattered points, a local Hermitian interpolation formula can be defined as

$$\phi(x)=\sum_{c.centres}\alpha_n\Psi\left(\left\|x-\xi^n\right\|\right)+\sum_{B.Operator}\alpha_n B_\xi\Psi\left(\left\|x-\xi^n\right\|\right)+\sum_{L.Operator}\alpha_n L_\xi\Psi\left(\left\|x-\xi^n\right\|\right)+P_{M-1}(x) \tag{2.7}$$

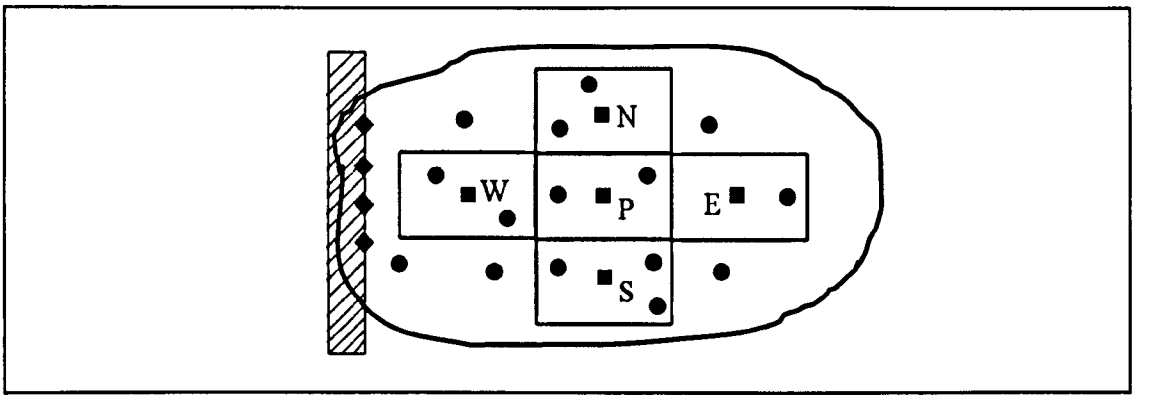

Figure 2.1 - Cell stencil and set of points used by the CV-K/HRBF scheme. Round symbols correspond to points where the internal (PDE) operator is imposed; square symbols for the Dirichlet operator and diamond symbols for the boundary operator

By evaluating the different operators (Dirichlet, PDE and boundary) on the interpolation formula (2.7) at the corresponding collocation points, the following algebraic system is obtained for the unknown interpolation coefficients

$$[A][\alpha]=[b] \tag{2.8}$$

where

$$[A]=\begin{pmatrix}[\Psi] & B_\xi[\Psi] & L_\xi[\Psi] & [P_{m-1}]\\ B_x[\Psi] & B_xB_\xi[\Psi] & B_xL_\xi[\Psi] & B_x[P_{m-1}]\\ L_x[\Psi] & L_xB_\xi[\Psi] & L_xL_\xi[\Psi] & L_x[P_{m-1}]\\ \left[P^T_{m-1}\right] & B_x\left[P^T_{m-1}\right] & L_x\left[P^T_{m-1}\right] & [0]\end{pmatrix} \quad [b]=\begin{bmatrix}\left[\bar{\phi}_{cells}\right]\\ [f_B]\\ [f_s(x)]\\ [0]\end{bmatrix} \tag{2.9}$$

and $\left[\bar{\phi}_{cells}\right]^T=\left(\bar{\phi}_P,\bar{\phi}_W,\bar{\phi}_E,\bar{\phi}_S,\bar{\phi}_N\right)$ are the values of the unknown field variable ϕ at the cell centres (see Figure 2.1). The matrix A in (2.9) corresponds to the Hermite RBF matrix obtained from the meshless collocation approach used to find the local approximate solutions of the governing equation. As commented in section 1.1.2 this matrix is non-singular according to Wu's theorems (see comments after equation (1.9) where in the case of (2.9) additional Dirichlet conditions are included).

At this stage it is not possible to determine the coefficients of the Hermitian interpolation, since one part of the right hand side of the system (2.8) is defined by the unknown field variable (i.e. the array $\left[\bar{\phi}_{cells}\right]$ made of the cell-centered values of the function ϕ). However, system (2.8) can be rewritten to express the interpolation coefficients as a function of the unknown values $\left[\bar{\phi}_{cells}\right]$ as

$$[\alpha]=[A]^{-1}[b] \tag{2.10}$$

The function ϕ at any point, x^I, inside the stencil, is obtained by substituting the interpolation coefficients given by (2.10) in (2.7)

$$\begin{aligned}\phi|_I = &\sum \alpha_n \left(\Psi\left(\|x-\xi^n\|\right)\right)\Big|_{x=x^I} + \sum \alpha_n \left(B_\xi \Psi\left(\|x-\xi^n\|\right)\right)\Big|_{x=x^I} \\ &+ \sum \alpha_n \left(L_\xi \Psi\left(\|x-\xi^n\|\right)\right)\Big|_{x=x^I} + \left(P_{M-1}(x)\right)\Big|_{x=x^I}\end{aligned} \tag{2.11}$$

while the corresponding gradient is obtained by differentiating equation (2.11)

$$\begin{aligned}\left.\frac{\partial \phi}{\partial x_j}\right|_I = &\sum \alpha_n \left(\frac{\partial}{\partial x_j}\Psi\left(\|x-\xi^n\|\right)\right)\Big|_{x=x^I} + \sum \alpha_n \left(\frac{\partial}{\partial x_j} B_\xi \Psi\left(\|x-\xi^n\|\right)\right)\Big|_{x=x^I} \\ &+ \sum \alpha_n \left(\frac{\partial}{\partial x_j} L_\xi \Psi\left(\|x-\xi^n\|\right)\right)\Big|_{x=x^I} + \left(\frac{\partial}{\partial x_j} P_{M-1}(x)\right)\Big|_{x=x^I}\end{aligned} \tag{2.12}$$

Since the coefficients $[\alpha]$ of the interpolation depend on the cell average values $\left[\bar{\phi}_{cells}\right]$, the function and its gradient expressed in Equations (2.11) and (2.12) will also do.

Equations (2.11) and (2.12) can be rearranged in a concise form

$$\phi|_I = C^I_{1n}\alpha_n \tag{2.13}$$

$$\left.\frac{\partial \phi}{\partial x_j}\right|_I = C^I_{2jn}\alpha_n \tag{2.14}$$

where

$$\left[C_{1n}^{I}\right]^{T}=\left(\left[\Psi\left(\left\|x-\xi^{n}\right\|\right)\right],\left[B_{x}\Psi\left(\left\|x-\xi^{n}\right\|\right)\right],\left[L_{\xi}\Psi\left(\left\|x-\xi^{n}\right\|\right)\right],\left[P_{M-1}(x)\right]\right)\Big|_{x=x^{I}} \tag{2.15}$$

$$\left[C_{2jn}^{I}\right]^{T}=\frac{\partial}{\partial x_{j}}\left(\left[\Psi\left(\left\|x-\xi^{n}\right\|\right)\right],\left[B_{x}\Psi\left(\left\|x-\xi^{n}\right\|\right)\right],\left[L_{\xi}\Psi\left(\left\|x-\xi^{n}\right\|\right)\right],\left[P_{M-1}(x)\right]\right)\Big|_{x=x^{I}} \tag{2.16}$$

Finally, substituting the values of ϕ and its gradient at the midpoint of each cell face in terms of the interpolation formulae (2.13) and (2.14), equation (2.6) reduces to

$$\sum_{I=1}^{Nsurf}\left(D_{ij}C_{2jn}^{I}-U_{i}C_{1n}^{I}\right)n_{i}^{I}S_{I}\alpha_{n}+K_{r}V_{P}\bar{\phi}_{P}=V_{P}\bar{f}_{sP} \tag{2.17}$$

Equation (2.17) is the final CV-HRBF formula which couples the field value at the central cell of the stencil, $\bar{\phi}_{P}$, with the values at the neighbouring cells centres, $\left(\bar{\phi}_{P},\bar{\phi}_{W},\bar{\phi}_{E},\bar{\phi}_{S},\bar{\phi}_{N}\right)$. By assembling equation (2.17) corresponding to all the stencils in the domain, a global system of equations for ϕ is obtained, therefore by inverting the corresponding global matrix the solution can be updated. After solving the global system of equations, the cell average values $\left[\bar{\phi}_{cells}\right]$ are known and the corresponding values of the local interpolation coefficients $\left[\alpha\right]$ are obtained from equation (2.10). With the values of $\left[\alpha\right]$ available, the value of the solution and its gradient, anywhere inside and in the vicinity of a cell can be reconstructed using equations (2.11) and (2.12).

It is important to observe that at this point the boundary conditions are already imposed at the level of the local interpolation, therefore it is not necessary to incorporate them in the global CV system. Further assessments about this issue will be discussed later in section 2.4.

The CV-KRBF can be obtained from the previous derivation where the Hermitian interpolation (2.7) is replaced but the simpler RBF interpolation used in the Kansa's approach:

$$\phi(x)=\sum_{n=1}^{N}\alpha_{n}\Psi\left(\left\|x-\xi^{I}\right\|\right)+P_{M-1}(x) \tag{2.18}$$

where N is the total number of points considered in the local interpolation, i.e. control volume centroids, boundary condition points and PDE points.

The CV-HRBF and CV-KRBF method can be considered as a high order scheme for calculating diffusive fluxes, given the high order accuracy of the RBF derivative approximation (Madych (1992); Fornberg and Flyer (2005)). Furthermore a kind of an analytical upwinding scheme is introduced by imposing the PDE operator in the interpolation formula which contains the desirable information about the advective velocity field. In this approach each local system is centrally defined, without the need of using interpolation stencils predefined according to the magnitude and direction of the local advective flow velocity, i.e. it is not necessary to use any kind of upwinding scheme. This aspect will be considered in detail in the next chapter.

2.3 Stencil configuration and size

In the previous section, the mathematical formulation for the proposed CV-K/HRBF method has been derived on the basis of a number of stencils equal to the number of elements used to discretise the physical domain. From here on, this approach will be named as the one-stencil-one-cell configuration. However this is not the only approach that can be considered in the implementation of the new CV approach proposed.

The conservativeness of the numerical scheme is the first condition that needs to be satisfied when choosing the stencil configuration; i.e. in order to conserve mass, the flux leaving a control volume through one of its faces, must be equal to the flux entering the neighbouring control volume that shares the same face. In the one-stencil-one-cell configuration, as the one sketched in Fig. 2.2, this property is guaranteed by coupling the neighbouring cells in the local problem formulation. To resolve a particular control volume or cell, the two cells adjacent to a face must be included in the local problem; for example five cells will be considered in Stencil 1 for the layout shown in Figure 2.2. The overlapping region formed by Cells 1 and 2 guarantees the uniqueness of the flux value for face A when computing the interpolations for stencils, 1 and 2. This is equivalent to solving two local boundary value problems that have the same governing equation and the same solution value in the points falling in the overlapping region. For this reason, at least from a theoretical point of view, the two solutions must be identical due to the uniqueness of the corresponding boundary value problem.

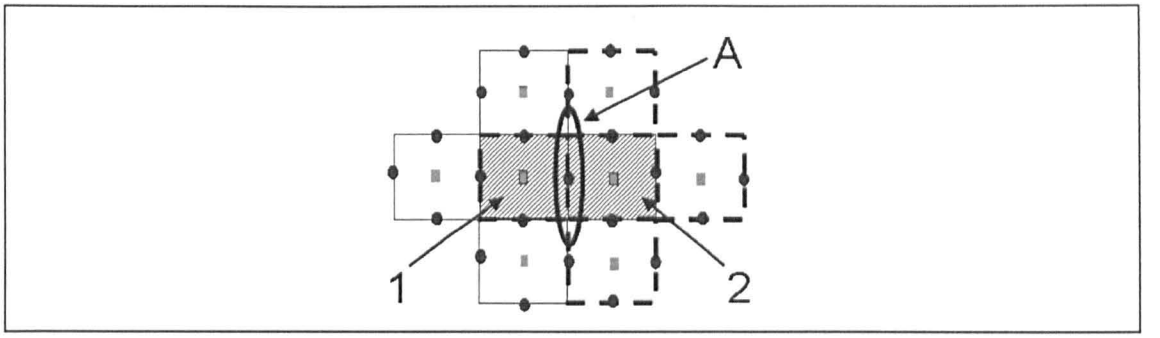

Figure 2.2 - One-stencil-one-cell configuration. Round symbols correspond to points where the internal (PDE) operator is imposed; square symbols for the Dirichlet operator.

An alternative to guarantee the conservativeness condition is to form a stencil for each cell face as shown in Figure 2.3. This is referred to as the one-stencil-one-face configuration. The face flux is computed only once for every cell face and the cell flux computation takes account of the number of stencils equal to the number of its faces. In Fig. 2.3 the basic cross stencil needed to calculate the fluxes at the faces of cell 1 is split into four simpler problems. This alternative requires the interpolation in those four regions containing the faces of cell 1, but with each of them having significantly less interpolation points in comparison with those used in the one-stencil-one-cell approach.

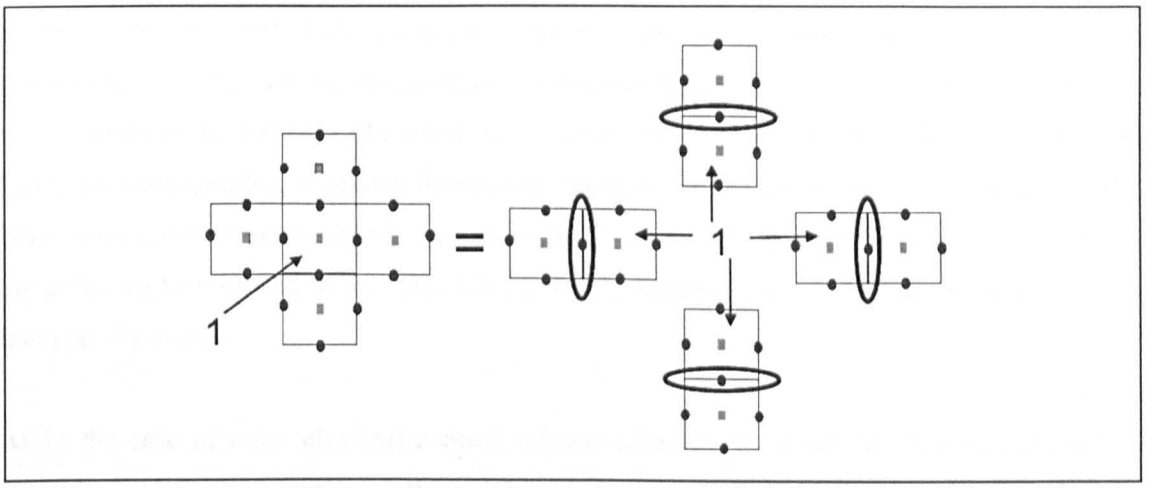

Figure 2.3 - One-stencil-one-face configuration. Round symbols correspond to points where the internal (PDE) operator is imposed; square symbols for the Dirichlet operator.

In terms of computational cost, the two configurations described above perform differently. In the one-stencil-one-cell configuration the total number of control volumes and stencils are the same and equal to the total number of elements ($Nele$). On the other hand, the one-stencil-one-face alternative requires a larger number of stencils than cells, with the number of stencils equal to $Nst = \beta Nele$ for $Nele$ cells, where β changes with the number of dimensions and the type of cell. For the case of 3D problems, the resulting value of β is between two (unstructured meshes) and four (structured meshes). However the impact on the computational cost of the

increment in the number of stencils, and consequently the number of local interpolations for the one-stencil-one-face alternative, is somehow balanced by the reduction on the stencil size, as it is evident by comparison of Figure 2.2 and Figure 2.3.

Although in principle the one-stencil-one-cell configuration guarantees the consistency of fluxes, due to the uniqueness of the solution induced by the overlapping region, numerically some discrepancies are observed due to the numerical error. On the other hand the one-stencil-one-face approach always guarantees the flux consistency since the flux reconstruction in a face shared by two cells is performed using the same interpolation.
Once the base for the stencil is chosen, either the cell-face or the cell-element, the points to be included in the interpolation need to be determined. The element structure can be exploited to choose a cloud of points that are well spaced between each other. In fact, having a smooth distribution of the radial distances between the trial centres of the interpolation significantly eases the solution of the local boundary value problem. The minimum number of control volume centres to be included in the interpolation must guarantee the coupling between the global unknowns. This number changes with the stencil configuration used. In the case of the one-stencil-one-cell configuration, the centre of the control volume and the cell centre of its neighbours must be included, Figure 2.1. Where the one-stencil-one-face configuration is adopted, the cell centres to be included are those of the two control volumes sharing the face considered. The PDE points can be placed in the face integration points and/or in the element nodes, while in the presence of domain boundaries, always coinciding with the control volume faces, the corresponding boundary differential operators can be applied to the face nodes and/or integration points. Due to the meshfree character of the local RBF interpolation, the selection of the points to be included in the stencil is extremely flexible and can be adapted depending on the type of problem.

As in the case of other classical control volume schemes, there are two ways of refining a numerical solution: by increasing the number of elements utilised to discretise the domain, and by improving the accuracy of the local interpolants. There are no particular differences to highlight for the first approach. Instead it is worth analysing the flexibility introduced by the RBFs in refining the local interpolation. As explored by Moroney and Turner (2006) (2007), the number of control volumes centre included in the interpolation can be increased considering the next level of neighbours. This strategy returns a global matrix with a larger number of non-zero entries, and it increases the size of the local system. However, it generally leads to a significant improvement in the solution. When polynomial functions are used rather than RBFs, enhancing the order of the interpolants for unstructured meshes is not trivial, and more importantly, it

requires the solution of local linear systems, which can present ill-conditioning issues also for small sizes, Abgrall (1994) and Dumbser and Kaser (2007).

In addition, the CV-K/HRBF method offers the possibility of improving the accuracy of the interpolants, increasing the number of the PDE points. This approach returns a larger local system without introducing any extra non-zero entries in the global sparse matrix. However, increasing the number of points where the local interpolation is required to satisfy the PDE operator behind a certain threshold does not improve the numerical solution due to the ill-conditioning issues related with the solution of the local system. If the number of PDE points used in the local interpolation is larger than a number as low as 10-15, the condition number of the local interpolation matrices quickly increases, and special numerical algorithms are required to find the corresponding inverses. In the numerical problems solved during this work, it was found that few PDE points were necessary at the local level to achieve considerable improvements. Also, increasing the number of data points, i.e. the number of control volume centres where the global unknowns are placed, leads to ill-conditioning issues. But for these points where the Dirichlet operator is applied, the practical threshold is remarkably larger (around 50). If it is necessary to further improve the accuracy of the solution locally, it is recommended to refine the CV mesh instead of increasing the number of interpolation points behind the indicated thresholds; this is to avoid large increments on the computational cost due to the use of special algorithms to invert the local interpolation systems. In this work, it was found that if the local system size goes above 50×50, the computation of a free-numerical-noise solution requires expensive methods, such as singular value decomposition or QR decomposition.

2.4 Boundary condition implementation

The meshless nature of the proposed method at local level impacts directly on the implementation of the boundary conditions (BC). Typical constraints of classical control volume schemes, such as the need for ghost or dummy cells at the boundaries, are removed by directly imposing the boundary conditions in the solution of the local meshless interpolation problem. In addition, boundary conditions can be applied everywhere inside the stencil without being confined to cell faces, opening great opportunities for the investigation of moving boundary problems. Imposing the BC on the local interpolation also allows an additional reinforcement to the global system terms (known) that express the BC in the sense of the classical CV approaches. In this way a more accurate and robust solution in the proximity of the domain boundaries can be obtained. Consider a domain boundary where a Neumann condition

is applied and a control volume face that falls in this boundary, e.g. face 1 in the example of Figure 2.4.

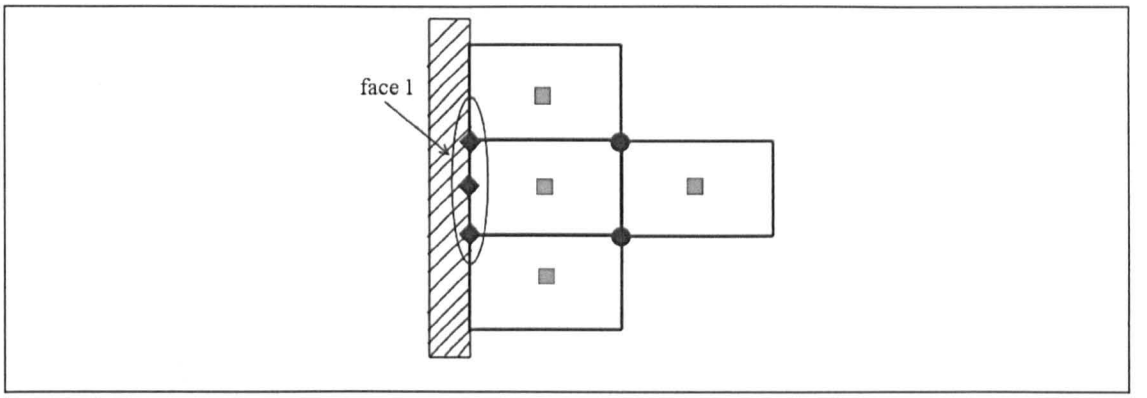

Figure 2.4 - Boundary condition implementation, boundary control volume. Round symbols corresponds to points where the internal (PDE) operator is imposed; square symbols for the Dirichlet operator and diamond symbols for the boundary operator.

The control volume equation (2.6) can be rewritten separating the numerical integration carried out on face 1

$$\left(D_{ij}\frac{\partial\phi}{\partial x_j} - U_i\phi \right)\Big|_1 n_i^1 S_1 + \sum_{l=2}^{Nsurf}\left(D_{ij}\frac{\partial\phi}{\partial x_j} - U_i\phi \right)\Big|_l n_i^l S_l + K_r V_P \bar{\phi}_P = V_P \bar{f}_{sP} \tag{2.19}$$

Since the projection of the gradient along the normal of the face is given by the Neumann condition, the diffusive contribution to the flux integral that appears in the first member of equation (2.19) is known and can be moved to the right hand side of the equation

$$\left(-U_i\phi\right)\Big|_1 n_i^1 S_1 + \sum_{l=2}^{Nsurf}\left(D_{ij}\frac{\partial\phi}{\partial x_j} - U_i\phi \right)\Big|_l n_i^l S_l + K_r V_P \bar{\phi}_P = V_P \bar{f}_{sP} - \left(D_{ij}\frac{\partial\phi}{\partial x_j} \right)\Big|_1 n_i^1 S_1 \tag{2.20}$$

The advective term of the integral requires the value of the function in the centre of the face. It will be reconstructed using the RBF interpolation, which already satisfies the BC at the boundary points of the stencil. On the contrary, if the known BC is of the Dirichlet type, the advective flux can be imposed in the control volume equation, i.e. given the value of ϕ on S_1 in equation (2.19), and the diffusive flux is reconstructed by the local RBF interpolation. This way of implementing the boundary conditions will be referred as BC-cvrbf.

Alternatively both terms of the flux integral on face 1 can be treated as unknowns and both the value of the function and its gradient will be reconstructed by the RBF interpolation; this method of imposing the boundary conditions will be named BC-rbf. This type of

implementation can be very useful if the boundary conditions are known only in the nodes of a boundary face but not in its integration points. In this case using the BC-rbf approach is equivalent to interpolating the BC values at the nodes of the face to reconstruct the values at the integration points.

A numerical example with a comparison between these two alternatives of implementing the BC is given in section 2.7.5

2.5 Computational cost considerations for the CV-KRBF and CV-HRBF

The global system obtained with the CV-K/HRBF method is sparse as those deriving from other classical CV discretisation schemes, while the bandwidth of its matrix depends on the number of control volume centres included in the local interpolation. For a fast solution of this type of system there are several sparse iterative solvers available in literature, and usually different type of preconditioners are used to accelerate the convergence algorithms, (Saad (1996), Saad (1988-2000)). Throughout the numerical experiments reported in this work, the Generalised Minimum Residual Method (GMRES) is used for the solution of the sparse linear system and a truncated incomplete LU factorization (ILUT) is adopted to precondition the system. This solution technique was found to be quite robust. However other efficient sparse system solution algorithms as the flexible GMRES (FGMRES) or the Conjugate Gradient (CG) algorithm were not tested because it was beyond the scope of this thesis.

The computational cost of the CV-K/HRBF diverges from the classical CV schemes due to the handling of the construction of the local interpolants. In fact, it is common practice for most of the CV schemes to reconstruct the cell faces fluxes using simple finite difference formulae that can be evaluated on the flight during the computation, see section 1.1.1. Instead, to obtain the local RBF interpolation of the CV-K/HRBF, a local linear system fully populated needs to be solved for each element of the mesh. This operation implies an extra computational cost of the order $Nst \times N^3$, where Nst is the total number of stencils and N is the number of points used for each local interpolation. Although this is an important cost to bear in mind for real life applications, it must be said that to achieve higher order CV schemes for unstructured meshes, other researchers ended up with the same problem (see Abgrall (1994), Dumbser and Kaser (2007) and Moroney and Turner (2006) (2007)).

In general, for the CV-K/HRBF, this cost can vary significantly with each type of application, according to the form of the PDE operator appearing in the local interpolation formula. Comments regarding this extra computational load will be given throughout the thesis for each application considered and for each variation of the numerical formulation.

2.6 The RBF free parameter computation

Up to this point, the formulation of the CV-K/HRBF has been presented considering a general RBF Ψ . In the practical implementation, one of the functions listed in the tables 1.1 and 1.2 must be chosen. The preferable function must feature a high order of convergence, and if a polynomial needs to be added in order to obtain an invertible interpolation matrix, the resulting number of polynomial terms should not be comparable with the number of trial centres typical of the CV-K/HRBF local interpolation (15-20 centres). In this extreme case the function would behave similarly to a multi dimensional polynomial, leading to the ill-conditioning issues already mentioned in section 1.1.2. The Thin-Plates Splines (TPS) are discarded because they require a large number of polynomial terms when used in three-dimensional problems, whereas multi-quadric (MQ), Gaussian (GA) and Compactly Supported (CS) are all valid candidates.

These three functions are all characterised by a free parameter that can in theory be chosen arbitrarily. In the case of the MQ and GA functions this parameter is indicated with c_S and it acts as a shape parameter. When c_S is small the resulting MQ interpolating surface is pulled tightly to the data points, forming cone-like basis functions. As c_S increases the peak of the cone gradually flattens. Similarly for the GA functions the interpolating surface around the centre decays more rapidly as the shape parameter decreases, and for extremely small values the interpolating function picks around the centre. Finally a CS function can be defined only if the radius that delimits its region of action is fixed, i.e. its compact support. In these three functions the free parameter has a dimension of a length, and it represents an intrinsic weight of the function on a point located at a prescribed distance from the centre that defines the RBF.

How to choose such a parameter is not a trivial task and is still subject of active research. Most of the work found in the literature relates to the MQ functions, which featuring an exponential rate of convergence, are the most attractive between the available RBFs. In general, when an interpolation problem is solved by the use of global RBF interpolants such as the MQ or GA, increasing the shape parameter leads to an improvement of the interpolation. If this value is pushed behind a certain threshold the condition number of the interpolating matrix becomes too

large, and special algorithms are needed to find a noise-free solution. In fact, the condition number of the interpolating matrix grows like c_S^{Pc}, where Pc is a positive integer that depends on the number and dimension of the nodes considered in the interpolation, Wright and Fornberg (2006). It has been shown that the accuracy of a RBF interpolant is inversely related to the condition number of the interpolating system, Schaback (1995). An interesting shape parameter optimisation based on this result is found in Cecil et al. (2004) where a local RBF interpolation is utilised to reconstruct the gradient in each node of the computational grid. Each interpolation stencil is formed including the closer neighbours of the node for which the gradient reconstruction is needed, and for each stencil an optimal shape parameter is computed. The value of c_S is increased iteratively until the condition number of the corresponding interpolating system remain smaller than a prescribed value. In practice the maximum condition number allowed is only related to the precision of the machine system used. Since they are solving a transient problem this is done prior to time evolution and optimal values of the shape parameter are stored in memory. This algorithm allows for optimisation on different parts of the domain where mesh spacing may vary greatly, but it is not practical if the interpolating matrix changes with time because the evaluation of the condition number is prohibitively expensive.

The value of the shape parameter does not have to be constant, i.e. in an interpolation formula each function can be assigned a different value. Based on this simple consideration, Kansa and Hon (2000) elaborate an empirical formula to relate the shape parameter of the MQ functions with the curvature of the function being interpolated. In this work the interpolation problem is solved twice: an approximated curvature of the function is first computed using a constant shape parameter value, then a second more accurate solution is found with an optimal variable shape parameter that is obtained from the curvature distribution previously computed. It is shown that using a variable shape parameter proportional to the function curvature leads to significant improvements, but this is obtained at the expense of an extra non-linearity that does not exist in the physics of the problem.

Only a few of the research works carried out on the shape parameter issues and selection algorithms have been mentioned in this section. More attempts and details about this problem that afflicts the RBF collocation methods can be found in Carlson and Foley (1991), Hardy (1971) and Rippa (1999).

None of the expensive optimisation methods reported above are adopted in this thesis to evaluate the RBF free parameter, though in principle they can all be applied to the local interpolation scheme of CV-K/HRBF formulation. Instead, simple empirical rules based on

geometrical considerations are used to compute a sensible value for the shape parameter contained in the MQ and GA functions and the compact support appearing in the CS function. For consistency, and due to the analogous geometrical meaning, the compact support radius will be also indicated with c_S.

When the element mesh that discretises the computational domain is uniform or it does not present great variation in the element sizes, a constant c_S can be adopted for all the interpolation stencils. In this case the value is usually taken to be proportional to the element edge length:

$$c_S = c_S^* L_E \tag{2.21}$$

The value of c_S^* can vary significantly when looking for an optimal solution, but in the problems solved in this work, using twice the element edge length always returned a good interpolation. A different approach is adopted in the case of strongly non-uniform meshes for which a different shape parameter value is computed for each interpolation stencil; this is taken as a fraction of the maximum distance found between the stencil points

$$c_S = c_S^* Lst_{max} \tag{2.22}$$

In this thesis, choosing c_S^* between 0.1 and 1.0 guaranteed nearly in every case good solutions (though not necessary the most accurate ones). This approach seems to be more suitable in the case of strongly non-uniform meshes because it allows a mesh-independent choice of the shape parameter value. However, it does not lead to any significant improvement because the optimal shape parameter value seems dependant on the interpolated function as well as on the distribution of the test points as explained in the introduction of this section.

In the remainder of this thesis, the absolute value of c_S will be indicated for those numerical experiments where a constant shape parameter is adopted, formula (2.21). Instead when a different shape parameter is computed for each stencil, equation (2.22), the value of c_S^* will be given.

2.7 Numerical results

One and three-dimensional numerical examples for which an analytical solution is known, are proposed to validate the CV-K/HRBF method. This assessment also aims to understand the

potential of this new numerical scheme in all its possible configurations: the accuracy and robustness of the CV-KRBF and the CV-HRBF are compared, and the performance of the different stencil configurations introduced in section 2.3 is analysed.

The relative percentage error, equation (2.23), and the L_2-norm error, equation (2.24), are used as estimators of the numerical results against the analytical solutions

$$E\% = \frac{\phi - \phi_{ana}}{\phi_{ana}} \times 100 \tag{2.23}$$

$$L_{2error} = \sqrt{\frac{\sum_{i=1}^{Nnodes} \left[\phi(x_i) - \phi_{ana}(x_i)\right]^2}{Nnodes}} \tag{2.24}$$

When a large variation of the function value occurs, a dimensionless L_2-norm error ($L^*_{2error} = L_{2error} / \phi_{max}$) is used to obtain an estimator that is scale effect-free. Unless stated otherwise, a multiquadric RBF is employed in the local interpolation algorithm and the value of the shape parameter is chosen experimentally (iteratively) in order to minimise the absolute L_2-norm error.

2.7.1 One-dimensional advection diffusion reaction problems: CV-KRBF / CV-HRBF comparison

The performance of the CV-KRBF and the CV-HRBF is compared in one-dimensional steady advection-diffusion reaction problems for which the advection is predominant. In all the test cases presented in this section only the one-stencil-one-face configuration sketched in Fig. 2.3 is adopted. Taking a stencil far away from any domain boundary, and considering only hexahedral elements, it is evident that even the largest interpolation is supported from a small number of points: 2 Dirichlet points located at the cell centres, and 11 PDE points placed at the cell face centres. The analysis is focused on the comparison between the CV-KRBF and the CV-HRBF using the same interpolation stencil. The performance and efficiency of the one-stencils-one-cell and one-stencil-one-face configurations will be discussed in section 2.7.2.

2.7.1.1 Advection-diffusion problem (shock profile)

In this section the steady-state advection-diffusion equation is considered in a channel of dimensions [1.0×0.2×0.2]. The governing equation is given by

$$D\frac{\partial^2\phi}{\partial x_i^2}-\frac{\partial U_i\phi}{\partial x_i}=0 \tag{2.25}$$

where D is the diffusion coefficient, U_i the component of the advective velocity in the i direction and ϕ the potential. The following boundary conditions are imposed

$\phi=1, \quad x=0, \quad 0<y<0.2, \quad 0<z<0.2$

$\phi=2, \quad x=1, \quad 0<y<0.2, \quad 0<z<0.2$

$\frac{\partial\phi}{\partial n}=0$ at the remaining walls of the channel.

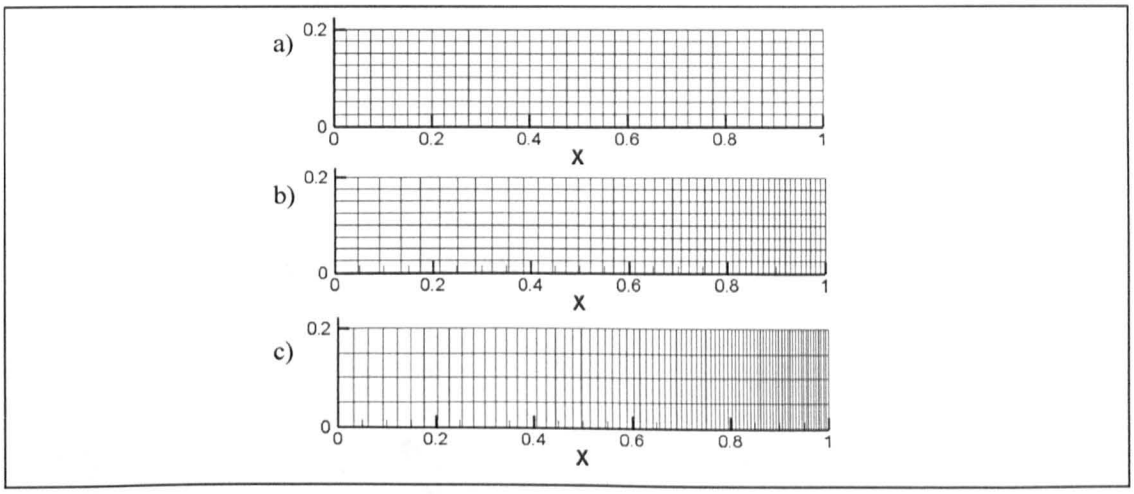

Figure 2.5 - Two-dimensional view at y=0.1 of the three meshes used to solve the diffusive shock: a) uniform with 9×9×41 points, b) non-uniform with 9×9×41 points, c) non uniform with 5×5×81 points

For a one-dimensional advective field, $U_1=const$ and $U_2=U_3=0$, the above problem has the following analytical solution

$$\phi(x)=2-\frac{1-\exp\left(U_1\left(x-1\right)\right)}{1-\exp\left(-U_1\right)} \tag{2.26}$$

The parameter that describes the relative influence of the advective and the diffusive components is the Péclet number, $Pe=UL_R/D$, where U is the velocity, L_R a reference length scale (the channel length in the present case) and D the diffusion coefficient. The above problem is solved for values of the Péclet number equal to 50, 100, 200 and 400.

The numerical experiments are carried out in a uniform mesh of 41×9×9 points for the solution corresponding to the case of a Péclet number of 50, a non uniform mesh of 41×9×9 for the case of a Péclet number of 100 and on a non-uniform mesh of 81×5×5 points for the cases of Péclet numbers of 200 and 400. A 2D view of the meshes described above in a cross section at $y = 0.1$ is shown in Figure 2.5

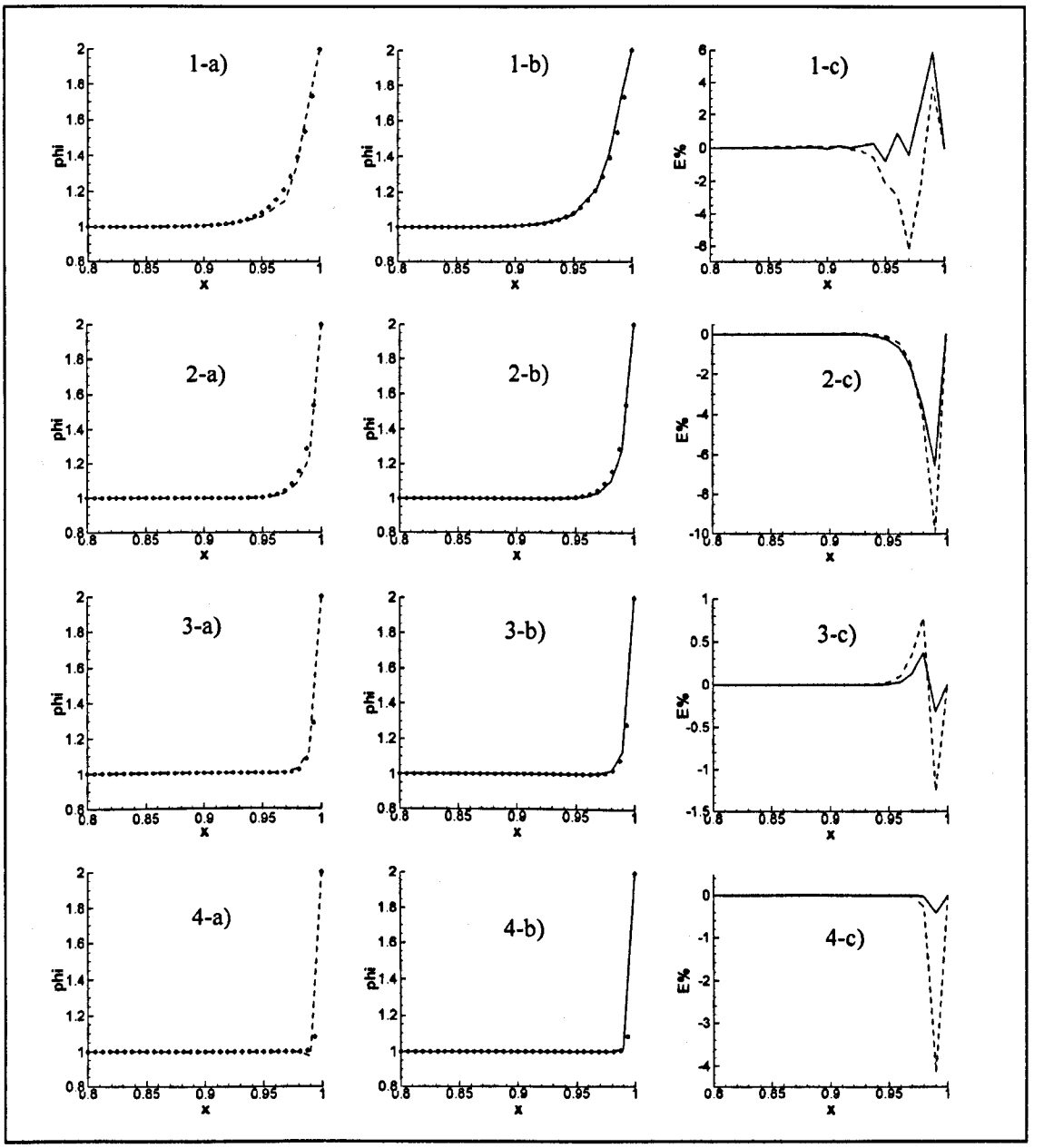

Figure 2.6 - One-dimensional advection diffusion problem (Advective-Diffusive front) predictions at four different *Pe* values: 1) *Pe*=50, 2) *Pe*=100, 3) *Pe*=200, 4) *Pe*=400; a), CV-KRBF; b), CV-HRBF; c), Relative percentage error. The symbols represent the analytical solutions; the dashed black lines refer to CV-KRBF; the full black lines refer to CV-HRBF.

The comparison between the results obtained with the CV-KRBF and CV-HRBF approaches, for the four different Péclet numbers considered, is shown in Figure 2.6. For clarity in the

presentation, the results are only shown for $x > 0.8$ since the value of the potential is almost constant for $x \leq 0.8$ in the cases considered here. As can be observed from the results in Figure 2.6, both approaches are capable of reproducing the analytical solution accurately for the values of the Péclet number tested. However, the CV-KRBF approach always exhibits a larger error at the shock front than that one obtained with the CV-HRBF approach. This is confirmed from Table 2.1 where minimum L_2-norm errors are reported and their corresponding optimal shape parameters are listed.

Péclet	CV-KRBF		CV-HRBF	
	L_2-norm error	c_S	L_2-norm error	c_S
50	1.10×10^{-2}	0.09	1.02×10^{-2}	0.02
100	1.43×10^{-2}	0.1	1.00×10^{-2}	0.01
200	1.66×10^{-3}	0.002	5.40×10^{-4}	0.002
400	4.21×10^{-3}	0.009	4.00×10^{-4}	0.002

Table 2.1 - Error and shape parameter values for the simulation of the one-dimensional advection diffusion problems for four different Péclet numbers

2.7.1.2 Axisymmetric Laplace problem

Consider the solution of the Laplace equation in a circular cylinder with an internal circular hollow cross section. At the internal and external surfaces a constant value of potential is prescribed. Under these conditions, in cylindrical co-ordinates, the problem is defined by the following axisymmetric equation

$$\frac{1}{r}\frac{d}{dr}\left(r\frac{d\phi}{dr}\right)=0 \tag{2.27}$$

where r is the radial coordinate and ϕ is the potential. By expanding the cylindrical Laplacian operator in equation (2.27), the following expression is obtained

$$\frac{d^2\phi}{dr^2}+\frac{1}{r}\frac{d\phi}{dr}=0 \quad \text{or} \quad \frac{d^2\phi}{dr^2}+\frac{d}{dr}\left(\frac{1}{r}\phi\right)+\frac{1}{r^2}\phi=0 \tag{2.28}$$

The analytical solution of this problem is given by

$$\phi(r)=A+B\ln(r) \tag{2.29}$$

where

$$A=\left(1-\frac{\ln(r_{MAX})}{\ln(r_{MAX}/r_{\min})}\right)\phi(R)+\frac{\ln(r_{MAX})}{\ln(r_{MAX}/r_{\min})}\phi(r_{\min}) \text{ and } B=\left(\frac{\Phi(r_{MAX})-\Phi(r_{\min})}{\ln(r_{MAX}/r_{\min})}\right)$$

with r_{MAX} and $r_{\min}$ as the external and internal radius, respectively. Equation (2.28) can be viewed as a one-dimensional advection-diffusion problem with a variable reaction coefficient, $1/r^2$ and featuring a compressible flow with a negative convective velocity, $-1/r$. In this way, this equation takes the same form of equation (2.1) with values of $D=1$, $U_1=-1/r$, $U_2=U_3=0$, $K_r=1/r^2$, $f_s=0$ and $\phi=\phi(r)$. As can be observed from Equation (2.29), the analytical solution of this boundary value problem has a singularity when $r=r_{\min}=0$. The solution of this problem is chosen here to examine the behaviour of the CV-K/HRBF numerical solution in the limit $r_{\min}\to 0$.

The one-dimensional problem defined by equation (2.28) with boundary conditions $\phi(r_{MAX})=2$ and $\phi(r_{\min})=1$ will be solved here as a 3D problem in a channel defined by the domain $r_{\min}\le x=r\le 1$, $0\le y\le 0.2$ and $0\le z\le 0.2$, with zero lateral flux and given constant potential at the inlet and outlet boundaries, i.e. $\phi(x=r_{\min})=1$ and $\phi(x=r_{\min})=1$. Two different values of $r_{\min}$ (r_{min} = 0.01 and r_{min} = 0.003) are tested and each of the cases is solved using a different mesh. Each mesh consists of 5 points in the y and z directions and 81 points in the x direction. However the mesh used for $r_{\min}=0.003$ features a larger point density close to the near-singularity, see Figure 2.7.b.

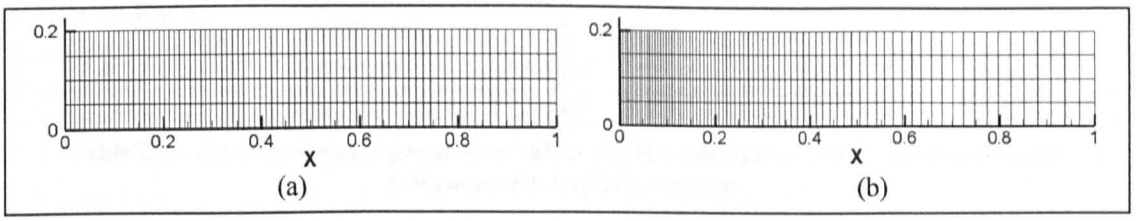

Figure 2.7 - 2D view at y=0.1 of the two meshes used for the computation of the axisymmetric Laplace problem: a) mesh used for r_{min} = 0.01, b) mesh used for r_{min} = 0.003

In Figure 2.8 the computed solutions are compared against the analytical solution for both cases. For the case of r_{min} = 0.01, both approaches are able to reproduce the analytical solution with a good degree of accuracy, indicating the ability of the CV-K/HRBF method to handle problems with a strongly varying velocity field and reaction coefficient. However for the case of $r_{\min}=0.003$, the CV-HRBF method is no longer able to resolve the problem accurately, whereas the CV-KRBF is still matching the analytical solution, see Figure 2.8.2a, Figure 2.8.2b. It

appears that the Kansa's scheme interpolation performs better than the Hermitian one in solving this problem. Increasing the number of points in the local interpolation stencil overcomes this drawback, but the solution of the CV-KRBF solution remains slightly more accurate. The effect of the local convergence and of adopting different stencil configurations will be investigated further in the following sections. Finally, the values of the optimal shape parameters found for this numerical test case are reported in table 2.2 together with their corresponding L_2-norm errors.

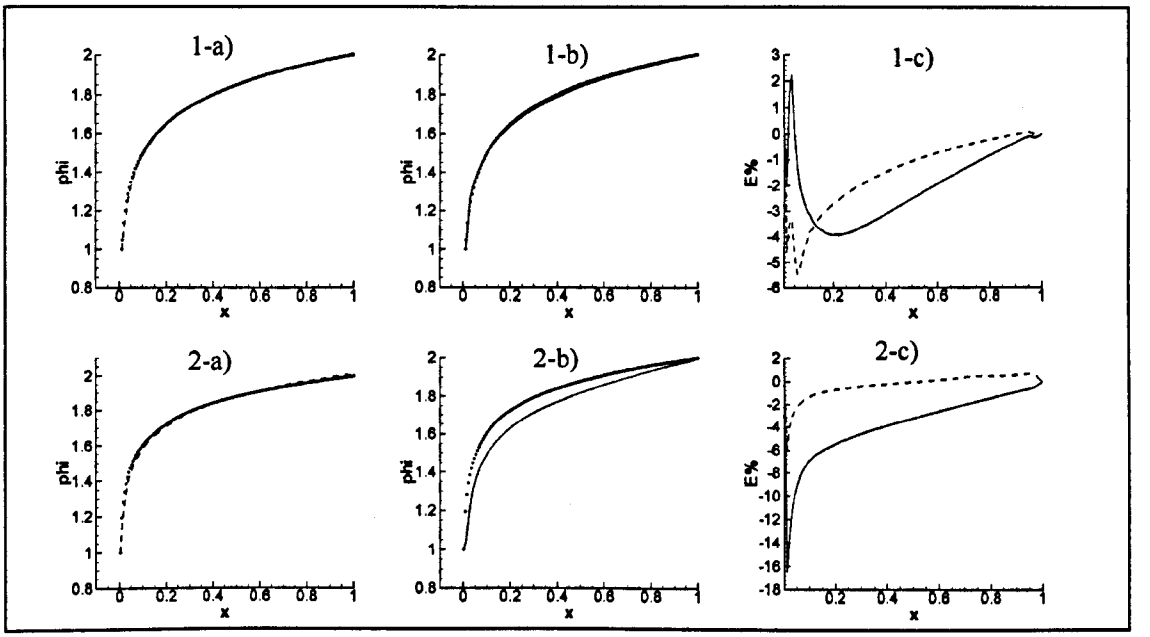

Figure 2.8 - One-dimensional axisymmetric Laplace problem: 1) r_{min}=0.01, 2) r_{min}=0.003; a), CV-KRBF; b), CV-HRBF; c), Relative percentage error. The symbols represent the analytical solutions; the dashed black lines refer to CV-KRBF; the full black lines refer to CV-HRBF.

Internal Radius	CV-KRBF		CV-HRBF	
	L_2-norm error	c_S	L_2-norm error	c_S
0.01	9.53×10^{-3}	0.07	1.09×10^{-2}	0.001
0.003	1.53×10^{-2}	0.03	7.41×10^{-2}	0.02

Table 2.2 - Error and shape parameter values for the simulation of the one-dimensional axisymmetric Laplace problem

2.7.1.3 Advection-diffusion problem with a variable velocity

In this section, a one-dimensional advection-diffusion problem with variable velocity is considered. The test case is implemented for a three-dimensional channel of dimension [1.0×0.2×0.2] and the advective velocity is assumed to be a linear function of the longitudinal direction. The governing equation to be solved is equation (2.25) where

$$U_1 = a_1 + a_2 x,\ U_2 = U_3 = 0,\ a_1 = \left(\ln \frac{\phi_{out}}{\phi_{in}} - \frac{a_2}{2} \right)$$

The above expression describes a hypothetical compressible flow with a velocity field changing direction within the domain. Here a_2 is a longitudinal shear stress intensity and ϕ_{in} and ϕ_{out} are the prescribed inlet and outlet constant values of the potential, respectively (with assigned values of $\phi_{in} = 300$ and $\phi_{out} = 100$). In the remaining domain surfaces, symmetry conditions (zero fluxes) are imposed to retain the one-dimensional characteristic of the solution. For simplicity, a unit value is assigned to the diffusion coefficient D.

This problem has a simple analytical solution given by

$$\phi(x) = \phi_{in} \exp\left(\frac{a_2 x^2}{2} + a_1 x \right) \tag{2.30}$$

In this case, two advective-diffusive fronts are formed at either ends of the domain, with the central region left relatively "empty". This effect is magnified as the value of a_1 increases. The solution of this problem presents numerical difficulties, as both the large values of ϕ around the shocks and the very small values around the centre of the domain must be predicted accurately. The values of $a_2 = 40$, $a_2 = 80$ and $a_2 = 120$, are tested and the computed solutions, using both CV-KRBF and CV-HRBF, are compared against the corresponding analytical solutions in Figure 2.9. A uniform mesh of (81×5×5) points is used for $a_2 = 40$, and a uniform mesh of (101×5×5) points for the other two values of a_2 (80 and 120).

The solution is reproduced reasonably well throughout the domain for all the a_2 values tested, with the CV-KRBF still performing slightly better than CV-HRBF, see Figure 2.9. It is important to point out that the apparent high relative error obtained at the centre of the domain is due to the dimensionless form used in the definition of the relative error (2.23) (absolute value of the difference between the numerical and analytical solutions divided by the absolute value of the analytical solution), which results in a division by a very small value of the potential in the centre region of the domain. An evaluation of the errors free from this type of scale effects is reported in Table 2.3 where the optimal shape parameter values and the dimensionless L_2^*-norm errors for the three values of a_2 tested are reported.

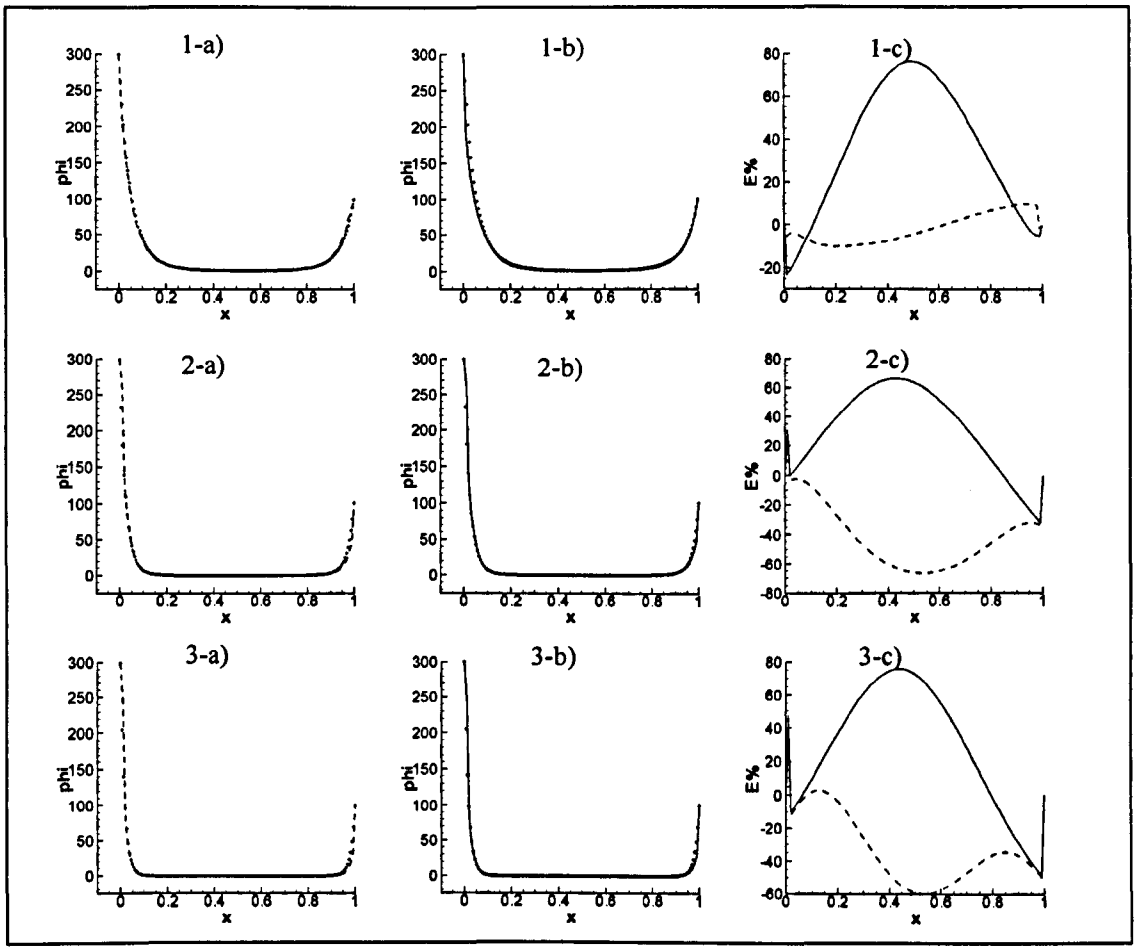

Figure 2.9 - One-dimensional advection diffusion problem with a variable velocity, at three different a_2 values: 1) a_2=40, 2) a_2=80, 3) a_2=120; a), CV-KRBF; b), CV-HRBF; c), Relative percentage error. The symbols represent the analytical solutions; the dashed black lines refer to CV-KRBF; the full black lines refer to CV-HRBF.

a_2	CV-KRBF		CV-HRBF	
	L_2^*-norm error	c_S	L_2^*-norm error	c_S
40	8.68×10^{-3}	0.04	2.83×10^{-2}	0.06
80	2.26×10^{-2}	0.001	2.21×10^{-2}	0.001
120	2.81×10^{-2}	0.001	2.78×10^{-2}	0.002

Table 2.3 - Error and shape parameter values for the simulation of the one-dimensional advection diffusion problem with a variable velocity

It is worth noting that the c_S-parameter dependency is very strong in this particular example and therefore a comparison between the two methods based on these results alone is inopportune. Changing the c_S parameter in a bounded range returns solutions which look quite different. In particular, for large value of a_2. Figure 2.10 exhibits evidence of the effect of the c_S parameter on the error along a longitudinal section over the entire domain for $a_2 = 120$. This makes clear that the shape factor c_S is a data-dependent parameter and does not only depend on the geometry of the problem as already discussed in section 2.6.

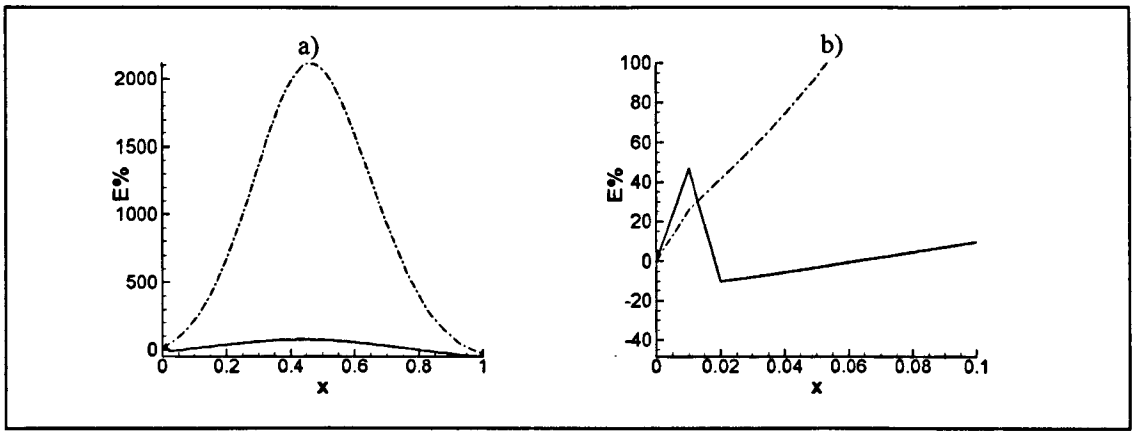

Figure 2.10 - One-dimensional advection diffusion problem with a variable velocity, CV-HRBF, a_2=120, influence of the c parameter on the solution. Full line, simulation using c=0.001; Dot dashed line, simulation using c=0.01; a), full scale plot; b) zoom on the bottom left corner of the full scale plot.

2.7.1.4 Comparison between CV-KRBF and CV-HRBF: remarks

The analysis carried out in the previous sections using the one-stencil-one-face interpolation stencil shows that the CV-KRBF and CV-HRBF methods are both suitable for the solution of advection-diffusion problems. Depending on the numerical test chosen, one of the schemes performs better than the other one, but during the numerical analysis presented so far no significant differences in accuracy have been found. The CV-HRBF usually allows smaller values of the shape parameter before the local system is seriously affected from ill-conditioning issues and becomes not solvable by the use of a standard direct solver (e.g. Gaussian elimination, LU factorization). This is probably due to the higher order of the derivatives that characterises the Hermitian interpolation, in which the boundary and the partial differential operators applied to the RBFs act as trial functions.

On the other hand, the CV-HRBF scheme offers the possibility of applying multiple linearly independent operators in the same location (see section 1.1.2) and this flexibility offers remarkable advantages to optimise the computational efficiency of the method in the case of unsteady and non linear problems as will be shown in the next chapter. In addition, the local system resulting from the CV-HRBF discretisation presents a matrix that is symmetric and that has been proven to be invertible. While the symmetry can be exploited to reduce the time required to solve the local systems, the fact that the solution existence for the HRBF has been proven makes the CV-HRBF more robust than the CV-KRBF. In fact there is no formal proof yet about the solvability of the system deriving from the KRBF collocation method, section (1.1.2).

Due to the reasons given above, the CV-HRBF is preferred over the CV-KRBF, and from now on all further developments related to the formulation are presented and tested only for CV-HRBF. However it must be said that the CV-KRBF has the advantage of being easier to implement due to the relatively simple interpolation formula. While this feature may not be of primary interest in a research work, it could play a crucial role for many complex industrial applications.

2.7.2 Three-dimensional advection-diffusion problem with variable velocity: comparison between different stencil configurations

The CV-HRBF is validated in a three-dimensional advection-diffusion problem with a variable velocity field, and the performance and sensitivity to the mesh of the two stencil configurations introduced in Section 2.3 are analysed. The equation solved is Equation (2.25) with the components of the advective velocity field given by $U_1 = a_1 x$, $U_2 = -a_2 y$ and $U_3 = a_3$. This corresponds to a linear shear compressible flow with a constant density and a constant mass source term $\rho(a_1 - a_2)$. The potential function given by the expression (2.31) is a general solution of the advection-diffusion equation with the parameters specified above

$$\phi = A\exp\left[\frac{1}{2D}\left(a_1 x^2 - a_2 y^2 + 2a_3 z\right)\right] \tag{2.31}$$

where are A is an arbitrary constant.

The CV-HRBF method is used to solve this three-dimensional advection-diffusion problem in a cubic domain of dimension [1×1×1] using the potential function given in (2.31) to prescribe Dirichlet boundary conditions on the six cube faces, and assigning to the constant parameters the following values: $A = 0.001$, $D = 0.1$, $a_1 = 0.5$, $a_2 = 1.0$ and $a_3 = 1.0$. The solution of this problem shows a strong advection towards one of the domain corners where a smooth front is formed.

In this example, two different meshes are tested, a coarser mesh with 26×26×26 points, corresponding to 15,625 cells, and a finer one with 36×36×36 points, corresponding to 42,875 cells. Both computational grids present a non-uniform point distribution with a refinement in the region of the expected shock, see Figure 2.11.

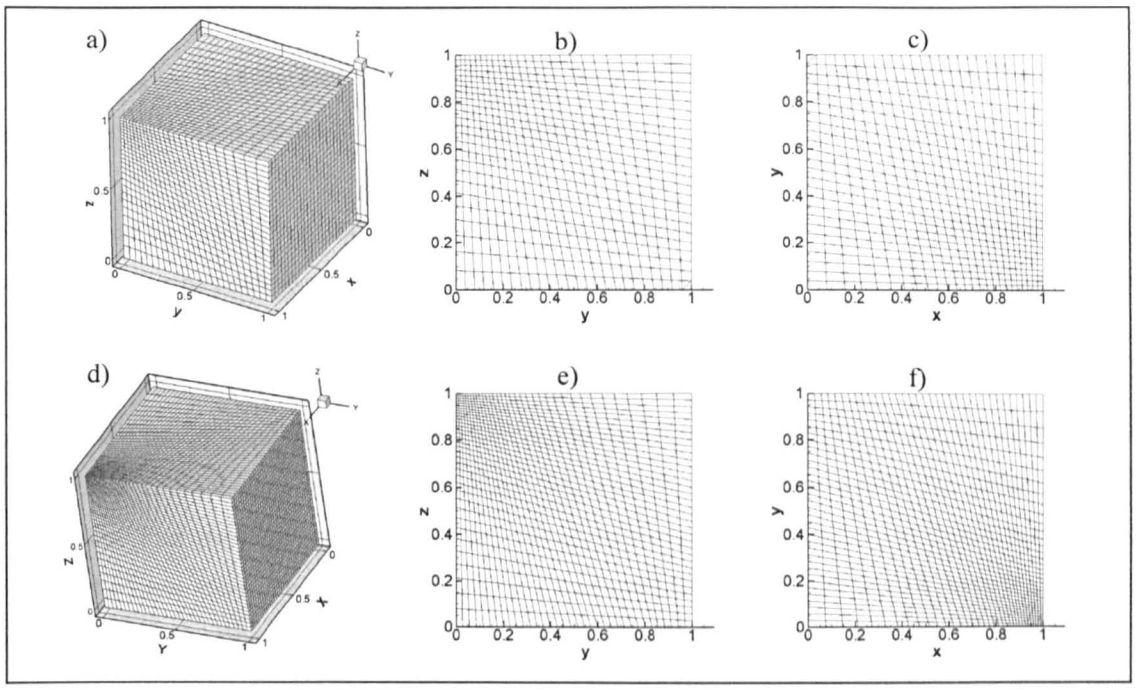

Figure 2.11 - Structured meshes used to solve the three-dimensional convection-diffusion problem: a) coarse mesh, three-dimensional view; b) coarse mesh, view at x=0.96; c) coarse mesh, view at z=0.96; d) fine mesh three-dimensional view; e) fine mesh, view at x=0.97; f) fine mesh, view at z=0.97;

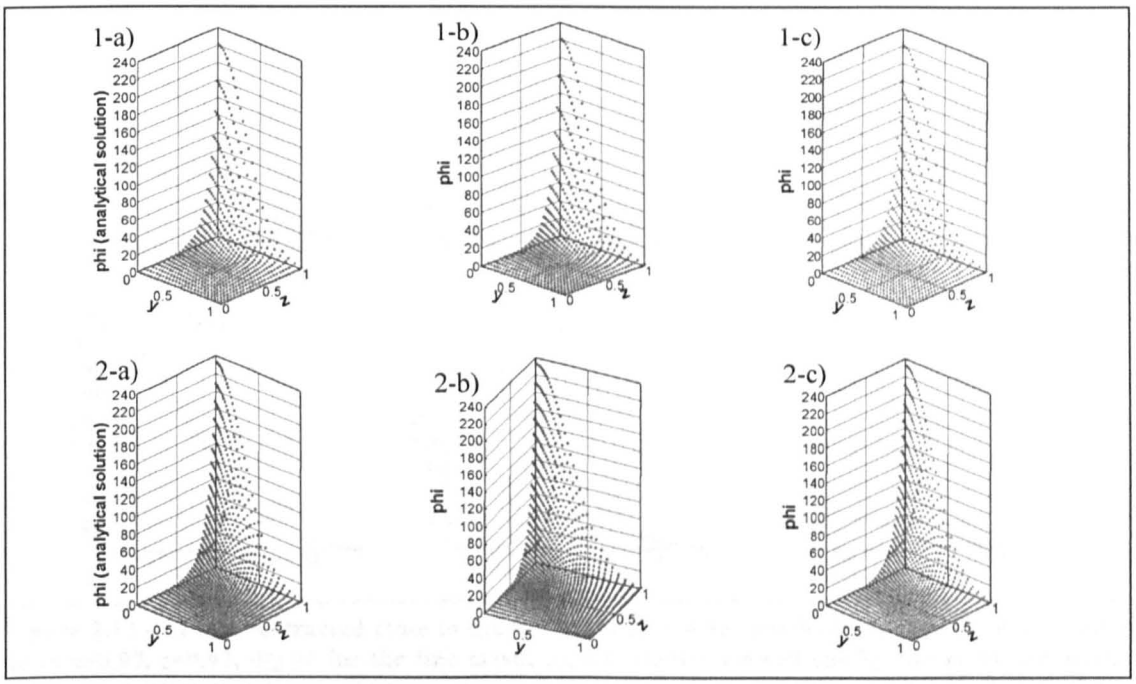

Figure 2.12 - Solution 3D plots: 1) x=0.96 for the coarse mesh, 2) x=0.97 for the fine mesh. a) analytical solution; b) one-stencil-one-cell solution, c) one-stencil-one-face solution.

To assess the accuracy of the method and the behaviour of the two proposed stencil configurations, the numerical results are presented in two slices close to the high gradient regions. The first is a plane of constant x value, at x=0.96 for the coarse mesh and x=0.97 for the fine mesh, and the second a plane of constant z value, at z=0.96 for the coarse mesh and z=0.97

for the fine mesh. For these two slices three-dimensional solution plots are reported in Figure 2.12 and Figure 2.14 for both meshes and both stencil configurations. The analytical solution is also plotted on these planes for comparison purposes.

Corresponding detailed profiles are plotted in two dimensions in Figure 2.13 and Figure 2.15 for clarity, where the analytical solution is also presented for comparison purposes. The one-stencil-one-face approach fails in the shock region when the coarse mesh is used. It undershoots the exact solution and is not able to predict the correct concave shape. This problem is not displayed in the case of the one-stencil-one-cell configuration where the single cell stencil employed is larger and guarantees a local interpolation that describes more accurately the solution in all directions. The drawback reported for the one-stencil-one-face configuration improves with the use of the finer mesh, but its solution still has a lower accuracy in comparison with the solution obtained with the one-stencil-one-cell configuration using the same finer mesh. It is also worth noticing that the slices and the profiles analysed for the finer mesh are closer to the shock front than the sections considered for the coarse mesh.

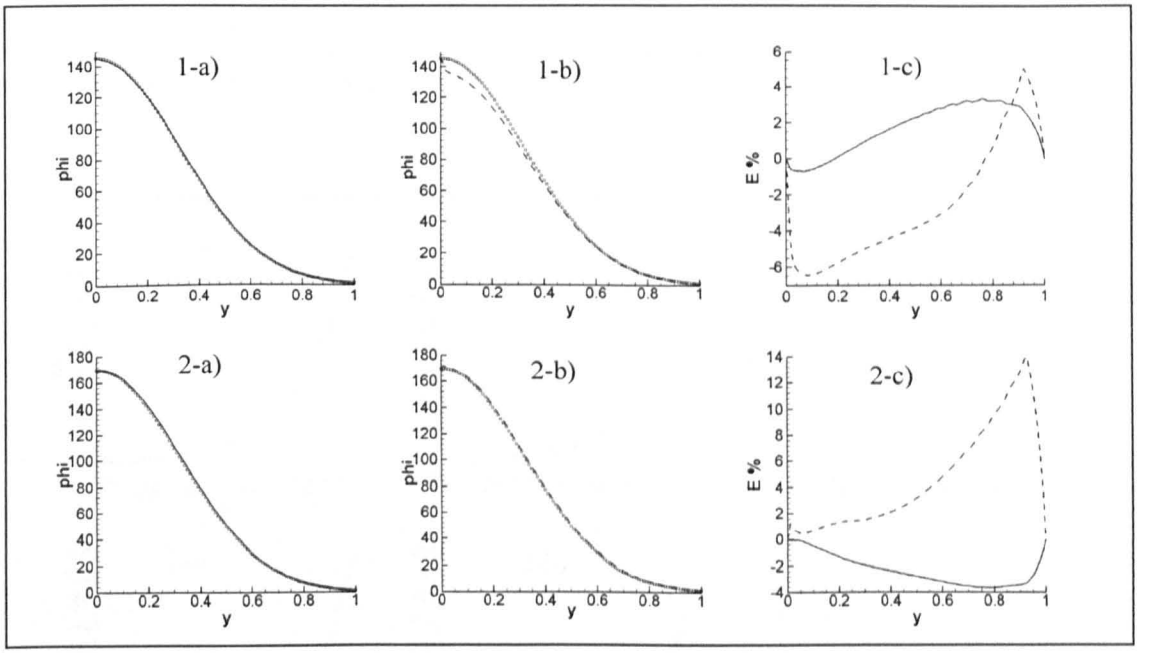

Figure 2.13 - Profiles extracted close to the shock: 1) at x=0.96, z=0.96, 0≤y≥1 for the coarse mesh; 2) at x=0.97, z=0.97, 0≤y≥1 for the fine mesh; a), one-stencil-one-cell configuration b), one-stencil-one-face configuration; c), Relative percentage error. The symbols represent the analytical solutions; the dashed lines refer to one-stencil-one-face configuration; the full lines refer to one-stencil-one-cell configuration.

An evaluation of the errors is reported in Table 2.4 where the optimal shape parameter values and the dimensionless L_2^*-norm errors for the two structured meshes tested are reported. The

L_2-norm error is scaled by a factor equal to the maximum potential value found in the upper corner of the computational domain (1.0,1.0,1.0).

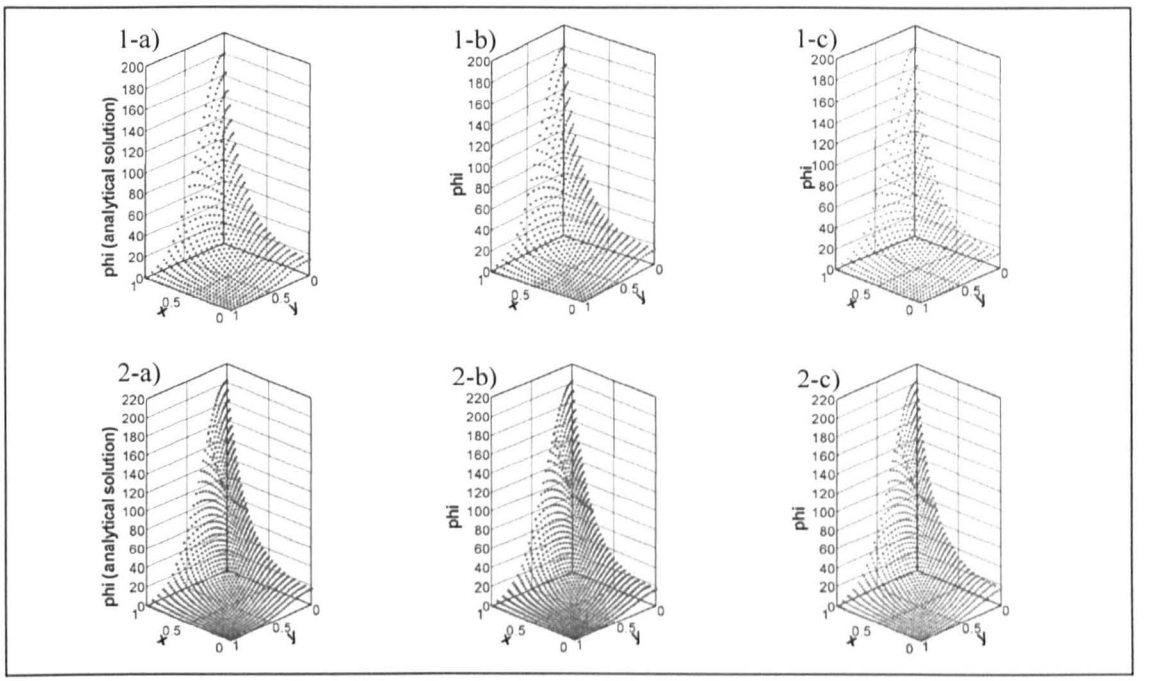

Figure 2.14 - Solution 3D plots: 1) z=0.96 for the coarse mesh, 2) z=0.97 for the fine mesh. a) – analytical solution; b) one-stencil-one-cell solution, c) one-stencil-one-face solution.

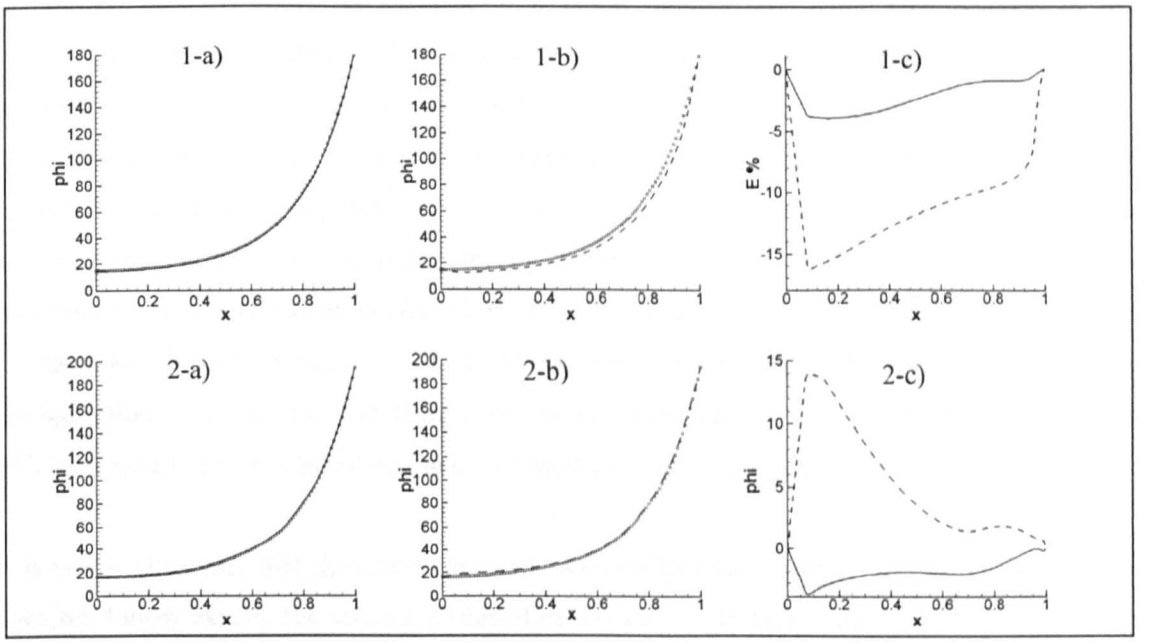

Figure 2.15 - Profiles extracted close to the shock: 1) at y=0.04, z=0.96, $0 \le x \ge 1$ for the coarse mesh; 2) at y=0.028, z=0.97, $0 \le x \ge 1$ for the fine mesh; a), one-stencil-one-cell configuration b), one-stencil-one-face configuration; c), Relative percentage error. The symbols represent the analytical solutions; the dashed lines refer to one-stencil-one-face configuration; the full lines refer to one-stencil-one-cell configuration.

Mesh	CV-HRBF one-stencil-one-face		CV-HRBF one-stencil-one-cell	
	L_2^*-norm error	c_S	L_2^*-norm error	c_S
15,625 cells	4.84×10^{-3}	0.1	1.72×10^{-3}	0.02
42,875 cells	6.25×10^{-3}	0.005	3.02×10^{-3}	0.01

Table 2.4 - Error and shape parameter values for the simulation of the three-dimensional advection diffusion problem with a variable velocity

The errors reported in Table 2.4 confirm that the solutions obtained with the one-stencil-one-cell configuration are more accurate, but increasing the number of cells increases the errors slightly for both stencils configurations. The result presented can be considered mesh independent, and the fact that small errors cannot be achieved is due in part to the topology of mesh used to discretise the computational domains. To refine the hexahedral mesh keeping the number of total cells limited, a distortion of the elements located around the corner where the diffusive shock takes place is needed. Since linear elements and the mid-point integration rule are used in the flux integration, the distortion of the cells introduces a significant error in the region where larger gradients are expected, which limits the accuracy of the CV-HRBF for this test case. In chapter 4, higher order integration and different mesh topology will be used to solve this problem again and significant improvements that support this hypothesis will be shown.

The drawback found for the one-face-one-stencil configuration sketched in Figure 2.3 (2 Dirchlet points located at the cell centres, and 11 PDE points placed at the face centres, for hexahedral meshes) could be removed if a larger number of points was included in the interpolation. Although this is always possible this is not an option considered in this work because it would result in a too expensive alterative of the method. As observed in section 2.3, if the one-stencil-one-face configuration is adopted the number of local systems to be solved would be much larger compared to the one-stencil-one-cell interpolation strategy. To keep the computational cost at a reasonable level, the extra number of local systems should be compensated by the reduction in size. Since it appears that including only two cell centres in the interpolation is not enough to obtain an accurate interpolation, the one-stencil-one-face configuration is discarded, and from now on the main efforts will be in finding the most efficient stencil of points based on the one-stencil-one-cell technique.

It is worth observing that the one-stencil-one-cell configuration used in the comparison above does not follow exactly the scheme sketched in section 2.3. In fact to have a contained number of PDE points, only the nodes of the central elements are used as PDE points, see S1-PDE configuration in Figure 2.16. For a mesh made of only hexahedrons, a stencil internal to the domain includes: 7 Dirichlet points (one each cell centre), and 8 PDE points (one each node of the central cell considered). The choice of placing the PDE points in the cell face centres, as

done for the one-face-one-stencil configuration, implies that in the location where the flux is reconstructed the interpolation is required to satisfy the governing equation yielding to a C^2 continuity of the function approximation. In theory this should improve the accuracy of the flux reconstruction and the numerical scheme accuracy, but in practice no significant differences are found when the PDE points are located in the element nodes rather than in the face integration points.

Another observation regards the number of points included in this type of interpolation stencil. As addressed in section 2.3 a larger number of nodes does not necessarily mean a more accurate interpolation, because of the ill-conditioning issues that affect the full populated local system. Different stencil sizes will be tested in the next section.

2.7.3 CV-HRBF: local and global convergence analysis

To analyse the convergence of the CV-HRBF method, the one-dimensional advection diffusion problem presented in section 2.7.1.1 and characterised by a Péclet number equal to 50 is considered. This case is chosen because it does not show a great dependency on the shape parameter and the attention can be focused on the convergence analysis. The computational domain and the boundary conditions are defined as in section 2.7.1.1, and 3 mesh resolutions are employed; $\Delta x = 1/40$ (M40), $\Delta x = 1/80$ (M80), $\Delta x = 160$ (M160). Two combined effects are investigated: refining the element mesh (global convergence), and increasing the stencil size that supports the local interpolation (local convergence). For each of the three meshes described above, 5 different stencil configurations, Figure 2.16 and Figure 2.17, are tested, and at each step the stencil size is increased either by adding some Dirichlet points or PDE points.

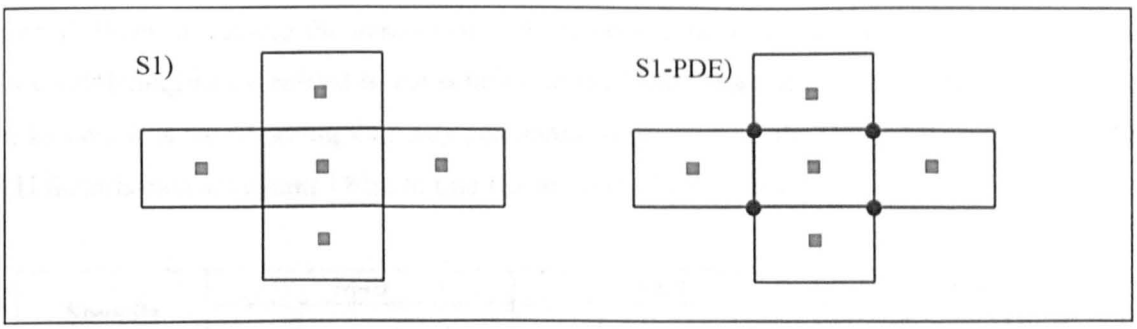

Figure 2.16 - Interpolation stencil stopped at the first level of neighbouring cells. S1), Only Dirichlet points; S1-PDE), Dirichlet points and 1 set of PDE points. Square symbols, Dirichlet points; Round Symbols, PDE points.

In the stencils S1 only the first level of neighbouring cells are included in the interpolation; instead in the stencils S2 another level is added.

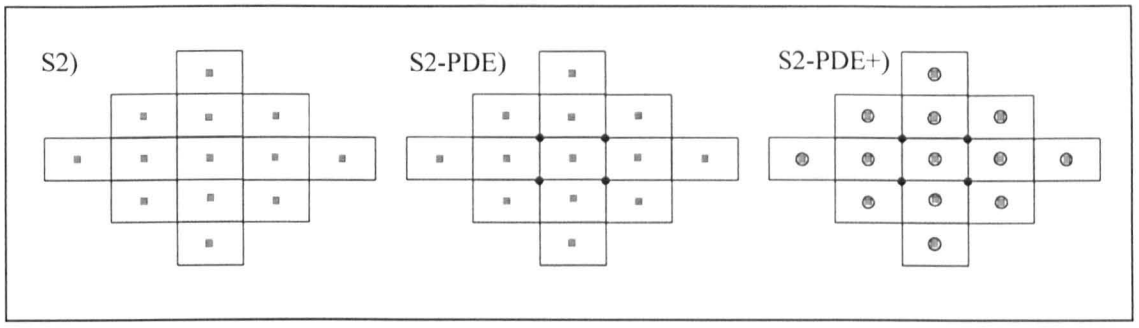

Figure 2.17 - Interpolation stencil stopped at the second level of neighbouring cells. S2), Only Dirichlet points; S2-PDE), Dirichlet and 1 set of PDE points; S2-PDE+), Dirichlet points and 2 sets of PDE points. Square symbols, Dirichlet points; Round Symbols, PDE points.

The first set of PDE points is located on the nodes of the central elements (S1-PDE and S2-PDE), whereas for the second set (S2-PDE+) the double collocation technique is used, and the PDE is applied on the top of the Dirichlet condition in the cell centres. The sketches of the stencils reported in Figure 2.16 and Figure 2.17 are two-dimensional for the sake of simplicity in the presentation, however the corresponding three-dimensional stencils in the case of hexahedral cells feature a total number of nodes equal to 7 for S1, 15 (7+8) for the S1-PDE, 33 for S2, 41 (33+8) for S2-PDE and 74 (33+33+8) for S2-PDE+. This number changes with the topology of element used.

The error of the analysis combining different meshes with different interpolation stencil sizes is reported in Table 2.5 and Table 2.6, together with the optimal shape parameter values. As expected refining the element mesh or/and increasing the number of cell centres in the interpolation stencil improves the solution significantly. It is interesting to observe the behaviour of the solution with and without PDE points. Adding a small set of only 8 PDE points improves the solution by a factor that ranges from 1.5 to 4 depending on the mesh, and in some cases using the S1-PDE stencil returns a solution more accurate than that obtained using the S2 stencil. When increasing the number of PDE points behind a certain threshold (S2-PDE+) the ill-conditioning issues related to the solution of the local system do not allow any further error reduction. It is worth noting that only conventional methods as the Gauss-Elimination and the LU factorisation are adopted here to find the solution of the local system.

Stencils	M40		M80		M160	
	L_2	c_S	L_2	c_S	L_2	c_S
S1	9.39×10^{-3}	0.02	2.91×10^{-3}	0.07	6.68×10^{-4}	0.07
S1-PDE	6.29×10^{-3}	0.02	9.20×10^{-4}	0.07	2.05×10^{-4}	0.07
S2	8.83×10^{-3}	0.02	2.35×10^{-4}	0.07	3.03×10^{-4}	0.06
S2-PDE	5.94×10^{-3}	0.02	1.82×10^{-4}	0.07	8.79×10^{-5}	0.07
S2-PDE+	1.25×10^{-2}	0.02	3.03×10^{-3}	0.07	1.87×10^{-4}	0.07

Table 2.5 - Convergence analysis: L_2-norm error and optimal shape parameter values

Stencils	M40	M80	M160
	Max $E\%$	Max $E\%$	Max $E\%$
S1	7.32	1,28	0.25
S1-PDE	4.71	0.52	0.17
S2	5.28	0.14	0.15
S2-PDE	3.28	0.11	0.05
S2-PDE+	6.71	4.60	0.18

Table 2.6 - Convergence analysis: Maximum percentange relative error

It is also interesting to observe the behaviour of the shape parameter optimal value, which for this test case seems not to vary significantly when switching from one mesh to another or even between different stencil configurations. At least for this particular case the shape parameter seems to depend mainly on the interpolated function and not so much on the point distribution.

From the convergence analysis presented in this section it appears that the S1-PDE stencil is definitively one of the most efficient: for a relatively small number of points in the local interpolation, 15, where only 7 of those are Dirichlet points and contribute to the global matrix, a very accurate solution that presents a high convergence rate is obtained. Unless stated otherwise, the S1-PDE stencil configuration will be used from now on in this work.

2.7.4 CV-HRBF: RBF free parameter sensitiveness analysis

Only the multiquadric (MQ) RBF has been used so far in the numerical tests presented, and for each simulation the optimal shape parameter value has been reported. Three different RBFs are tested in this section with the aim to study the accuracy of the CV-HRBF as the free parameter varies. The advection diffusion problem presented in section 2.7.1.1 is taken as a test case for this assessment, and a Péclet number equal to 200 is chosen because the solution is characterised by a sharp advective-diffusive front that makes the numerical solution quite sensitive to the RBF free parameter. In addition, it seems that for this problem the shape parameter does not change with the distribution of points (see section 2.7.3), and this circumstance makes this test case ideal to investigate the free parameter sensitivity when different RBFs are used.

The same domain, mesh and boundary conditions described in section 2.7.1.1 are used to simulate this advection diffusion problem with the CV-HRBF method in which the MQ, the Gaussian (GA) and the Compact Supported (CS) RBFs are tested in the local interpolation. For each function, a set of c_S values are tested and the corresponding L_2-norm errors are computed to assess the accuracy of the numerical solution against the analytical one, Figure 2.18. The c_S values shown in Figure 2.18 are those for which a reasonable error is found. Taking a value out

of the range shown would return a solution with a large instability and for which the error diverges from reasonable values.

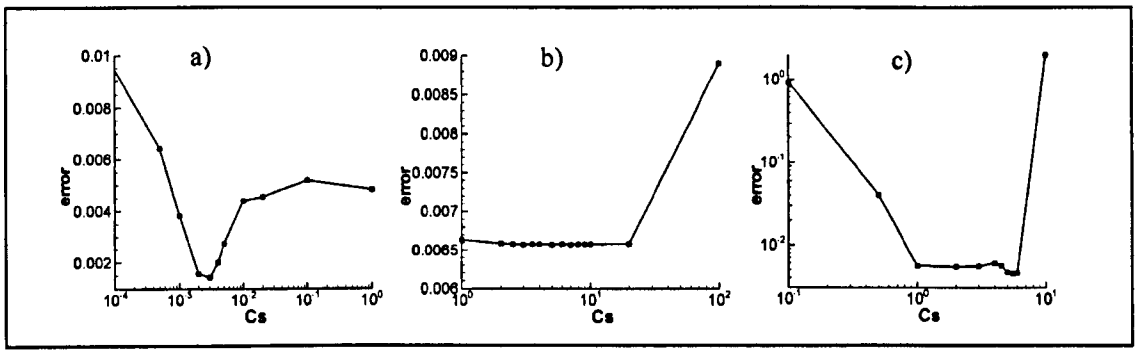

Figure 2.18 - RBF free parameter assessment. a), MQ RBF; b), GA RBF; c) CS RBF.

The minimum errors obtained using the three RBFs are shown in Table 2.7

MQ		GA		CS	
L_2	c_S	L_2	c_S	L_2	c_S
1.44×10^{-3}	0.003	6.57×10^{-3}	3.0	4.51×10^{-3}	5.5

Table 2.7 - Minimum errors obtained with three different RBFs and optimizing the free parameter

For GA and the CS RBFs the range of the c_S values for which an accurate solution is obtained spans an order of magnitude (from 1 to 10). This range becomes wider when using the MQ functions; in fact reasonable values for the error are computed for values of the shape parameter that range from 0.001 to 1. In addition the MQ returns the smallest achievable error. This analysis shows that the MQ RBFs are potentially the most accurate functions as already found by other researchers working on global interpolants method, e.g. Madych and Nelson (1990). Also the free parameter selection is a problem for all the RBF tested in this section, and even if it seems that the MQ are the most sensitive to the selection of such a parameter, they show a large range of values that lead to a very accurate solution.

2.7.5 Boundary condition implementation: comparison between two different approaches

The two approaches to implement the boundary condition introduced in section 2.4, the BC-cvrbf and BC-rbf, are tested here repeating the simulation of the advection diffusion problem with variable velocity presented in section 2.7.1.3. The case with highest advection is chosen for this validation ($a_1 = 120$) to have a demanding numerical test that will allow magnification of the differences between the BC-cvrbf and the BC-rbf. The same domain, computational grid and boundary conditions described in section 2.7.1.3 are used in here. When the boundary condition

implementation is carried out following the BC-cvrbf approach, the advective flux of the cell faces placed at the inlet and outlet of the channel (Dirichlet BC) are considered as known, whereas for the cell faces located in the lateral walls (zero flux BC) it is the diffusive flux that can be considered as known. It is important to say that in the local interpolation the BCs are prescribed only in the face nodes and not in the integration points. The percentage relative error along the domain using the two approaches, Figure 2.19, shows a slightly smaller error in the case of the BC-cvrbf approach as expected. In fact imposing known fluxes will always be more precise than approximating them with an interpolation, although the improvement is not significant. The same optimal shape parameters was found for the two simulations that use the BC-rbf and BC-rbf approaches, $c_S = 0.02$.

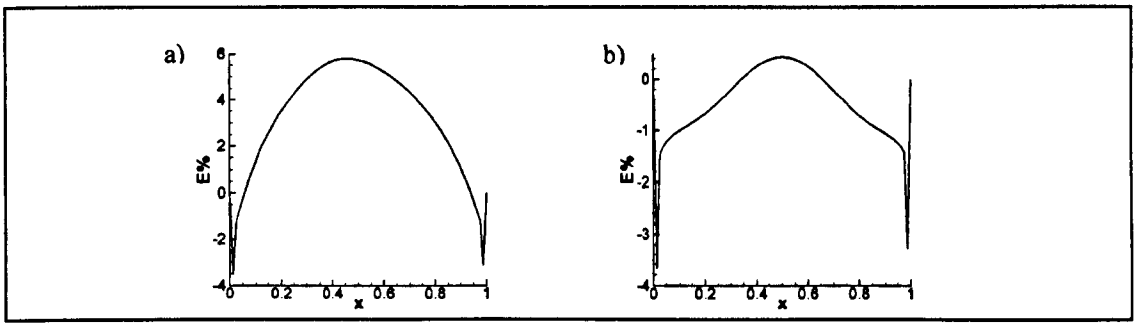

Figure 2.19 - BC-rbf/cvrbf comparison. Relative error along the domain for the one-dimensional advection diffusion problem with reactive velocity and a_1=40. a), BC-rbf; b), BC-cvrbf

Figure 2.20 shows the solution in a profile extracted for $x = 0.9875$, $z = 0.02$ and $0 \le y \le 0.05$ in the region close to the right boundary of the channel where a diffusive shock takes place. The analytical solution in this profile is a horizontal straight, but its numerical approximation presents a variation which results in being wider in the case of the BC-rbf approach. Also in this case the BC-cvrbf method appears to be more accurate in the prediction of the Neumann condition near the wall, but not significantly.

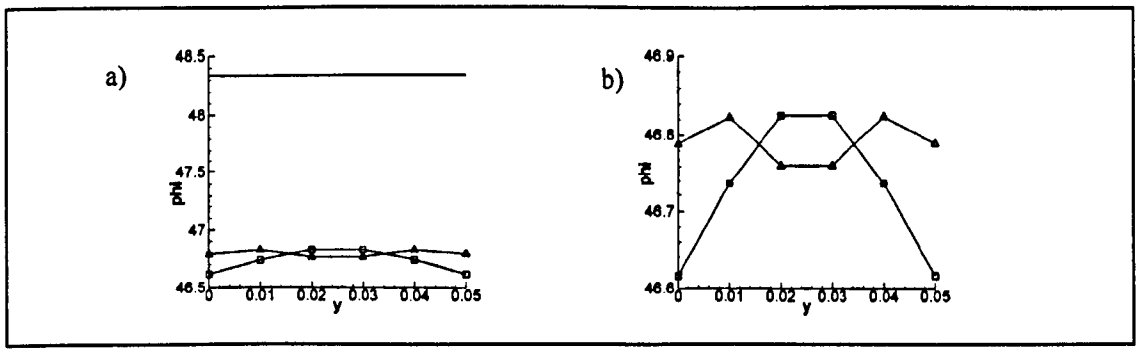

Figure 2.20 - BC-rbf/cvrbf comparison. Solution plotted for a transversal profile extracted in the region of the right front for the one-dimensional advection-diffusion problem with variable velocity. Square symbols, BC-rbf; Delta symbols BC-cvrbf; line with no symbols, analytical solution. a), plots with the analytical solution; b) zoom on the two numerical solutions

To conclude, it can be said that when possible it is always preferable to use the BC-cvrbf approach in the boundary implementation, but the BC-rbf method can be considered very reliable too, offering a valuable flexibility in those cases where the BCs are not known in the cell face integration points.

2.8 Conclusion

A general formulation of the CV-K/HRBF for the solution of boundary value problems has been presented, developing the idea of having approximate solutions of the governing equation as local interpolants. The flexibility and the accuracy gained by using a RBF meshless collocation method in the control volume reconstruction step have been shown from a theoretical point of view as well as in a number of numerical examples. The numerical experiments presented suggested that the most practical stencil configuration for the local interpolation is the one based on the mesh element, while having found the same level of accuracy between the CV-KRBF and CV-HRBF the second one is preferred due to its robustness and to the possibility of applying more than one linearly independent operators in the same location (e.g. 'double collocation technique').

3 INITIAL/BOUNDARY VALUE PROBLEMS - TRANSPORT PROBLEMS

3.1 Introduction

The groundwater quality is a well known problem that affects many countries around the world due to the high population density and the domestic/industrial wastes. Numerical models can greatly help in quantitative analyses of the migration of reactive substances in soil and groundwater, providing an important support tool for pollution control. In general these models should consider the concentrations of several species and should be able to simulate both solute transport processes, such as advection and dispersion, and chemical reactions, such as complexation, adsorption and precipitation. However the model can be significantly simplified based on the problem studied and on what the most relevant processes of the analysis are. Sometime it is appropriate and convenient to describe the transport of a single species through a porous media with a simple first-order rate law which has no feedbacks to other chemical species in the system. In other cases a complex chemical system must be taken into account, and the mathematical model of the transport problem requires the solution of large systems of equations, often non-linear and very demanding from a computational point of view.

In this chapter the CV-HRBF presented in chapter 2 for the solution of general boundary value problem problems will be extended to study general transport problems, Orsini et al. (2009). To introduce the formulation the transport of a single species is considered, successively an example on how the method can be applied to non-linear multispecies systems is given. In both cases it is interesting to analyse the formulation of the local problem, which is the main novelty of the CV-HRBF method. In fact, to be consistent with what has been presented so far, the interpolation used in the cell flux reconstruction must continue to be a local approximation of the governing equation of the problem being solved. In the unsteady formulation of the CV-HRBF an initial/boundary value problem is solved locally for each mesh element using the same time integration scheme adopted to update the global CV solution. Doing so, the same order of accuracy is retained for the time discretisation of the local and global solutions.

A similar approach is followed in the case of non-linear transport, where the non-linear contribution that appears in the local problem is taken at the previous non-linear iteration and moved to the right hand side.

In the case of non linear problems the local formulation offers different alternatives of implementations. Since the non-linear governing equation is solved globally and locally, different solution techniques can be combined to reduce the overall number of non-linear iterations. For example, the Newton–Raphson could be applied to the global solution, and the Picard iteration technique to the local problem. During this thesis no work was carried out on highly non-linear problems (e.g. Navier-Stokes equations) because it was beyond the scope of the project that funded this research. However it is worth reporting the theoretical flexibility found in the CV-HRBF formulation that could be further investigated in future works. In the quasi-linear transport example presented in this chapter, only one possible way of linking the local problem to the non-linear global iterations will be considered.

3.2 The CV-HRBF unsteady formulation – Transport of a single species

The governing equation for the transport of a component in an *nd*-dimensional space can be written as:

$$\frac{\partial \phi}{\partial t} = \frac{\partial}{\partial x_i}\left(D_{ij} \frac{\partial \phi}{\partial x_j} \right) - \frac{\partial U_i \phi}{\partial x_i} + K_r \phi \qquad i, j = 1, nd \tag{3.1}$$

where ϕ is a general scalar variable being transported, D_{ij} is the diffusivity tensor, U_j is the component of the advective velocity along the j-direction, K_r the reactive coefficient.

Equation (3.1), together with the following initial and boundary conditions (3.2) and (3.3)

$$\phi(x,0) = \phi_0 \qquad \text{on} \qquad \Omega \tag{3.2}$$

$$B(\phi) = f_B(x) \qquad \text{on} \qquad \partial\Omega \tag{3.3}$$

describes an initial/boundary value problem having a unique solution.

Discretizing the time derivative by the weighted Crank-Nicholson time-stepping scheme, equation (3.1) can be rewritten as follows

$$\Delta t\theta\left(\frac{\partial}{\partial x_i}\left(D_{ij}\frac{\partial\phi^t}{\partial x_j}\right)-\frac{\partial U_i^t\phi^t}{\partial x_i}+K_r\phi^t\right)-\phi^t=$$
$$\Delta t(\theta-1)\left(\frac{\partial}{\partial x_i}\left(D_{ij}\frac{\partial\phi^{t-\Delta t}}{\partial x_j}\right)-\frac{\partial U_i^{t-\Delta t}\phi^{t-\Delta t}}{\partial x_i}+K_r\phi^{t-\Delta t}\right)-\phi^{t-\Delta t} \tag{3.4}$$

where ϕ^t and $\phi^{t-\Delta t}$ indicate the solution at the time t and $t-\Delta t$, respectively, and $0\le\theta\le1$ is a weighting parameter (for $\theta=0.5$ the scheme can be considered second order in time). In the proposed time stepping algorithm, the original initial/boundary value problem reduces at each time step to the solution of a boundary value problem, defined by the non-homogeneous partial differential equation (3.4). The non-homogeneous term is given in terms of the solution at the previous time step.

Defining the following two partial differential operators

$$L_t(\bullet)=\Delta t\theta\left(\frac{\partial}{\partial x_i}\left(D_{ij}\frac{\partial(\ )}{\partial x_j}\right)-\frac{\partial U_i^t(\ )}{\partial x_i}+K_r(\ )\right)-1(\ ) \tag{3.5}$$

$$L_{t-\Delta t}(\bullet)=\Delta t(\theta-1)\left(\frac{\partial}{\partial x_i}\left(D_{ij}\frac{\partial(\ )}{\partial x_j}\right)-\frac{\partial U_i^{t-\Delta t}(\ )}{\partial x_i}+K_r(\ )\right)-1(\ ) \tag{3.6}$$

The time discretisation form of governing equation (3.1), i.e. equation (3.4), can be rewritten in a more concise form, as

$$L_t(\phi)=L_{t-\Delta t}(\phi) \tag{3.7}$$

Following the approach of the classical cell-centred CV scheme, equation (3.4) is integrated over the grid elements, leading to

$$\Delta t\theta\int_S\left(D_{ij}\frac{\partial\phi^t}{\partial x_j}-U_i^t\phi^t\right)n_i dS+(\Delta t\theta K_r-1)V_P\bar{\phi}_P^t=$$
$$\Delta t(\theta-1)\int_S\left(D_{ij}\frac{\partial\phi^{t-\Delta t}}{\partial x_j}-U_i^{t-\Delta t}\phi^{t-\Delta t}\right)n_i dS+(\Delta t(\theta-1)K_r-1)V_P\bar{\phi}_P^{t-\Delta t} \tag{3.8}$$

where the divergence theorem has been applied. The volume and surface flux in the integration formula (3.8) are treated numerically as explained in section 2.2 and the flux reconstruction is

carried out using an RBF interpolation, which for each time step is the solution of the local boundary value problem defined by Equation (3.2), (3.3) and (3.7).

In the case of the unsteady formulation, the interpolation formula 2.7 presents the PDE operator L_t that can vary with respect to the time, and so the collocation system (2.8). In addition, it is clear from equation (2.9) that for each point where the interpolation is required to satisfy the governing equation, the values of the operator $L_{t-\Delta t}$ need to be reconstructed starting from the solution at the previous time step. In fact, this is the non-homogeneous term that fills the local right hand side. The interpolation of the solution at the previous time step is also necessary to reconstruct the cell flux needed for the computation of the integral that appears in the right hand side of equation (3.8). When both the right hand sides of the global and local problems are computed, the solution can be advanced solving the local systems first, and then the global sparse linear system, from which the values of the unknowns in the cell centres at the new time are computed.

3.3 The CV-HRBF formulation to solve multi-species reactive transport

A mathematical description of a multi-species reactive transport for the saturated zone of the aquifer is given by

$$\frac{\partial c_n}{\partial t} = \frac{\partial}{\partial x_i}\left(D_{ij}^S \frac{\partial c_n}{\partial x_j} \right) - \frac{1}{\eta}\frac{\partial q_i c_n}{\partial x_i} + R_n\left(c_l\right) \quad \text{with} \quad n = 1, N_{sp} \tag{3.9}$$

where c_n is the concentration of one of the N_{sp} species considered in the system, D_{ij}^S is the dispersivity tensor, η is the porosity of the medium, q_i the water flux, $R_n\left(c_l\right)$ is the reaction term that in general depends from all the species ($l = 1, N_{sp}$). Equation (3.9) can be rewritten in a more concise form dividing the transport operator from the reaction operator

$$\frac{\partial c_n}{\partial t} = L^{AD}\left(c_n\right) + R_n\left(c_l\right) \tag{3.10}$$

where

$$L^{AD}(\ ) = \frac{\partial}{\partial x_i}\left(D_{ij}^{S} \frac{\partial(\ )}{\partial x_j} \right) - \frac{1}{\eta} \frac{\partial q_i(\ )}{\partial x_i} \tag{3.11}$$

The operator L^{AD} takes account only of the advective-dispersive transport while R_n expresses the interaction between the species considered, and its model is strictly related to the nature of the chemical reactions.

Some of the chemical processes take place so fast that they can be considered practically instantaneous when compared to the transport phenomena speed, i.e. the reaction is in equilibrium. The fact that equilibrium can be assumed for a part or all the reactions considered in the chemical system, determines the type of formulation chosen to solve the problem, Steefel and MacQuarrie (1996). When all of the species can be considered to be at equilibrium, the chemical problem can be completely decoupled from the transport, and local speciation driven by algebraic expressions based on mass action expressions are considered to take account of the chemistry. In this case it is common practice to divide the species in 'primary species' (or 'components') and secondary species (or 'non-components'), with the number of secondary species equal to the number of equilibrium reactions. In order to reduce the number of equations that need to be discretised globally, only the transport for the total concentration of the 'primary species' is solved, which by definition is reaction free, Saaltink et al. (1998), Steefel and MacQuarrie (1996). Note that the total concentration of a primary species is the stoichiometric sum of the concentrations of the species that contains the primary species (e.g. $TOT\left[Ca^{2+}\right] = \left[Ca^{2+}\right] + \left[CaCO_3\right]$). In this approach the extra equations needed to close the system and to compute the individual concentrations of each species are given by the mass action laws of the equilibrium reactions. These expressions relate the secondary and the primary species with the total concentrations, and even though these algebraic equations are local, they are usually non-linear.

Different approaches must be adopted when part of the reactions cannot be assumed in equilibrium. The species involved in such reactions must be treated kinetically, which means that a transport equation of the form (3.9) must be solved for them. Due to the slowness of such processes, they interact with the transport, and cannot be decoupled from it. Even where fast reactions need to be included, however, it is possible to use a fully kinetic formulation, Chilakapati (1995); Steefel and MacQuarrie (1996). The fully kinetic approach obviates the need to solve the set of mixed algebraic and differential equations which characterise mixed equilibrium-kinetic systems and avoids the ad hoc iteration schemes which are often employed in solving the system.

The fully kinetic formulation is the only one considered in this chapter to give an example of how the CV-HRBF can be applied to solve multi-species reactive transport problems.

In equation (3.9) the non-linearity is due to the reactive term that depends on the concentration c_l. Several methods have been proposed to solve the coupled set of equations. The most straightforward way conceptually, but the most demanding from a computational efficiency point of view, is to solve the governing equations, including both reaction and transport terms, simultaneously. This approach is referred to as a one-step, global implicit or Direct Substitution Approach (DSA) and it uses Newton–Raphson for the solution of the non-linear system, KEE et al. (1985); Steefel and Lasaga (1994). Alternatively, it is possible to use operator splitting techniques to decouple the reaction and transport calculations. This approach which is an implementation of the Picard method includes the Sequential Non Iteration Approach (SNIA) and the Sequential Iteration Approach (SIA). The SNIA consists of solving the reaction and transport equations within a single time step in sequence, with no iteration between the two. In the SIA the reaction and transport are solved separately but iteration between the two calculations is carried out until a converged solution is obtained. A general overview of these methods can be found in Saaltink et al. (2004), Steefel and MacQuarrie (1996) while in Saaltink et al. (2001) a comparison in performance between the SIA and the DSA is carried out.

Here the DSA is discarded in favour of the SIA method avoiding the construction and manipulation of the large matrix typical of the global implicit approach. At the same time the SIA should be more accurate than the SNIA approach, allowing the solution to converge before advancing to the next time step.

The reaction operator $R_n(c_l)$ that appears in equation (3.10) is divided into two parts to highlight the term that contains the concentration of the species c_n being transported

$$R_n(c_l) = K_r(c_l)c_n + R_n^0(c_l) \tag{3.12}$$

where $K_r(c_l)$ acts as a reaction coefficient for c_n and it depends on other species, and $R_n^0(c_l)$ is the remaining part of the reaction term not containing c_n. In general it will be $l = 1, N_{sp}$ with $l \neq n$.

Now substituting expression (3.12) into equation (3.10) and introducing a weighted Crank-Nicholson time-stepping scheme, the system of equations that describe the reactive transport problem can be rewritten as

$$L_t^{AD}\left(c_n^t\right)+K_r\left(c_l^t\right)c_n^t+R_n^0\left(c_l^t\right)=L_{t-\Delta t}^{AD}\left(c_n^{t-\Delta t}\right) \tag{3.13}$$

Where the two partial differential operators L_t^{AD} and $L_{t-\Delta t}^{AD}$ can be defined similarly to those ones of equations (3.5) and (3.6)

$$L_t^{AD}(\ )=\Delta t\theta\left(\frac{\partial}{\partial x_i}\left(D_{ij}^S\frac{\partial(\ )}{\partial x_j}\right)-\frac{1}{\eta}\frac{\partial q_i(\ )}{\partial x_i}\right)-1(\ ) \tag{3.14}$$

$$L_{t-\Delta t}^{AD}(\ )=\Delta t(\theta-1)\left(\frac{\partial}{\partial x_i}\left(D_{ij}^S\frac{\partial(\ )}{\partial x_j}\right)-\frac{1}{\eta}\frac{\partial q_i(\ )}{\partial x_i}\right)-1(\ ) \tag{3.15}$$

Equation (3.13) can be linearised taking the values of the concentration c_l at the previous non-linear iteration and moving the reaction term R_n^0 to the right hand side

$$L_t^{AD}\left(c_n^{t,m}\right)+K_r\left(c_l^{t,m-1}\right)c_n^{t,m}=L_{t-\Delta t}^{AD}\left(c_n^{t-\Delta t}\right)-R_n^0\left(c_l^{t,m-1}\right) \tag{3.16}$$

where m is the non–linear iteration index. Integrating equation (3.16) over each control volume of the mesh, and applying the CV-HRBF method, a linear system of equation for the unknown $c_n^{t,m}$ is obtained. The solution of such system allows to update the reaction terms R_n^0 and the reaction coefficient K_r, and a new system to refine $c_n^{t,m}$ can be formed. This procedure continues until the following convergence criteria is satisfied

$$\varepsilon_n=\left|\frac{c_n^{t,m}-c_n^{t,m-1}}{c_n^{t,m-1}}\right|_\infty\le\varepsilon_{tol} \tag{3.17}$$

where ε_{tol} is the value prescribed for the tolerance.

In the formulation of the local problem the linearisation of equation (3.13) is more substantial in order to reduce the computational cost, and the first order reaction term K_rc_n is entirely evaluated at the previous iteration and moved to the right hand side

$$L_i^{AD}\left(c_n^{t,m}\right) = L_{i-\Delta t}^{AD}\left(c_n^{t-\Delta t}\right) - K_r\left(c_i^{t,m-1}\right)c_n^{t,m-1} - R_n^0\left(c_i^{t,m-1}\right) \tag{3.18}$$

In this way the matrix of the local system does not need to be inverted at each non-linear iteration. In fact the operator L_i^{AD} remains unchanged. The algorithm explained above must be applied to all the species present in the system ($n = 1, N_{sp}$), but it is clear that only one species a time is evaluated and the resulting global matrix is considerably smaller than the one obtained using the DSA. A flow diagram of the algorithm is given in Figure 3.1.

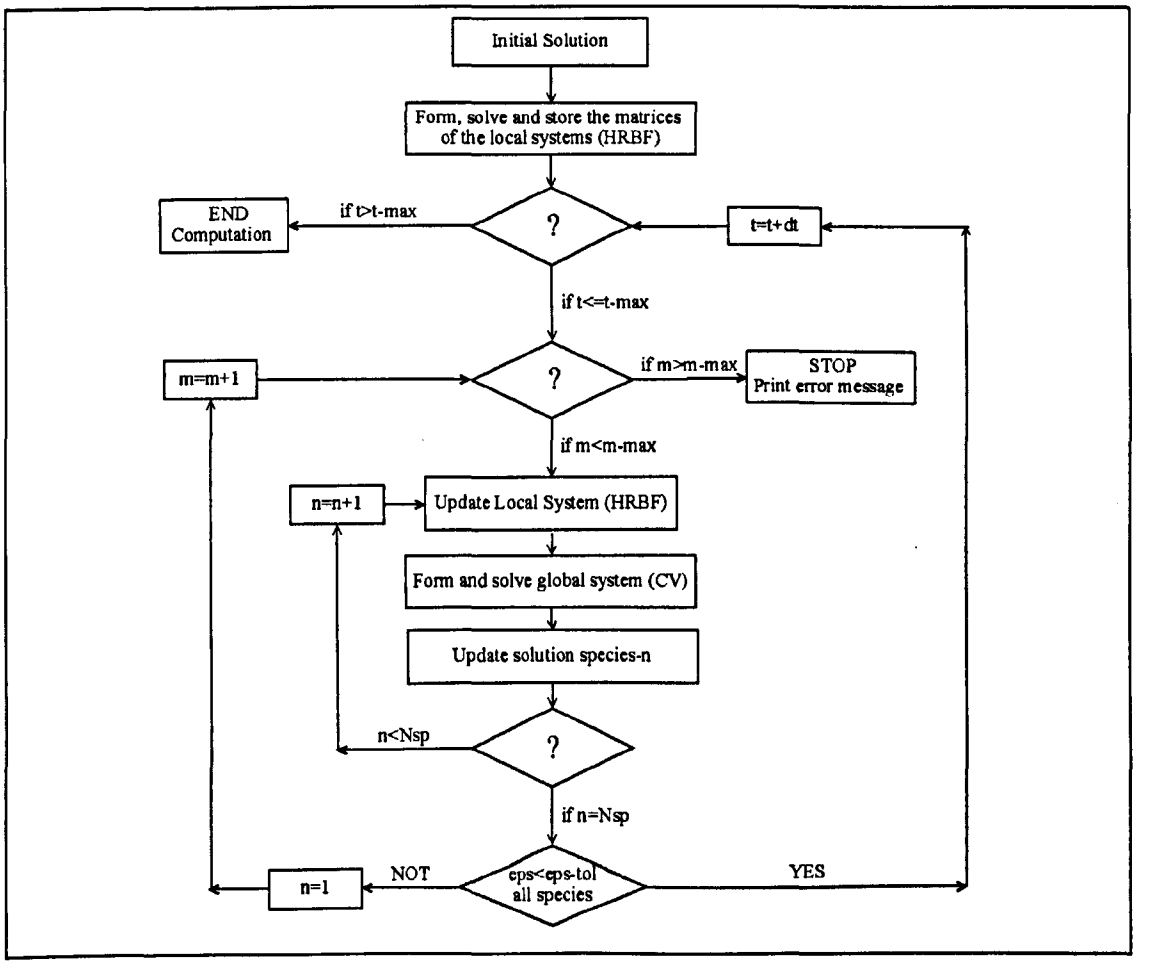

Figure 3.1 - Diagram of the non-linear transport algorithm used by the CV-HRBF. Nsp, number of species; m-max, maximum number of non-linear iteration; t-max, maximum value for the physical time.

In the SIA applied to the CV-HRBF method, the interpolation used to reconstruct the cell flux is still an approximation of the governing equation and it can benefit of the analytical upwinding discussed in chapter 2. More details on the computational cost will be given in the next section.

3.4 Computational cost consideration for the transport formulation of the CV-HRBF

The extra computational cost due to the solution of the local systems has been already analysed in section 2.5, however when the unsteady formulation of the CV-HRBF is considered this cost can vary significantly depending on the form of the PDE operator appearing in the local interpolation formula. If the PDE operator changes with respect to the time (e.g. due to a transient velocity field) the local systems must be solved at each time step, if instead the expression of L_t remains constant the inverse matrices of the local systems are computed as a pre-processing step at the beginning of the computation and stored in memory. The same consideration applies to the case of the reactive transport formulation presented in the previous section. For this particular case it is interesting to note that all the species share the same velocity field, and that in first approximation the dispersevity coefficients are very often taken to be the same for all the species. Under these assumptions, the local systems corresponding to the different species concentrations, and associated with a single element, share the same matrix. If for example ten species are considered for the transport model, than having L_t^{AD} that varies with time will involve re-inverting only one local matrix for each element at each time step. For this statement to be true it is also required that the same interpolation stencil is used for all the transported variables, a choice that appears to be as one of the most efficient anyway, as will be shown in the remaining of this section.

The formulation of the CV-HRBF has been presented in section 2.2 considering a random distribution for the set of points used in the interpolation, and in theory this is always possible due to the local meshless character of the method. However, an ad-hoc choice of the points included in the local RBF interpolation can improve significantly the efficiency of the method for unsteady problems. When $\vartheta = 1$ the method is fully implicit in time and equation (3.7) simplifies to

$$L_t(\phi) = -\phi^{t-\Delta t} \tag{3.19}$$

In this case, to fill up the right hand side of the local system one must reconstruct the solution ϕ at the previous time step at all those points where the PDE operator L_t has been applied. The computation involved in the reconstruction of $\phi^{t-\Delta t}$ can be avoided if the PDE points of the interpolation have the same location as the cell centres used to interpolate the values of ϕ. In fact such values come directly from the solution of the global system once it has been assumed

that the cell average values coincide with the values of the function at the cell centres. This type of double collocation scheme is permitted since the local Hermitian RBF interpolation scheme is adopted (see Section 1.1.2). In this case, the unit operator, i.e. the value of function (Dirichlet condition), and the PDE operator at each cell centre points are imposed. The local stencil which results from this double collocation strategy is shown in Figure 3.2. When $0<\vartheta<1$ the simplification in (3.19) does not hold anymore, and the operator $L_{t-\Delta t}\left(\phi^{t-\Delta t}\right)$ needs to be reconstructed from the previous time step solution, as explained before.

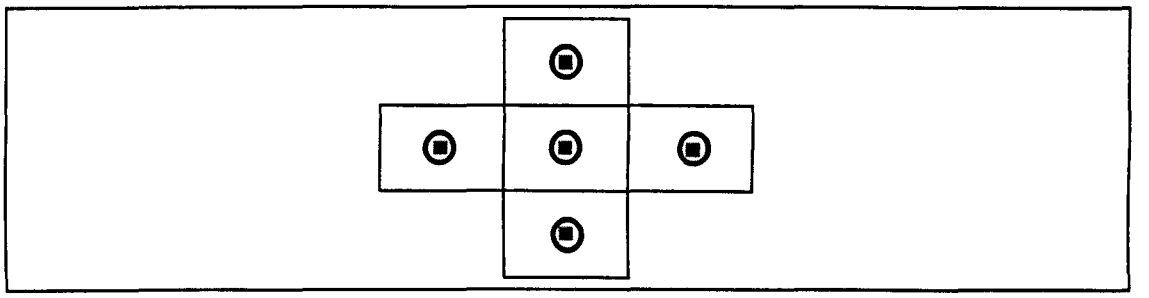

Figure 3.2 - Double collocation stencils: Square symbols, Dirichlet points; Circles, points where the PDE operator is applied (in this case they coincide with the previous ones)

The use of the stencil sketched in Figure 3.2 brings to an extra computational cost saving in the case of the non-linear transport formulation introduced in section 3.3. When the full implicit time stepping is considered, the linearised governing equation (3.18) applied to the local interpolation reduces to:

$$L_l^{AD}\left(c_n^{t,m}\right)=-c_n^{t-\Delta t}-K_r\left(c_l^{t,m-1}\right)c_n^{t,m-1}-R_n^0\left(c_l^{t,m-1}\right) \tag{3.20}$$

If all the species concentrations adopt the same double collocation stencil, then $c_n^{t-\Delta t}$, $c_n^{t,m-1}$ and $c_l^{t,m-1}$ are directly available from the solution of the global systems, and since the coefficient $K_r\left(c_l^{t,m-1}\right)$ and the operator $R_n^0\left(c_l^{t,m-1}\right)$ usually depend only on the values of the concentration and not from their gradient, no reconstructions are required during the non-linear iteration or to evaluate the solutions at the previous time step.

3.5 Numerical results

As an initial numerical test, an unsteady one-dimensional advection-diffusion problem in which the advection term is dominant is considered. In this test case the effect of the CV-HRBF implicit upwind is assessed by increasing the Péclet number up to the point where only the

advection component of the PDE operator is retained and the solution features a discontinuous travelling shock. Additionally, a series of reactive transport problems at low Péclet numbers are considered to evaluate the accuracy of the transient formulation in cases where the solution is characterised by smooth profiles.

Where possible the numerical solutions are validated with their corresponding analytical solutions and the resulting numerical errors assessed as the number of control volume cells increases. Since the numerical simulations are carried out using three-dimensional software, the one-dimensional problems are solved in 3D channels applying no-flux boundary conditions at the lateral boundaries to retain the one-dimensional characteristics of the problem. A multiquadric RBF is employed in the local interpolation algorithm and the value of the shape parameter chosen experimentally (iteratively) in order to minimise the L_2-norm (see Equation 2.24) in few prescribed instants.

The optimal values of the shape parameter found for the numerical examples presented in the next sections are listed all together in section 3.5.4. The stencil sketched in Figure 3.2, which is stopped at the first level of neighbouring cells, is used throughout this numerical section. When hexahedral meshes are considered this configuration features 14 points (7 Dirichlet + 7 PDE points), whereas for tetrahedral elements the total number of interpolation nodes is equal to 10 (5+5), see Figure App1 in the appendix.

3.5.1 One-dimensional transport of a single species

A one-dimensional transport problem for a single species c can be formulated in dimensionless parameters as

$$\frac{\partial c}{\partial t}+\frac{\partial c}{\partial x}=\frac{1}{Pe}\frac{\partial^2 c}{\partial x^2} \tag{3.21}$$

where Pe is the Péclet number. When equation (3.21) is solved in a semi-infinite domain with the following boundary and initial conditions

$$\begin{aligned} &c(x,0)=0 \qquad x\geq 0 \\ &c(0,t)=1, \qquad \lim_{x\to\infty}\frac{\partial c(x,t)}{\partial n}\to 0 \qquad t\geq 0 \end{aligned} \tag{3.22}$$

its analytical solution is (Van Genuchten and Alves (1982))

$$c_{ana}(x,t)=\frac{1}{2}erfc\left(\frac{x-t}{2\sqrt{t/Pe}}\right)+exp(xPe)erfc\left(\frac{x+t}{2\sqrt{t/Pe}}\right) \tag{3.23}$$

The problem described by equations (3.21) and (3.22) can only be solved numerically in a finite domain. In the numerical solution presented here, the semi-infinite one-dimensional domain of the above initial/ boundary value problem is taken as a bounded three-dimensional channel of size $[1,3\Delta x,3\Delta x]$ where Δx is the discretisation increment in the x direction. A series of computational grids featuring three elements in each of the lateral directions, y and z, and a uniform distribution of elements with different values of Δx in the x longitudinal direction are used for the simulation of this test case. A zero flux boundary condition is imposed at the lateral walls as well as at the end cross section of the computational domain, i.e. at $x=1$.

3.5.1.1 High Péclet number

Values of the Péclet number of 500, 1000 and infinity are considered and, in each case, 3 mesh resolutions are employed; $\Delta x=1/40$ (M40), $\Delta x=1/80$ (M80), $\Delta x=1/200$ (M200).

To compare the results obtained with the analytical solution (3.23) the simulations must be stopped before the travelling wave reaches the end of the computational domain, at $x=1$, i.e. before numerical reflexion affects the solution field in the domain considered. Unless stated otherwise, a time step equal to 0.001 is used and the simulation stopped at t=0.5, allowing the front to propagate until the middle point of the computational domain. A convergence analysis using a full implicit time integration scheme comparing the numerical results with the corresponding analytical solutions is presented in Figure 3.3.

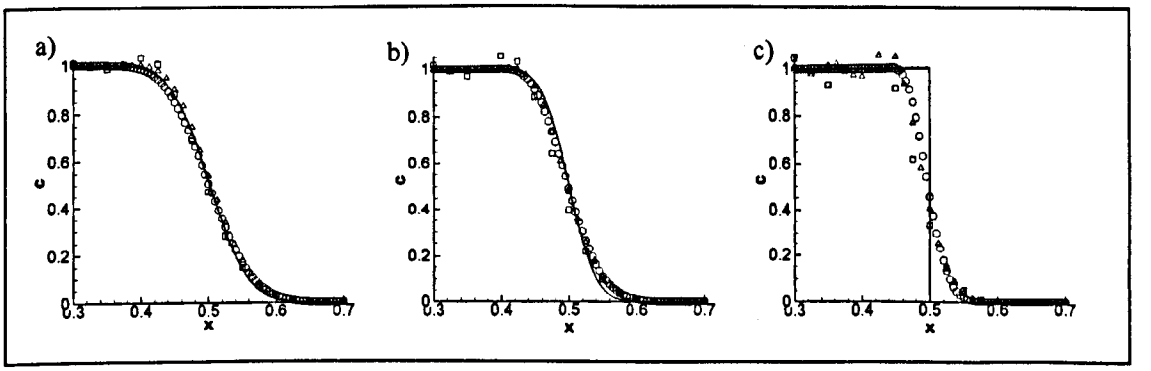

Figure 3.3 - Convergence analysis on three meshes: square symbols, M40; triangular symbols, M80; round symbols, M200. The full lines refer to the analytical solution. Time-stepping scheme: full implicit. a) Pe=500; b) Pe=1000; c) Pe=infinity

As can be observed from the above results, when using the coarsest mesh, the fully implicit numerical solution exhibits both diffusive and dispersive errors, i.e. underestimation of the

gradient and spurious oscillations respectively. The magnitude of these two errors becomes larger as the Péclet number increases. However, by increasing the number of collocation point, it is possible to reduce the dispersive error significantly, damping it completely when using the denser mesh, even in the case of the infinite Péclet number.

In the case of the lower Péclet numbers, $Pe = 500$ and $Pe = 1000$, using the densest discretisation, M200, the analytical solution is reproduced with a very small diffusive error. This artificial diffusivity can be attributed to the use of the first order discretisation in time, and it can be improved when a higher order scheme is adopted. The results obtained using the second order Crank-Nicholson time stepping scheme with a blending parameter ϑ equal to 0.5 are shown in Figure 3.4, from which the previous statement is confirmed.

The use of the Crank-Nicholson scheme significantly reduces the diffusive error in the two cases of finite Péclet number (*Pe*=500 and *Pe*=1000) without introducing any dispersive error or instability. In those cases, when using the densest mesh the analytical solution is almost identically reproduced. On the other hand, in the case of pure advection (infinite Péclet number), the numerical solution predicted by the Crank-Nicholson second order scheme captures the front of the moving shock better, reducing the diffusive error. However, the solution features a large dispersive error or instability. This is not surprising, because for this type of problem the second order Crank-Nicholson scheme is not the most suitable approach. Instead other high order time stepping schemes should be implemented (e.g. implementing the Richardson extrapolation or using a front-tracking algorithm). No further investigation on this topic was carried out because this is beyond the scope of the present work.

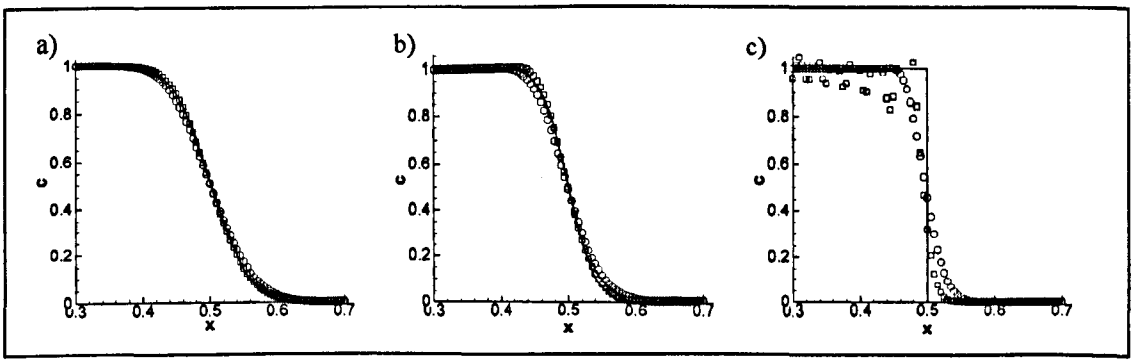

Figure 3.4 - Comparison full implicit / Crank-Nicholson (CN) time-stepping schemes. Round symbols, full implicit; square symbols, CN.The full lines refer to the analytical solution. Mesh: M200. a) *Pe*=500; b) *Pe*=1000; c) *Pe*=infinity

The effect of varying the Crank-Nicholson weighting factor ϑ on the stability is shown in Figure 3.5, where the solution obtained using an increasing value of ϑ (0.7, 0.85, 1) are

compared along with the analytical solution for the case of infinite Péclet number and using the M200 mesh. As expected, increasing the value of ϑ makes the numerical solution more stable but also more diffusive.

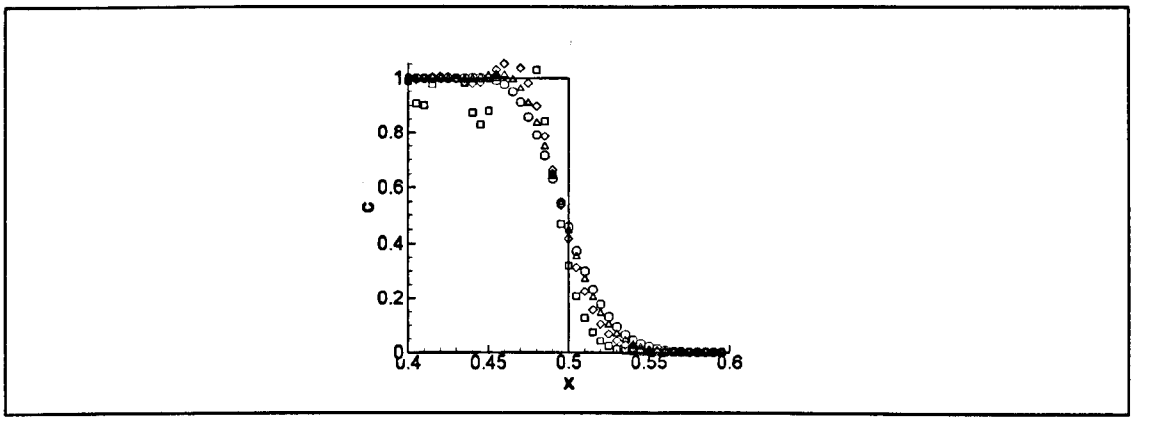

Figure 3.5 - Effect of the weighting factors on the Crank-Nicholson scheme: Square symbols, $\vartheta = 0.5$; Diamond symbols, $\vartheta = 0.7$; Delta symbols, $\vartheta = 0.85$; Round symbols, $\vartheta = 1$

To assess the effect of the time step on the stability of the CV-HRBF scheme, the case of infinity Péclet number is simulated for three different time step values (0.1, 0.01 and 0.001). The simulations are carried out for a longer evolution time than in the previous simulations, until $t = 1$, to verify that the scheme does not deteriorate the solution as the time advances. The solutions obtained using the fully implicit time discretisation for the three values of the time step considered are compared with the analytical solution for two instants, $t = 0.5$ and $t = 1$, Figure 3.6. The computational domain is twice the size of that used in the previous simulations, and the mesh characterised by $\Delta x = 1/200$. As expected, the diffusive error increases with the time step, but the solution remains stable in all cases and the accuracy does not worsen significantly as the front shock moves downstream.

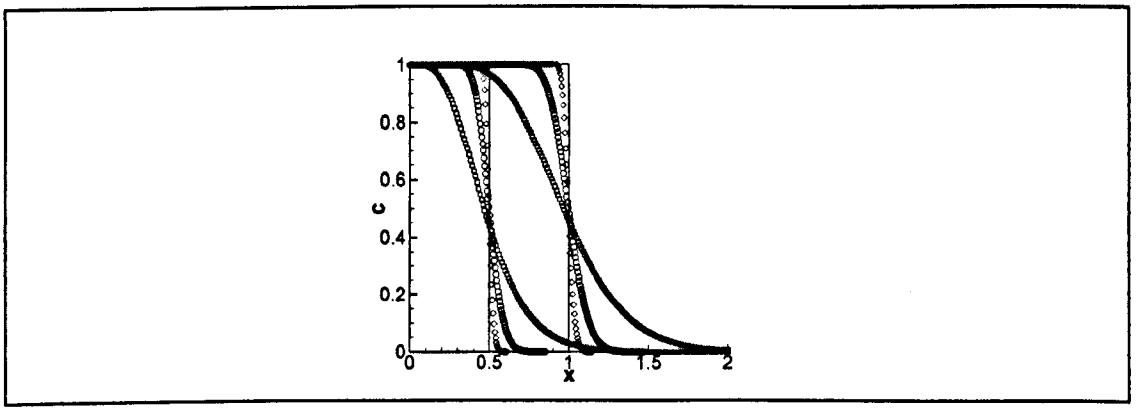

Figure 3.6 - Solution comparison for increasing value of the time step (Pe=infinity; mesh, Δx=1/200): square symbols, Δt=0.1; round symbols, Δt=0.01; diamonds symbols, Δt=0.001. First evaluation interval taken at t=0.5 and the second one at t=1.0. Full lines, analytical solution.

In the test cases reported so far, the local interpolation satisfies the PDE operator at the centre of all the cells defining the interpolation stencil, i.e. using the double collocation configuration sketched in Figure 3.2. To assess the stabilising effect of the implicit upwind introduced by the PDE operator in the interpolation formula, the test cases at Péclet number 1000 and infinity are simulated with the CV-RBF scheme proposed by Moroney and Turner (2006) (2007), i.e. without the use of the PDE operator for the local interpolation and without any kind of upwinding scheme, using the same implicit time stepping scheme used in the previous examples. Comparisons between the results obtained with the CV-RBF and the CV-HRBF approaches are reported in Figure 3.7, showing the benefit of the proposed implicit upwind. As can be observed, the inclusion of the local PDE in the interpolation improves the stability of the solution, becoming more and more significant as the Péclet number increases, i.e. in the cases of advection dominant problems, Figure 3.7.b. It is important to point out that the results reported in this section, except those given in Figure 3.6, are shown in a zoomed-in region close to the moving front. Consequently the magnitude of the respective errors appears to be magnified.

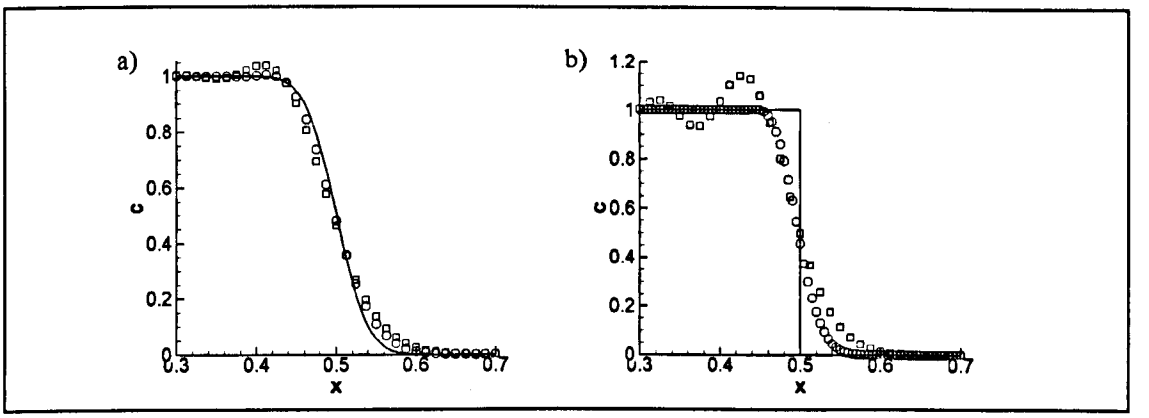

Figure 3.7 - Comparison with/without PDE in the local interpolation. Round symbols, with PDE; square symbols, no PDE. The full lines refer to the analytical solution. a) *Pe*=1000, M81; b) *Pe*=infinity, M201;

Finally, increasing the number of points where the local interpolation is required to satisfy the PDE operator does not significantly improve the numerical solution for the ill-conditioning issues related with the solution of the local system as previously explained in section 2.3.

3.5.1.2 Stability analysis

To further assess the stability of the proposed CV-HRBF approach, the analysis of standing waves perturbation, $\eta(x,t) = a(x)\exp(\lambda t)$, imposed to the moving front solution at infinity Péclet number of equation (3.21) is considered. Due to the linearity of the problem the evolution of the perturbation waves is also governed by equation (3.21), with $Pe = \infty$, and homogeneous boundary conditions. Therefore, the wave amplitude is a solution of the equation

$\lambda a(x)+\partial a(x)/\partial x=0$. By using the proposed CV-HRBF approach the above problem reduces to the following eigenvalue problem

$$\left([A_{GLB}]+\lambda\right)[a]=0 \tag{3.24}$$

where $[A_{GLB}]$ is the global matrix obtained after carrying out the Hermitian interpolation at the local levels of the wave amplitude and its advective flux, and $[a]$ is the control volume solution vector of the wave amplitude at the cell centres.

The eigenvalues $[\lambda]$ of the matrix $[A_{GLB}]$ characterise the time evolution of the standing waves perturbation and consequently their stability. Therefore, the moving front solution at infinity Péclet number of equation (3.21) will be stable or not to the imposed standing waves perturbation provided that:

a) asymptotically stable if and only if the real part of the eigenvalues are all negative, i.e. $\mathrm{Re}[\lambda]<0$
b) neutral stable if and only if the real part of eigenvalues are all equal to zero
c) unstable if the real part of one or more eigenvalues are positive. In this case the moving front will be unstable to the wave modes, eigenvectors, corresponding to these positive eigenvalues.

In the determination of the global matrix $[A_{GLB}]$ the denser mesh, M200, used in previous sections is employed, resulting in a matrix system of 1800×1800. As can be observed, in this case the analysis of the stability is not affected by a time stepping algorithm due to the selected form of the imposed perturbation, i.e. proportional to $\exp(\lambda t)$.

The eigenvalues of the global matrix $[A_{GLB}]$, real and imaginary parts, are computed numerically and reported in Figure 3.8, showing their values and complex conjugate values. All the eigenvalues are characterised by a very small negative real part, with the closest value to zero equal to -6.0×10^{-10}, corresponding to asymptotically stable solution having a very small artificial numerical diffusivity (in the present case of infinity Péclet number), where the larger absolute value of the real part of λ is of the order of -3.0×10^{-7}.

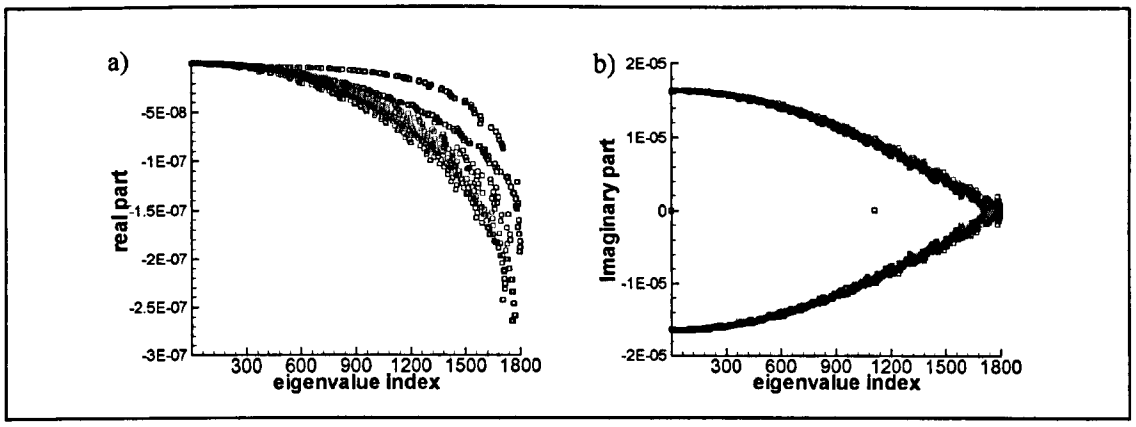

Figure 3.8 - Stability analysis. Matrix eigenvalues analysis: a) real part, b) imaginary part

3.5.1.3 Low Péclet number

To test the performance of the transient CV-HRBF scheme in problems where the diffusion is dominant the test case described above is solved again assigning a Péclet number of 12. A relative coarse mesh corresponding to $\Delta x = 1/80$, M80, and a time step equal to 0.001 are used. The numerical results are compared against the analytical solution (3.23), at t1=0.03, t2=0.06, t3=0.15, t4=0.24 and t5=0.3, Figure 3.9.

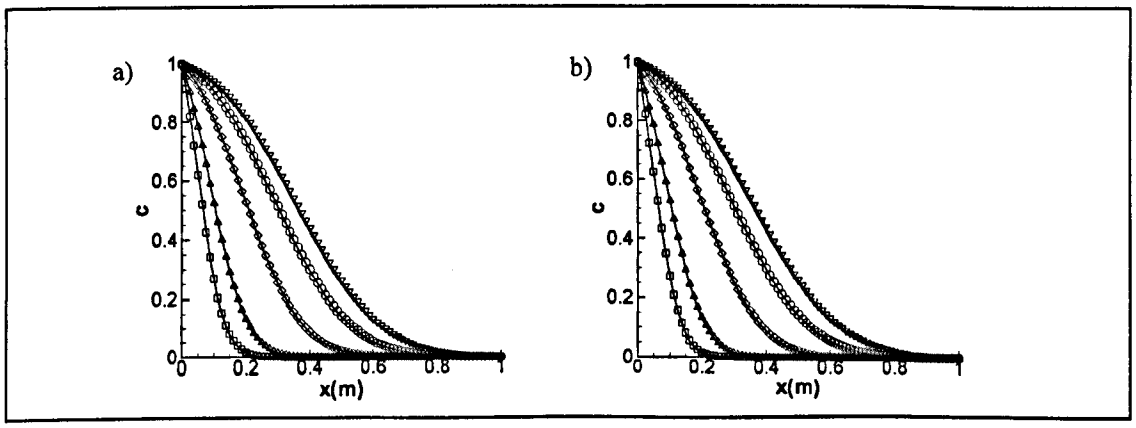

Figure 3.9 - Comparison full implicit / Crank-Nicholson (CN) time-stepping schemes. Square symbols, t=0.03; Delta symbols, t=0.06; Diamond symbols; t=0.15; Round Symbols, t=0.24; Gradient symbols, t=0.3. The full lines refer to the analytical solution. a) implicit; b) CN

The numerical results are in a very good agreement with the analytical solution. In order to appreciate the gain in accuracy due to the use of the Crank-Nicholson scheme, an error analysis is reported in Table 3.1. Here the benefits of the Crank-Nicholson scheme on the numerical solution are evident, in particular at the beginning of the simulation. It is important to point out that in the present case, some numerical reflection from the artificial boundary at $x = 1$ is affecting the numerical results towards the end of the simulation; this is the reason why the evaluated L^t_{2error} appears to increase as time increases.

	t = 0.03	t = 0.06	t = 0.15	t = 0.24	t = 0.3
Implicit	1.6×10-3	9.2×10-4	1.3×10-3	2.3×10-3	2.9×10-3
CN	6.1×10-4	7.3×10-4	1.0×10-3	1.2×10-3	1.3×10-3

Table 3.1 - L^t_{2error} comparison, implicit - Crank-Nicholson (CN) at different time steps.

As in the previous examples, in this case at the beginning of the simulation a discontinuity front needs to be captured, requiring the use of a very small time step to achieve the desired accuracy. A solution similar to the one reported in the table above can be obtained by using a variable time step, increasing its magnitude as the time progresses and the solution becomes smoother. In the present case, similar results can be obtained by gradually increasing the value of the time step until 0.01. In section 3.5.2 the effect of the different time steps will be discussed in more details.

3.5.2 Reactive-transport of a single species

In this section the CV-HRBF capabilities in the solution of single species reactive transport problems are investigated in one and three-dimensional test cases.

3.5.2.1 One-dimensional test case

The three-dimensional equation (3.1) reduces to a one-dimensional problem when the following parameters are assigned:

$$D_{ij} = 1.0\frac{m^2}{s} \text{ for } i=j; \quad D_{ij} = 0.0 \text{ for } i \neq j$$

$$U_1 = 6.0\frac{m}{s}, \quad U_2 = 0.0, \quad U_3 = 0.0, \quad k = 0.278\frac{1}{s}$$

The one-dimensional problem considered in this section is prescribed by the following boundary and initial conditions

$$c(x,0) = 0.0$$

$$c(0,t) = 300.0\frac{kg}{m^3}$$

$$\frac{\partial c}{\partial n}(\ell,t) = 0.0$$

where ℓ is the length of the computational domain (6 metres in this case). The analytical solution to this problem is given by Van Genuchten and Alves (1982). As in the previous case,

the numerical solution is computed in a three-dimensional domain $[6,3\Delta x,3\Delta x]$, using a structured mesh with 3 elements in each of the lateral directions and a uniform distribution in the longitudinal direction characterised by $\Delta x = 1/80\,m$. Zero flux boundary conditions are imposed at the lateral walls to preserve the one-dimensional character of the problem. Both the implicit and the second order Crank-Nicholson schemes are tested using a time step equal to $0.001s$, see Figure 3.10. As before, a discontinuous front needs to be captured initially by the numerical simulation. In this case it is possible to increase the value of the time step several order of magnitude as the evolution progresses.

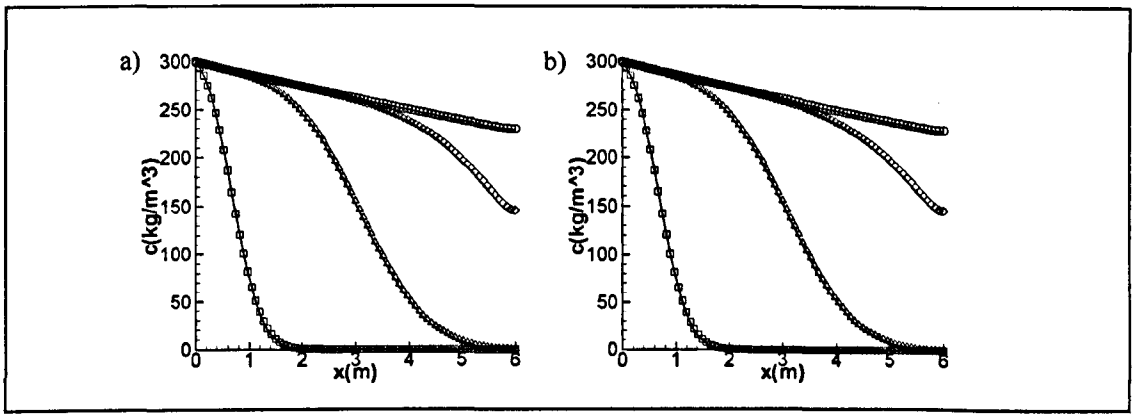

Figure 3.10 - Comparison full implicit / Crank-Nicholson (CN) time-stepping schemes. Square symbols, t=0.1s; Delta symbols, t=0.5s; Diamond symbols; t=1.0s; Round Symbols, t=2.0s. The full lines refer to the analytical solution. a) implicit; b) CN

For this case the Crank-Nicholson second order time integration scheme significantly reduces the error as the solution advances in time, Table 3.2.

	t=0.1s	t=0.5s	t=1.0s	t=2.0s
Implicit	1.4×10^{-3}	6.0×10^{-3}	6.0×10^{-3}	6.5×10^{-3}
CN	7.0×10^{-4}	7.6×10^{-4}	5.6×10^{-4}	1.5×10^{-4}

Table 3.2 - L^{*t}_{2error} comparison, implicit - Crank-Nicholson (CN) at different instants.

In this case a dimensionless L_2-norm error ($L^{*t}_{2error} = L^{t}_{2error} / c_{max}$) has been used to evaluate the accuracy of the solution to obtained an estimator that is scale effect-free, in fact a large variation of the function value occurs in the considered domains (0-300 kg/m^3).

3.5.2.2 Three-dimensional test case

A substance is assumed to be instantaneously injected at a point source into a fluid which is moving at a constant velocity. The substance is non-conservative and is assumed to decay at a rate which is proportional to the concentration. This problem can be described by equation (3.1) modelling the injection by an instantaneous point source located at x_S, y_S, z_S. If the x axis is

aligned with the direction of the constant fluid velocity, i.e. $U_1 = U$, $U_2 = 0$, $U_3 = 0$, and the diffusivity is homogeneous and anisotropic with the principal components in the x, y, z directions, then the analytical solution to the problem is given by the fundamental solution, singular solution (Carslaw and Jaeger (1959))

$$c = \frac{M}{\rho(4\pi t)^{3/2}(D_1 D_2 D_3)^{1/2}} exp\left[-\left(\frac{(d_x - Ut)^2}{4D_1 t} + \frac{d_y^2}{4D_2 t} + \frac{d_z^2}{4D_3 t} + kt\right)\right] \qquad (3.25)$$

where the three components of the distance from the source are defined as $d_x = x - x_S$, $d_y = y - y_S$ and $d_z = z - z_S$. M represents the total amount of mass of substance introduced and ρ is the density of the mixture of the substance and fluid which can be taken as a constant equal to the density of the receiving fluid. As $t \to 0$, the concentration tends to zero at all points except at the location of the point source (x_S, y_S, z_S) where the concentration becomes infinite. As before, at the beginning of the simulation a strong front needs to be captured, on the other hand, as $t \to \infty$ the concentration tends to zero everywhere.

In this example, the source solution (3.25) along with the equation (3.1) are used to define an initial boundary value problem in a parallelepiped ([$1.0m \times 0.25m \times 0.5m$]) centred at the point ($0.75m$, $0m$, $0m$). In order to avoid the singularity, the source is located outside the computational domain at $x_S = 0, y_S = 0.25m, z_S = 0.25m$, i.e. outside the parallelepiped but close to one of its upper edges. The analytical solution is used to assign transient Dirichlet boundary conditions to all the six faces of the parallelepiped, and zero concentration is taken as initial condition everywhere inside the domain. The following values are assigned to the rest of the parameters and coefficients:

$$D_1 = D_3 = 1.0\frac{m^2}{s}, \quad D_2 = 0.5\frac{m^2}{s}$$

$$K_r = 0.2\frac{1}{s}, \quad U = 6.0\frac{m}{s}; \quad M = 1.0kg, \quad \rho = 1.0\frac{kg}{m^3}$$

A uniform grid made of 40x20x20 hexahedron-cells is initially employed and two time step values of $0.01s$ and $0.001s$ are tested. The numerical results are reported at the time intervals of t=$0.02s$, t=$0.05s$, t=$0.1s$ and t=$0.15s$. The exact solution taken in the plane $y = 0.2375m$ at the

four time intervals above mentioned is shown in a three-dimensional plot in Figure 3.11: During the time evolution the peak of the concentration flattens as it travels downstream in the channel.

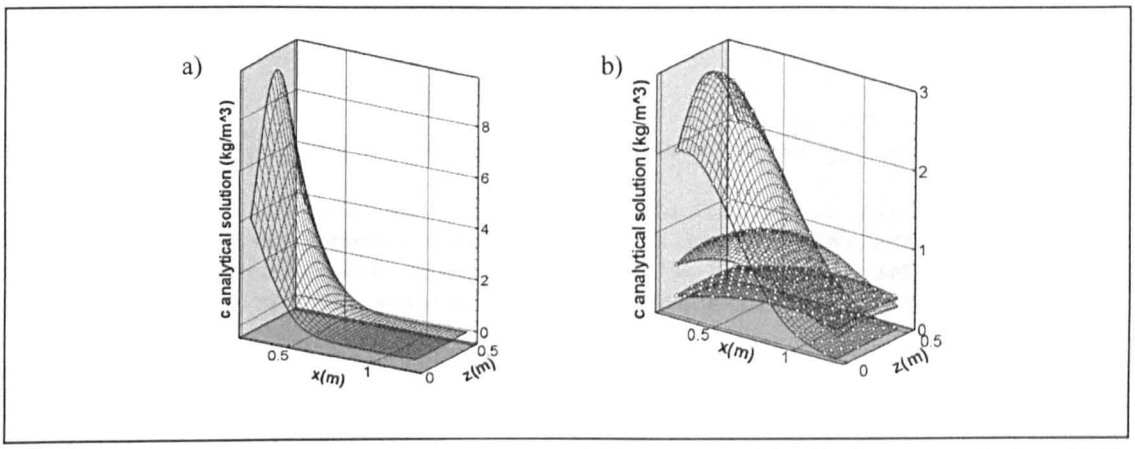

Figure 3.11 - Analytical solution in the plane at x_2=0.2375m. a): t=0.2s; b): Square symbols, t=0.05s; Delta symbols, t=0.1s; Diamond symbols; t=0.15s

To compare the results with the analytical solution, a transversal (at $x = 0.75m$) and a longitudinal (at $z = 0.25m$) profile are extracted from the plane $x_2 = 0.2375m$ where the higher gradients are expected. Figure 3.12 and Figure 3.13 report the results obtained using the fully implicit and second order Crank-Nicholson schemes for a time step equal to $0.001s$.

Either using the full implicit time integration scheme (Figure 3.12) or the Crank-Nicholson alternative (Figure 3.13) a good agreement between the computed results and the analytical solution is observed, however higher accuracy is always found when the Crank-Nicholson scheme is employed, Table 3.3. The comparison between the L^t_{2error} values obtained using Δt_1=0.01s and Δt_2 =0.001s show the first order convergence of the finite difference approximation used in the implicit formulation of the time derivative in equation (3.1) and a higher order of convergence in the case of Crank-Nicholson. In the present case, it is not possible to increase more the time step due to the fast time decay experienced by the analytical solution of the problem (see Figure 3.11).

To conclude this first validation of the transient version of the CV-HRBF proposed in this chapter, the three-dimensional reactive transport problem described above is simulated again using an unstructured mesh. The new computational grid which features about 18,000 tetrahedrons and 3,800 nodes, is shown in Figure 3.14.

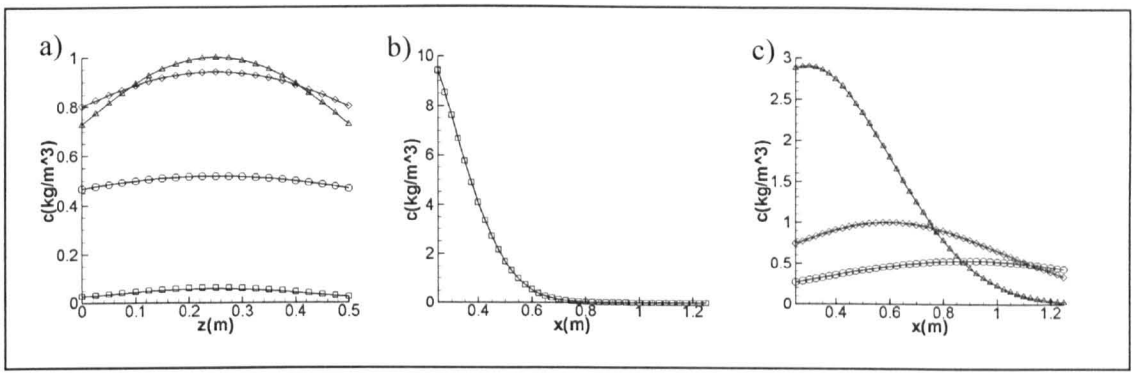

Figure 3.12 - Implicit, comparison with analytical solution. Square symbols, t=0.02s; Delta symbols, t=0.05s; Diamond symbols, t=0.1s; Round symbols, t=0.15s. The full lines refer to the analytical solution..a) profile at x=0.2375m and y=0.75m; b)-c) profile at y=0.2375m and z=0.25m.

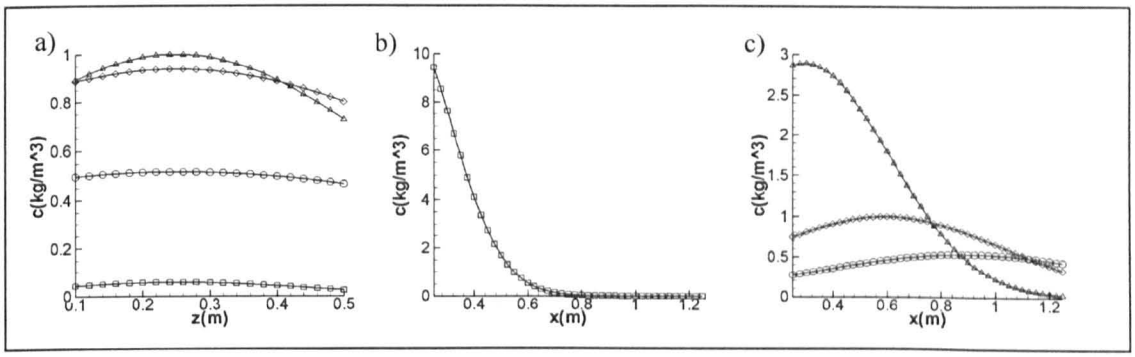

Figure 3.13 - Crank-Nicholson, comparison with analytical solution. Square symbols, t=0.02s; Delta symbols, t=0.05s; Diamond symbols, t=0.1s; Round symbols, t=0.15s. The full lines refer to the analytical solution..a) profile at x_2=0.2375m and x_1=0.75m; b)-c) profile at x_2=0.2375m and x_3=0.25m ;

	t = 0.02s		t = 0.05s		t = 0.1s		t = 0.15s	
	Δt_1	Δt_2	Δt_1	Δt_2	Δt_1	Δt_2	Δt_1	Δt_2
Im.	8.2×10^{-2}	1.4×10^{-2}	2.9×10^{-2}	3.3×10^{-3}	5.8×10^{-3}	5.9×10^{-4}	2.0×10^{-3}	1.8×10^{-4}
CN	5.0×10^{-2}	2.5×10^{-3}	5.5×10^{-3}	4.5×10^{-4}	9.0×10^{-4}	1.6×10^{-4}	3.0×10^{-4}	6.8×10^{-5}

Table 3.3 - Structured mesh: L^t_{2error} comparison, implicit - Crank-Nicholson (CN) at different instants. Δt_1=0.01, Δt_1=0.001.

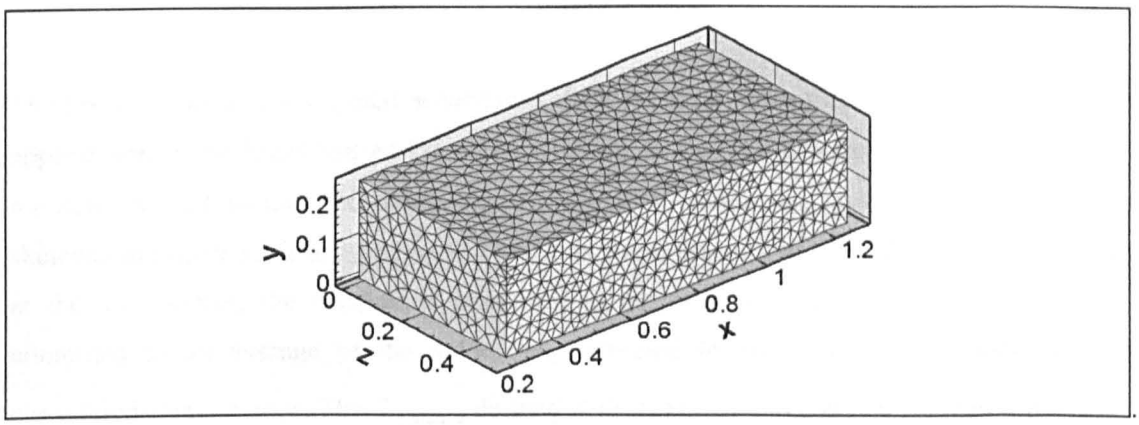

Figure 3.14 - Three-dimensional unstructured mesh view: 18200 tetrahedrons, 3800 nodes

It is not possible to note any significant difference between the results obtained using the structured and the unstructured mesh when plotting the same profiles considered in Figure 3.12 and Figure 3.13; in both cases the computed solution is very close to the analytical one. So instead of reporting another series of profile plots, only the L^t_{2error} analysis is reported below for the solution computed in the unstructured grid, Table 3.4. In this case, both time integration schemes have similar convergence rate, with larger value for the Crank-Nicholson approach, as can be observed from the result in Table 3.4 for the two time steps used.

	t = 0.02s		t = 0.05s		t = 0.1s		t = 0.15s	
	Δt_1	Δt_2	Δt_1	Δt_1	Δt_1	Δt_2	Δt_1	Δt_2
Im.	8.0×10^{-2}	3.5×10^{-2}	2.4×10^{-2}	1.0×10^{-2}	4.6×10^{-3}	3.8×10^{-3}	1.1×10^{-3}	2.0×10^{-3}
CN	5.5×10^{-2}	3.2×10^{-2}	9.8×10^{-3}	8.0×10^{-3}	2.3×10^{-3}	2.4×10^{-3}	1.2×10^{-3}	1.4×10^{-3}

Table 3.4 - Unstructured mesh: L^t_{2error} comparison, implicit - Crank-Nicholson (CN) at different instants. Δt_1=0.01, Δt_1=0.001.

From the comparison between the L^t_{2error} values reported in Table 3.3 and Table 3.4, it is clear that the precision of the CV-HRBF approach is reduced when the unstructured mesh is employed. In spite of this the accuracy obtained is still acceptable.

For this test case a global residual is also used to estimate how the accuracy of the solution changes as the shape parameter varies. This can be useful in those cases where the analytical solution is not known. Such residual can be computed using the local HRBF interpolations after the global system has been solved and the interpolation coefficients are known. A number of points inside and nearby the HRBF interpolation stencil can be selected and for each of them the PDE operator (3.7) reconstructed to compute a local residual as follows

$$res_i = \left(L_t(\phi) - L_{t-\Delta t}(\phi)\right)\Big|_{x=x^i} \tag{3.26}$$

The residuals must be computed in locations different from those where the PDE operator was applied before the formation of the global system. In fact these points satisfy equation (3.7) numerically and would not return any contribution. Since the local stencil configuration sketched in Figure 3.2 is adopted for the transient formulation, with the PDE operator collocated at the cell centres, the residual is computed at the element nodes. Each nodal residual is computed as an average of the values reconstructed by the interpolations that share the considered element node. The $L^t_{2residual}$ defined in (3.27) is used as a global residual estimator.

$$L^t_{2residual} = \sqrt{\frac{\sum_{i=1}^{Nnodes} [res_i]^2}{Nnodes}} \tag{3.27}$$

The computation of the residual defined by Eqs. (3.26) and (3.27) is assessed evaluating L^t_{2error} and $L^t_{2residual}$ for two different values of the shape parameter, $c^*_S = 0.04$ and $c^*_S = 0.4$. The corresponding values of the obtained L^t_{2error} and $L^t_{2residual}$ as the evolution time progresses are given in Table 3.5 and Table 3.6. Although there is not a linear correlation between the reduction of the $L^t_{2residual}$ and L^t_{2error}, as the value of the shape parameter increases, the comparison between the errors and the residuals shows that the $L^t_{2residual}$ is a good indicator for the selection of the optimal shape parameter, which in this case is achieved using the implicit time stepping scheme when its value is close to 0.4. Increasing further the value of the parameter leads to a significantly erroneous solution, with L^t_{2error} and $L^t_{2residual}$ diverging quickly from reasonable values.

c^*_S	t = 0.02s	t = 0.05s	t = 0.1s	t = 0.15s
0.04	5.8×10^{-2}	2.7×10^{-2}	7.2×10^{-3}	2.3×10^{-3}
0.4	3.5×10^{-2}	1.0×10^{-2}	3.8×10^{-3}	2.0×10^{-3}

Table 3.5 - Unstructured mesh, full implicit: L^t_{2error} comparison using two different values of the shape parameter

c^*_S	t = 0.02s	t = 0.05s	t = 0.1s	t = 0.15s
0.04	5.7×10^{-2}	2.1×10^{-2}	7.4×10^{-3}	3.4×10^{-3}
0.4	5.3×10^{-2}	1.9×10^{-2}	6.4×10^{-3}	2.7×10^{-3}

Table 3.6 - Unstructured mesh, full implicit: $L^t_{2residua}$ comparison using two different values of the shape parameter

3.5.3 Magnesite dissociation in a column experiment

A semi-infinite column filled homogeneously with crushed magnesite ($MgCO_3$) is considered. The medium is saturated with water which is initially in chemical equilibrium with the mineral. A water with different concentrations of each species, in equilibrium with the mineral is injected at the inlet of the column ($x = 0$) with a constant flux ($q_1 = q$). Since the velocity is constant, the dispersivity will also have a constant value (D^S). As the two waters characterised by different chemical signatures mix, a reaction take places to re-equilibrate the system. In order to ensure that the speciation of dissolved inorganic carbon is negligible, it is assumed that the pH is significantly higher than 10.3, which is the pKa of the carbonate-bicarbonate system; in

addition the effect of variations of ionic strength on the equilibrium constant is neglected, Sanchez-Vila et al. (2007).

Dissociation of magnesite is described by:

$$MgCO_3 \leftrightarrow Mg^{2+} + CO_3^{2-} \tag{3.28}$$

A typical reaction time scale for this reaction is of the order of 54 days, Azaroual et al. (2003), and local non equilibrium conditions are considered in the mixing process. The problem is treated with the kinetic approach introduced in section 3.3. A model proposed by Lasaga et al. [1994] is taken for the reaction rate, with $R > 0$ indicating precipitation

$$R = -\tau_R^{-1}\sqrt{K_{MgCO_3}}\left(1-\Omega^{IA}\right) \tag{3.29}$$

where τ_R is the effective reaction time, K_{MgCO_3} is the local equilibrium constant and Ω^{IA} is the ion activity product defined as

$$\Omega^{IA} = \frac{[Mg^{2+}][CO_3^{2-}]}{K_{MgCO_3}} \tag{3.30}$$

Two transport time scales are considered, the advection time scale $\tau_a = L_{MIX}/q$, and the dispersion time scale $\tau_D = L_{MIX}^2/D^S$ where L_{MIX} is the characteristic length scale of the portion of space for which the species can be assumed to be well mixed. The Péclet number defined as $Pe = \tau_D/\tau_a$ quantifies the relative importance between the dispersive and the advective transport mechanisms.

Local scale equilibrium can be assumed to hold if the reaction time τ_R is small compared to a typical dispersion time scale τ_D. The dispersion scale is compared to the reaction time scale τ_R by the non-dimensional Damköhler number Da, defined as

$$Da = \frac{\tau_D}{\tau_R} \tag{3.31}$$

Note that dispersion is the relevant mass transfer mechanism in the context of the mixing-limited reactions that are considered here, whereas the advective transport has the effect of a pure translation of a fluid element in space.

If non-dimensional variable are considered ($x' = x/L_{MIX}$, $t' = t/\tau_D$ and $c' = c/\sqrt{K_{MgCO_3}}$) then two transport equations can be written as

$$\frac{\partial [Mg^{2+}]'}{\partial t'} - \frac{\partial^2 [Mg^{2+}]'}{\partial x'^2} + Pe\frac{\partial [Mg^{2+}]'}{\partial x'} = -R' \tag{3.32}$$

$$\frac{\partial [CO_3^{2-}]'}{\partial t'} - \frac{\partial^2 [CO_3^{2-}]'}{\partial x'^2} + Pe\frac{\partial [CO_3^{2-}]'}{\partial x'} = -R' \tag{3.33}$$

where

$$R' = Da\left(1 - \Omega'^{1/4}\right) \tag{3.34}$$

From now on the superscript that indicates non-dimensional variables will be omitted for the sake of compactness in the presentation.

The normalised concentrations in the water of the column before the injection are taken to be equal to $[Mg^{2+}]_0 = 0.537$ and $[CO_3^{2-}]_0 = 1.858$ (their product is equal to 1, which indicates chemical equilibrium). The injected water is also in equilibrium but with different concentrations: $[Mg^{2+}]_0 = 2.148$ and $[CO_3^{2-}]_0 = 0.465$. A Péclet number equal to 0.1 is chosen to define the injection velocity.

The problem is solved numerically in a bounded three-dimensional channel of size $[10, 2\Delta x, 2\Delta x]$ where $\Delta x = 0.0125$ is the discretisation increment in the x direction. A zero flux boundary condition is imposed at the lateral walls as well as at the end cross section of the computational domain, i.e. at $x = 10$ for both variables. The simulations must be stopped well before the reacting front reaches the end of the computational domain, at $x = 10$, i.e. before numerical reflexion affects the solution field in the domain considered. No analytical solution is known for the concentration of the two species. However, a free-reaction transport equation for the conservative component $[Mg^{2+}] - [CO_3^{2-}]$ is found subtracting equation (3.33) from (3.32). This expression has the same form of equation (3.21), for which an analytical solution is given by equation (3.23).

In the simulations carried out to assess the reactive transport formulation of the CV-HRBF method, three values of the Damköhler number are tested (1, 10 and 100). The first of the three values ($Da=1$) corresponds to a situation where the reaction time is comparable with the dispersive time scale, whereas in the last case ($Da=100$) the reaction is very fast and can be considered nearly in equilibrium when compared with the transport.

The time is discretised using a full implicit time integration scheme, $\vartheta=1$ in equations (3.14) and (3.15), and a normalised time step equal to 0.001 is adopted for all the cases simulated. The tolerance value imposed for the convergence criteria (3.17) is $\varepsilon_{tol}=10^{-6}$, and the maximum number of non-linear iterations, fixed to 20, is never reached during the simulations.

As a post processing operation, the difference between the two species concentrations, $[Mg^{2+}]-[CO_3^{2-}]$, is computed and compared against the analytical solution (3.23) at the instant $t=1$, Figure 3.15.

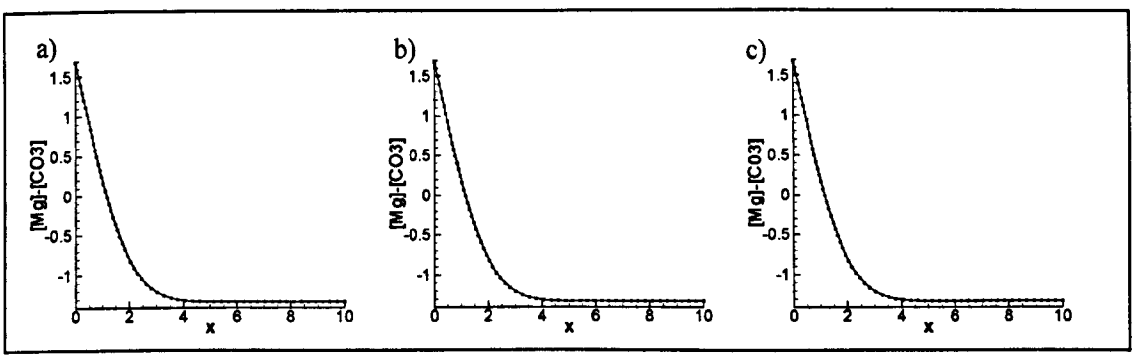

Figure 3.15 - Magnesite dissociation, distribution of the conservative component, at the time t=1. Full lines CV-HRBF solution; symbols, analytical solution. a) Da=1; b) Da=10, c) Da=100.

For the three values of Damköhler number simulated, a very good agreement is found between the numerical solution of the conservative component and its corresponding analytical solution, this is confirmed by the small L2-errorrs reported in table Table 3.7.

Damköhler number	1	10	100
L^t_{2error}	6.41×10^{-3}	6.40×10^{-3}	6.30×10^{-3}

Table 3.7 - L^t_{2error} comparison for different Damköhler numbers at t=1

In Figure 3.16 the distribution of the concentrations along the channel at the same time considered above ($t=1$) are reported. For smaller Damköhler numbers the mixing-reaction region is clearly more extended, and this is due to the larger influence of the dispersion on the chemical reaction. As the reaction gets slower, there is an increase of the mass transfer that

takes place due to the dispersion before the reaction can equilibrate. This local non-equilibrium effect is even more noticeable in the reaction plots shown in Figure 3.17.a).

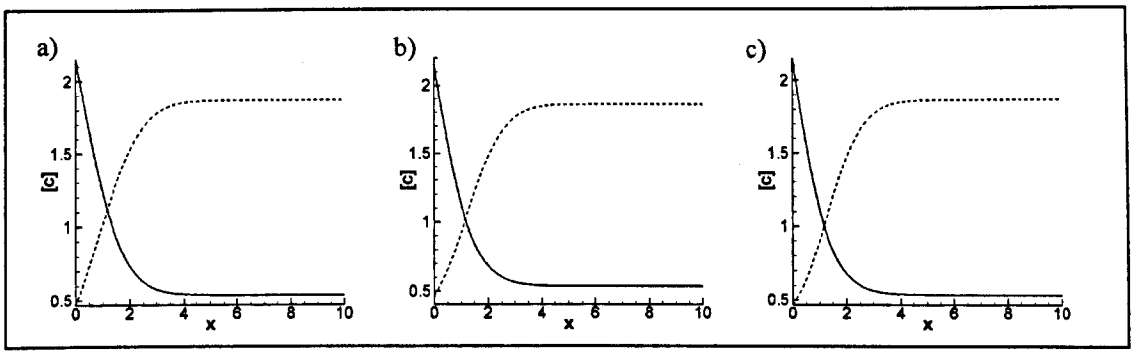

Figure 3.16 - Magnesite dissociation, distribution of the Mg^{2+} and CO_3^{2-} component, at the time t=1. a) Da=1; b) Da=10, c) Da=100.

As the Damköhler number decreases the mass transfer due to dispersion leads to a broader spatial distribution for the reaction term, indicating a wider area of chemical activity. Slower reactions correspond also to the higher values of the reaction term, circumstance that reflects the better mixing conditions.

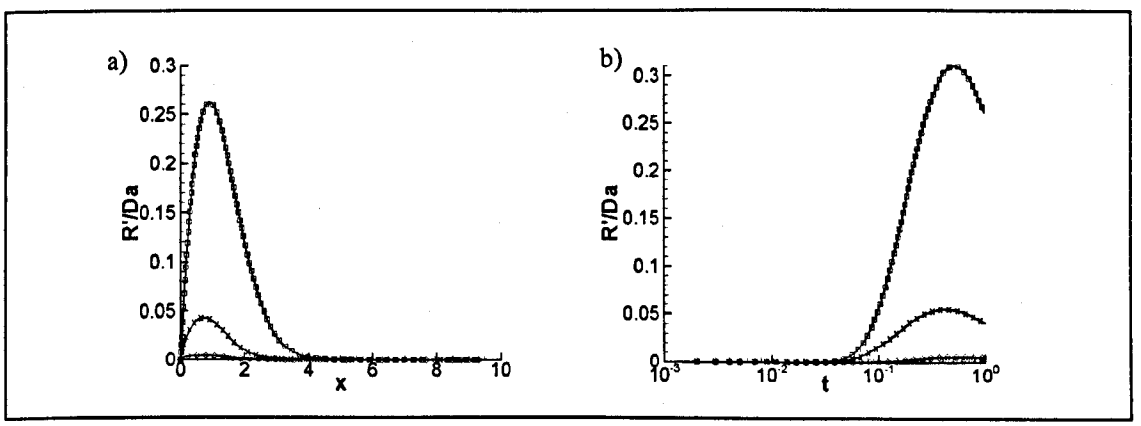

Figure 3.17 - Magnesite dissociation, reaction terms plots. a) distribution along the domain for t=1; b) evolution in time at the location x=1. Square symbols, Da=1; cross symbols Da=10; diamond symbols, Da=100.

In Figure 3.17.b) the attention is focused on a point located at $x = 1$, where the evolution of the reaction over the time is shown. Following the considerations reported above, it is important to address that the reaction affects this location located downstream the inlet of the column for longer times in the case of stronger non-equilibrium conditions.

3.5.4 Shape parameter values

The optimal shape parameter values used in the numerical example presented in this chapter are summarised in the tables below reported, following the same structure of the comparisons found in the description of the results.

Mesh	Péclet number		
	500	1000	Infinity
M40	0.02	0.02	0.02
M80	0.02	0.02	0.02
M200	0.03	0.03	0.009

Table 3.8 - Shape parameter values, c_S, used in the convergence analysis carried out for the high Péclet number cases reported in section 3.5.1.1

Time spepping scheme	Péclet number		
	500	1000	infinity
Implicit	0.03	0.03	0.009
CN	0.03	0.02	0.009

Table 3.9 - Shape parameter values, c_S, used in the comparison between the implicit and the CN time stepping schemes carried out for the hight Péclet number cases reported in section 3.5.1.1

Blending Par. ϑ	0.5	0.7	0.85	1.0
Shape Parameter c_S	0.009	0.009	0.009	0.009

Table 3.10 - Shape parameter values, c_S, used in CN blending parameter analysis carried out for the infinity Péclet number case reported in section 3.5.1.1

Time step	0.1	0.01	0.001
Shape Parameter c_S	0.01	0.01	0.009

Table 3.11 - Shape parameter values, c_S, used in time step analysis carried for the infinity Péclet number case reported in section 3.5.1.1

	PDE yes	PDE no
Pe=1000	0.02	0.075
Pe=infinity	0.009	0.02

Table 3.12 - Shape parameter values, c_S, used in PDE points analysis carried out for the high Péclet number cases reported in section 3.5.1.1

Time stepping scheme	Implicit	CN
Shape Parameter c_S	0.02	0.03

Table 3.13 - Shape parameter values, c_S, used in time stepping scheme analysis carried out for the low Péclet number case reported in section 3.5.1.3

Time stepping scheme	Implicit	CN
Shape Parameter c_S	0.02	0.04

Table 3.14 - Shape parameter values, c_S, used in time stepping scheme analysis carried out for the one dimensional reactive transport case reported in section 3.5.2.1

	Δt_1	Δt_2
Implicit	1.0	1.0
CN	1.5	1.5

Table 3.15 - Shape parameter values, c^*_S, used in time stepping scheme analysis carried out for the three dimensional reactive transport case – structured mesh - reported in section 3.5.2.2

	Δt_1	Δt_2
Implicit	0.4	0.4
CN	0.5	0.5

Table 3.16 - Shape parameter values, c^*_S, used in time stepping scheme analysis carried out for the three dimensional reactive transport case – unstructured mesh - reported in section 3.5.2.2

Finally, a constant shape parameter, c=0.01, is used in the magnesite dissociation one-dimensional example, section 3.5.3.

It is worth noting that the variable shape parameter method defined in chapter 2 in formula (2.22) is used here for the first time in the three dimensional reaction problem reported in section 3.5.2.2, see also Table 3.15 and Table 3.16.

In addition it is observed that the optimal shape parameter value does not change considerably when using a higher order time step integration as CN, and that the value stays more or less unchanged varying the time step within a reasonable range.

3.6 Conclusion

A transient formulation of the CV-HRBF scheme has been implemented and tested on a series of reactive transport problems. This validation shows that the implicit upwinding that characterises the method leads to significant improvements in the stabilisation of the numerical solution, in particular in those cases where advection is dominant. In addition to the fully implicit time stepping scheme, the weighted Crank-Nicholson scheme has also been tested, showing remarkable improvements in some of the problems considered.

The main CV-HRBF idea of having flux reconstruction functions that satisfy locally the governing equation can be applied also in case of non-linear problems. The fully kinetic formulation presented in this chapter for the solution of multispecies reactive transport problems is an example of how the non-linearity can be handled at local level. Although in this work only quasi-linear problems have been considered, the technique can be applied in principle to more complex applications characterised by high non-linearity such as the Navier-Stokes system of equations, i.e. viscous flow problems. The task of obtaining a local approximation that satisfies

the Navier-Stokes equations within the interpolation is a topic of ongoing research by several research groups. In particular, it is not clear how the non-linearity is to be considered at the local level. From previous experience, Florez et al. (2000), it is expected that a robust non-linear solver needs to be implemented at the global level, but most likely a simple Picard iteration can be used at the local level.

4 IMPROVING THE CONVERGENCE OF THE CV-HRBF FOR UNSTRUCTURED MESHES

4.1 Introduction

Although the CV-HRBF method is independent from cell shape and mesh type, one of the last numerical examples presented in chapter 3 shows that the use of unstructured meshes leads to a loss of accuracy that can be up to one order of magnitude, see section 3.5.2.2. This is expected. In fact the irregularity that characterises an unstructured element mesh, not only makes the integration schemes less accurate, but also introduces a certain degree of randomness in the distribution of points that act as base for the interpolants used in the flux reconstruction. Due to the meshless character of the local HRBF interpolation, the causes of deterioration in precision for the CV-HRBF method must be researched in the control volume formulation rather than in the flux reconstruction.

In the CV-HRBF scheme presented in chapter 2 and 3, the volume and flux integrations make use of the mean value theorem, which limits the accuracy of the method to the first order in space. This constraint cannot be removed using high order interpolants in the flux reconstruction, Holger (2005), and a more accurate integration scheme is required to exploit the high order convergence of the RBFs.

In this chapter, two alternative solutions are proposed to improve the convergence of the CV-HRBF scheme on unstructured meshes, both aiming to amend the cell face and volume integration schemes, Orsini et al. (2009). The first consists of increasing the order of the numerical integration schemes for the cell faces and volumes directly on the cell centred (CC) control volume. The second approach investigates the possibility of applying the CV-HRBF method to the vertex centred (VC) control volume first introduced in the CVFEM of Baliga and Patankar (1980) and then used in a numerous CV schemes included the CV-RBF scheme of Moroney and Turner (2006); (2007). It will be shown later during this chapter that the VC scheme, based on an intrinsic mesh refinement, also enhances the accuracy of integration. In addition, this technique guarantees a scheme which is numerically conservative; in fact the flux reconstruction at each face shared by two control volumes uses the same interpolation function. This feature makes this method very attractive, however more memory is generally required to

store the control volume mesh on the top of the element mesh, along with a larger number of reconstruction vectors.

4.2 CV-HRBF – Cell centred (CC) control volume scheme: increasing the order of the numerical integration

In the particular case of unstructured meshes made of tetrahedral elements, high order integration formulae which do not require any mapping into the isoparametric reference system are available. In this chapter only this type of mesh will be considered, though the extension to more general discretisations is feasible by decomposing more complex elements into tetrahedrons, which is always possible. In addition, there is no reason why the isoparametric transformation could not be used in conjunction with the CV-HRBF as done in the CV-RBF method proposed by Moroney and Turner (2007).

Taking the same advection diffusion reaction problems considered in section 3.2, the numerical integration of the flux for a tetrahedral control volume can be written as the sum of the flux integrals over its four triangular faces

$$\int_S \left(D_{ij} \frac{\partial \phi}{\partial x_j} - U_i \phi \right) n_i dS = \sum_{l=1}^{Nsurf} \sum_{m=1}^{Nsint} \left(D_{ij} \frac{\partial \phi}{\partial x_j} - U_i \phi \right)\Big|_{x=x^m} w^m n_{li} S_l \qquad (4.1)$$

In equation (4.1) a general formula for the flux integration over the single face is used, where $Nsint$ is the number of integration points and w^m is the weight associated with the integration point m. The position of the Gauss integration points can be defined universally in natural coordinates (*Lma,Lmb,Lmc*) on a two-dimensional Cartesian reference frame for which one of the axes is one of the triangle edges, see Figure 4.1.

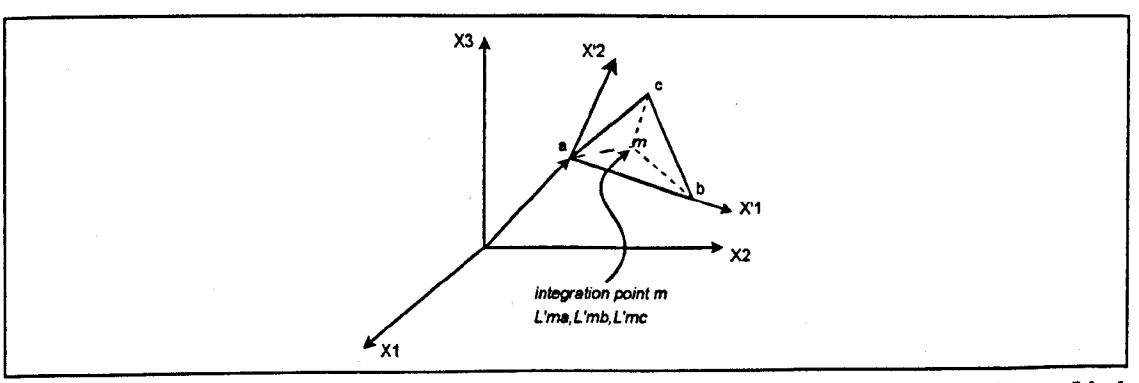

Figure 4.1 - Triangular face flux integration. X'1,X'2: local reference frame axes. *L'ma, L'mb, L'mc*: natural coordinates of the gauss integration point *m*. a, b, c: triangle vertices.

When the face vertex positions are known in the local reference frame, the coordinate (x'_1, x'_2) of each integration point is computed by the use of equation (4.2), Huebner (1975):

$$\begin{aligned} x'^{m}_{1} &= L'^{m}_{a}\, x'^{a}_{1} + L'^{m}_{b}\, x'^{b}_{1} + L'^{m}_{c}\, x'^{c}_{1} \\ x'^{m}_{2} &= L'^{m}_{a}\, x'^{a}_{2} + L'^{m}_{b}\, x'^{b}_{2} + L'^{m}_{c}\, x'^{c}_{2} \end{aligned} \tag{4.2}$$

It is worth noting that the natural coordinates L'^{m} are ratios of areas: for example L'^{m}_{a} can be written as $L'^{m}_{a} = A_a / A_{abc}$, with A_a being the area of the sub-triangle $\overline{mbc}$, and A_{abc} is the area of the entire triangular face. Although in this procedure a change of reference system is required, the flux reconstruction and integration still takes place in the global reference system. In fact the local integration point coordinates are transformed back with a simple change of reference formula $\left(x'^{m}_{1}, x'^{m}_{2}\right) \rightarrow \left(x^{m}_{1}, x^{m}_{2}, x^{m}_{3}\right)$. The natural coordinate and the weights of the three Gauss points formula used in the flux integration over the triangular face are reported in Table 4.1.

Integration point	L'^{m}_{a}	L'^{m}_{b}	L'^{m}_{c}	weight
1	1/2	1/2	0	1/3
2	0	1/2	1/2	1/3
3	1/2	0	1/2	1/3

Table 4.1 - Gauss point natural coordinates and corresponding weights used in the flux integration for triangular faces

An analogue method is implemented for the numerical integration over the tetrahedral control volume. The volume average value of the function which appears in equation (3.8) is replaced with a numerical integration formula:

$$\int_{V_P} \phi dV = \sum_{m=1}^{Nvint} \phi\big|_{x=x^m}\, w^m V_P \tag{4.3}$$

The Gauss point locations are given in natural coordinates, but in this case their global coordinates can be expressed directly in terms of the tetrahedron vertex positions without any change of reference system using equations (4.4), Figure 4.2:

$$\begin{aligned} x^{m}_{1} &= L^{m}_{a} x^{a}_{1} + L^{m}_{b} x^{b}_{1} + L^{m}_{c} x^{c}_{1} + L^{m}_{d} x^{d}_{1} \\ x^{m}_{2} &= L^{m}_{a} x^{a}_{2} + L^{m}_{b} x^{b}_{2} + L^{m}_{c} x^{c}_{2} + L^{m}_{d} x^{d}_{2} \\ x^{m}_{3} &= L^{m}_{a} x^{a}_{3} + L^{m}_{b} x^{b}_{3} + L^{m}_{c} x^{c}_{3} + L^{m}_{d} x^{d}_{3} \end{aligned} \tag{4.4}$$

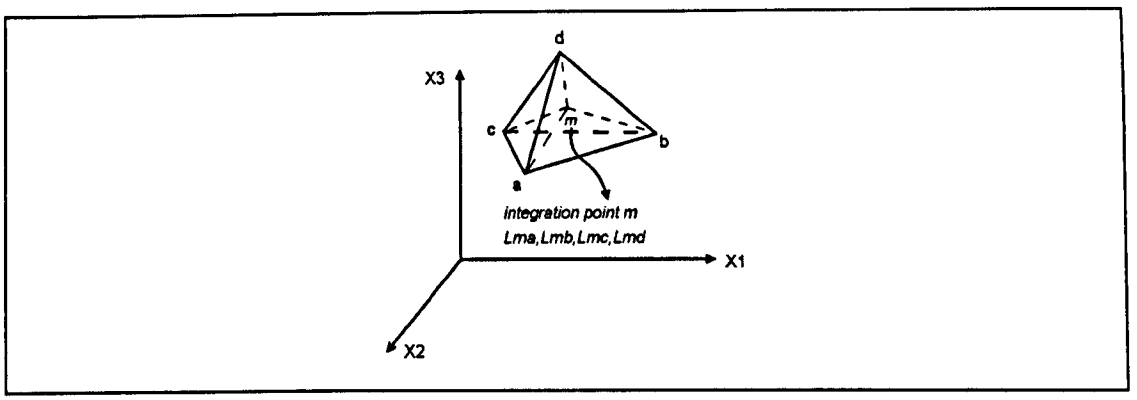

Figure 4.2 - Tetrahedral control volume integration. *Lma, Lmb, Lmc, Lmd*: natural coordinates of the gauss integration point *m*. a, b, c, d: Tetrahedron vertexes.

As in the case of the triangular face the natural coordinates have a geometric interpretation. They can be viewed as ratios between volumes: for example L_b^m can be written as $L_b^m = V_b / V_{abcd}$, where V_b is the sub-volume formed by the integration point m with the vertices a, c, d, and $V_{abcd} = V_P$ is the volume of the tetrahedron. The natural coordinate and the weights of the four Gauss points formula used in the volume integration are reported in Table 4.2.

Integration point	L_a^m	L_b^m	L_c^m	L_d^m	weight
1	0.58541020	0.13819660	0.13819660	0.13819660	1/4
2	0.13819660	0.58541020	0.13819660	0.13819660	1/4
3	0.13819660	0.13819660	0.58541020	0.13819660	1/4
4	0.13819660	0.13819660	0.13819660	0.58541020	1/4

Table 4.2 - Gauss point natural coordinate and corresponding weights used in the volume integration for the tetrahedral cell

Replacing the surface and volume first order integrations appearing in the integral equation (3.8) with the second order integration formulae (4.1) and (4.3) the following equation is obtained

$$\Delta t\theta \sum_{l=1}^{Nsurf} \sum_{m=1}^{Nsint} \left(D_{ij} \frac{\partial \phi^t}{\partial x_j} - U_i^t \phi^t \right)\Big|_{x=x^m} w^m n_i^l S_l + \left(\Delta t\theta K_r - 1\right) \sum_{m=1}^{Nvint} \phi^t\big|_{x=x^m} w^m V_P =$$

$$\Delta t(\theta - 1) \sum_{l=1}^{Nsurf} \sum_{m=1}^{Nsint} \left(D_{ij} \frac{\partial \phi^{t-\Delta t}}{\partial x_j} - U_i^{t-\Delta t} \phi^{t-\Delta t} \right)\Big|_{x=x^m} w^m n_i^l S_l \qquad (4.5)$$

$$+\left(\Delta t(\theta - 1) K_r - 1\right) \sum_{m=1}^{Nvint} \phi^{t-\Delta t}\big|_{x=x^m} w^m V_P$$

The function and its gradient at the integration points can be expressed in terms of the local interpolation as done in section 2.2

$$\left(\Delta t\theta\sum_{l=1}^{Nsurf}\sum_{m=1}^{Nsint}\left(D_{ij}C_{2jn}^{m,t}-U_i^tC_{1n}^{m,t}\right)w^m n_i^l S_l+\left(\Delta t\theta K_r-1\right)\sum_{m=1}^{Nvint}C_{1n}^{m,t}w^m V_P\right)\alpha_n^t=$$
$$\Delta t\left(\theta-1\right)\left(\sum_{l=1}^{Nsurf}\sum_{m=1}^{Nsint}\left(D_{ij}C_{2jn}^{m,t-\Delta t}-U_i^{t-\Delta t}C_{1n}^{m,t-\Delta t}\right)w^m n_i^l S_l\alpha_n^{t-\Delta t}\right) \tag{4.6}$$
$$+\left(\Delta t\left(\theta-1\right)K_r-1\right)\sum_{m=1}^{Nvint}C_{1n}^{m,t-\Delta t}\alpha_n^{t-\Delta t}w^m V_P$$

where the reconstruction vectors $\left[C_1^{m,t}\right]$ and $\left[C_{2j}^{m,t}\right]$ that refer to the integration point m show dependence with respect to the time in the case of unsteady problems with a transient PDE operator, see section 2.2. It is worth noting that in case of a transient PDE also the interpolation coefficients $\left[\alpha^t\right]$ present a dependence on the time. The equation (4.6) can be rewritten in a synthetic form as follows

$$Ir_n^{E,t}\alpha_n^t=Ir_n^{E,t-\Delta t}\alpha_n^{t-\Delta t} \tag{4.7}$$

where the element integration reconstruction vectors $\left[Ir^{E,t}\right]$ and $\left[Ir^{E,t-\Delta t}\right]$ are defined below

$$\left[Ir^{E,t}\right]^T=$$
$$\left[\left(\Delta t\theta\sum_{l=1}^{Nsurf}\sum_{m=1}^{Nsint}\left(D_{ij}C_{2jn}^{m,t}-U_i^tC_{1n}^{m,t}\right)w^m n_{li}S_l+\left(\Delta t\theta K_r-1\right)\sum_{m=1}^{Nvint}C_{1n}^{m,t}w^m V_P\right)\right] \tag{4.8}$$

$$\left[Ir^{E,t-\Delta t}\right]^T=$$
$$\left[\left(\begin{array}{l}\Delta t\left(\theta-1\right)\sum_{l=1}^{Nsurf}\sum_{m=1}^{Nsint}\left(D_{ij}C_{2jn}^{m,t-\Delta t}-U_i^{t-\Delta t}C_{1n}^{m,t-\Delta t}\right)w^m n_{li}S_l+\\ \left(\Delta t\left(\theta-1\right)K_r-1\right)\sum_{m=1}^{Nvint}C_{1n}^{m,t-\Delta t}w^m V_P\end{array}\right)\right] \tag{4.9}$$

This representation will be more suitable for the computational cost analysis reported in section 4.4.

4.3 CV-HRBF – Vertex centred (VC) control volume scheme

In the VC scheme, the control volumes do not coincide anymore with the mesh elements; they are instead built around the mesh nodes. The geometrical construction of such control volumes, which will be referred to as node-control volumes, requires the generation of a number of auxiliary points. Each element centroid is joined to the face midpoints, and the formation of the sub-volumes is completed by connecting every face mid point to the edge mid points belonging to the face. Applying this procedure to a tetrahedron generates four hexahedral sub-volumes that feature no-coplanar faces and a degree of distortion strongly dependent on the original element mesh, Figure 4.3.

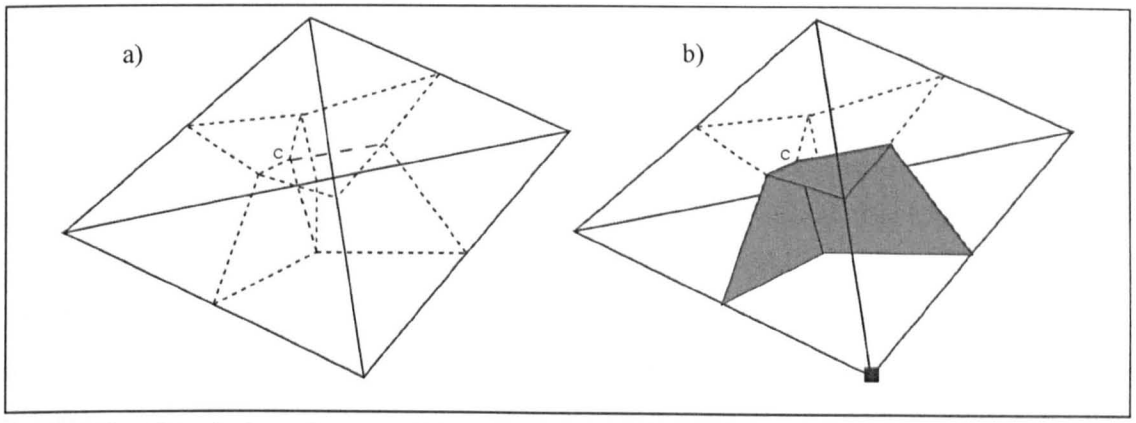

Figure 4.3 - Tetrahedron decomposition to construct node-CVs: a) 4 sub-volumes definitions; b) highlight of the front sub-volume faces considered for the flux integration (gray shaded)

The final node-control volume is a polyhedron formed by adding all the sub-volumes converging in a single mesh node, and it features a larger number of faces when compared with an element based control volume, see Figure 4.4.

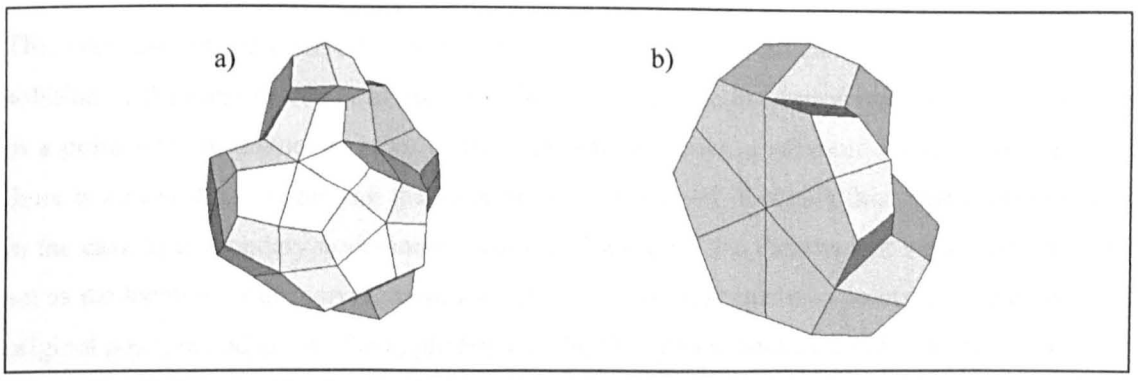

Figure 4.4 - Node-control volumes: a) Node-control volume internal to the domain; b) Node-control volume placed in a domain boundary

The CV-HRBF can be adapted to use the VC discretisation. The main change in the local problem formulation between the CC and the VC schemes is the location of the test points in

which the value of the function is unknown. In the CC scheme these tests points are placed in the cell centred of the element and of its neighbours, whereas in the VC scheme the unknown data points coincide with the element vertices, Figure 4.5-a).

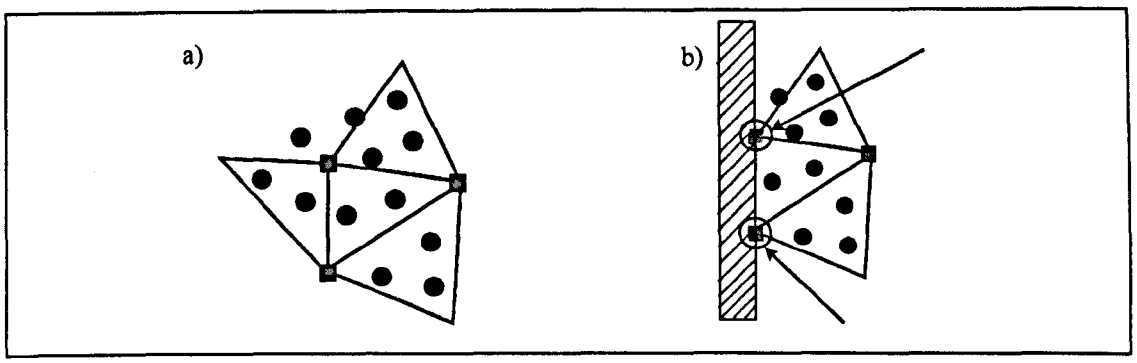

Figure 4.5 - VC scheme, stencil of points used in the local interpolation: a) internal stencil; b) stencil in the proximity of a domain boundary. Square symbols, Dirichlet Operator; Round symbols, PDE operator

This circumstance brings an extra complication in the case of node-control volumes located in the domain boundary where the Dirichlet condition must be imposed. The CV-HRBF satisfies the boundary conditions by the direct application of the boundary operator to the local interpolation at those points of the stencil located in the domain boundaries. Some of these points coincide with the element vertices, where the value of the function is considered to be unknown in the VC discretisation. It is obvious that if a prescribed value is given for a node placed in the boundary, this cannot be an unknown of the problem, and mathematically this situation causes a singularity in the local system matrix which would end up having two identical lines. In fact the Dirichlet operator should be applied twice in the same location: once considering the element vertex as unknown of the problem, and again in order to impose the known value given in the domain boundary, Figure 4.5-b).

This problem can be overcome by exploiting the meshless character of the CV-HRBF in the solution of the local problem. In the VC scheme at every node-control volume must correspond to a point with an unknown value of the function for which a solution needs to be found, but there is no constraint regarding the location of such a point. Keeping this observation in mind, in the case of a boundary node-control volume, Figure 4.4-b), the element vertex which should act as the location of the corresponding unknown can be split into two points: one remains in the original position and allows the application of the Dirichlet boundary condition, the other moves internally to the domain and it becomes the new location of the unknown. The boundary node-control volume centroid is the natural choice for the new position of such an unknown, in Figure 4.6 the arrows show this new location and its original position.

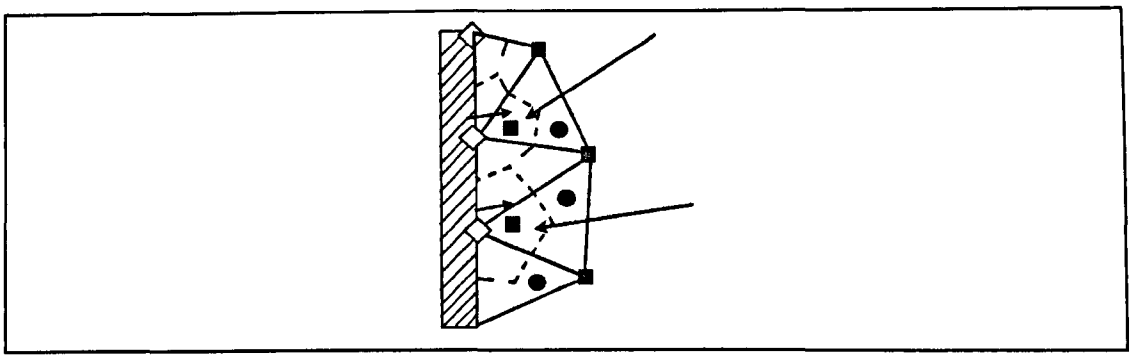

Figure 4.6 - VC scheme, shift of the unknown locations for boundary control volumes. Square symbols, Dirichlet Operator for the unknowns; Diamond symbols, boundary operator; Round symbols, PDE operator.

Merging the boundary control volumes to their internal neighbours is another elegant solution to the same problem. In this way the boundary control volumes no longer require their corresponding unknown values of the function, and the global matrix size reduces. This approach has also been taken into account. However, the difficulties encountered in the definition of the new control volume containing the boundary ones, e.g. to which of its neighbours should a boundary control volume be added to, along with the poor solution points coupling due to the loss of the unknowns close to the domain boundary, made the previous method preferable due to its robustness.

In the VC scheme it is convenient to write the integral equation of the problem as the sum of the integrals over the sub-volumes which form the node-control volume. Starting from equation (3.7) where the time discretisation has already been included, the following equation can be written

$$\sum_{i=1}^{ns} \int_{V_{Si}} L_t(\phi) dV = \sum_{i=1}^{ns} \int_{V_{Si}} L_{t-\Delta t}(\phi) dV \tag{4.10}$$

where ns is the number of sub-volumes belonging to the node-control volume, and V_{Si} is the volume of the sub-volume i. Each of these integrals can be treated numerically as explained in section 2.2 for the CC scheme, using the mean value theorem for the flux and volume integrations, leading to the to the following final sub-volume discretisation formula:

$$\begin{aligned} &\Delta t\theta \sum_{l=1}^{Nsurf_{Si}} \left(D_{ij} C_{2jn}^{l,t} - U_i^l C_{1n}^{l,t} \right) n_i^l S_l \alpha_n + \left(\Delta t \theta K_r - 1 \right) V_{Si} \bar{\phi}_{Si}^t = \\ &\Delta t(1-\theta) \sum_{l=1}^{Nsurf_{Si}} \left(D_{ij} C_{2jn}^{l,t-\Delta t} - U_i^{t-\Delta t} C_{1n}^{l,t-\Delta t} \right) n_i^l S_l + \left(\Delta t(1-\theta) K_r - 1 \right) V_{Si} \bar{\phi}_{Si}^{t-\Delta t} \end{aligned} \tag{4.11}$$

where $Nsurf_{Si}$ are the sub-volume faces which delimit the boundary of the node-control volume, Figure 4.3-b), and $\overline{\phi}^{t}_{Si}$ is the sub-volume mean value which is going to be approximated by the value of the function at the sub-volume centroid. This value is not an unknown in the global matrix as in the case of the CC scheme, and an interpolation is required in order to express $\overline{\phi}^{t}_{Si}$ in terms of the nodal values. Using the RBF interpolation once again to reconstruct the value of the function in the sub-volume centroid, equation (4.11) becomes

$$\left(\Delta t\theta \sum_{l=1}^{Nsurf_{Si}} \left(D_{ij} C^{l,t}_{2jn} - U^{t}_{i} C^{l,t}_{1n}\right) n^{l}_{i} S_{l} + \left(\Delta t\theta K_{r} - 1\right) V_{Si} C^{Si,t}_{1n}\right) \alpha^{t}_{n} =$$
$$\left(\Delta t(1-\theta) \sum_{l=1}^{Nsurf_{Si}} \left(D_{ij} C^{l,t-\Delta t}_{2jn} - U^{t-\Delta t}_{i} C^{l,t-\Delta t}_{1n}\right) n^{l}_{i} S_{l} + \left(\Delta t(1-\theta) K_{r} - 1\right) V_{Si} C^{Si,t-\Delta t}_{1n}\right) \alpha^{t-\Delta t}_{n} \tag{4.12}$$

A synthetic form of equation (4.12) can be written as follows

$$Ir^{Si,t}_{n} \alpha^{t}_{n} = Ir^{Si,t-\Delta t}_{n} \alpha^{t-\Delta t}_{n} \tag{4.13}$$

where the sub-volume integration reconstruction vectors are defined as

$$\left[Ir^{Si,t}\right]^{T} = \left[\left(\Delta t\theta \sum_{l=1}^{Nsurf_{Si}} \left(D_{ij} C^{l,t}_{2jn} - U^{t}_{i} C^{l,t}_{1n}\right) n^{l}_{i} S_{l} + \left(\Delta t\theta K_{r} - 1\right) V_{Si} C^{Si,t}_{1n}\right)\right] \tag{4.13}$$

$$\left[Ir^{Si,t-\Delta t}\right]^{T} =$$
$$\left[\left(\Delta t(1-\theta) \sum_{l=1}^{Nsurf_{Si}} \left(D_{ij} C^{l,t-\Delta t}_{2jn} - U^{t-\Delta t}_{i} C^{l,t-\Delta t}_{1n}\right) n^{l}_{i} S_{l} + \left(\Delta t(1-\theta) K_{r} - 1\right) V_{Si} C^{Si,t-\Delta t}_{1n}\right)\right] \tag{4.14}$$

The local problems associated with the elements, which contribute to the node-control volume formation, are coupled together by equation (4.10). In this assembling algorithm the flux reconstruction of a face shared by two control volumes uses the same function. In fact every internal face is contained inside an element and the local interpolations are element based, i.e. one each element, Figure 4.3-b). This feature guarantees a scheme which is numerically conservative. In the CC scheme the flux conservation is obtained by the overlapping region between the two local interpolations used by the face, requiring that such interpolations satisfy the same PDE operator, see section 2.3. In principle this should guarantee the uniqueness of the

function and its gradient at the flux integration points and so the flux conservation. The numerical solutions reported later in this chapter show that this does not happen numerically; instead there is a very small discrepancy between the left and right flux which can grow with the solution error, and in some cases it can cause a loss or gain of mass.

Finally it must be said that if the same order of integration is employed in the VC and CC formulations, the VC will result in being the more accurate method. This should be obvious when observing the element decomposition required by the VC discretisation, Figure 4.3. The element is split into a number of sub-volumes equal to the number of vertices, and the PDE is integrated in each of them rather than in the entire element. This approach acts as a kind of mesh refinement, which results in an improvement of the numerical integration in the control volume equation.

4.4 CV-HRBF computational cost: comparison between CC and VC control volume schemes

For a fair comparison between two methods featuring the same order of accuracy, the CC-second order integration (see section 4.2) and the VC-first order integration (mean value theorem) will be considered. In the case of VC, only a first order integration is used because the element partition results in an increase of the order of integration. A first analysis, with the aim of highlighting the main difference between the two schemes, is carried out considering single variable problems, full implicit time stepping ($\vartheta = 1$) and local interpolations identical in size.

4.4.1 Memory requirements

Firstly the VC requires more memory to store the node-control volume mesh on the top of the element mesh. However, the main reason for this approach being more memory demanding is the larger number of reconstruction vectors needed for the integration. The computation of these vectors (Eqs. (4.8), (4.9), (4.13) and (4.14)) is quite expensive, and for an efficient computation it is strongly recommended to store them in memory rather than recomputing them at every time step. In addition, such vectors must be multiplied by the inverse of the local system before being used to compute the entries of the global system. Taking for example equation (4.7), the coefficient $\left[\alpha^l\right]$ of the interpolation must be expressed in terms of the local system as in equation (2.10), obtaining

$$\left[Ir^{E,t}\right]\left[A^{t}\right]^{-1}\left[b^{t}\right]=\left[Ir^{E,t-\Delta t}\right]\left[A^{t-\Delta t}\right]^{-1}\left[b^{t-\Delta t}\right] \tag{4.15}$$

Equation (4.15) can be rearranged introducing the arrays which store the multiplication of the reconstruction vectors time the local inverse

$$\left[IrAinv^{E,t}\right]\left[b^{t}\right]=\left[IrAinv^{E,t-\Delta t}\right]\left[b^{t-\Delta t}\right] \tag{4.16}$$

The vectors $\left[IrAinv^{E,t}\right]$ and $\left[IrAinv^{E,t-\Delta t}\right]$ can now be directly used to form the global system. The vector-matrix multiplication which leads to equation (4.16) is also a very expensive operation if it must be done every time step. So unless the local system needs to be reformed (for example because the PDE is changing with respect to the time), the most efficient option is to store $\left[IrAinv^{E,t}\right]$ and $\left[IrAinv^{E,t-\Delta t}\right]$ in memory. It should be clear at this point why the VC scheme is more memory demanding than the CC scheme: two vectors must be stored each sub-volume rather than two each element. The amount of extra memory required varies with the type of element, see Table 4.3.

Element type	Number of element sub-volumes	VC – Nr. reconstruction vector per element	CC – Nr. reconstruction vector per element
Tetrahedron	4	8	2
Pyramid	5	10	2
Prism	6	12	2
Hexahedron	8	16	2

Table 4.3 - Number of reconstruction vectors need for the integration in the CC and VC schemes

The exact amount of memory can be computed by keeping in mind that the size of $\left[IrAinv^{E,t}\right]$ is equal to the number of points used in the local interpolation, usually around 15-20.

The situation can be significantly different for the memory required to store the global system, which has a number of lines equal to the number of control volumes. In the unstructured meshes the number of nodes can be up to a fifth of the number of elements, and the VC discretisation can produce a global system with less lines than would be obtained by the CC scheme. This gain is partially lost because the VC tends to form a sparse global matrix with a bandwidth two or three times larger than the CC, but in the end the number of non zero entries obtained with the VC scheme is about half. This situation is not valid anymore when structure meshes are adopted, because in this case the number of nodes is larger than the number of elements.

4.4.2 CPU cost

In the computation regarding the local problem the VC scheme is more demanding, once again due to the larger number of reconstruction vectors required for the integration. If the local systems do not need to be updated the only extra cost comes from the computation of the global right hand side. In fact the vector-vector multiplication which figures in equation (4.16) is performed for every sub-volume instead of every element as in the CC scheme. This situation worsens if the local system need to be updated every time step and both vectors and local system need to be recomputed.

The sparse matrix deriving from the VC discretisation scheme can have a considerably smaller number of non zero entries, up to half of the number obtained with the CC scheme. This speeds up the solution of the global system, only partially compensating the higher CPU demand due to the local computation.

4.5 Numerical results

A number of test problems presented in the previous chapters are simulated again here discretising the computational domain with an unstructured mesh rather than a structured one. The idea is to analyse the spatial convergence of the higher order methods whose formulations have been introduced in section 4.2 and 4.3. All the test cases are validated with their corresponding analytical solutions and with numerical solutions computed on a sufficiently fine structured mesh that will represent a reference in term of accuracy. To have a fair comparison with the previous solutions on structured meshes, the same MQ RBF function is employed, and the value of the shape parameter chosen experimentally (iteratively) in order to minimise the absolute L_2-norm error as done for the other numerical experiments (the optimal values are reported in section 4.5.5).

Some abbreviation is adopted for the sake of compactness: CC1 and CC2 will indicate the CV-HRBF cell centred schemes with first and second order integration respectively, whereas VC will be used to refer to the CV-HRBF vertex centred method described in section 4.3. Only the full implicit time stepping ($\vartheta = 1$) is considered for the transient problems.

For the CC1 and CC2 schemes, the interpolation stencil S1-PDE is used (see section 2.7.3). While in the case of the VC only the nodes of the element are considered in the interpolation, applying both PDE and Dirichlet conditions in the same location, see Figure 4.7. Unless stated

otherwise, the stencil stopped at the first level will be adopted, which in the case of tetrahedral elements will correspond to 4 Dirichlet plus 4 PDE points, for a total of 8 points.

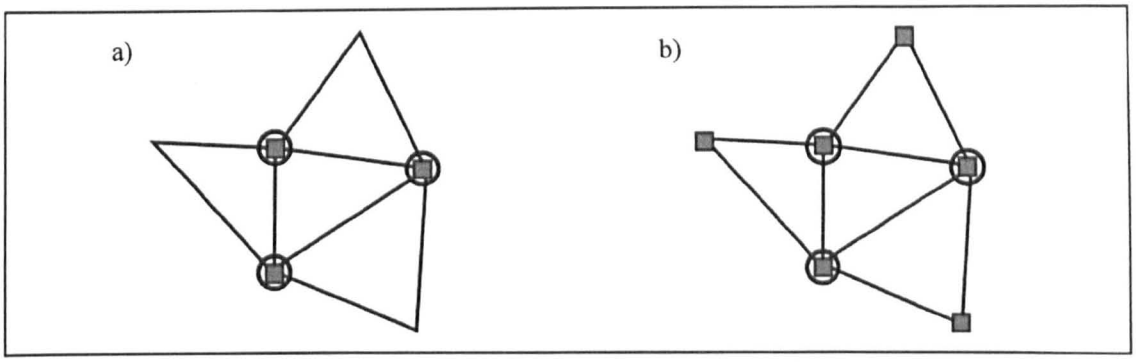

Figure 4.7 - VC scheme, stencil of points used in the local interpolation: a) stencil stop at the first neighbouring nodes level; b) stencil stop at the second neighbouring nodes level. Square symbols, Dirichlet Operator; Round symbols, PDE operator

4.5.1 One-dimensional advection-diffusion problem with a variable velocity

The numerical example presented previously in section 2.7.1.3 is run again. Due to its high advection around the two shock regions, and to the very small values to be predicted in the middle, it is a very good test case to investigate the flux computation. Fixing $a_2 = 80$, a reference solution is computed using a uniform structured mesh of 5120 hexahedrons (80X8X8), the convergence analysis is then performed on three, progressively refined unstructured meshes: 1860, 5182 and 11199 tetrahedrons, Figure 4.1.

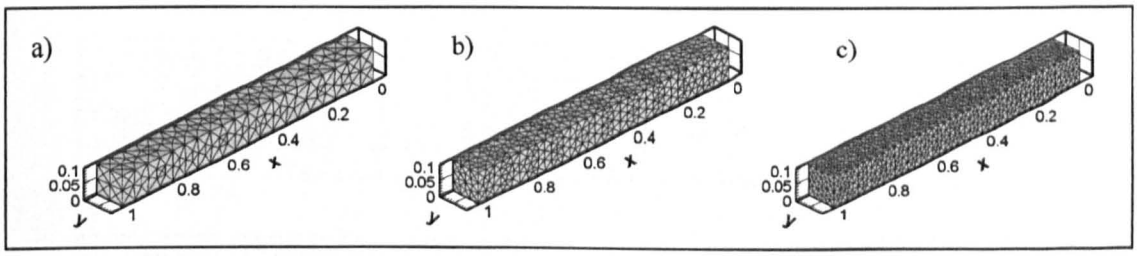

Figure 4.8 - The three Unstructured meshes used for the convergence anlysis: a) 1860, b) 5182 and c) 11199 tetrahedrons

The numerical solutions obtained by running the CC1 method in the structured mesh and in the coarsest of the three unstructured meshes (1860 tetrahedrons) are plotted together with the analytical solution to show the difference between the more and less accurate computations for this problem, Figure 4.9. A reasonable agreement is found even in the case of the worst solution where the two shocks are still computed without any presence of instability.

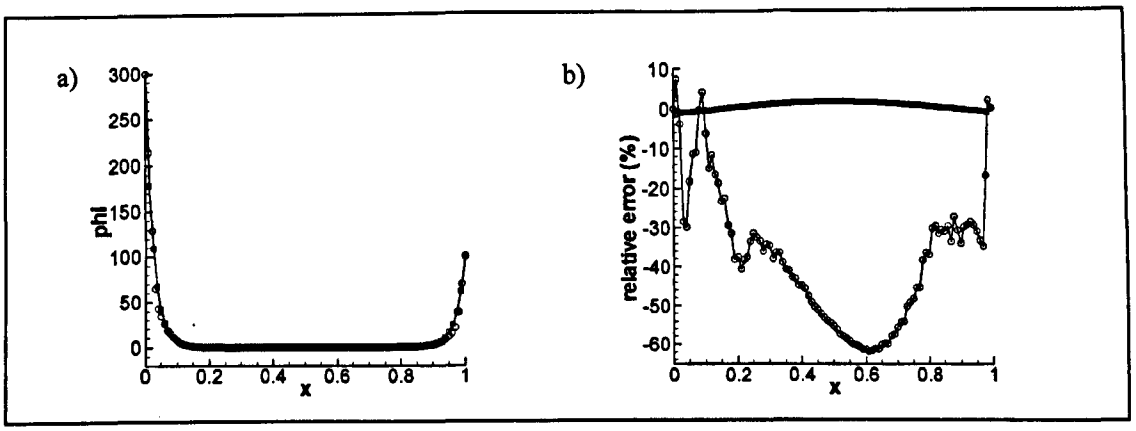

Figure 4.9 - a) Comparison between analytical and numerical solutions obtained by the CC1 scheme: square symbols, structured mesh of 5120 hexahedrons; round symbols, unstructured mesh with only 1860 tetrahedrons; full black line, analytical solution b) Realtive percentage error: square symbols, structured mesh of 5120 hexahedrons; round symbols, unstructured mesh with only 1860 tetrahedrons.

To summarise the convergence analysis of the CC1, CC2 and VC schemes, the relative errors plots are shown in Figure 4.10, and the L_2 -norm error is computed for every solution together with the maximum relative error value, Table 4.4, Table 4.5 and Table 4.6.

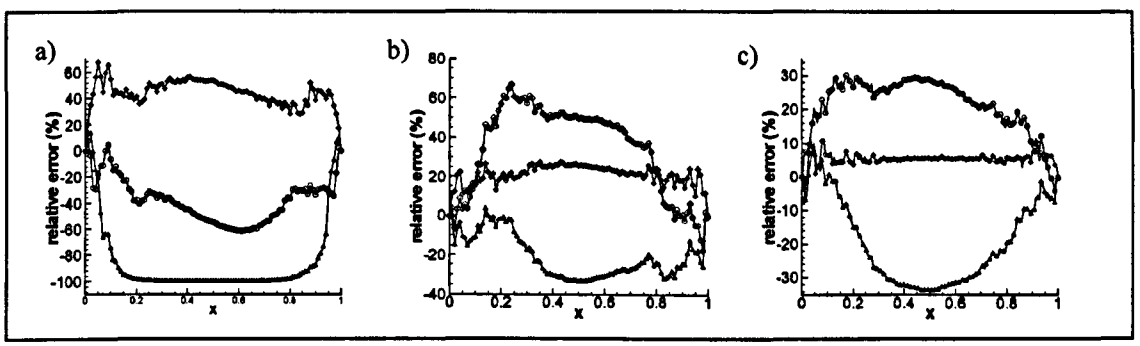

Figure 4.10 - Relative error plots: round symbols, CC1; delta symbols, CC2; diamond symbols, VC. a) 1860 tetrahedrons mesh; b) 5182 tetrahedrons mesh; c) 11199 tetrahedrons mesh

Mesh 1860 tetr.	CC1	CC2	VC
L^*_{2error}	1.76×10^{-2}	1.25×10^{-2}	1.84×10^{-2}
Max. relative error	63.9%	99.9%	66%

Table 4.4 - Error analysis: Mesh 1860 tetrahedrons

Mesh 5182 tetr.	CC1	CC2	VC
L^*_{2error}	6.96×10^{-3}	1.45×10^{-2}	9.36×10^{-3}
Max. relative error	64,8%	42%	26,3

Table 4.5 - Error analysis: Mesh 5182 tetrahedrons

Mesh 11199 tetr.	CC1	CC2	VC
L^*_{2error}	4.60×10^{-3}	8.7×10^{-3}	4.3×10^{-3}
Max. relative error	35%	34%	11%

Table 4.6 - Error analysis: Mesh 11199 tetrahedrons

It is important to point out that the apparent high relative error obtained mainly at the centre of the domain, is due to the dimensionless form used in the definition of the relative error (Eq. 2.23). This results in a division by a very small value of the potential in the centre region of the domain. The error tables show that increasing the order of integration in the cell centred scheme leads to a very small improvement, whereas a more significant reduction of the errors is observed in case of the VC scheme. The VC is the only method able to compute a solution nearly as accurate as that one obtained using the structured mesh ($L^{*}_{2error}=9.0\times10^{-4}$ and maximum relative error equal to 1,82%).

In the comparison between the structured and unstructured mesh results, it must be said that the finest unstructured, mesh made of 11199 tetrahedrons, features a characteristic length (tetrahedron edge) which is double the size of the space interval adopted to build the 5120 hexahedrons mesh. The better performance of the VC scheme is not a surprise for this problem, where the mass conservation is crucial in the two shock regions characterised by high advection. To understand more about the conservativeness of the numerical schemes investigated here, a comparison between the computed and the analytical flux is shown in Figure 4.11. With the help of the analytical solution (2.30) it can be shown that the analytical flux function is equal to zero all over the domain. This is due to the particular function chosen for the velocity field.

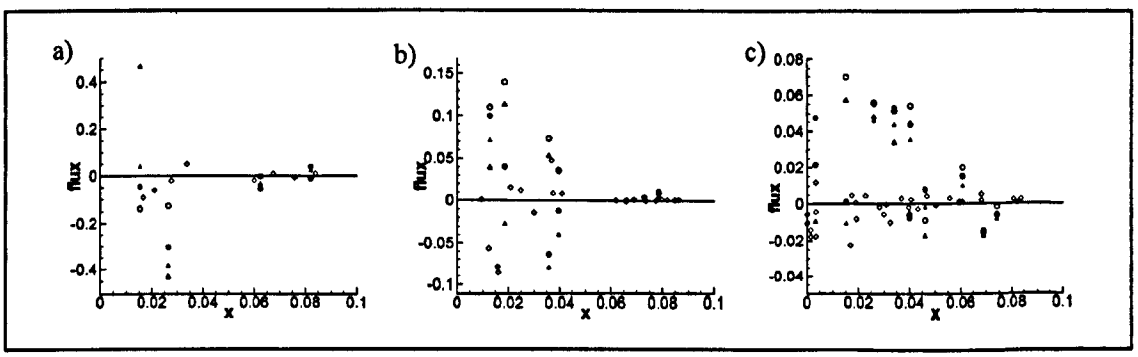

Figure 4.11 - Comparison computed/analytical flux: round symbols, CC1; delta symbols, CC2; diamond symbols, VC. Full line, analytical. Empty symbols, left flux; Full symbols, right flux. a) 1860 tetrahedrons mesh; b) 5182 tetrahedrons mesh; c) 11199 tetrahedrons mesh

For clarity, only a few sample faces are selected for the flux analysis which focuses on the higher gradient region corresponding to the left shock. In the case of the CC1 and CC2 schemes, the flux in each face is reconstructed twice using the interpolations which are associated with the two control volumes (left and right) sharing the face. Although the left and the right values of the flux computed by the CC1 and CC2 schemes should be identical in principle (see section 4.3), a difference which reduces as the function gradient becomes smaller can be observed, Figure 4.11. In addition to the gap between the left and right values, CC1 and CC2 feature a flux error which is much larger than that one which characterises VC.

4.5.2 Three-dimensional advection-diffusion problem with variable velocity

In this section the CC1, CC2 and VC schemes are validated in the three-dimensional advection-diffusion problem with a variable velocity field presented in section 2.7.2. In this example, two different meshes are tested: a structured mesh with 36×36×36 points corresponding to 42875 cells, and an unstructured one characterised by 31494 tetrahedrons and 6276 nodes. Both computational grids present a non-uniform points distribution with a refinement in the region where the diffusive shock is expected, see Figure 4.12. The number of non zero entries of the global system matrix for the unstructured mesh is equal to 153486 in the case of CC1 and CC2 and to 85798 in the case of VC. To assess the accuracy of the CC1, CC2 and VC methods, the profile extracted from a diagonal of the plane xy at z=0.98, which joins the high gradient region corner with its opposite one, is considered. The solution and the relative error plotted in this profile are shown in Figure 4.13.

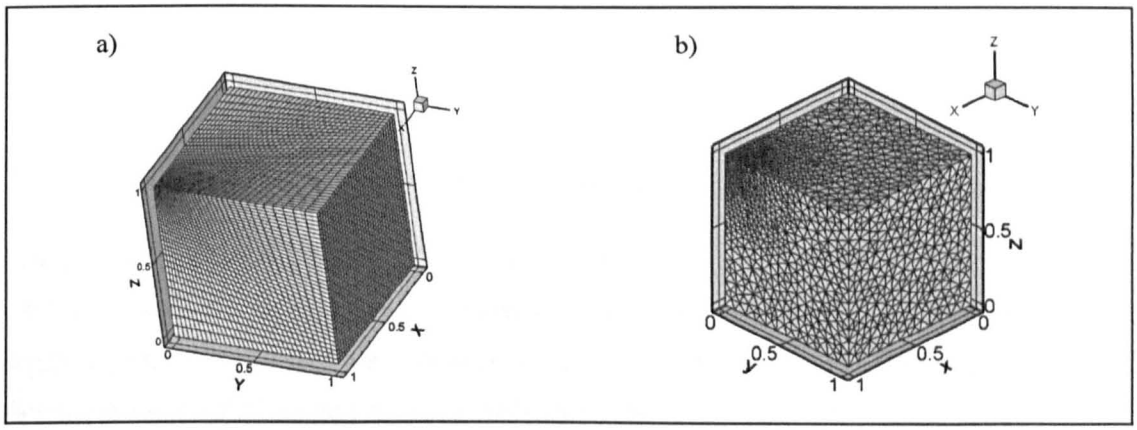

Figure 4.12 - Meshes used for the solution of the three-dimensional advection diffusion problem: a) structured mesh, 42875 hexahedrons; b) unstructured mesh 31494 tetrahedrons.

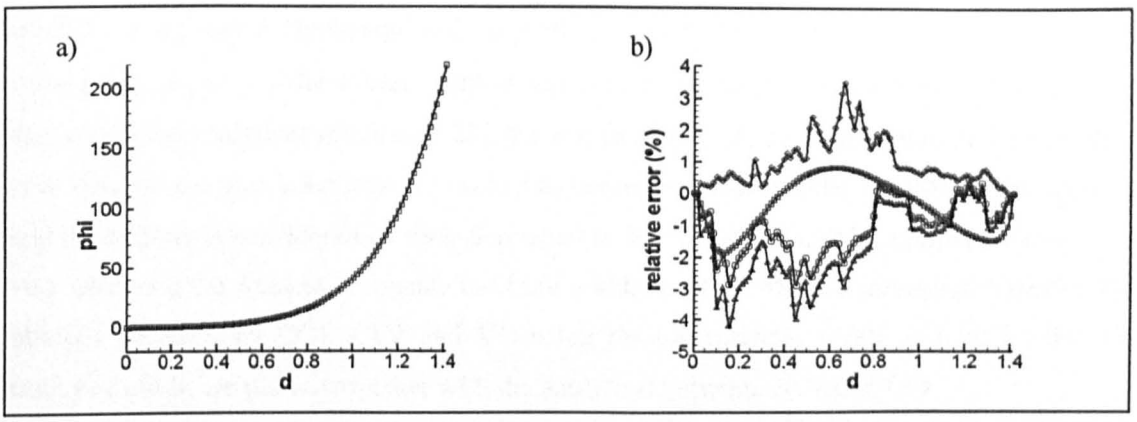

Figure 4.13 - Solution and relative error plots in the diagonal profile of the plain xy at z=0,98. Diagonal end points: (x_1=1, y_1=0), (x_2=0, y_2=1). a) Comparison between the CC1-structured mesh solution with the analytical solution. b) relative error plots: square symbols, CC1-structured mesh; round symbols, CC1-unstructured mesh; delta symbols, CC2-unstructured mesh; diamond symbols, VC-unstructured mesh

The analysis is completed with the computation of the L_2-norm and maximum relative error reported in Table 4.7.

Unstructured Mesh	CC1	CC2	VC
L^*_{2error}	1.57×10^{-3}	1.53×10^{-3}	5.59×10^{-4}
Max. relative error	49.8%	31.1%	21%

Table 4.7 - Error analysis: Mesh 11199 tetrahedrons

Finally, the CC1 solution on the structured mesh produced an L^*_2-norm error equal to 3.05×10^{-3} and a maximum relative error equal to 96%. The apparent high relative error is due to the dimensionless form used in the definition of the relative error (Eq. 2.23), which results in a division by a very small value of the potential in the region opposite to the corner where the shock occurs. While no major differences are noticed in the relative error plots, more interesting information is contained in the global error analysis reported in Table 4.7. For this particular problem, the use of a structured mesh produces less accurate solutions. This is due to the refinement required in the shock region which causes a significant element distortion when hexahedral elements are employed to discretise the domain. For the unstructured mesh the method which features the lowest errors is the VC scheme.

4.5.3 Unsteady One-dimensional advection-diffusion problem

The one-dimensional advection-diffusion problem for a single species c described in section 3.5.1 is considered here again to investigate the effect of the unstructured meshes. Two computational grids already introduced in section 4.5.1 are used for the simulation: a uniform structured mesh of 5120 hexahedrons (80X8X8), and the unstructured mesh made of 11199 tetrahedrons which features a characteristic length scale (tetrahedron edge) double in size when compared to the space interval of the structured mesh, Figure 4.8. A zero flux boundary condition is imposed at the lateral walls as well as at the end cross section of the computational domain, i.e. at $x=1$. The Péclet number tested is equal to 500. To compare the numerical results with the analytical solution (3.23), the simulations must be stopped before the travelling wave reaches the end boundary at $x=1$, i.e. before numerical reflexion affects the solution field in the domain considered. A time step equal to 0.001 is used, and the simulation stopped at t=0.5, allowing the front to propagate until the middle point of the computational domain. The solutions obtained by CC1, CC2 and VC using the unstructured mesh, and CC1 using the structured mesh, are plotted together with the analytical solution in Figure 4.14.

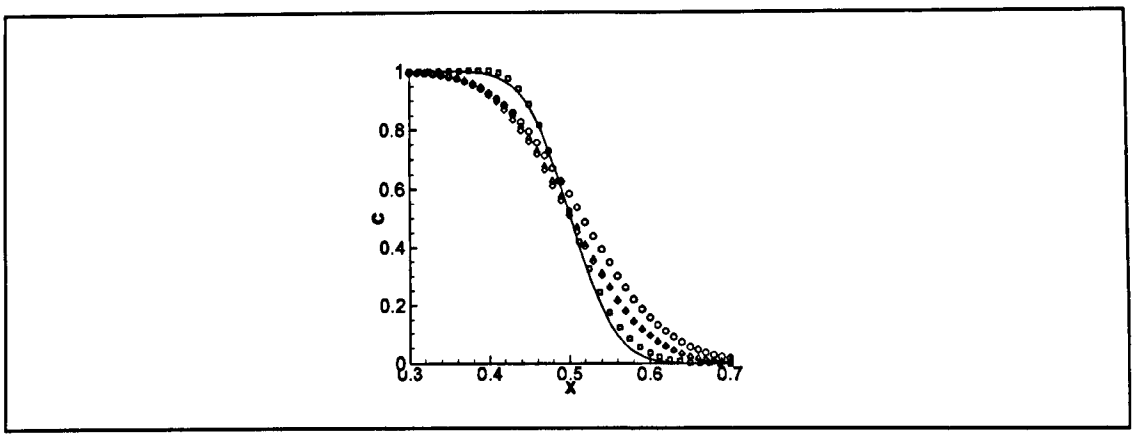

Figure 4.14 - Solution comparison, zoom around the diffusive shock region [0.3-0.7]. Square symbols, CC1-structured mesh; round symbols, CC1-unstructured mesh; delta symbols, CC2-unstructured mesh; diamond symbols, VC-unstructured mesh

The use of the unstructured mesh introduces an additional diffusive error which can be reduced by increasing the order of the integration (CC2, and VC). In the case of the cell centred scheme, there is also the problem of the mass conservation, which becomes more important for unstructured meshes. In this problem the conservativeness of the method plays a key role, and the discrepancy between the left and right flux observed for the CC1 and CC2 schemes in section 4.5.1 can produce solutions which are significantly no-mass conservative, Table 4.8.

Numerical method and mesh	Value of the flux function at x=0,5 for t=0,5 (analytical value equal to 0,5)
CC1 S1-PDE – Structured mesh	0,5237
CC1 S2-PDE – Structured mesh	0.4947
CC1 – Unstructured mesh	0,5833
CC2 – Unstructured mesh	0,5246
VC – Unstructured mesh	0,5001

Table 4.8 - Mass conservation analysis for the single species transport problem at Pe=500: Mesh 11199 tetrahedrons

This problem can be mitigated by increasing the order of the integration. In fact switching from CC1 to CC2 improves the mass conservation. In table 4.8 a comparison between the stencil S1-PDE and S2-PDE is also reported for the CC1 solutions on the structured mesh. In this case, adopting larger interpolation enhances the conservativeness of the method. However, this does not happen in the case of unstructured meshes.

4.5.4 Unsteady three-dimensional reactive-transport problem

The unsteady reactive-transport problem described in section 3.5.2.2 is simulated again using unstructured meshes to test the accuracy of the CC1, CC2 and VC schemes. A uniform grid made of 40x20x20 hexahedron-cells and an unstructured mesh which features about 18,000 tetrahedrons and 3,800 nodes, are employed to discretise the domain, Figure 4.15. The number

of non zero entries of the global system matrix for the unstructured mesh is equal to 95766 in the case of CC1 and CC2 and to 55440 in the case of VC.

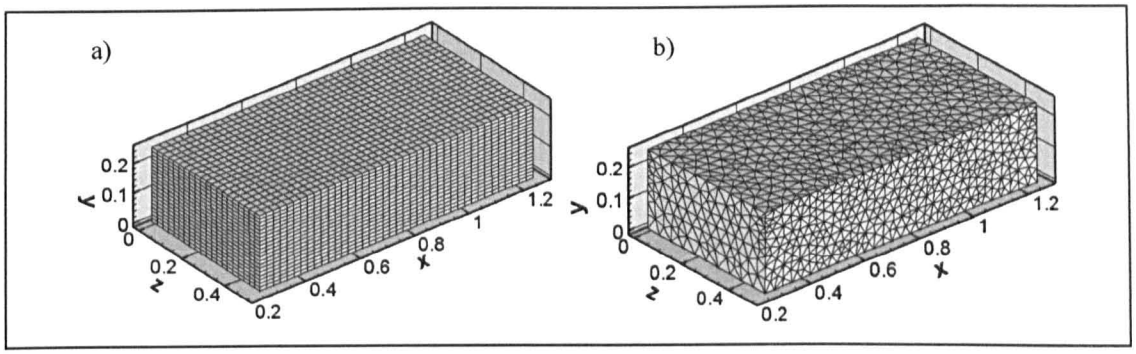

Figure 4.15 - Mesh used in the computation of the three-dimensional advection diffusion reaction problem: a) structured mesh, 16000 hexahedrons; b) unstructured mesh, 18000 tetrahedrons.

A time step of $0.001s$ is used and the numerical results at the time intervals of t=$0.02s$, t=$0.05s$, t=$0.1s$ and $0.15s$ are analysed. It is not possible to note any significant difference between the results obtained using the structured and the unstructured mesh when plotting the same profiles considered in Figure 3.12 (chapter 3); in both cases the computed solution is very close to the analytical one. So instead of reporting another series of profile plots, the L_2-norm error analysis for the solution computed in the unstructured grid is reported in Table 4.9.

Method and mesh used	t = 0.02s	t = 0.05s	t = 0.1s	t = 0.15s
CC1 – structured	1.4×10^{-2}	3.3×10^{-3}	5.9×10^{-4}	1.8×10^{-4}
CC1 - unstructured	3.5×10^{-2}	1.0×10^{-2}	3.8×10^{-3}	2.0×10^{-3}
CC2 - unstructured	4.2×10^{-2}	1.2×10^{-2}	2.1×10^{-3}	8.4×10^{-4}
VC - unstructured	2.5×10^{-2}	6.6×10^{-3}	1.8×10^{-3}	8.8×10^{-4}

Table 4.9 - Unsteady three-dimensional advection-diffusion-reaction problem, L_{2error} error analysis mesh

For this problem, the error analysis shows that the improvements achieved by increasing the order of integration in the cell centred scheme (CC2), and by using the VC dicretisation are of the same order.

4.5.5 Shape Parameter Values

The optimal values of the shape parameter are collected in tables following the same structure and order of the numerical example presented in the section.

	CC1	CC2	VC
Mesh 1860 tetr.	1.0	0.1	1.0
Mesh 5182 tetr.	1.0	1.0	0.01
Mesh 11199 tetr.	1.0	1.0	4.0

Table 4.10 - Shape parameter values, c^*_S, used in the convergence analysis of the CV-HRBF on unstructured meshes carried out in section 4.5.1

Unstructured Mesh	CC1	CC2	VC
Shape parameter c_S*	1,0	1.0	3.00

Table 4.11 - Shape parameter values, c^*_S, used in the steady three-dimensional simulation carried out to test the CV-HRBF on unstructured meshes, section 4.5.2

Numerical method and mesh	Shape parameter c_S*
CC1 S1-PDE – Structured mesh	1,0
CC1 S2-PDE – Structured mesh	2.0
CC1 – Unstructured mesh	0.1
CC2 – Unstructured mesh	0.5
VC – Unstructured mesh	0.01

Table 4.12 - Shape parameter values, c^*_S, used in the single species one-dimensional transport problem carried out to test the CV-HRBF on unstructured meshes, section 4.5.3

Method and mesh used	Shape parameter c_S*
CC1 – structured	1.0
CC1 - unstructured	0.4
CC2 - unstructured	0.6
VC - unstructured	0.1

Table 4.13 - Shape parameter values, c^*_S, used in the single species three-dimensional reactive transport problem carried out to test the CV-HRBF on unstructured meshes, section 4.5.4

4.6 Conclusion

A second order integration scheme and the vertex centred (VC) discretisation have been implemented in the CV-HRBF method to improve the convergence of the scheme for unstructured meshes. The numerical solution of one and three-dimensional advection-diffusion problems suggested that both approaches lead to good improvements, and that the VC is strongly recommended when the mass conservation is a crucial parameter of the problem being solved.

5 NUMERICAL SOLUTIONS FOR A SATURATED ZONE OF THE SEMI-CONFINED AQUIFER

5.1 Introduction

Good groundwater management is of crucial importance in many arid areas of the world, where the majority of the water for domestic and agriculture use is supplied by the aquifer system. In general, a continuous monitoring of the quantity and the quality of the water stored in the aquifer, along with accurate studies of the groundwater system, are needed to fulfil this task. A few monitoring wells are used to measure a series of parameters, but not much information is available between the measurement points. This lack of information can be tackled with the numerical modelling of the groundwater system, which also provides a very powerful tool to simulate future scenarios after an adequate calibration with the measure data.

Different numerical techniques have been proposed for simulating groundwater systems during the last three decades. The finite differences method has been used in one of the most popular groundwater flow software, MODFLOW (US-Geological-Survey); which is still widely used by the scientific community and the industry. Its success is due not only to the simplicity of its formulation, but also to the code's relative openness, in particular since the advent of MODFLOW 2000 and the (perceived) associated ease of meshing complex problems, especially among practitioners. However such simplicity and customisation ability have its downside. In particular, the code's inability to represent complex boundaries and the associated boundary conditions as a result of its formulation, Henk et al. (2001), or the difficulty to accurately compute large gradients found in the vicinity of injection or pumping wells, Warren and Martin (1997).

Another numerical technique applied successfully to solve subsurface flow problems in both confined and unconfined aquifers is finite the element method (FE) method. Some examples can be found in (Ahmed (2005), Yeh et al. (1993), Srivastava and Yeh (1992), Paniconi and Putti (1994)). In all these works, Galerking FE methods were used to solve the partial differential equation. A well known software that uses this technique is FEMWATER, Yeh (1987). Yet the classical Galerkin FE still suffers from local mass conservation issues, a key consideration for water management applications. More sophisticated variants have appeared more recently, e.g.

CVMFEM by Cai et al. (1997), which can be seen as an evolution of the so called mixed FE method, itself an enhancement on the Galekin formulation.

.

Finite volume has not been used so widely up to now. All groundwater flow applications based on the CV approach, which have been found during this literature review, are no more than ten years old. Jinglian and Bharat (1998) applied an unstructured CV scheme to model groundwater contaminant transport. Liu et al. (2002), (2003) and (2005) used an unstructured CV method to simulate salt water intrusion in costal aquifers, transport in heterogeneous aquifers systems, and saturated and unsaturated flow respectively. All models reported in these applications are two-dimensional.

In this chapter the CV-HRBF method is applied to a series of three-dimensional groundwater flow problems, modelling the saturated zone of an unconfined aquifer. Because the unsaturated zone is not included in the computational domain, the phreatic surface acts as a moving boundary, where the free surface kinematic and dynamic conditions must be imposed.

Different approaches to track the phreatic surface during its transient evolution are available in the literature. In Lagrangian methods the computational mesh moves together with the fluid, featuring the well known drawback of a rapid increase in element aspect-ratio as the grid deforms, introducing a significant numerical error. A more robust approach is the Arbitrary-Lagrangian-Eulerian (ALE) method, Hirt et al. (1972). In this case the mesh is free to move with respect to the fluid, and algorithms to adapt a time-varying grid to the phreatic surface can be adopted. The ALE method has been applied successfully to many free surface problems, e.g. Mayer et al. (1998), Souli and Zolesio (2001), Lo and Young (2003). Although, it requires a high computational cost due to the global re-meshing procedure, particularly in three-dimensional problems. Finally, there are different Eulerian methods available, which do not involve any kind of mesh motion by definition. Between these, the 'marker and cell' approach (MAC) of Welch et al. (1966) (see also Viecelli (1969)) and the 'volume of fluid' (VOF) method of Hirt and Nichols (1981) are the most popular. The main idea of these two approaches is to track fluid regions rather than a moving boundary. In the MAC method the dynamic pressure condition is applied to the entire cell containing the free surface, whereas in the VOF this condition is applied more precisely to the moving boundary. In fact VOF approximates the dynamic boundary position inside a cell by means of a volume fraction function. In these two approaches, loss of accuracy is found by not imposing correctly the free surface conditions of the moving interface. However they are very simple to implement.

To describe a free surface more accurately with the Euler method, one could use a height function. This approach can be impractical when the configuration of the free surface is complex, but is very well suited to the case of the phreatic surface, for which the motion is constrained to be vertical, and only small gradients are expected. However, when the use of the height function is combined with the CV or FE method, redefining the mesh as the phreatic surface intersects more elements is not a trivial problem. This procedure requires a re-meshing algorithm which acts only locally to the phreatic surface, so that the aspect-ratio and skewness of the involved elements remain bounded between reasonable values.

In this chapter, an efficient algorithm is presented in order to perform a local re-meshsing as the phreatic surface elevation varies inside the aquifer. The algorithm is valid for any moving boundary that follows a constrained direction. However, it is not suitable for moving boundaries that features large gradients.

5.2 Governing equation

When only the saturated zone of the aquifer is modelled, the governing equation is given by the conservation of mass (Eq. 5.1), obtained under the assumption of Darcy flow

$$S_0 \frac{\partial \phi}{\partial t} = \frac{\partial}{\partial x_i}(K_{ij} \frac{\partial \phi}{\partial x_j}) + \Gamma \qquad i,j = 1, nd \tag{5.1}$$

In (5.1) $\phi = z + {}^{p}/_{\rho g}$ is the piezometric head, with z being the elevation, p the pressure, ρ the density of the fluid, g the gravity acceleration and nd the number of dimensions; S_0 is the specific storativity (volume of water added to storage, per unit volume of porous medium, per unit rise in piezometric head), $[K]$ is the hydraulic conductivity tensor, and Γ represents source points in the aquifer. The seepage velocity and the Darcy's flux are given respectively by

$$q_i = -K_{ij} \frac{\partial \phi}{\partial x_j} \tag{5.2}$$

$$v_i = \frac{q_i}{\eta} \tag{5.3}$$

where η is the soil porosity. For small or medium scale problems, the conservation of mass expressed by (5.1) can be simplified assuming zero storativity and dropping the time dependent

term, Bear (1987). Under this assumption the problem becomes quasi-static, with the governing equation given by the steady non-homogeneous diffusion equation

$$\frac{\partial}{\partial x_i}(K_{ij}\frac{\partial \phi}{\partial x_j})+\Gamma=0 \tag{5.4}$$

and the transient component defined only by the boundary conditions.

Considering the porous medium as homogeneous but anisotropic, the tensor $[K]$ can be written as

$$[K]=\begin{bmatrix} K_1 & 0 & 0 \\ 0 & K_2 & 0 \\ 0 & 0 & K_3 \end{bmatrix} \tag{5.5}$$

with K_1, K_2 and K_3 constant all over the domain, and a reference frame coinciding with the principal directions of the anisotropic porous medium. To model the springs and the sinks placed in the aquifer the following source terms are taken:

$$\Gamma=\sum_m W^m(x^m,t)\delta(x-x^m)+\sum_n P^n(x^n,t)\delta(x-x^n) \qquad x\in\Re^{nd} \tag{5.6}$$

where W^m and P^m are the strength of the point sources and point sinks respectively and $\delta(x-x^m)$ denotes the dirac-delta function at x^m. However, when the screen of a pumping well is quite long it cannot be approximated as a point sink. A more accurate model is given by describing the pump as an array of point sinks, each point being a segment of the well or by using a line integrated sink singularity.

In the saturated model, the transition region between the saturated and unsaturated zones is not modelled, but is instead considered to be a simple surface (phreatic surface). With this assumption, the media below the phreatic surface is completely saturated and the phreatic surface acts as a moving boundary of the domain being simulated. If z is the vertical direction, the phreatic surface at a given time t can be described by a two-dimensional function, $z=h(x,y,t)$. This equation can be rewritten in implicit form as follows

$$F^S(x,y,z,t)=z-h(x,y,t)=0 \tag{5.7}$$

In the absence of natural replenishment and other superficial sources or sinks, only the dynamic and kinematic boundary conditions must be applied on the phreatic surface, i.e. imposing the pressure to be equal to the atmospheric value, and the material derivative of F^S to be equal to zero. Using the seepage velocity definition, the kinematic and the dynamic conditions take the following form

$$\begin{aligned} &\phi = h \\ &\frac{\partial h}{\partial t} - \frac{K_{ij}}{\eta}\frac{\partial \phi}{\partial x_j} n_i^S \left|\nabla F^S\right| = 0 \end{aligned} \tag{5.8}$$

where n_i^S is the *i*-component of phreatic surface normal vector.

5.3 Mathematical formulation

After dividing the computational domain into a number of non-overlapping control volumes, the differential equation (5.4) can be integrated over each of these as follows

$$\int_V \frac{\partial}{\partial x_i} K_{ij} \frac{\partial \phi}{\partial x_j} dV = -\int_V \Gamma dV \tag{5.9}$$

The left hand side of equation (5.9) is discretised using the CV-HRBF method as shown in chapter 2. The source term in the second member is implemented in a numerical code, bearing in mind the Dirac delta function properties, and the fact that it is equal to the sum of the pumping and injecting rate values of the sink/source points present in the volume.

$$\Gamma = \begin{cases} \sum_m W^m(x^m,t)\delta(x-x^m) + \sum_n P^n(x^n,t)\delta(x-x^n) & x^m, x^n \in V \\ 0 & x^m, x^n \notin V \end{cases} \tag{5.10}$$

5.4 Phreatic surface tracking

The algorithm reported below has been developed for simulation of groundwater flow problems with a view to tracking the phreatic surface. The points placed on the moving boundary are constrained to move only vertically and the phreatic surface is always expected to be continuous and smooth without large elevation gradients.

In this formulation, only prisms aligned with the vertical direction are allowed to mesh the region swept by the moving boundary. This assumption is the key point of the present algorithm (see Orsini et al. (2009)), which exploits the fact that the moving boundary points (MBPs) move in a prefixed direction. Consider a prism that has the top triangular face place on the dynamic boundary, and the quadrilateral faces parallel to the direction of the moving boundary motion, Figure 5.1. The three track points P1, P2, and P3 are used to assign the kinematic and the dynamic conditions and to compute the local displacements of the moving boundary. Since the direction of the displacements is known a priori, the edges e1, e2, and e3, Figure 5.1, can be adjusted in length to track the surface. This approach can be adopted only when the displacements are relatively small in comparison to the size of the cells. For large displacements, additional cells must be added as the dynamic boundary is moving away from the domain, whereas some cells need to be removed as the dynamic boundary is moving in, reducing the size of the domain. This procedure avoids the generation of deformed elements characterised by large aspect-ratio and skewness.

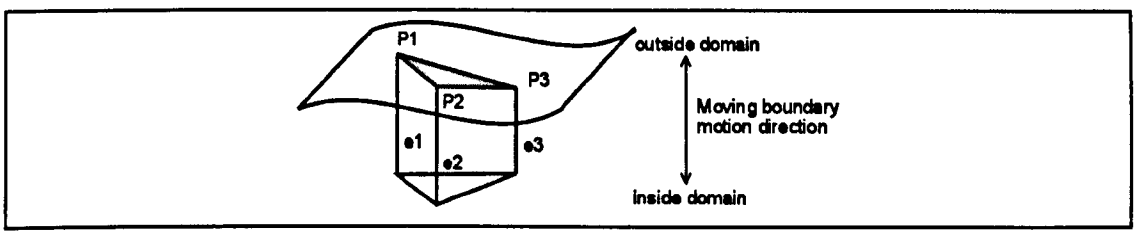

Figure 5.1 - Prism cut by the moving boundary

To develop an adding-removing cells algorithm, columns of prisms can be adopted, and the points of the dynamic boundary are free to move on the vertical lines that define the columns. Each prism in every column is investigated to determine whether or not it has to be included in the domain for a certain configuration of the moving boundary. The analysed prism is considered to be inside the computational domain if at least one of the MBPs is above its mid plane, Figure 5.2 (here the computational domain is below the moving boundary).

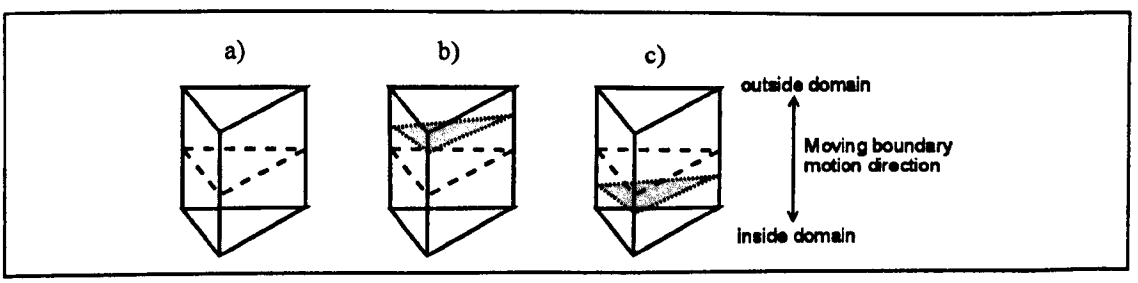

Figure 5.2 - Prism position detection: a) prism and its mid plane; b) the cell is inside the domain; c) the cell is outside the domain

If the prism is inside the domain, one must determine whether the dynamic boundary will change its original shape or not. To do so, a region (the M-region in Figure 5.3) is defined between the mid planes of the prism under investigation and the one above it. The element is reshaped in two circumstances: if at least one MBP is inside the M-region or if there is at least one point above and one below the M-region.

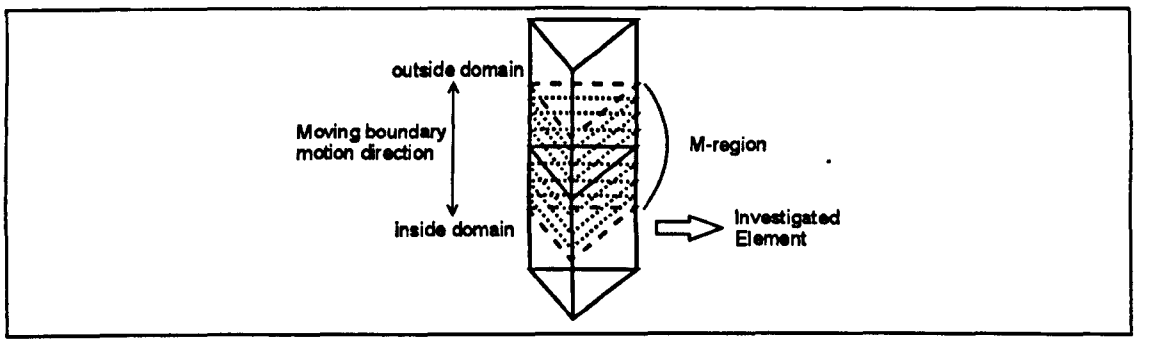

Figure 5.3 - Definition of M-region for the element under investigation

The cell change depends on the number of MBPs placed in, above and below the M-region. The following rules drive the local remeshing process.

- When a MBP falls inside the M-region the corresponding corner of the top face of the prism will be moved on the MBP itself.
- Once the cell is inside the domain, if there are MBPs placed below the M-region they will become the corners of the new cell. In fact every MBP found below the M-region will lead to the corresponding vertical edge to collapse on the MBP itself.

A few examples of possible local mesh modifications are given next to help understand how the algorithm works. With three MBPs in the M-region the cell will remain a prism but the top face will move to track the boundary, Figure 5.4. When two MBPs are placed on the M-region the position of the third has to be taken into account to determine the new type and shape of the element. If the third point is above the M-region, then the cell will still be a prism, with its top face internal to the domain, Figure 5.5. If instead the third point is below the M-region, then the new cell type will be a pyramid, with one of the faces placed on the moving boundary, Figure 5.6. When only one MBP stays in the M-region, it is possible to distinguish three more sub-cases depending on the position of the other two. If one of the two is above and the second one is below the M-region, the new element will be a pyramid without any face placed on the moving boundary, Figure 5.7.

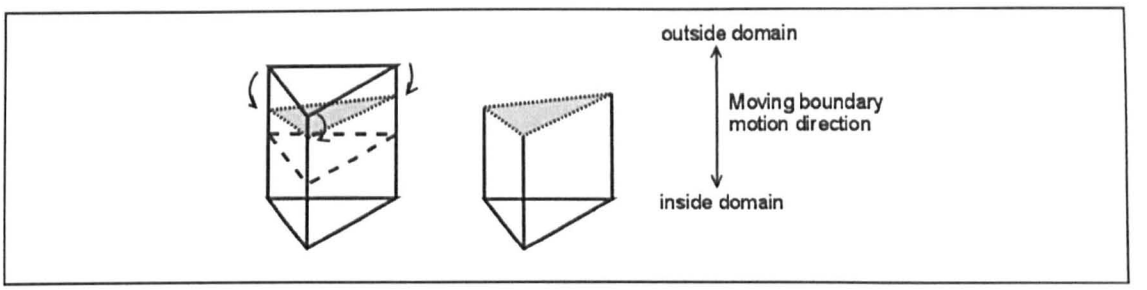

Figure 5.4 - Local remeshing: all three moving boundary points are placed on the M-region;

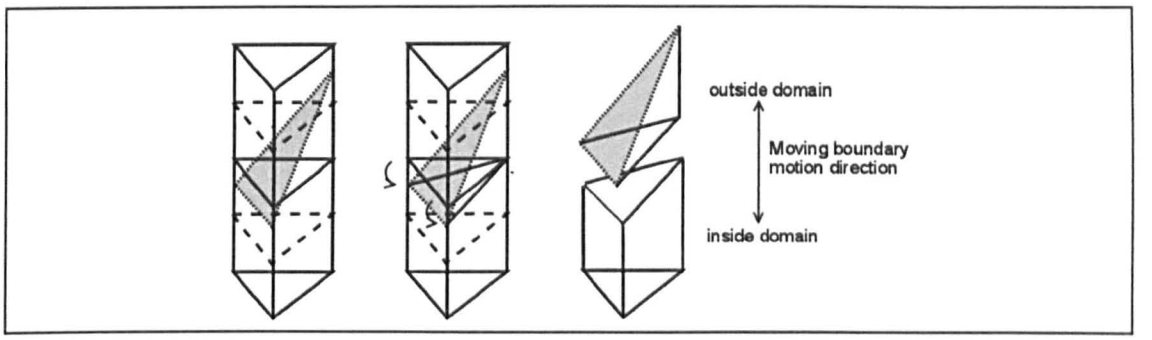

Figure 5.5 - Local remeshing when two moving boundary points fall in the M-region: the third one is above the M-region

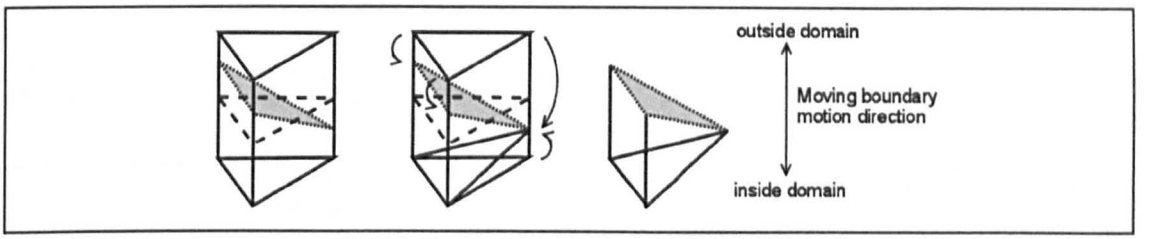

Figure 5.6 - Local remeshing when two moving boundary points fall in the M-region: third one is below the M-region

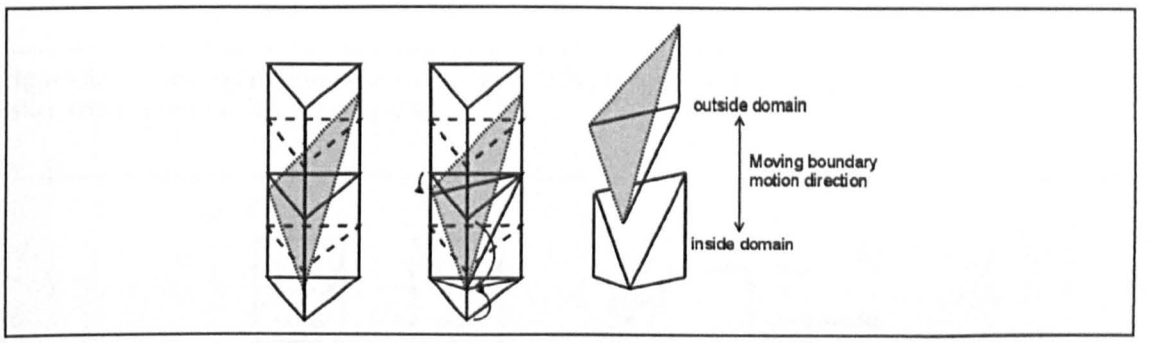

Figure 5.7 - Local remeshing when only one moving boundary points is placed in the M-region: the other two are one below and one above the M-region.

When both are above the M-region then the element will remain a prism with only one point in the moving boundary, Figure 5.8. Finally, when both are below the M-region the new element will be a tetrahedron with one of the four faces placed on the moving boundary, Figure 5.9. The last case worth considering is encountered in the event of one (or more) whole prism(s) being crossed by the moving boundary; this happens when the circumstance previously mentioned of

at least one MBP above and one below the M-region occurs. An example is shown in Figure 5.10 where two of the three MBPs are below the M-region and one is above it. In this case the element under consideration turns into a tetrahedron without any face placed on the dynamic boundary. Note that in this instance the top element is quite distorted, and becomes even more so, as the number of elements crossed by the moving boundary in the same column increases. One of the assumptions under which the present algorithm has been developed, is the absence of large elevation gradients. If this hypothesis is not satisfied, the procedure can generate elements characterised by very high values of skewness, reducing the accuracy of the flux computation and generating ill-posed local problems to be solved inside the CV-HRBF scheme. However this is unlikely for groundwater flow applications.

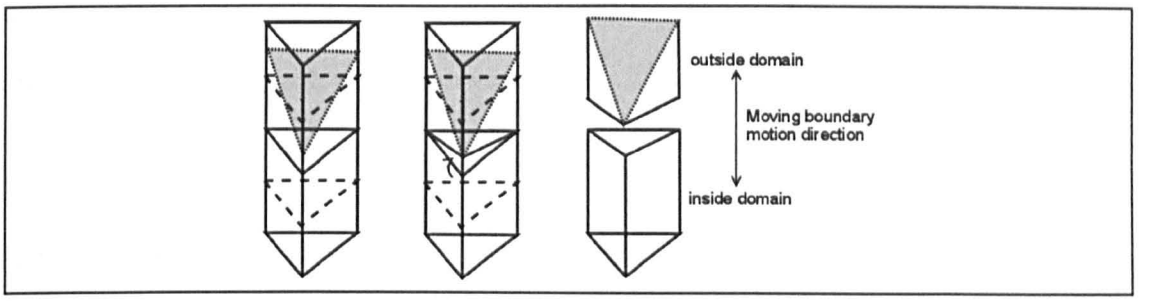

Figure 5.8 - Local remeshing when only one moving boundary points is placed in the M-region: the other two are both above the M-region.

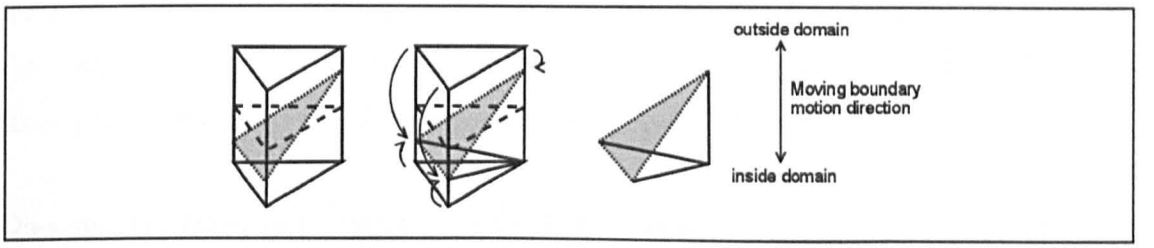

Figure 5.9 - Local remeshing when only one moving boundary points is placed in the M-region: the other two are both below the M-region.

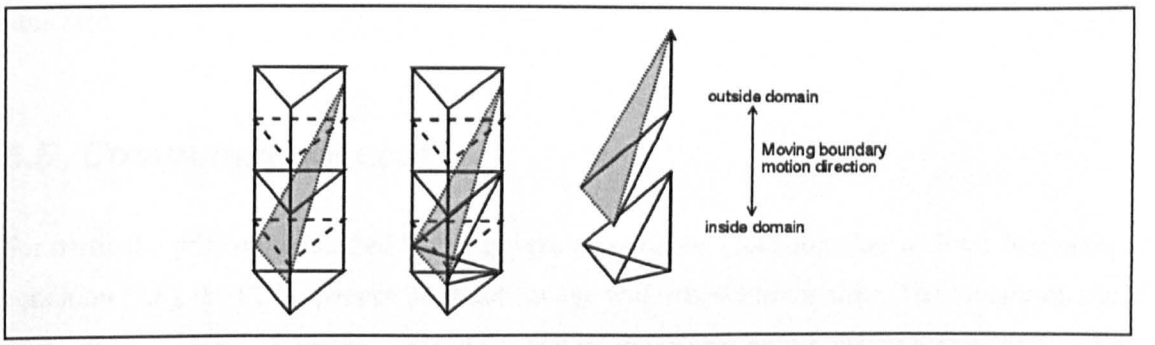

Figure 5.10 - Local remeshing when one moving boundary points is placed above the M-region and the other two are placed below it

The algorithm described above adapts the computational mesh to the phreatic surface configuration, which is updated at every time step. The quasi-static assumption introduced in

section 5.2 linearises the problem with respect to the dynamic boundary. Then, starting from the solution at the previous time step, the kinematic condition is used to move the phreatic surface on the new configuration. The displacement increment for every point of the surface can be obtained from the second of the equations (5.8) when rewriting the normal vector as a gradient of the implicit function F^S ($\frac{\partial F^S}{\partial x_i} = \left|\nabla F^S\right| n_i^S$)

$$dh_{MBP} = \left(K_{ij} \left.\frac{\partial \phi}{\partial x_j}\right|_{MBP} \frac{\partial F^S}{\partial x_i} \right)\Bigg|^{t-\Delta t} \frac{dt}{\eta} \tag{5.11}$$

It is evident from equation (5.11), that in order to obtain dh_{MBP} one must compute the piezometric head gradient, and the derivatives of F^S on the considered MBP. The gradient $\left(\frac{\partial \phi}{\partial x_n}\right)\Big|^{t-\Delta t}_{MBP}$ is reconstructed using the RBF interpolations in which the MBP has been collocated during the solution at the previous time step. When more than one interpolation formula is available, the average of the multiple reconstructed values seems to be the most stable alternative. To compute the derivative of the phreatic surface shape function F^S, a two-dimensional RBF interpolation (see section 1.1.1, Equations from (1.1) to (1.4)) is performed for every MBP. Such two-dimensional interpolation is local, i.e. only the MBP and a few of its neighbours (about 10-15) are considered to interpolate F^S locally.

Once the phreatic surface configuration has been updated, the new boundary location and the value of the piezometric head required to impose the dynamic condition are known. A new steady problem (5.4) can then be solved to find the piezometric head distribution of the next time step.

5.5 Computational cost

For particular problem described by the governing equation (5.4), together with the free-surface condition (5.8), the PDE operator does not change with respect to the time. The inverse matrices of the local systems, or the reconstruction vectors multiplied by the inverses (see section 4.4), are computed as a pre-processing step at the beginning of the computation and stored in memory. This cannot be done for local systems associated with the deforming elements that are located in proximity of the phreatic surface. For such elements not only the system needs to be

reformed, but also the interpolation stencil. However this only happens for a small percentage of the total number of elements, i.e. the elements that contain the phreatic surface, and their first or second level neighbours, depending on the type of stencil configuration adopted. All the operations related to the re-meshing that is caused by the moving boundary are local. This makes the entire algorithm very efficient.

5.6 Numerical results

First a three-dimensional test case is run in order to validate the accuracy of the CV-HRBF method in solving anisotropic diffusion equations. The method is then used to simulate a series of groundwater problems, which consider the operations of extraction and recharge in a semi-confined aquifer. A convergence analysis has been carried out for all test cases reported in this section. Thus, the results presented for each example correspond to the obtained mesh-independent solutions. A multiquadric RBF is employed in the interpolation algorithm, both in the validation test case and in the groundwater simulations. The shape parameter is computed for each interpolation stencil as a fraction of the maximum distance, see section 2.6, but different approaches are adopted in the selection of the c_S^* values. In the validation test case, where an analytical solution is available for comparison with the numerical results, the value of the shape parameter is chosen iteratively, using a 'guessing and check' method in order to minimise the absolute L_2-norm error. Instead, for the groundwater simulations the value of c_S^* is taken to be equal to 0.16, a value that leads to a good level of accuracy.

Only the first order CC control volume scheme is used throughout the simulations, though in principle there is no reason why the VC scheme introduced in chapter 4 could not be applied to the problems presented in the following section. In addition, the configuration S1-PDE described in section 2.7.3 is adopted to form the interpolation stencils, which in the case of prismatic elements gives a total number of 12 points (6 dirichlet + 6 PDE points).

5.6.1 Validation: Three-dimensional anisotropic diffusion problem

In this section the CV-HRBF is validated in a three-dimensional problem characterised by a homogeneous but anisotropic diffusion for which an analytical solution exists. The equation solved is

$$\frac{\partial}{\partial x_i}(D_{ij}\frac{\partial \phi}{\partial x_j}) = \delta(x - x^c) \qquad i,j = 1,nd \tag{5.12}$$

where nd is the number of dimensions, $\boldsymbol{x}$ is the generic position vector and $\boldsymbol{x}^c$ gives the location of a source point placed outside the computational domain. The diffusion tensor is considered to be diagonal

$$[D]=\begin{bmatrix} D_1 & 0 & 0 \\ 0 & D_2 & 0 \\ 0 & 0 & D_3 \end{bmatrix}$$

Equation (5.12) has a general analytical solution given by

$$\phi = \frac{1}{\sqrt{D_1 D_2 D_3}} \frac{1}{\tilde{r}} \tag{5.13}$$

where

$$\tilde{r} = \frac{(x_1 - x_1^c)^2}{D_1} + \frac{(x_2 - x_2^c)^2}{D_2} + \frac{(x_3 - x_3^c)^2}{D_3}$$

The domain chosen for this simulation is a cube with a unitary length edge [1×1×1]. The origin of the reference frame is placed in the geometric centre of the cube, and the source point coordinates are equal to $(0.75, 0.75, 0.75)$. Dirichlet boundary conditions are imposed in the six faces using the analytical solution (5.13), where the diagonal terms of the diffusion tensor are taken as $D_1 = D_3 = 1$ and $D_2 = 0.1$. As it can be inferred from equation (5.13), the potential ϕ decays with a rate which is inversely proportional to the distance from the source point, thus larger gradients are expected to occur in the region closest to the source point. In this case a mesh refinement around the corner (0.5, 0.5, 0.5) of the chosen domain is required in order to reproduce the solution gradients, Figure 5.11.

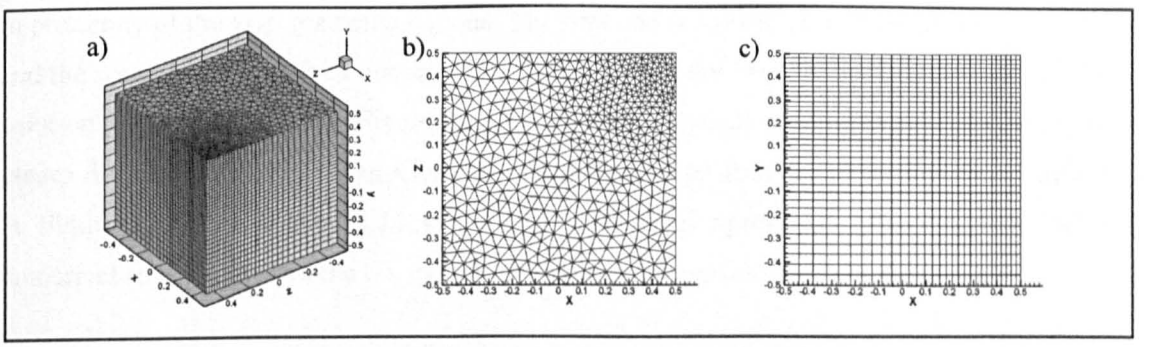

Figure 5.11 - Mesh used to solve the three-dimensional anisotropic diffusion problem: a) three-dimensional view; b) view at *y*=0.5; b) view at *z*=0.5;

The semi-unstructured mesh used for the computation is generated by extrusion from a triangular two-dimensional grid; it features about 41000 prisms and is of the same type of the meshes used later in this chapter for groundwater problems. The optimal value of c_S^* found is equal to 0.8, for which $L_{2error}^* = 3.5\times10^{-3}$.

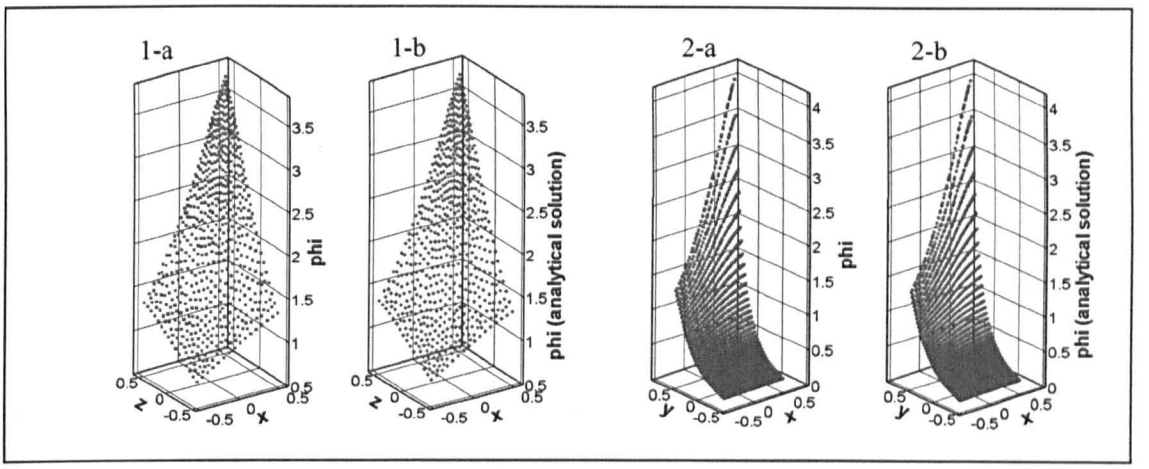

Figure 5.12 - Solution 3D plots: 1) y=0.48, 2) z=0.48. a) – analytical solution; b) CV-RBF solution.

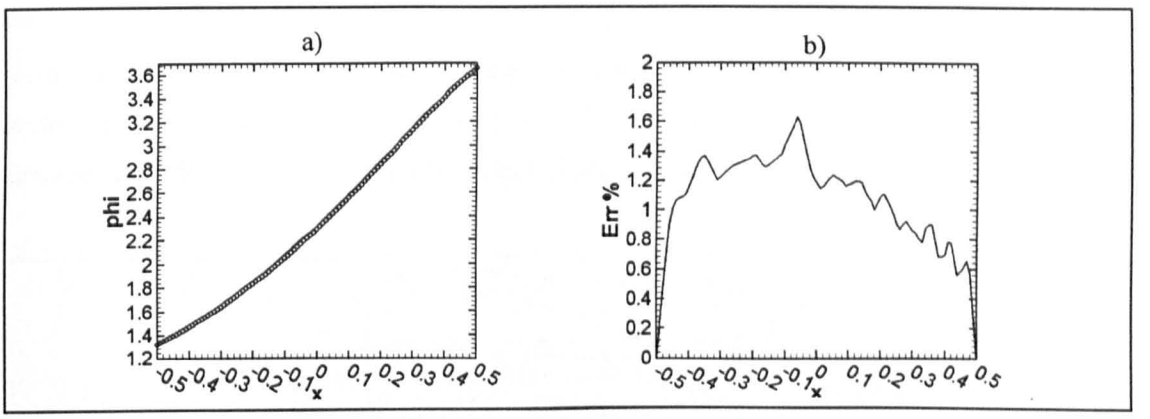

Figure 5.13 - Profile extracted at y=0.48, z=0.47, -0.5≤y≤0.5; a), comparison between the CV-HRBF and the analytical solution b), relative percentage error. The symbols represent the analytical solutions; the full lines refer to CV-RBF solution

To assess the accuracy of the method, the numerical results are presented in two slices extracted in proximity of the high gradients regions. The first one is a plane of constant y value, at y=0.48, and the second one a plane of constant z value, at z=0.48. For these two slices three-dimensional solution plots are reported in Figure 5.12, where the analytical solution is also plotted on these planes for comparison purposes. Corresponding detailed profiles are plotted in two dimensions in Figure 5.13 and Figure 5.14 for clarity. The good agreement between analytical and numerical solutions shows the CV-HRBF ability to solve anisotropic diffusion problems.

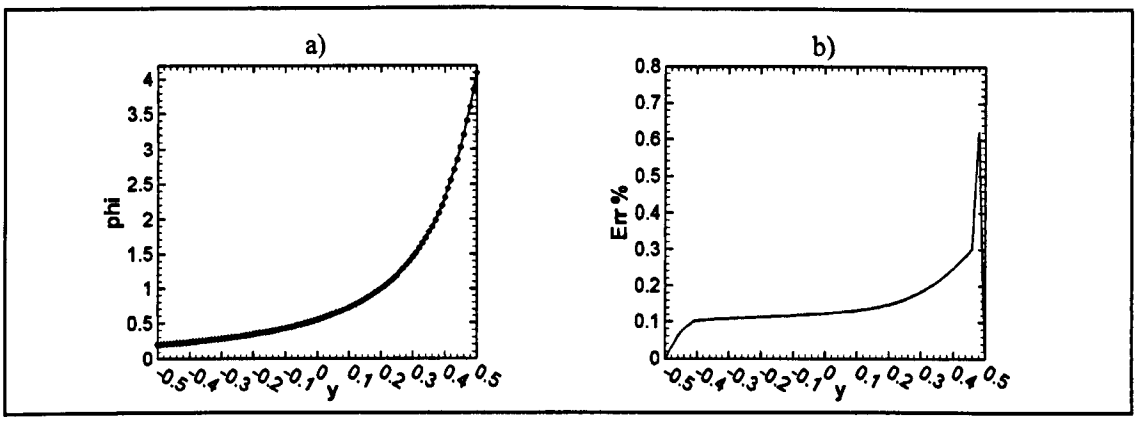

Figure 5.14 - Profile extracted at z=0.48, x=0.47, -0.5≤y≤0.5; a), comparison between the CV-HRBF and the analytical solution b), relative percentage error. The symbols represent the analytical solutions; the full lines refer to CV-HRBF solution.

5.6.2 Pumping-injecting

In this problem, two wells placed 20 meters below the phreatic surface are modelled. One is used to inject water into the aquifer and the other to pump water out. The effects of the recharging and extracting actions on the aquifer are investigated. Starting from an unperturbed field, the time necessary to reach the balance and the final configuration of the phreatic surface are the main answers expected from a numerical simulation. The considered domain is a strip of semi-confined aquifer 550 meters long and 150 meters wide, where a constant height distribution of 50 metres represents the initial configuration of the phreatic surface, Figure 5.15.

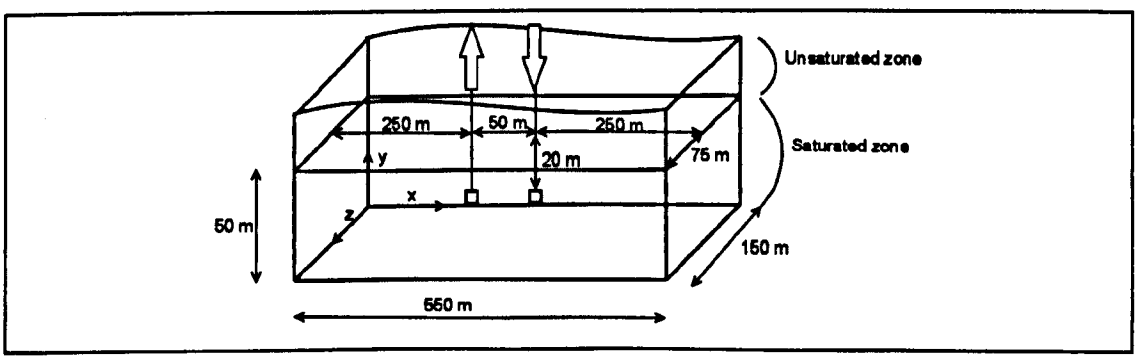

Figure 5.15 - Pumping injecting: geometry

The two wells, placed in the centre of the computational domain, are 50 meters apart and 20 meters from the bottom of the aquifer. Each well is modelled as two source (or sink) points having the same strength, and placed at the ends of a 2.5 meters long vertical segment. The pumping rate, chosen to match the injecting rate, is 50 m^3/h. No flux is allowed in two of the four side boundaries, at $z = 0m$ and $z = 150m$, which are taken to be impervious along with the bottom of the aquifer. Finally, in the two remaining side boundaries, at $x = 0m$

and $x = 550m$ a constant piezometric head equal to 50 meters is imposed (the boundary conditions used for the simulation are summarised in Table 5.1).

Boundary position	Boundary condition equation
x=0m, x=550m	$\phi = 50m$
z=0m, z=150m, y=0m	$\partial\phi/\partial n = 0$
Phreatic surface	Eq. (5.8)

Table 5.1 - Pumping injecting, boundary conditions

The porous medium is considered to be homogeneous and anisotropic, with an effective porosity $\eta = 0.2$ and a hydraulic conductivity in the vertical direction which is ten times smaller than in the horizontal ($K_x = K_z = 1.0\,m/h$; $K_y = 0.1\,m/h$).

The computational mesh is made of prisms. In fact, due to the small scale of the problem, prisms are used throughout, giving the moving boundary freedom to sweep the entire height of the domain. The original mesh features 24 layers, uniformly distributed in the vertical direction, covering a total height of 60 meters and allowing a maximum positive displacement of 10 meters (the initial elevation of the phreatic surface is equal to 50 meters). About 40,000 cells are used, with a refinement around the region where the pumping and injecting wells are placed, Figure 5.16.

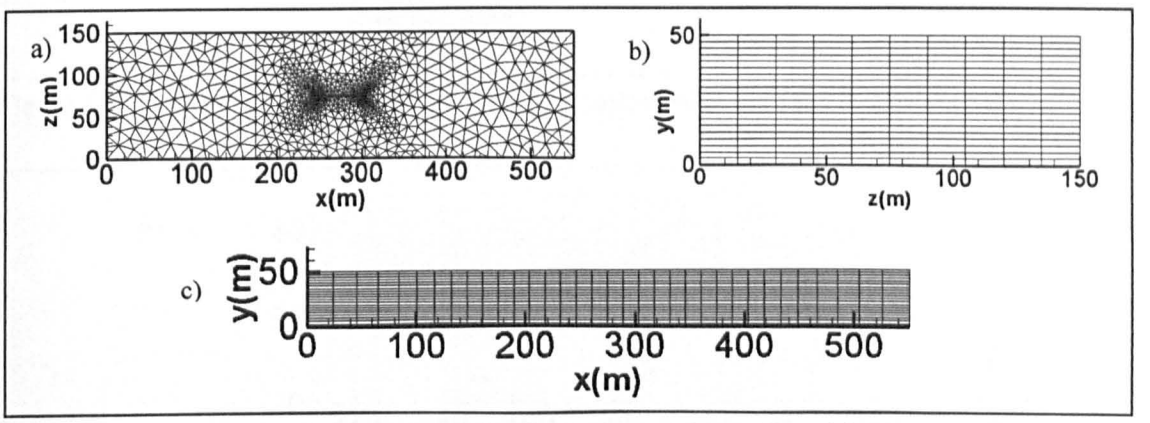

Figure 5.16 - Injecting, computational mesh: a) top view; b) front view; c) lateral view;

A quasi-static approximation is taken, solving (5.4) as a steady problem between each time step of the motion of the phreatic surface. Using a time step equal to 1 hour, the simulation is stopped after 300 hours, by which time the solution is deemed to have reached steady state. The increments of the phreatic surface point displacements computed at every time step, are used in order to monitor the global change in the solution. Only when the L_2-norm of all increments is less then $10^{-4}m$ the solution is considered to be converged to a steady state configuration. The

final solution is also checked to guarantee that any flux imbalance is negligible. The three-dimensional configuration of the phreatic surface at the steady state solution is shown in Figure 5.17. It is possible to observe the maximum displacements occurring in the region above the two wells, as expected: the maximum computed deflection equal to -2.33m is found at ($x_{Mdef} = 213m; z_{Mdef} = 75m$), whereas the maximum elevation of 0.76m occurs at ($x_{Mel} = 358m; z_{Mel} = 75m$). The asymmetry between maximum deflection and elevation can be explained by consideration of the distance between the moving boundary points and the wells. The points placed above the recharging well are pushed up, moving away from the well, hence reducing its influence on the surface. Conversely, the phreatic surface points above the pump are drawn down towards the aquifer, experiencing an enhanced influence from the well as they move closer to it.

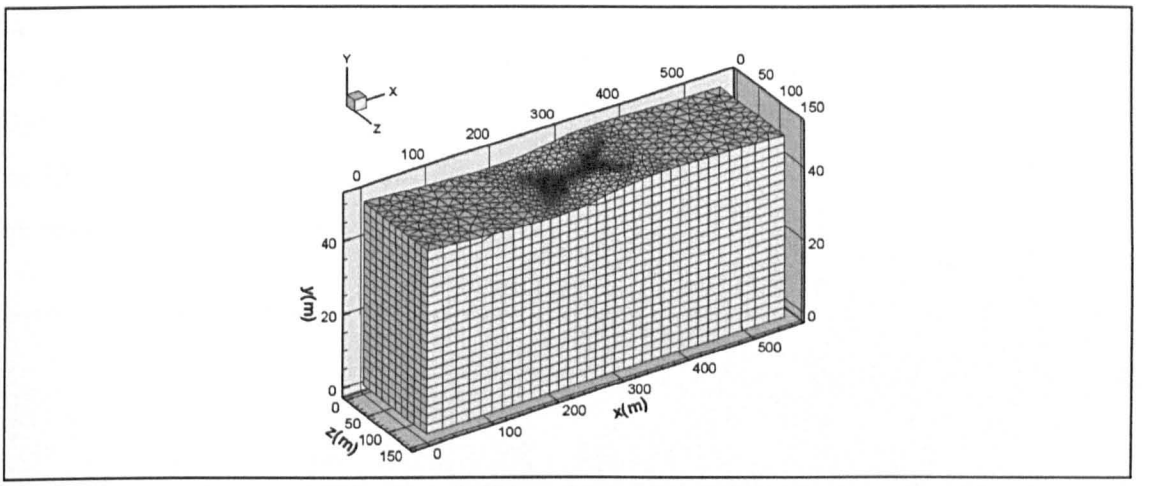

Figure 5.17 - Pumping Injecting: 3D plot of the phreatic surface once the flux balance is reached

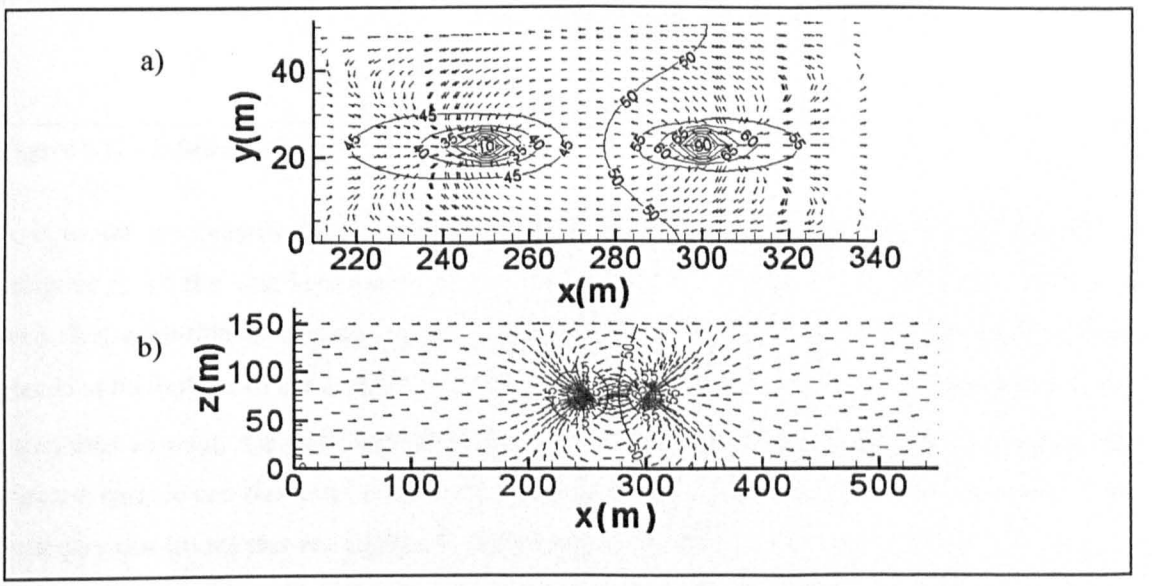

Figure 5.18 - Pumping Injecting, contour and vectors plot: a) plane at z=76 m; b) plane at y=22.5 m

Finally, the constant piezometric head contours and the velocity field are shown in Figure 5.18 for two cross sections which split the domains in two vertical parts in its centre. The first plane is parallel to the vertical direction, $z = 75m$, whereas the second one is an horizontal cross section through the centre of the pumps at $y = 22.5m$. Flow recirculations are observed in both sections due to presence of the impervious walls and of the phreatic surface, which are in close proximity to the wells.

5.6.3 Infiltration well

An infiltration well is subsequently modelled, which recharges the aquifer directly into the saturated zone. The well features a diameter equal to 3 meters and is long enough to go through the unsaturated zone to reach the ground surface. The domain modelled consists of a small square area (2500 m^2) of a semi-confined aquifer with a constant phreatic surface elevation, equal to 31 meters in the initial configuration, Figure 5.19. Following the beginning of the recharge operation, a rise in the position of the phreatic surface is expected, with the displacement of the phreatic surface depending on how the recharge is carried out. In this model, the well is kept at a constant piezometric head, 4 meters higher than the phreatic surface elevation, i.e. the piezometric head at the bottom of the well is 35 meters.

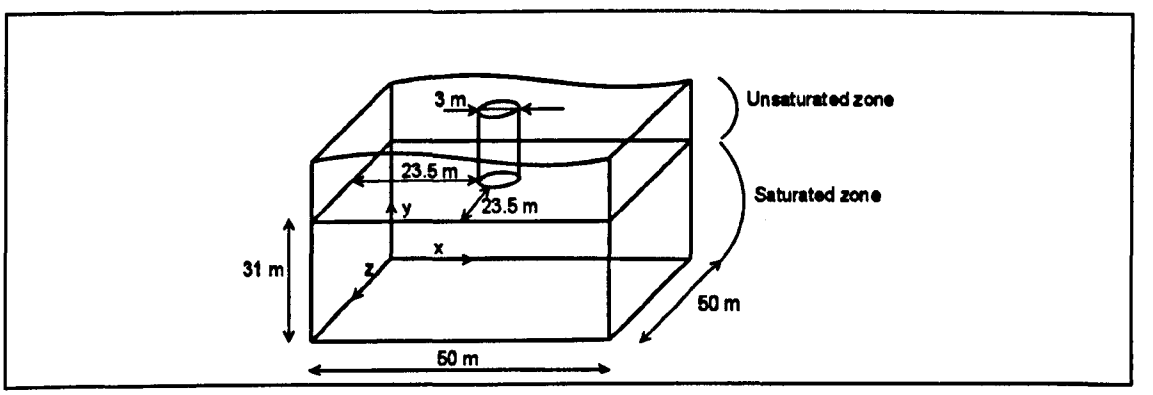

Figure 5.19 - Infiltration well model

A constant piezometric head equal to the initial phreatic surface elevation (31 meters) is assigned to all the side boundaries, at $x = 0m, x = 50m$, $z = 0m$, and $z = 50m$, whereas a zero flux condition is imposed at the vertical walls of the well and in the impervious layer placed at the bottom of the aquifer, $y = 0m$. Although the unsaturated zone of the aquifer is not taken into account, the well vertical walls must be included in the model. This is because the phreatic surface can rise around the walls of the infiltration well. In Table 5.2 a summary of the boundary conditions that are applied to the model is reported.

Boundary position	Boundary condition equation
x=0m, x=50m, z=0m, z=50m	$\phi = 31m$
z=0m, vertical walls of the well	$\partial\phi/\partial n = 0$
Bottom opening of the well	$\phi = 35m$
Phreatic surface	Eq. (5.8)

Table 5.2 - Infiltration well, boundary conditions

The porous medium is considered homogeneous and anisotropic, with $K_x = K_z = 1.0\,m/h$; $K_y = 0.3\,m/h$, and with an effective porosity $\eta = 0.2$. About 60000 prisms are used to generate the original mesh, and a significant refinement is provided below and around the infiltration well, Figure 5.20. Due to the discontinuity in the piezometric head required to model the infiltration well, large gradients are present in both the vertical and horizontal directions in this region.

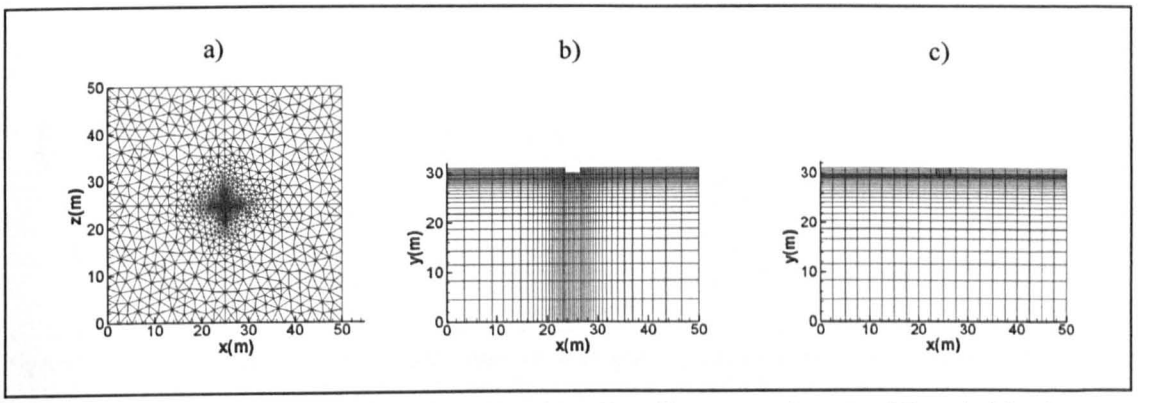

Figure 5.20 - well, computational mesh: a) top view; b) well cross section at z=25m; c) side view

The recharge operation is simulated using a relatively small time step equal to 6 minutes, in order to avoid the instability of the high gradient region. The experiment is stopped after 270 hours, when a steady state solution is reached (i.e. the L_2-norm of the displacement increments of the phreatic surface points is less than 10^{-4}m). For this configuration the maximum phreatic surface elevation occurs around the well, and the displacement compared to the initial solution is 1.3m, Figure 5.21. Two slices are extracted to analyse the steady solution inside the domain: a vertical cross section at $z = 25m$ and a horizontal cross section at $y = 28m$ just below the infiltration well, Figure 5.22. In the vertical plane, the velocity field features recirculations below the opening of the infiltration well and in the region where the phreatic surface is interrupted by the walls of the well. In this small scale problem, the prediction of such recirculations is crucial to accurately represent the final configuration of the phreatic surface. An erroneous prediction of the maximum elevation around the infiltration well would introduce

a large error in the whole domain. Finally it is worth noting that the model is able to correctly predict the radial behaviour of the horizontal velocity field, Figure 5.22.c.

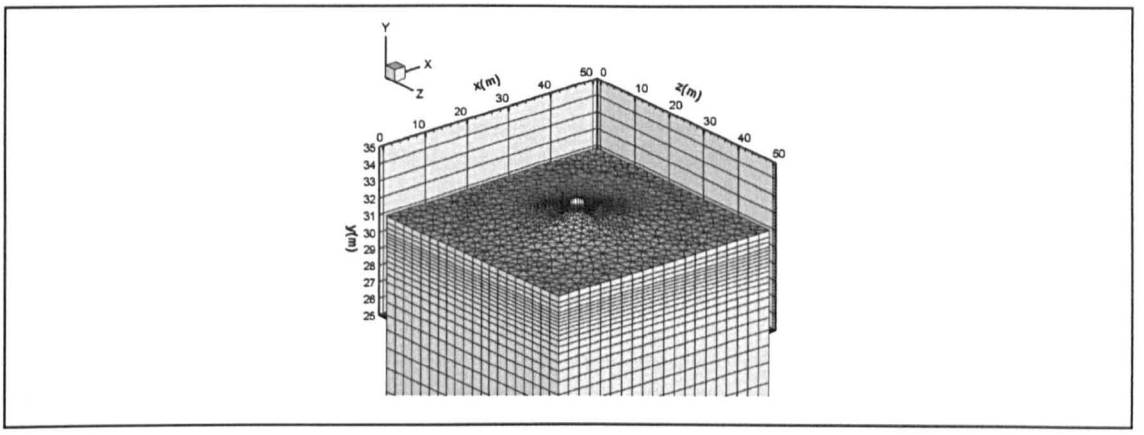

Figure 5.21 - Infiltration well: 3D plot of the phreatic surface for the steady solution

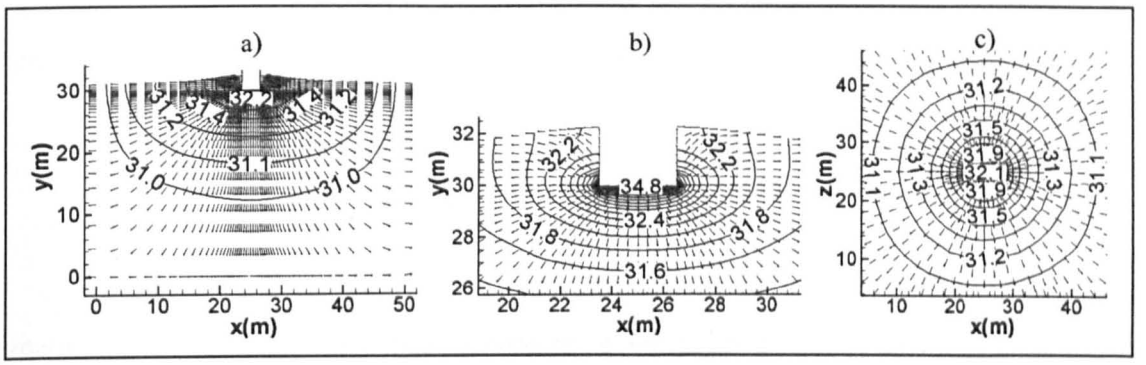

Figure 5.22 - Infiltration well, contour and vectors plot a) plane at z=25 m; b) plane at z=25 m, zoom in the region around the infiltration well; c) plane at y=22.5 m.

5.6.4 Infiltration well – Pumping

In this problem, the coupling between an infiltration well and an extraction pump placed 15 meters below the phreatic surface is modelled. The infiltration well recharges the aquifer directly into the saturated zone, and the quantity of water available for the infiltration is taken to be equal to the amount of water extracted by the nearby pumping well. This extracting well is placed only 25 meters away from centre of the infiltration well, Figure 5.23.

The infiltration well and the pump are implemented in a strip of a semi-confined aquifer, 75 meters long and 50 meters wide. The phreatic surface elevation is equal to 31 meters everywhere in the initial configuration.The simulation is designed to monitor how the aquifer responds when the infiltration and the pumping are simultaneously started. The imposed infiltration rate is close to the limit of what the aquifer can absorb, and is equal to the pumping rate of the water being extracted

$$I = Q = 5.17\left(m^3/h\right)$$

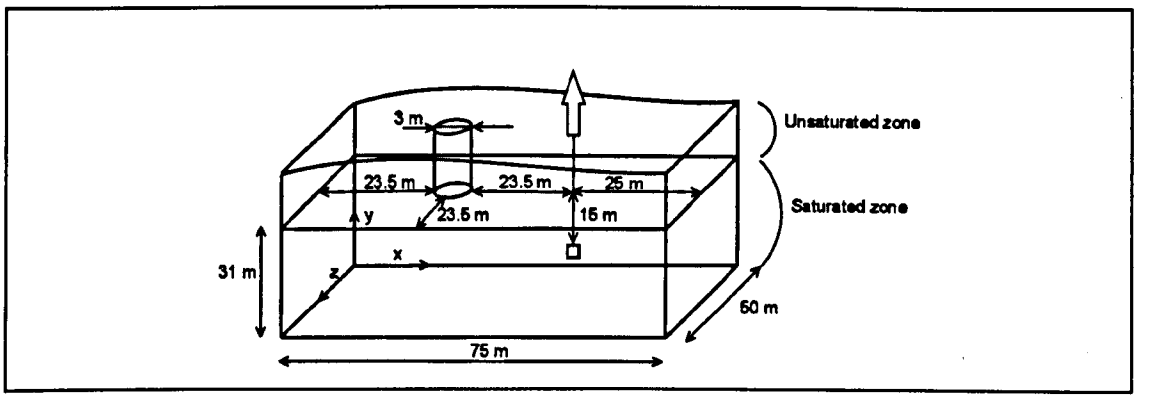

Figure 5.23 - Infiltration well-pumping model

Once the infiltration rate is fixed, it is possible to infer the piezometric head gradient, and the Neumann boundary condition imposed in the bottom opening of the infiltration well. Since the opening surface is horizontal, only the vertical components are considered

$$I = K_y \left.\frac{\partial \phi}{\partial y}\right|_{A_{well}} A_{well} \tag{5.14}$$

where A_{well} is the area of the bottom opening of the infiltration well and K_y the hydraulic conductivity in the vertical direction. The pump is represented with a point sink placed 15 meters below the phreatic surface. A constant piezometric head equal to the initial phreatic surface elevation (31 meters) is assigned in all the side boundaries ($x = 0m$, $x = 75m$, $z = 0m$, $z = 50m$), whereas a zero flux condition is imposed at the vertical well walls and at the impervious layer placed at the bottom of the aquifer ($y = 0m$). A summary of the boundary conditions is presented in Table 5.3 below.

Boundary position	Boundary condition equation
x=0m, x=50m, z=0m, z=50m	$\phi = 31m$
z=0m, vertical walls of the well	$\partial\phi/\partial n = 0$
Bottom opening of the well	$\partial\phi/\partial n = -v_I\eta/k_y$
Phreatic surface	Eq. (4)

Table 5.3 - Infiltration well-Pumping, boundary conditions

The porous medium is modelled as homogeneous and anisotropic, with $K_x = K_z = 1.0\,m/s$; $K_y = 0.3\,m/s$, and a porosity $\eta = 0.2$. About 60000 prisms have been used to mesh the domain with a mesh refinement around and below the infiltration well, Figure 5.24.

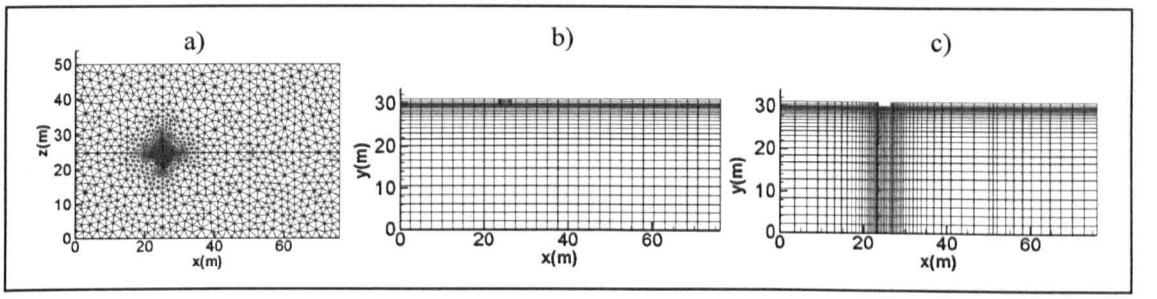

Figure 5.24 - Infiltration well-Pumping, computational mesh: a) top view; b) well cross section at z=25m; c) side view

A time step equal to 6 minutes is used here and the simulation is stopped after 30 hours when a steady state solution is reached. The L_2-norm of the displacement increments of the phreatic surface points is equal to 10^{-4} m and a flux balance is achieved. In the steady state configuration, the phreatic surface shows a maximum elevation equal to 0.4m around the infiltration well, and a minimum deflection of -0.14m in the region above the pump, Figure 5.25. The velocity field computed in the vertical section across the infiltration well, Figure 5.26.a, shows three main flow regimes: the circulation between the pump and the infiltration well, the water sucked by the pump from the aquifer, and finally the motion of the infiltrated water towards the outside of the considered domain. As can be observed in Figure 5.26.a, the majority of the water infiltrated into the aquifer is taken in directly by the pump. The velocity field in the horizontal plane at y=29 meters, just below the infiltration well, Figure 5.26.b, shows the interaction between the three flow regimes.

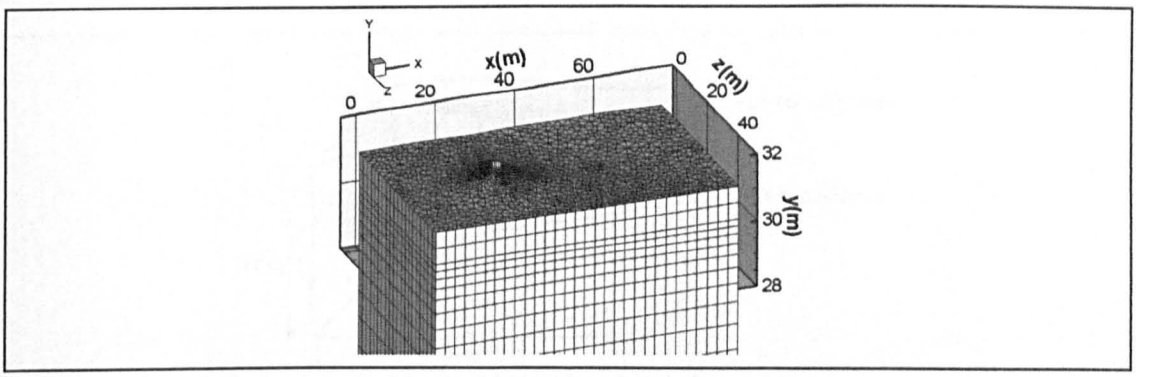

Figure 5.25 - Infiltration well-Pumping: 3D plot of the phreatic surface for the steady solution

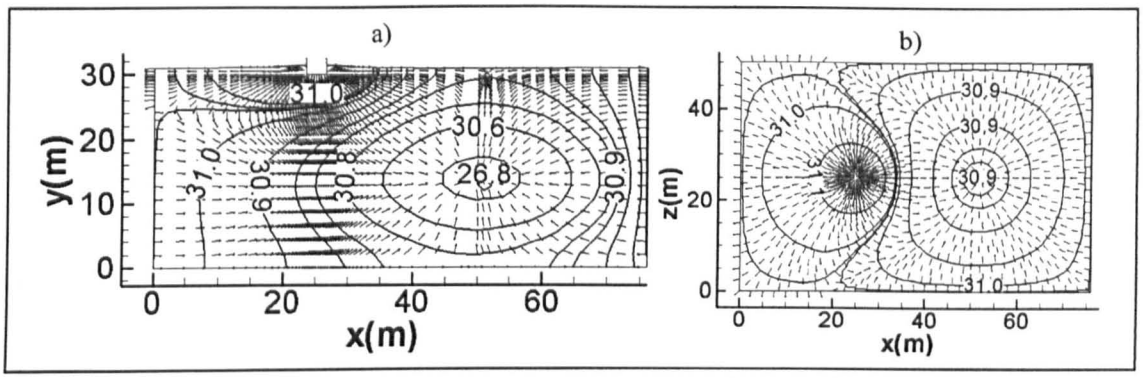

Figure 5.26 - Infiltration well-Pumping. contours at constant piezometric head (m) and vectors. a) Plane at z=25 m; b) plane at y=29 m

5.6.5 Injection field test case in a large diameter well performed in Campina De Faro (Portugal)

Another infiltration well is modelled to simulate the experiments carried out from one of the GARBADINE project partners in the field test site of Campina De Faro, south Portugal. Between the different techniques proposed to recharge the aquifer, the direct injection into the saturated zone was also considered during the GARBADINE project, and in the site of Campina De Faro a recharge prototype station based on this idea was built. The water pumped out from a deep confined aquifer was injected into the above semi-confined aquifer through a large diameter well. The confined and the semi-confined aquifers are separated by an impermeable layer, and they can be considered two independent systems. The estimated water table elavation of the semi-confined aquifer is about 50 *m*, and the 5 meters diameter well is immersed 7 meters into the saturated zone. Only a portion of 50 m x 50 m of the semi-confined aquifer is modelled in this section, since the deeper aquifer where the water is extracted does not have any effect on the zone under recharge. The sketch of the model is shown with dimensions in Figure 5.27.

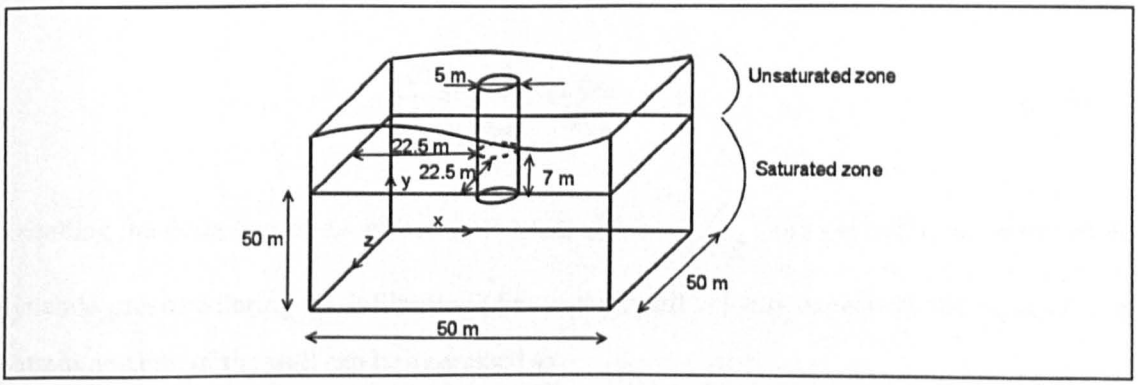

Figure 5.27 - Infiltration well model of the experimental site of Campina De Faro in Portugal

Three different injection experiments were carried out, and between each of them the semi-confined aquifer was allowed to recover the original configuration to avoid overlapping effects. No other pumping actions were taking place in the area, except the experiment in question. The longest injection, which is the main interest of the model considered here, was performed by supplying the well with water at a constant rate of 20 m^3/h for 50 hours. During the entire experiment, the water level in the well was recorded to investigate the absorbing capacity of the aquifer.

In the numerical model, a constant piezometric head equal to the initial phreatic surface elevation (50 meters) is assigned to all the side boundaries, at $x = 0m$, $x = 50m$, $z = 0m$, and $z = 50m$, whereas a zero flux condition is imposed at the vertical walls of the well and in the impervious layer placed at the bottom of the aquifer, $y = 0m$. For the bottom opening of the well neither the value of the piezometric head nor the water flux are known: the only data which is given is the well recharge rate, $Q = 20\,m^3/h$. During an interval Δt the volume of water supplied to the well, minus the volume of water that infiltrates into the aquifer, gives the increment or decrement of the water contained in the well

$$A_{well}\Delta h = Q\Delta t - q_w\Delta t \tag{5.15}$$

where A_{well} is the area of the bottom opening of the infiltration well, Δh is the increment of the water level inside the well, q_w is the volumetric rate of the water infiltrating into the aquifer. This mass balance can be exploited to derive a Robbin (or mixed) condition to be applied at the bottom opening of the well.

Considering an infinitesimal interval, equation (5.15) can be rearranged as follows

$$\frac{dh}{dt} = \frac{Q}{A_{well}} - \frac{q_w}{A_{well}} \tag{5.16}$$

Recalling the definition of the piezometric head, $\phi = z + {}^{p}/_{\rho g}$, and neglecting the effect of the dynamic pressure during the infiltration (due to the small velocity expected), the value of ϕ at bottom opening of the well can be expressed as

$$\phi = H + \frac{\rho g h}{\rho g} = H + h \tag{5.17}$$

where H is the elevation of the bottom opening (43 m in this case), which is a constant. So in equation (5.16), the differential of the water level at the bottom of the well can be taken to be equal to the differential of the piezometric head, $dh = d\phi$. Taking the increment dh positive for increasing y, see Figure 5.27 for the reference system, and expressing q_w by the Darcy's law,

$$q_w = -q_y = A_w K_y \frac{\partial \phi}{\partial y} \tag{5.18}$$

equation (5.16) can be rewritten as

$$\frac{d\phi}{dt} = \frac{Q}{A_{well}} - K_y \frac{\partial \phi}{\partial y} \tag{5.19}$$

Finally using a first order finite difference approximation to discretise the time in equation (5.19) the following expression is obtained

$$\phi^t + \Delta t K_y \frac{\partial \phi^t}{\partial y} = \Delta t \frac{Q}{A_{well}} + \phi^{t-\Delta t} \tag{5.20}$$

Equation (5.20) is the Robbin condition that will be applied to the bottom opening of the well. A summary of the boundary conditions is presented in Table 5.4 below.

Boundary position	Boundary condition equation
x=0m, x=50m, z=0m, z=50m	$\phi = 50m$
z=0m, vertical walls of the well	$\partial\phi/\partial n = 0$
Bottom opening of the well	Eq. (5.20)
Phreatic surface	Eq. (5.8)

Table 5.4 - Campina De Faro infiltration well, boundary conditions summary

The unconfined aquifer is mainly made of sand, for which a porosity $\eta = 0.33$ is used in the model. The values of the hydraulic conductivity are varied during the calibration in order to match the well water level data recorded during the experiments, and approximated initial values are computed based on the infiltration rate observed during the experiment (35-45 meters/day). About 150000 prisms are used to generate the original mesh, and a significant refinement is provided below and around the infiltration well, Figure 5.28.

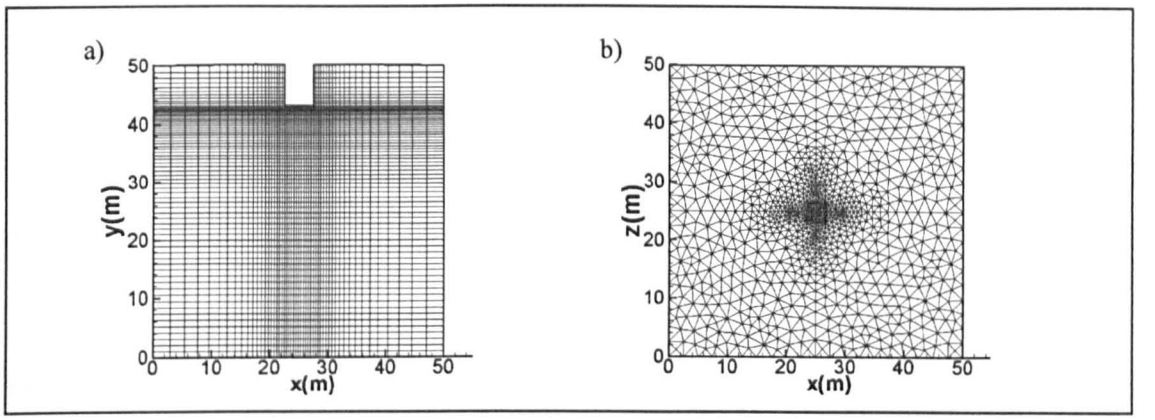

Figure 5.28 - Campina De Faro infiltration well, computational mesh: a) well cross section at z=25m; b) top view

Following the experiments, the injection starts with the phreatic surface and the water level inside the well having the same elevation (50 meters), so that the system is in equilibrium. In equation (5.20) $Q = 20 m^3/h$ is imposed for the first 50 hours of the simulation. After which the well water supply is stopped, and the recharge operation continues with water accumulated in the well for another 50 hours, at which point the simulation is stopped. A relatively small time step equal to 3 minutes is used, in order to avoid the instability caused by the high gradient region. The flow paths and the piezometric contours plots look very similar to those reported for the infiltration well studied in section 5.6.3, while the maximum elevation of the phreatic surface computed for $t = 50h$ at the wall of the well is equal to 0.27 meters. The calibration of the model is carried out by comparing the evolution in time of the experimental water level inside the well with the computed one. Repeating the simulation for different values of the hydraulic conductivity, the best match is found for $K_x = K_z = 1.0 m/h$ and $K_y = 0.04 m/h$, see Figure 5.29.

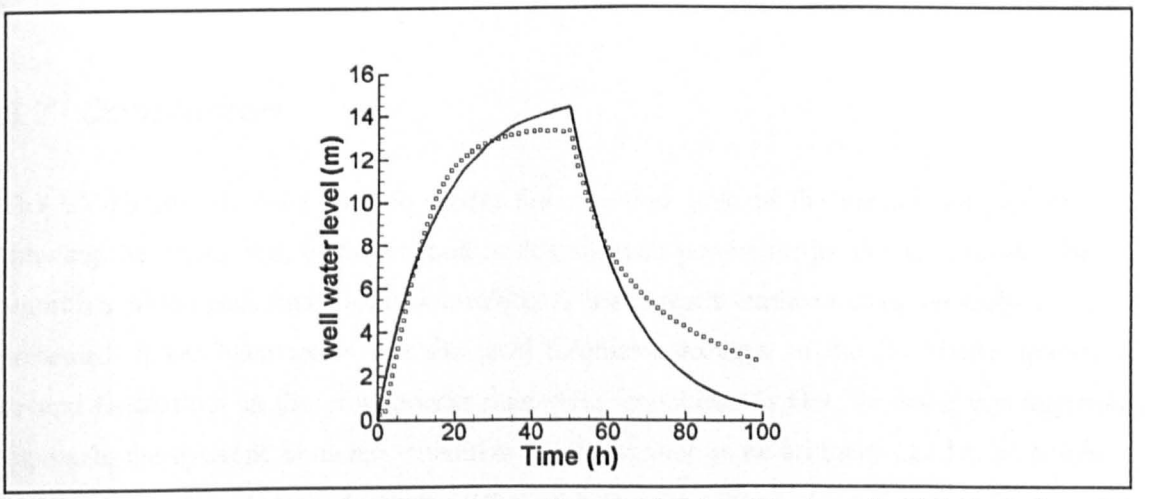

Figure 5.29 - Campina De Faro infiltration well: water level inside the well. Full black line, CV-HRBF; Symbols, experimental data.

The well water level reported in Figure 5.29 is relative to the elevation of the well bottom opening ($H = 50m$). Such a level is computed at each time step as the average of the piezometric head values that are reconstructed on the nodes located at the bottom opening of the well, and by substracting H from the average. In fact, the peizometric head values computed in the centre of the opening are larger than those found near the wall. This is due to the dynamic pressure effects, which are neglected in this model. However such variation is less than a meter.

As can be observed from Figure 5.29, the numerical simulation is able to reproduce the experiments, although it shows some discrepancies in the region where the water supplied to the well is equal to the amount of water that infiltrates into the aquifer. This happens 40 to 50 hours after the recharge starts, where the experimental data shows that the water level inside the well tends to flatten. The numerical solution also seems to be different from the field data during the water level drop; and this is probably a consequence of the inaccurate prediction in the previous phase.

The error found between the experimental data and the numerical solution reflects the uncertainty of the data available for the mathematical model. The thickness of the saturated zone, which is assumed to be equal to 50 meters, is only estimated. Probably another calibration should be performed by varying this value. In addition, by looking at the field data it appears that the modelled recharged operation started when the effects of the previous recharge were still present, and the system was not completely in equilibrium. Finally, in this simple model the clogging is not taken into account. This is another phenomena that could also affect the distribution of the piezometric head and water level, in particular during the phase of non-pumping, where the difference between the numerical and experimental results appear to be larger.

5.7 Conclusion

The CV-HRBF has been used to model the saturated zone of the unconfined aquifer, thus showing the capabilities of the method in dealing with porous media flows. A mesh adapting algorithm which performs a local re-meshing as the phreatic surface moves vertically has been presented. It has been found that the local meshless character of the CV-HRBF introduces several flexibilities in the groundwater numerical modelling. In fact, by using this numerical approach, the dynamic boundary condition can be applied in an arbitrary number of points on the phreatic surface, independently from the mesh element.

6 MULTI-DOMAIN PROBLEMS

6.1 Introduction

Domain decomposition methods are often used in numerical analysis to tackle engineering applications where the solution in a single domain would be impossible due to the nature or the size of the problem. Consider for example a problem where two adjacent regions require the solution of a different type of partial differential equations (e.g. fluid-structure interaction), in this case the coupling is only possible via splitting the domain in two parts and imposing some adequate matching conditions at the interface between the two. In other problems, the type of partial differential equation to be solved is the same all over the computational domain, but the material properties are strongly heterogeneous. In this circumstance, some of the parameters that appear in the equation to be discretised can be practically considered discontinuous. In order to capture the discontinuities caused by this type of heterogeneities, the domain can be divided in different zones that individually feature a smooth variation of the physical properties. This approach, commonly named as multi-zone, has been used for a long time in the numerical analysis of solid mechanics problems but applications can also be found also for heat transfer problems. Another recent application of the domain decomposition technique is due to the growing popularity of parallel processing over the last two decades. The parallel processing is adopted when the problem to be solved does not fit in the memory of a single machine. It is also used to reduce the computational time needed to complete a simulation. In general, the computational domain is divided into sub-domains and each of them is assigned to a different processor, which might share memory with other processors or not depending on the computer architecture, Saad (1996). The number of software packages that use the parallel computation technology is growing quickly, in fact no significant improvements are expected for the single CPU speed in the near future and computer development is now focused on parallel processing.

In the literature, the domain partitioning algorithms are divided into two main categories: the overlap and the non overlap domain decomposition. In the overlapping approach, the original domain is divided into a prescribed number of non-overlapping sub-domains. Each sub-domain is then extended including a relatively small overlapping region between the neighbouring sub-domains. Each sub-domain is treated independently as a singular boundary value problem and it communicates with its neighbours through the overlapping regions, where artificial boundary conditions are updated repeatedly by the use of iterative algorithms (e.g. Schwarz iterative

approach). The overlapping region makes this method unsuitable for cases where the sub-domains are characterised by different partial differential equations or high heterogeneous material properties. In fact this technique is mainly adopted for parallel computation, Quarteroni and Valli (1999). On the contrary, the non-overlap domain decomposition methods are more universal, and can be used for multizone problems as well as for parallel processing. The domain is divided into non-overlapping sub-domains that share interface surfaces, and in each sub domain the original numerical scheme is implemented. The boundary conditions to be applied at the sub-domain surfaces are generally unknown because they depend on the solution of the global domain. In the case of a direct solution physical matching conditions (e.g. function and flux continuity for second order PDEs) can be considered to close the system. Instead in the case of iterative approaches, there is not a real constraint on the type of boundary conditions that can be imposed at the zone interfaces, as long as these are suitable to define a well-posed boundary value problem for the adjacent sub-domain (e.g. alternative Schwarz iterative scheme).

A few recent works have been found in the area of the control volume methods that use non-overlapping domain decomposition methods based on iterative approaches. An overview can be found in Cautres et al. (2004), where a domain decomposition algorithm for non-matching cell centred finite volume meshes is proposed. In this work, a mixed (Robbin) condition is used at the sub-domain interface, which presents the inconvenience of a weighting coefficient for the Dirichlet contribution that can be chosen arbitrarily, and that can significantly affect the convergence rate of the algorithm.

Direct solution methods such as substructuring or Schur compliment methods have also been applied to finite volume schemes in the case of non-overlapping domain decomposition. Faille et al. (2004) compare the performance of different transmission operators for non matching finite volume grids and highly heterogeneous coefficient both across and inside the sub-domains. The continuity of the solution and its normal derivative on the interface is guaranteed by imposing 'mortar matching conditions'; i.e. considering two adjacent sub-domains Ω_1 and Ω_2, at the interface, $\partial\Omega_{12}$, Ω_1 imposes the value of the function on Ω_2, while Ω_2 imposes the value of the derivative on Ω_1. The sub-domain Ω_1 is called the master because it imposes the value of the function and Ω_2 is called the slave. The transmission operators relate the function value and its derivative of the two sub-domains (e.g. for non matching grids some interpolation operator is required). More details about other available interface conditions can be found in the references quoted in this work.

In this chapter, a non-overlapping non-iterative multi-domain formulation for the CV-HRBF scheme will be presented. The main idea is to exploit the local Hermitian RBF meshless collocation method to satisfy a physical matching condition at the subdomain boundaries. In the last decades, different domain decomposition methods have been applied to the RBF meshless collocation methods with the intent of overcoming the well known ill-conditioning problems. Wong et al. (1999), developed a multizone algorithm for the mutiquadric scheme to reduce the matrix size in order to simulate the flow circulation pattern in a real-life hydrodynamic model. Zhou et al. (2003) tested the overlapping domain decomposition with both multiplicative and additive Schwarz iterative techniques for the Kansa's (unsymmetric) RBF collocation method to circumvent the ill-conditioning problems resulting from the use of RBF as a global interpolant. More interesting for the remainder of this chapter, Hernandez Rosales and Power (2007), proposed a non-overlapping domain decomposition algorithm for the Hermite radial basis function meshless collocation method. In this work both the continuity of the function and of its flux across the zone boundary interfaces are imposed, and both conditions are satisfied simultaneously at each interface nodal point using a Hermitian interpolation. The same algorithm will be adopted in the local matching of the non-overlapping domain decomposition approach proposed for the CV-HRBF method.

6.2 Non-overlapping non-iterative domain decomposition formulation for the CV-HRBF method

Without loss of generality, the non-overlapping domain decomposition algorithm and the schematic diagram showing implementation details are presented for two-dimensional structured volume elements. However, the proposed method is also valid for *nd*-dimensional problems, using structured and unstructured meshes.

The unsteady advection-diffusion-reaction problem described in section 3.2 is considered here again to introduce the multi-zone formulation of the CV-HRBF. The entire domain Ω delimited by $\partial\Omega$ is partitioned into $Nsub$ non-overlapping subdomains,
Figure 6.1, each of them presenting smooth variation of diffusion and velocity. The partitioning can be described as follows

$$\Omega_n \qquad n=1,Nsub \text{ with } \Omega_n \cap \Omega_m = \varnothing \qquad n \neq m$$

$$\partial\Omega_n = \partial_d\Omega_n \cup \partial\Omega_{nm}$$

Where $\partial_d\Omega_n$ is the intersection between the sub-domain n and the physical boundary $\partial\Omega$, and $\partial\Omega_{nm}$ contains the interfaces between Ω_n and its neighbouring sub-domains.

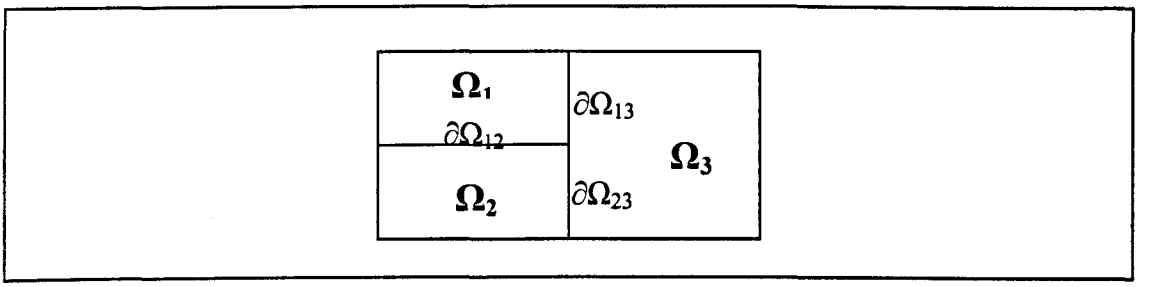

Figure 6.1 - Non-overlapping domain decomposition

In the sub-domain n the problem is defined by the following partial differential equation

$$\frac{\partial\phi^n}{\partial t}=\frac{\partial}{\partial x_i}\left(D_{ij}^n\frac{\partial\phi^n}{\partial x_j}\right)-\frac{\partial U_i\phi^n}{\partial x_i}+K_r\phi^n \qquad i,j=1,nd \tag{6.1}$$

together with the following boundary and initial conditions

$$\phi(x,0)=\phi_0 \qquad \text{on} \qquad \Omega_n \tag{6.2}$$

$$B^n[\phi^n]=f_B^n(x) \qquad \text{on} \qquad \partial_d\Omega_n \tag{6.3}$$

where ϕ^n is the generic variable (e.g. temperature, concentration, etc), D_{ij}^n is the term ij of diffusivity tensor in the sub-domain n and U_i the component i of the velocity. Discretising the time derivative by the weighted Crank-Nicholson time-stepping scheme as done in section 3.2, equation (6.3) can be rewritten in a concise form

$$L_t^n(\phi)=L_{t-\Delta t}^n(\phi) \tag{6.4}$$

where the operators $L_t^n(\phi)$ and $L_{t-\Delta t}^n(\phi)$ valid in the domain Ω_n are defined as follows

$$L_t^n(\ )=\Delta t\theta\left(\frac{\partial}{\partial x_i}\left(D_{ij}^n\frac{\partial(\ )}{\partial x_j}\right)-\frac{\partial U_i(\ )}{\partial x_i}+K_r(\ )\right)-1(\ ) \tag{6.5}$$

$$L_{t-\Delta t}^n(\ )=\Delta t(\theta-1)\left(\frac{\partial}{\partial x_i}\left(D_{ij}^n\frac{\partial(\ )}{\partial x_j}\right)-\frac{\partial U_i(\ )}{\partial x_i}+K_r(\ )\right)-1(\ ) \tag{6.6}$$

Each sub-domain is discretised with an element mesh, and the elements located in the two sides of the sub-domain interfaces are considered matching. In the case of the cell centred CV-HRBF scheme, the only one considered for this presentation, equation (6.4) is integrated over a finite number of control volumes coinciding with the mesh elements as explained in chapter 2. The flux reconstruction of each control volume uses an element based RBF interpolation, which will be required to satisfy adequate matching conditions in the case of proximity to a sub-domain interface. Consider for example the element E_1 adjacent to the sub-domain boundary $\partial\Omega_{1m}$, Figure 6.2; in this case two of the four neighbouring elements belong to different sub-domains (Ω_2, Ω_3) and they are not included in the stencil of the element E_1. This stencil interpolation is formed by the three elements contained in the sub-domain Ω_1 and that have as centroids $\mathbf{C_{11}}$, $\mathbf{C_{12}}$ and $\mathbf{C_{13}}$.

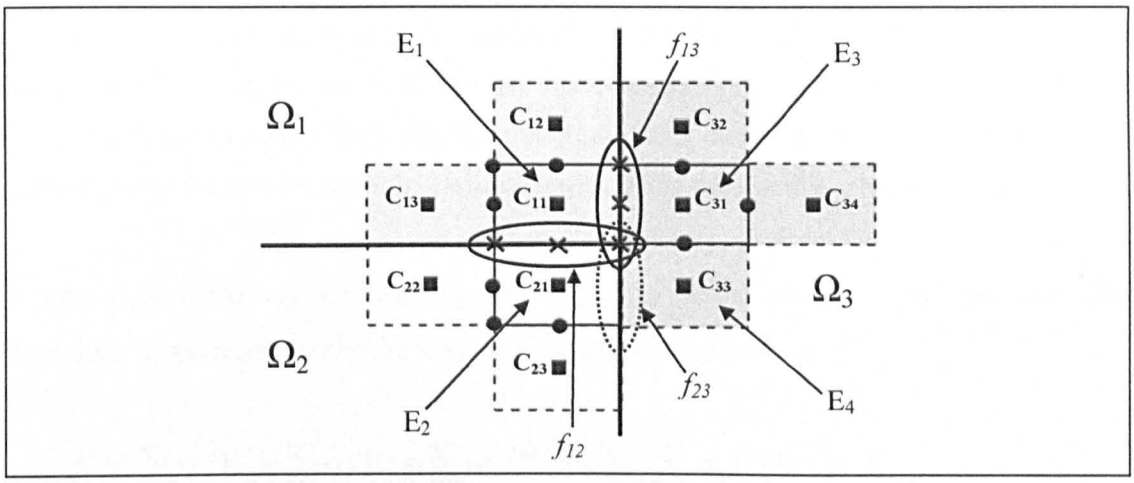

Figure 6.2 - Interpolation stencil for an element located in the sub-domain interface. Round symbols, PDE points; square symbols, control volume centroids (Dirichlet operator); cross symbols, sub-domain interface points (Matching conditions points). The three different shades of grey indicate the three stencils that belong to the three sub-domains Ω_1, Ω_2 and Ω_3.

The Hermitian interpolation ϕ^1 defined by the elements with centres C_{11}, C_{12}, C_{13}, and associated with E_1 is used to reconstruct the flux over the corresponding control volume. Such interpolation must satisfy continuity of the function and flux across the faces f_{12} and f_{13} placed in the sub-domain interfaces $\partial\Omega_{12}$ and $\partial\Omega_{13}$ respectively. Being defined inside the domain Ω_1, ϕ^1 will include only the trial centres that belong to Ω_1, $\partial\Omega_{12}$ and $\partial\Omega_{13}$

$$\phi^1 = \sum_{nele_1} \alpha_j \Psi_j + \sum_{nf_{12}} \alpha_j \Psi_j + \sum_{nf_{12}} \alpha_j F^1\left(\Psi_j\right) + \sum_{nf_{13}} \alpha_j \Psi_j + \sum_{nf_{13}} \alpha_j F^1\left(\Psi_j\right) \sum_{nLop_1} \alpha_j L_i^1\left(\Psi_j\right) + P_{M-1} \tag{6.7}$$

where $nele_1$ is the number of neighbour elements included in the interpolation stencil, nf_{12} and nf_{13} are numbers of matching points considered for the faces f_{12} and f_{13} respectively, and $nLop_1$ is the number of points where the PDE operator L_i^1 is applied. Finally the flux operator F^n is defined as

$$F^n(\ ) = n_i^{Int}\left(D_{ij}^n \frac{\partial(\ )}{\partial x_j} - U_i(\ ) \right) \tag{6.8}$$

where n_i^{Int} is the i-component of the sub-domain interface normal pointing out the sub-domain Ω_n.

In the interpolation (6.7) the number of trial centres in which the continuity of the function will be imposed is equal to the number of centres where the flux condition will be applied. This is not a coincidence, in fact as in Hernandez Rosales and Power (2007), the same location is chosen to simultaneously satisfy the two conditions. This double collocation technique can be adopted due to the robustness of the Hermite interpolation used in this scheme.

In order to apply the required matching conditions to ϕ^1 at the sub-domain interface, two other interpolations associated with the elements E_2 and E_3 need to be defined

$$\phi^2 = \sum_{nele_2} \alpha_j \Psi_j + \sum_{nf_{12}} \alpha_j \Psi_j + \sum_{nf_{12}} \alpha_j F^2\left(\Psi_j\right) + \sum_{nLop_2} \alpha_j L_i^2\left(\Psi_j\right) + P_{M-1} \tag{6.9}$$

$$\phi^3 = \sum_{nele_3} \alpha_j \Psi_j + \sum_{nf_{13}} \alpha_j \Psi_j + \sum_{nf_{13}} \alpha_j F^3\left(\Psi_j\right) + \sum_{nLop_3} \alpha_j L_i^3\left(\Psi_j\right) + P_{M-1} \tag{6.10}$$

Note that in the present implementation, the expressions (6.9) and (6.10) for the interpolations ϕ^2 and ϕ^3 respectively, are valid only for the formation of the local system associated with the element E_1. In this local problem, only the fluxes of interest for the control volume that coincides with E_1 are considered. For example, when the problem associated with the element E_2 is under construction, an interpolation formula ϕ'^2 that differs from that reported in equation (6.9) will be used. Similarly to the matching conditions considered for ϕ^1, in ϕ'^2, the fluxes across both f_{21} and f_{23} will be taken into account.

Returning to the example of the local problem associated with E_1, it is worth noting that the Hermitian interpolations (6.7), (6.9) and (6.10) do not present any boundary operator. In fact for the sake of simplicity the stencils in Figure 6.2 have been chosen away from any domain boundary. If a boundary condition needs to be satisfied, the boundary operator can be introduced in the Hermitian interpolation as explained in chapter 2. The continuity of the function and of the flux in those stencil points located in the interfaces $\partial\Omega_{12}$ and $\partial\Omega_{13}$ can be expressed as

$$\phi^1 = \phi^2, \quad F^1\left(\phi^1\right) = F^2\left(\phi^2\right) \tag{6.11}$$

$$\phi^1 = \phi^3, \quad F^1\left(\phi^2\right) = F^3\left(\phi^3\right) \tag{6.12}$$

As observed above, the function and the flux continuity can be imposed in the same location, since a Hermitian interpolation is being used. This circumstance leads to a simplification of the flux operator in the case of a continuous velocity field across the zone boundary. In fact, having imposed the same value of the function for the two interpolations across the interface, and having a continuous velocity, the flux operator reduces to:

$$F^n(\ ) = n_i D_{ij}^n \frac{\partial(\ )}{\partial x_j} \tag{6.13}$$

The local problem needed to define the interpolation ϕ_1, can now be formulated applying the Dirichlet condition on the control volume centroids of the three stencils (to make the value of the global unknowns explicit in the right hand side), the operator L_i^1, L_i^2 and L_i^3 to their corresponding PDE points, and the matching conditions (6.11) and (6.12) to the interface points in order to close the local system $[A][\alpha] = [b]$.

The procedure explained above, to form the local problem associated with an element E_n that belongs to a sub-domain Ω_n and adjacent to a sub-domain interface, can be generalised by fixing a practical rule. The local problem corresponding to the element E_n will only include the matching conditions in cell faces that are shared with elements located in other sub-domains Ω_m, with $m \neq n$. Indicating with N_{EOD} the number of neighbouring elements of E_n located in different sub-domains Ω_m, the general interpolation associated with E_n can be expressed as

$$\phi^n = \sum_{nele_n} \alpha_j \Psi_j + \sum_{m=1}^{N_{EOD}} \left(\sum_{nf_{nm}} \alpha_j \Psi_j + \sum_{nf_{nm}} \alpha_j F^n(\Psi_j) \right) + \sum_{nLop_n} \alpha_j L_t^n(\Psi_j) + P_{M-1} \qquad (6.14)$$

The remaining N_{EOD} 'supporting interpolations' contain only one cell face in which the matching conditions are applied

$$\phi^m = \sum_{nele_m} \alpha_j \Psi_j + \sum_{nf_{nm}} \alpha_j \Psi_j + \sum_{nf_{nm}} \alpha_j F^m(\Psi_j) + \sum_{nLop_m} \alpha_j L_t^m(\Psi_j) + P_{M-1} \qquad (6.15)$$

with m=1, N_{EOD}

This algorithm is easy to implement for a control volume method, because it exploits the mesh structure already available, to select the elements and therefore the interpolations, to be included in a local problem where multiple sub-domains must be considered. In addition, it avoids the formation of relative large local systems, because the matching conditions are only applied where necessary. For example, in the case of Figure 6.2, the system associated with the element E_1 only takes account of the flux across f_{12} and f_{13} of primary importance for the cell flux computation considered, while that across f_{23} is not included. Excluding such flux, avoids the solution of a system that couples 4 interpolations (corresponding to E_1, E_2, E_3, E_4) in favour of a small one that takes account of only three (corresponding to E_1, E_2, E_3). However in the global assembling procedure, the flux across f_{23} will also be considered in the flux reconstruction for the control volumes coinciding with the element E_2 and E_4.

The matrices of the local systems present a block structure whose general form is shown in equation (6.16)

$$[A] = \begin{bmatrix} A_n & MTR_{n,1} & \cdots & MTR_{n,N_{EOD}} & 0 & 0 & 0 \\ MTST_{1,n} & MTT_{1,1} & \cdots & MTT_{1,N_{EOD}} & MTST_{1,n} & 0 & 0 \\ \vdots & \vdots & \ddots & & \vdots & \vdots & \vdots \\ MTST_{N_{EOD},n} & MTT_{N_{EOD},1} & \cdots & MTT_{N_{EOD},N_{EOD}} & 0 & 0 & MTST_{N_{EOD},n} \\ 0 & MTR_{1,n} & 0 & 0 & A_1 & 0 & 0 \\ 0 & \vdots & \vdots & \vdots & 0 & \ddots & 0 \\ 0 & 0 & 0 & MTR_{1,n} & 0 & 0 & A_{N_{EOD}} \end{bmatrix} \qquad (6.16)$$

and the corresponding interpolation coefficient and right hand side arrays are shown in (6.17) and (6.18)

$$[\alpha]^T = \begin{bmatrix} \alpha_n & \alpha_{Int,1} & \cdots & \alpha_{Int,N_{EOD}} & \alpha_1 & \cdots & \alpha_{N_{EOD}} \end{bmatrix} \tag{6.17}$$

$$[B]^T = \begin{bmatrix} B_n & 0 & \cdots & 0 & B_1 & \cdots & B_{N_{EOD}} \end{bmatrix} \tag{6.18}$$

In equations (6.16), (6.17) and (6.18), A_n, α_n and B_n correspond to the points of the interpolation ϕ^n located strictly inside the sub-domain Ω_n, while A_m, α_m and B_m are associated with the trial centres of ϕ^m defined in Ω_m. In the block matrices (6.16), $MTR_{n,m}$ and $MTST_{n,m}$ couple the interpolation ϕ^n and ϕ^m at the interface points that belong to $\partial\Omega_{nm}$ viewed as trial and test points respectively; whereas $MTT_{m,m}$ represent the relation between the matching points. The explicit matrix for the example of Figure 6.2 is reported in section **Error! Reference source not found.** for further clarifications.

The coefficients of the interpolation ϕ_n are contained in a subset of the array $[\alpha]$, with part of them associated with the trial centres internal to the sub-domain Ω_n ($[\alpha_n]$), and the remaining part with those centres located at the sub-domain interfaces ($\begin{bmatrix} \alpha_{Int,1} & \cdots & \alpha_{Int,N_{EOD}} \end{bmatrix}$). Due to the coupling introduced by the matching conditions, these coefficients depend not only on the unknowns values of cell centres located in the zone Ω_n, but also on the unknown values of the zones Ω_m, with m=1, N_{EOD}. The flux reconstruction of the control volume built on the element E_n, corresponds to a line on the global matrix that couples the unknown values at the cell centres (ϕ_C^n, ϕ_C^m) coming from different sub-domains.

In the example illustrated in Figure 6.2 at the beginning of this section, the element E_1 with faces on two different zones, has intentionally been chosen to show the wide flexibility of this method in handling sub-domain interface conditions. The local meshless character of the CV-HRBF method allows continuity of the flux to be imposed in the face integration points, ensuring a very accurate mass conservation across the zone boundaries. Also, due to the use of a Hermitian interpolation, multiple matching conditions can be imposed in a singular point shared by more than two sub-domains. For example, the continuity of the flux across both f_{12} and f_{13} can be guaranteed at the cross point that belongs to Ω_1, Ω_2 and Ω_3, see Figure 6.2; in fact in such a location both matching conditions shown in formula (6.11) and (6.12) can be applied.

An additional flexibility is the freedom to apply the PDE operator on the top of the matching conditions. This technique has already been proven to be very effective in previous works, where it significantly improved the accuracy of the interpolation in proximity of a domain boundary, La Rocca and Power (2008). In the case of the CV-HRBF multi-domain formulation, the PDE operators of the zones converging in the interface points can be applied, in addition to the matching conditions. Figure 6.3 shows two interpolation stencils located in the proximity of the zone boundary $\partial\Omega_{12}$ where the PDE operators L_t^1 and L_t^2 of the left and right sub-domains are both applied to the left and the right RBF interpolations in the same locations where the matching conditions are satisfied.

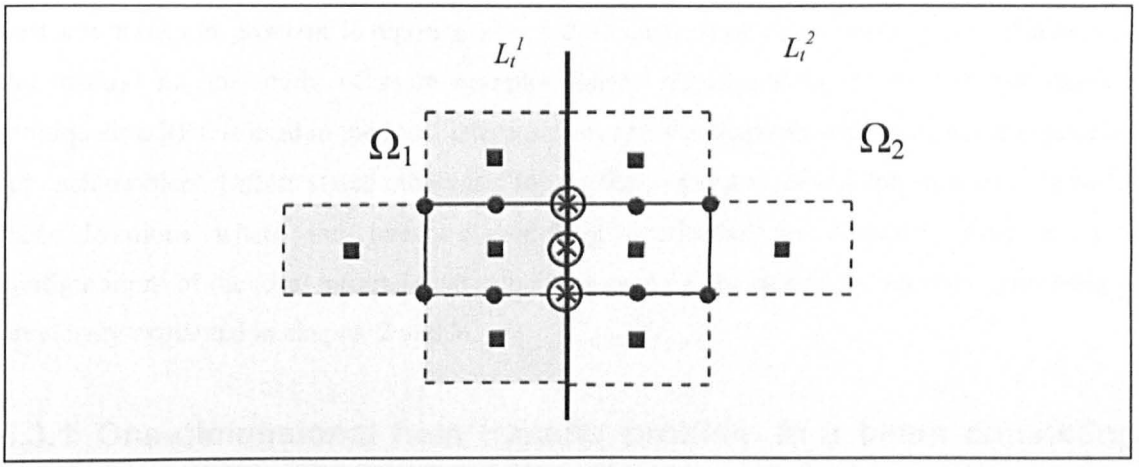

Figure 6.3 - PDE collocation for sub-domain boundary points. Interpolation stencil located at the zone boundary $\partial\Omega_{12}$. Round full symbols, PDE points; Round empty symbols, points where both operators L_1 and L_2 are applied; square symbols, control volume centroids (Dirichlet operator); cross symbols, subdomain interface points (Matching conditions)

This collocation strategy returns a non-singular local system, providing that the PDE operators are linearly independent from the matching operators. In the case of identical PDEs, the local system will still be non singular, because the PDE operators are applied to different interpolations. The zone boundary points must satisfy the PDE operators defined in the converging zone. This acts as a refinement of the interpolation stencil; in fact it increases the size of the local system. In some cases this extra cost is justified by a significant improvement in the interpolation, and it can avoid a refinement of the element mesh in the region nearby the zone boundary. This will be shown in the numerical tests presented in this chapter.

Although the cell centred discretisation scheme is adopted to present and test the proposed multi-domain formulation of the CV-HRBF method, the same approach can be applied without any restriction to the vertex centred scheme introduced in chapter 4. This is a direct consequence of the fact that the matching condition is applied to the RBF interpolations

associated with the mesh elements, and at this local level the CV-HRBF cell centred and vertex centred schemes differ only for the collocation strategy.

6.3 Numerical result

The multi-zone formulation of the CV-HRBF is validated in two steady state one-dimensional problems, for which an analytical solution is available. Two and three-dimensional steady state problems, characterised by high heterogeneity and for which only a numerical solution is possible are also presented to investigate the capabilities of the multi-domain CV-HRBF method in dealing with multi-dimensional geometries. Finally a test in a one-dimensional unsteady transport problem is reported as a preliminary result of an on-progress validation of the method for the study of more complex transport phenomena. In all the test cases a multiquadric RBF is used in the local interpolation, and the shape parameter values are specified for each problem. Unless stated otherwise, the multiple operator collocation strategy is used for those locations where the interface matching conditions are satisfied. Two different configurations of the local interpolation stencil are used for the steady and unsteady problems as previously explained in chapter 2 and 3.

6.3.1 One-dimensional heat transfer problem in a beam consisting of three piecewise homogeneous zones

A one-dimensional channel 6 metres long is divided in three sub-domains having same length, and in each of them a pure diffusion steady problem ($D^n \partial^2\phi^n/\partial x^2 = 0$) is imposed as the governing equation. The problem can be considered as a linear one-dimensional heat transfer problem in a beam composed of three sections made of a different material. Dirichlet boundary conditions are assigned at the two ends of the beam ($T(0)=2$, $T(6)=1$). The analytical solution inside each sub-domain is given by:

$$T^n = a^n + b^n x \tag{6.19}$$

Where the constants a^n and b^n can be determined by imposing the continuity of the temperature, $T^n = T^{n+1}$ and of the flux, $D^n \partial T^n/\partial x = D^{n+1} \partial T^{n+1}/\partial x$, across the sub-domain interfaces, and taking into account the boundary conditions.

The problem is solved numerically in a three-dimensional channel of dimensions [$6m$ X $0.5m$ X $0.5m$], and zero-flux conditions are imposed in the side boundaries to retain the one-

dimensionality of the solution. A structured computational grid with 60 cells in the longitudinal direction x and 5 cells in the transversal directions y and z is adopted in the numerical tests. Two sets of heat transfer coefficients were chosen for the validation of the numerical scheme

$$D^1 = 100 m^2/s \quad D^2 = 1 m^2/s \quad D^3 = 100 m^2/s \tag{6.20}$$

$$D^1 = 1 m^2/s \quad D^2 = 100 m^2/s \quad D^3 = 1 m^2/s \tag{6.21}$$

The CV-HRBF solutions, obtained by using a constant value to the multiquadric RBF shape parameter, c_S=1.0, are shown in Figure 6.4 for the two sets of coefficients (6.20) and (6.21).

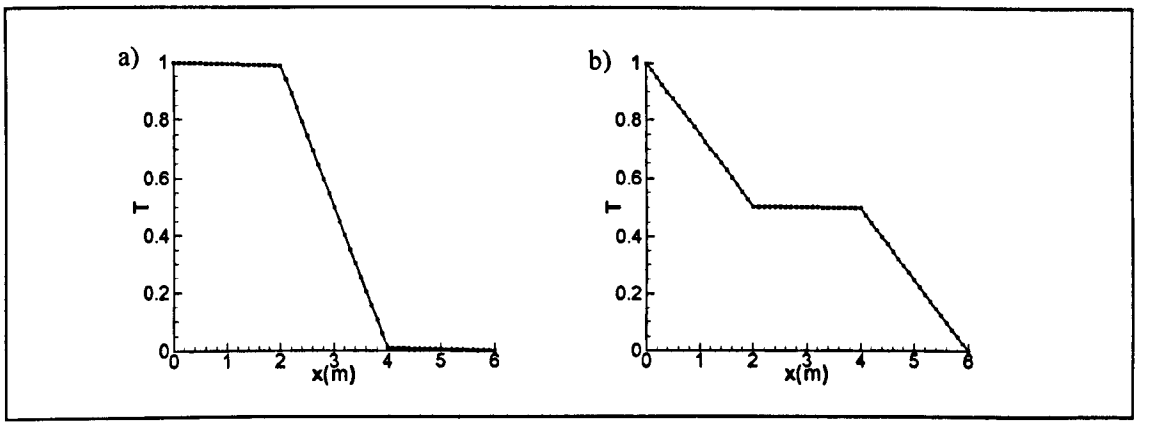

Figure 6.4 - Comparison between numerical and analytical solutions. Full line, numerical solutions; symbols, analytical solutions. a) – set of coefficients (6.20); b) - set of coefficients (6.21)

The numerical solutions show a very good agreement with the analytical ones, and this is confirmed from a very small L_{2error}: 4.89×10^{-5} in the case of (6.20) and 7.38×10^{-6} for (6.21)

The results shown above are obtained by applying the PDE operators in the same location of the matching conditions as explained in the section 6.2, Figure 6.3. It is interesting to observe the benefit of such collocation strategy, and for that reason another test is carried out, applying only the matching conditions to the points located in the zone boundary. The results are shown in Figure 6.5. The spurious oscillations for the set of diffusion coefficients (6.21) appear when reconstructing the solution in the mesh nodes close to the region nearby the sub-domain interfaces. It is clear that at least for this case the PDE operators applied to the matching points, despite returning a larger local system, significantly improve the local interpolation. Two alternatives were found to be effective to remove the error shown in Figure 6.5. Instead of using the multiple collocation technique, increase the size of the control volume stencil for the local interpolation including more data points (stencil S2-PDE, section 2.73), or refine the element mesh in proximity of the zone boundaries. Both approaches lead to a more demanding computational cost in the solution of the global system, in fact including more data points in the

interpolations adds non-zero entries to the global matrix, and refining the element mesh increases the size of the global matrix.

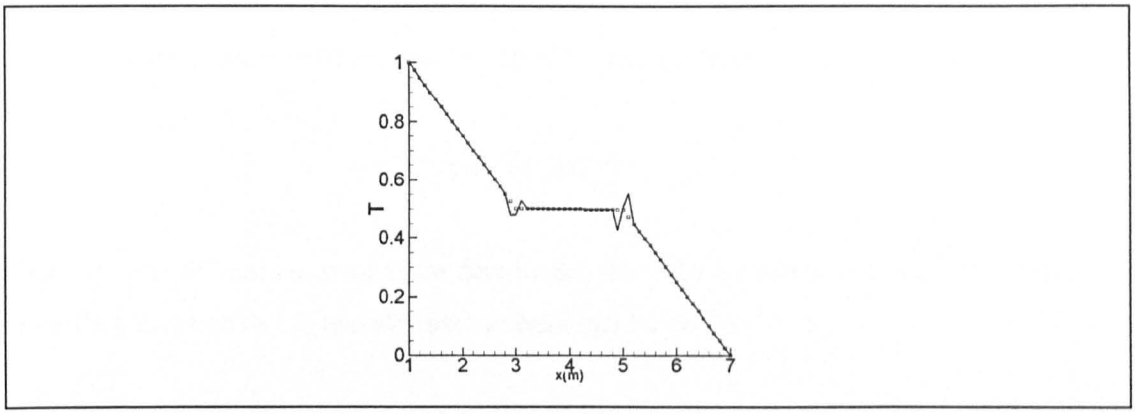

Figure 6.5 - Comparison between numerical and analytical solutions in the case of only matching conditions applied to the zone boundary points, set (6.12). Full line, numerical solutions; symbols, analytical solutions.

6.3.2 Heat transfer problem in a circular cylinder with a circular hollow

An infinite circular cylinder made of three rings characterised by constant but different properties is considered, Figure 6.6. In absence of an advection velocity and heat sources, the governing equation that drives the heat transfer inside each ring can be expressed in cylindrical coordinate coordinates as follows

$$\frac{D^n}{r}\frac{\partial}{\partial r}\left(r\frac{\partial T^n}{\partial r}\right)=0 \qquad n=1,3 \tag{6.22}$$

where D^n is the thermal conductivity in the ring n and r is the radial distance.

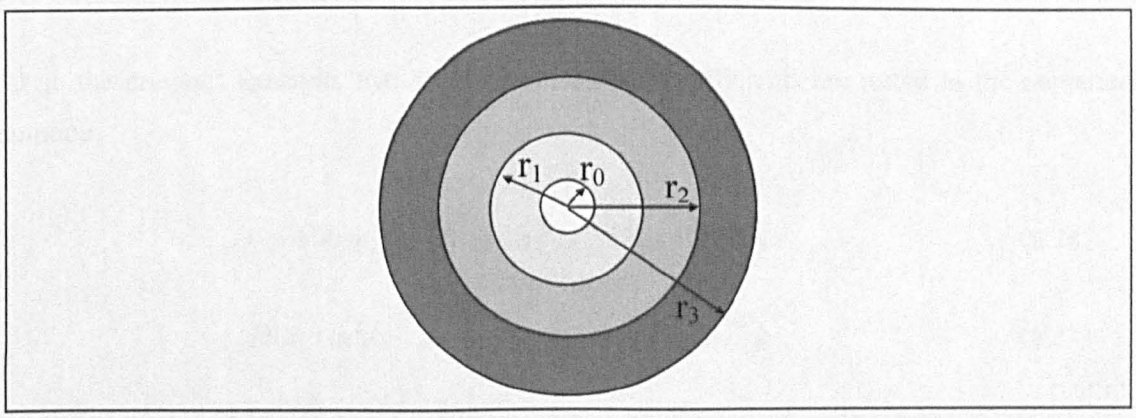

Figure 6.6 - Cylindrical domain consisting of three rings with different thermal properties, cross section.

Two different values of temperature are imposed in the inner and outer circular boundaries, $T^1(r_0)=1$ and $T^3(r_3)=2$, and continuity of flux and temperature are applied at the contact region between two rings ($T^n=T^{n+1}$, $D^n\,\partial T^n/\partial r = D^{n+1}\,\partial T^{n+1}/\partial r$ for $r=r^m$ with m=1,2). A general analytical solution of the equation (6.15) is expressed by Carslaw and Jaeger)

$$T^n = a^n + b^n ln(r) \tag{6.23}$$

where a^n and b^n are constant to be determined from the boundary and matching conditions. Expanding equation (6.22) two alternative forms can be derived

$$D^n \frac{\partial^2 T^n}{\partial r^2} + \frac{D^n}{r}\frac{\partial T^n}{\partial r} = 0 \tag{6.24}$$

$$D^n \frac{\partial^2 T^n}{\partial r^2} + \frac{\partial}{\partial r}\left(\frac{D^n}{r}T^n\right) + \frac{D^n}{r^2}T^n = 0 \tag{6.25}$$

Equations (6.25) describes a one-dimensional advection-diffusion problem with a variable reaction coefficient, D^n/r^2, and a negative advective velocity, $-D^n/r$. The discretisation process of this problem with the CV-HRBF method uses both forms (6.24) and (6.25): Equation (6.24) is more suitable for the local strong formulation, whilst equation (6.25) must be adopted in the control volume equation to apply the divergence theorem to the advection term. The problem is solved numerically in a three-dimensional channel whose geometry is defined by:

$r_0 \le x = r \le r_3$, with $r_0 = 1m$ and $r_3 = 7m$

$0 \le y \le 0.5m$, $0 \le z \le 0.5m$, $r_1 = 3m$ and $r_2 = 5m$

As in the previous example, two sets of heat transfer coefficients are tested in the numerical solution

$$D^1 = 100\,m^2/s \quad D^2 = 1\,m^2/s \quad D^3 = 100\,m^2/s \tag{6.26}$$

$$D^1 = 1\,m^2/s \quad D^2 = 100\,m^2/s \quad D^3 = 1\,m^2/s \tag{6.27}$$

The mesh used is fairly coarse and it features 61 cells in the x-direction, 20 each sub-domain and 5 cells in the y and z-directions, all uniformly distributed. The numerical solutions obtained

using a constant shape parameter, c_S = 1.0, are shown in Figure 6.7, where a good agreement with the analytical solutions can be observed. The corresponding values of the L_{2error}, 3.84×10^{-4} for the set of coefficients (6.26), and 6.18×10^{-3} for the set of coefficients (6.27), confirm the accuracy of the two solutions.

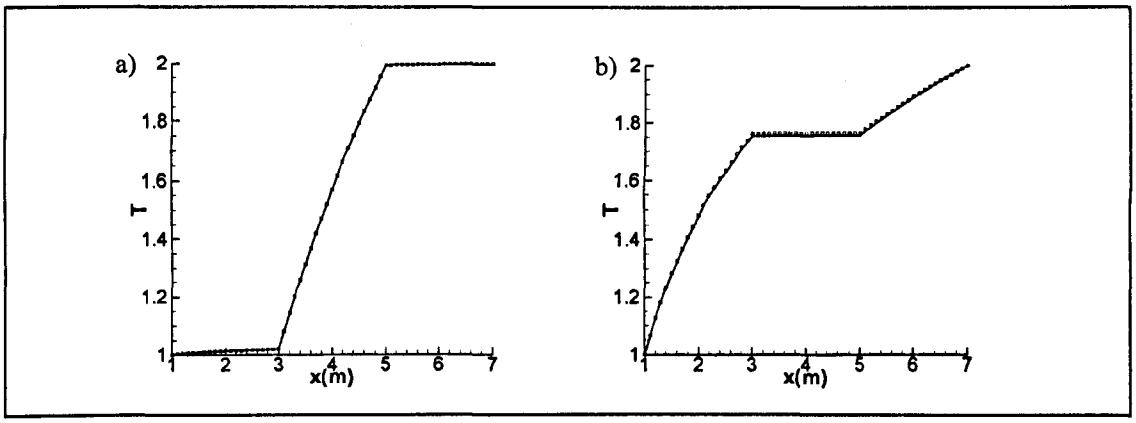

Figure 6.7 - Comparison between numerical and analytical solutions. Full line, numerical solutions; symbols, analytical solutions. a) – set of coefficients (6.26); b) - set of coefficients (6.27)

Having established the robustness of the CV-HRBF approach in dealing with multizone problems, by the comparison of the obtained solutions with the corresponding analytical ones in the previous two examples, in the next three cases more general problems without analytical solution are presented.

6.3.3 Two-dimensional heat transfer problem in a plate consisting of three piecewise homogeneous zones

The heat transfer in a rectangular two-dimensional plate consisting of three piecewise homogeneous materials is considered, Fig. 6.6.

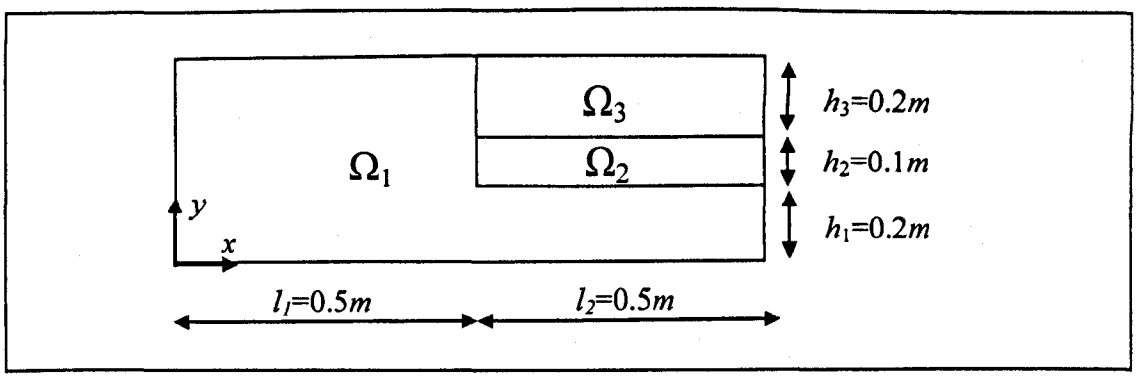

Figure 6.8 – Two dimensional heat transfer problems in a plate consisting of three piecewise homogeneous materials, geometry.

This numerical test presents a single point shared by more than two zones, and it is appropriate to validate the multiple matching condition of the CV-HRBF multi-domain formulation. The non-overlapping domain decomposition, follows the material topology of the plate. In each sub-domain the heat transfer equation is given by $D^n \partial^2\phi^n / \partial x_i^2 = 0$. The heat transfer coefficients of the material are taken to be $D^1 = 100\,m^2/s$, $D^2 = 1\,m^2/s$ and $D^3 = 10\,m^2/s$, and the problem definition is completed by imposing the following boundary conditions:

$$T = 2 \qquad x = 0m,\ \ 0m \le y \le 0.5m$$
$$T = 1 \qquad x = 1m,\ \ 0m \le y \le 0.5m$$
$$\frac{\partial T}{\partial n} = 0 \qquad y = 0m,\ \ y = 0.5m,\ \ 0m \le x \le 1m$$

The matching conditions are obtained by imposing the continuity of the temperature, $T^n = T^{n+1}$, and of the heat flux along the normal direction to the zone interface, $D^n \left(\partial T^n / \partial x_i\right) n_i^{Int} = D^{n+1} \left(\partial T^{n+1} / \partial x_i\right) n_i^{Int}$.

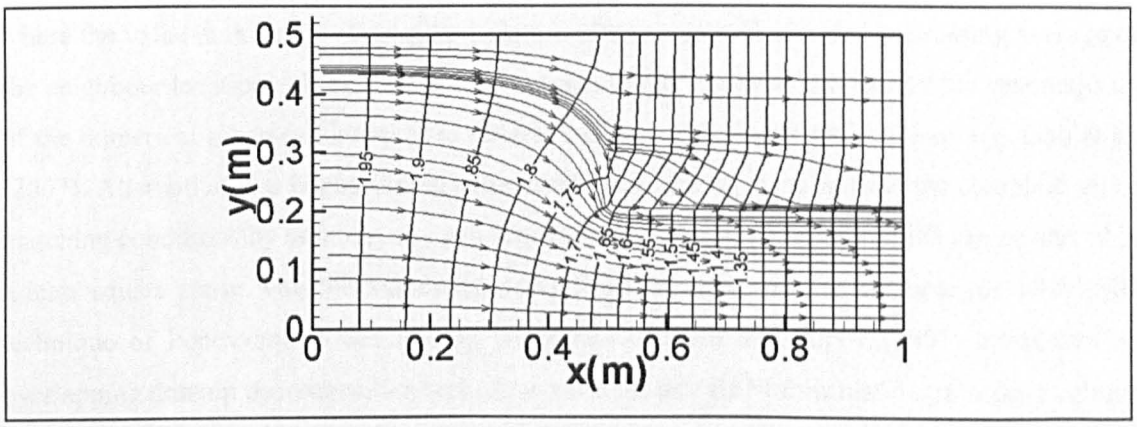

Figure 6.9 - Isothermal contours and heat flux lines in the plate.

Although the physical domain is a two-dimensional plate, the problem is solved numerically in a three-dimensional slice, $0.05m$ thick and imposing zero-flux conditions in the two side boundaries (z=$0m$ and z=$0.05m$). The mesh used to discretise the domain features 80 cells in the x-direction, 40 cells in the y-direction and 4 cells in the z-direction, all uniformly distributed. For this problem there is no analytical solution, and a convergence analysis was carried out to ensure that the results reported are mesh-independent. In Figure 6.9 the isothermal contours and the heat flux pathways show the thermal field obtained from the numerical solution using a constant shape parameter in the multiquadric RBF, $c_S = 0.05$.

In figures 6.8-a) and 6.8-b), cross profiles extracted at different locations in the domain are reported. In the point (x = 0.5, y = 0.3) where the three zones Ω_1, Ω_2 and Ω_3 converge the solution reconstructed by the use of the local RBF interpolation shows obvious gradient discontinuities.

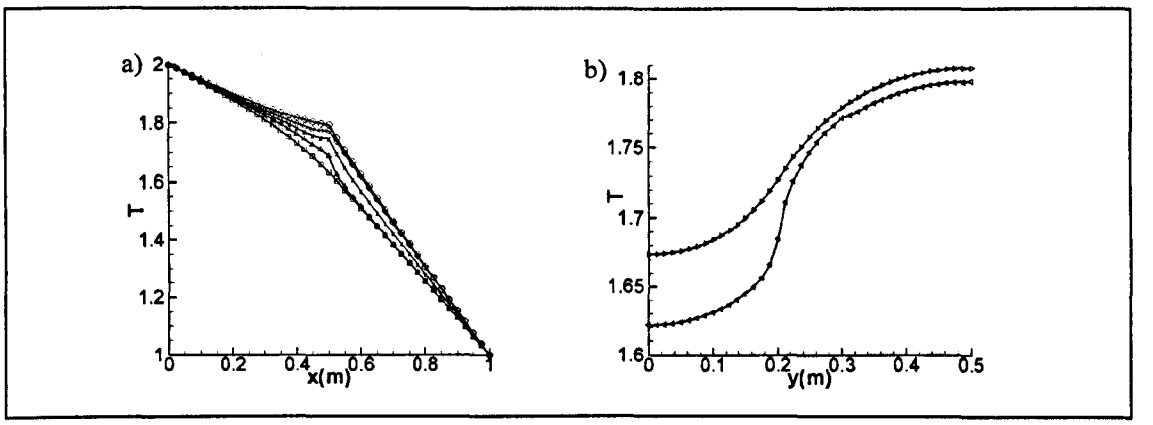

Figure 6.10 - Cross profiles. a) - profiles at constant y: square symbols, y=0.1; delta symbols, y=0.2; cross symbols, y=0.25; diamond symbols, y=0.3; round symbols, y=0.4. b) – profiles at constant x: right triangle symbols, x=0.45; left triangle symbols, x=0.5.

No artificial smoothing effects are introduced, as it happens in classical multi-zone approaches where the value in this type of singular points is often computed as a post-processing average of the neighbour location values. This kind of singular point is usually ignored by the vast majority of the numerical schemes that recur to several tricks to circumvent the problem, e.g. Gao et al. (2007). Alternatively, it is possible in some numerical techniques to impose the complete set of matching conditions by defining an over-determined system of equations which can be solved in a least square sense with the associated approximation error, see for example the DRM-MD technique of Popov and Power (1999). More recently Bui and Popov (2009) introduced an overlapping domain decomposition technique valid for any BEM formulation, in order to obtain a system of equations that is always closed.

6.3.4 Pumping into a confined aquifer in presence of a clay layer

The groundwater flow inside an aquifer characterised by different geological layers, is another engineering application for the multi-zone approach. The properties of the medium can vary drastically from one layer to another one (e.g. in presence of a sand or clay layer) and at the interface between the two, the hydraulic conductivity features a discontinuity. The natural domain partitioning for this type of problem consists of assigning a sub-domain to each geological layer. Inside which, the soil properties present a smooth variation. If only the saturated zone of the aquifer is taken into account, and only small scale problems are considered, the governing equation in each layer is taken directly from equation (5.4)

$$\frac{\partial}{\partial x_i}(K_{ij}^n \frac{\partial \phi^n}{\partial x_j}) + \Gamma = 0 \tag{6.28}$$

As explained in chapter 4, $\phi^n = z^n + p^n/\rho g$ is the piezometric head with z^n being the elevation, p^n the pressure, ρ the density of the fluid, g the gravity acceleration; $\left[K^n\right]$ is the hydraulic conductivity tensor, and Γ represents source points in the aquifer. Note that the superscribing n refers to the sub-domain n. Equation (6.28) differs from equation (6.1) only for the source term Γ, so considering $\partial \phi_i^n / \partial t = 0$, $U_i^n = 0$, $K_r = 0$ and taking the diffusion tensor equal to the hydraulic conductivity tensor, all the considerations reported in section 6.2 remain valid.

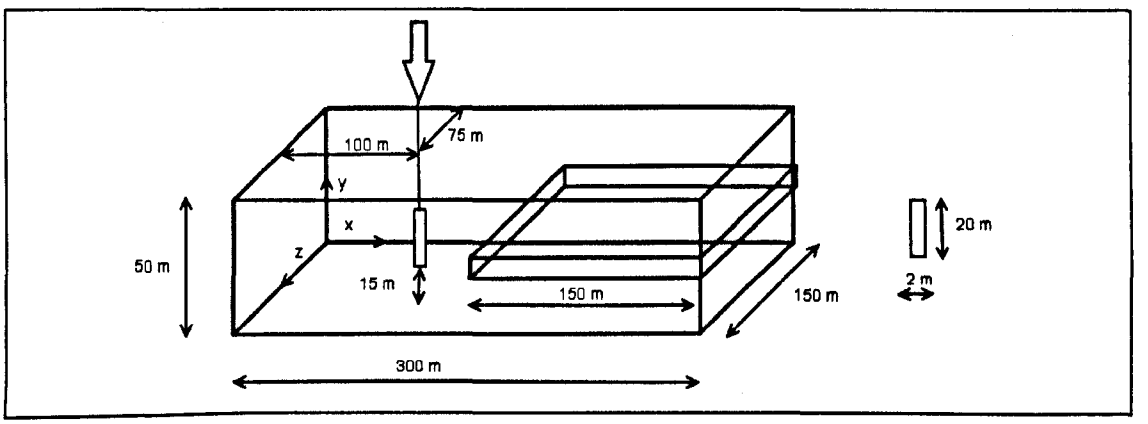

Figure 6.11 - Single Pump model geometry

A single pump injection into a confined aquifer that is characterised by geological layers with different soil properties is considered in this test problem. A well screen is placed in a portion of a confined aquifer 300 meters long and 150 meters wide, and a clay layer 10 metres thick is situated opposite the pump, 15 metres from the bottom of the aquifer, Figure 6.11. Only the active part of the screen well is modelled. The conductivity of the clay layer is considered to be homogeneous and isotropic, while the surrounding medium is assigned an anisotropic conductivity constant in space, Table 6.1.

Zone	Conductivity Tensor
Aquifer	$K_x^1 = K_z^1 = 1.0 m/h \;\; K_y^1 = 0.3 m/h$
Clay Layer	$K_x^2 = K_y^2 = K_z^2 = 0.01 m/h$

Table 6.1 - Single Pump model, Soil properties

The pumping rate is 50 m^3/h, and the well is modelled as an array of eight point sources, with each point being a segment of the well $2.5m$ long. A constant piezometric head of 50 meters is

imposed in the side boundaries, and no flux is allowed in the bottom and top surfaces of the confined aquifer.

Boundary position	Boundary condition equation
$x = 0m, x = 300m, z = 0m, z = 150m$	$\phi = 50m$
$y = 0m, y = 50m$	$\partial\phi/\partial n = 0$

Table 6.2 - Single pump model, Boundary conditions

The matching conditions are given by

$$\phi^n = \phi^{n+1}$$

$$n_i^{Int} K_{ij}^n \frac{\partial \phi^n}{\partial x_j} = n_i^{Int} K_{ij}^{n+1} \frac{\partial \phi^{n+1}}{\partial x_j}$$

About 58000 hexahedral cells are used to discretise the problem, and the computational grid is made of 20, uniformly distributed layers. A slight refinement is present around the well to capture the high gradient expected in the vicinity of the injection points, Figure 6.12.

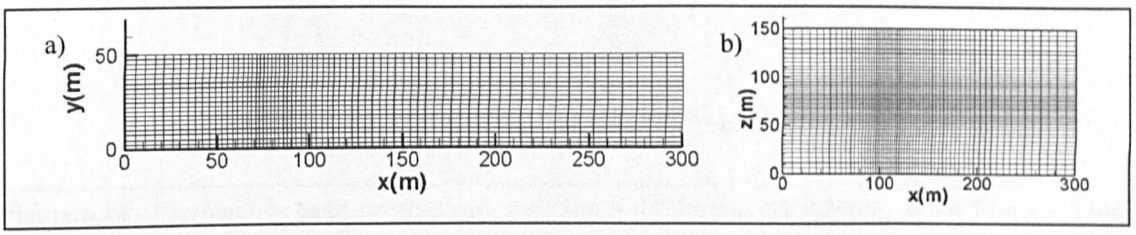

Figure 6.12 - Single Pump model mesh: a) lateral longitudinal view, b) top view

As in the previous test case, no analytical solution can be found for this problem. Therefore, the validation of the solution was carried out by refining the mesh until the point where no significant changes were observed in the numerical results. After this analysis, the mesh shown in Figure 6.12 was found to be fine enough to obtain a converged solution. A variable shape parameter (see section 2.6), $c_S^* = 1.0$, is used in this simulation to take account of the non uniform distribution of the cell. The piezometric head contours and the flow path obtained from the numerical solution are shown for two cross sections at $z = 75$m and $y = 25$m, Figure 6.13. From the vertical section, $z = 75m$, it can be observed that most of the water flows around the clay layer as expected, whereas in the horizontal section, $y = 25m$, it is interesting to notice the path modifications for the part of the flow that infiltrates into the clay layer. Finally, two piezometric head profiles extracted from the cross section at $z = 25m$ are reported in Figure 6.14 to show more in detail the discontinuities that occur across the clay layer interface.

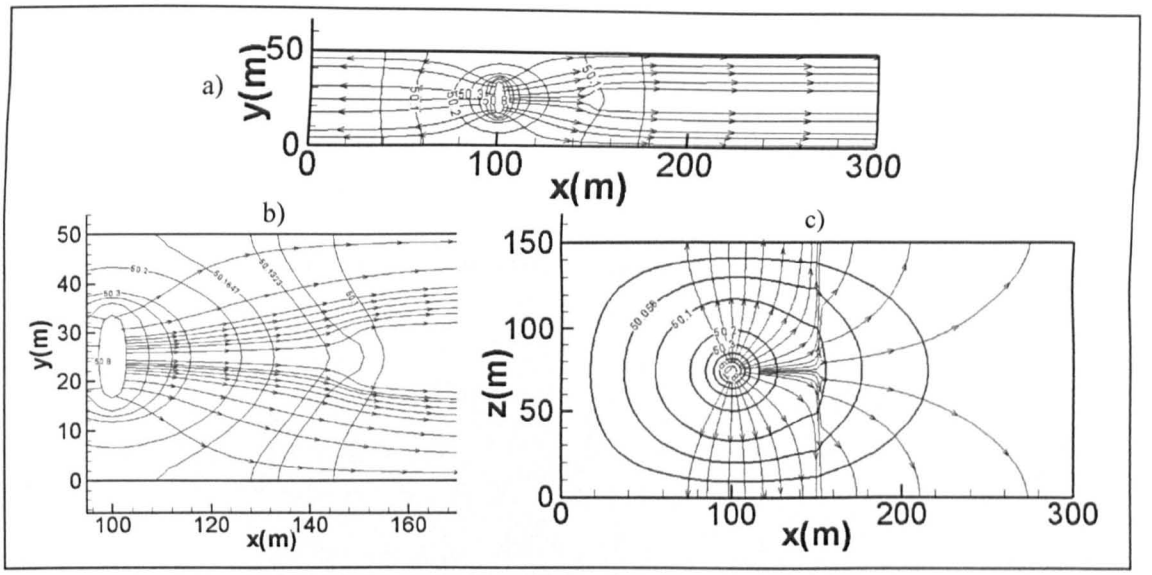

Figure 6.13 - Piezometric head contours and flow path: a) $z = 75m$, entire domain; b) $z = 75m$, zoom in the region nearby the well; c) $y = 25m$.

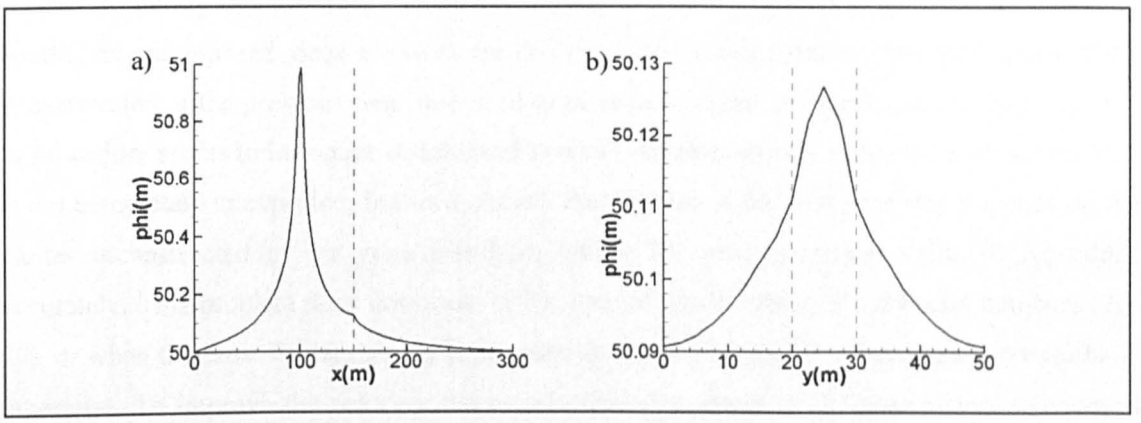

Figure 6.14 - Piezometric head profiles : a) $z = 75m$, $y = 25m$, $0m \leq x \leq 300m$, b) $z = 75m$ $x = 150m$, $0m \leq y \leq 50m$

6.3.5 One-dimensional unsteady transport problem in a channel consisting of two zones featuring different Peclet number

A one-dimensional transport problem for a single species c in a channel consisting of two adjacent zones is considered in this section. The governing equation inside each sub-domain can be formulated in dimensionless parameters as

$$\frac{\partial c^n}{\partial t} + \frac{\partial c^n}{\partial x} = \frac{1}{Pe^n} \frac{\partial^2 c^n}{\partial x^2} \tag{6.29}$$

where Pe^n is the Péclet number for the zone n. The two sub-domains are taken to be of the same length, $\ell = 0.5$, and the following initial and boundary conditions are imposed

$$c^1(x,0)=1 \qquad 0\le x\le \ell$$
$$c^2(x,0)=1 \qquad 0\le x\le 2\ell$$
$$c^1(0,t)=2 \qquad c^2(2\ell,t)=1$$

whereas the matching condition the zone interface, at $x=\ell$, can be expressed as follows

$$c^n = c^{n+1}$$
$$\frac{1}{Pe^n}\frac{\partial c^n}{\partial x} = \frac{1}{Pe^{n+1}}\frac{\partial c^{n+1}}{\partial x}$$

with $n = 1$ for this simple case where only two sub-domains are considered.

It is worth noting that applying the left and right PDEs in the same points where the matching conditions are imposed, does not work for this test case. In this circumstance, the values of the concentration at the previous time step need to be reconstructed in such locations, and this kind of procedure seems to introduce instabilities that can develop quickly as the time advances. This is not completely unexpected; in this approach the solution at the new time step depends on the values reconstructed at the zone interface, which are always critical value to reproduce accurately. This problem does not occur in the case of small values of the Peclet numbers (20-30), or when the same Peclet number is imposed in the two zones, but it becomes uncontrollable otherwise. To improve the solution and avoid dispersive errors of the type of those shown in Figure 6.5, larger stencil of cells are considered to form the local interpolations in proximity of the zone interface. As explained in section 6.3.1 this approach leads to a global matrix with larger number of non-zero entries, although when only the interpolations close to the zone interfaces are enlarged, the extra computational cost in the solution of the global system is contained.

No analytical solution can be found for the present problem, and the accuracy of the solution is estimated using the global residual (3.26). The numerical solution is computed in a three-dimensional mesh of size $[2,5\Delta x,5\Delta x]$ where Δx, equal to 0.0125, is the discretisation increment in the x direction and zero flux conditions are applied to the lateral boundaries to retain the one-dimensionality of the problem. Two pairs of Péclet number are tested, (6.31) and (6.32), and their values are chosen by fixing the first value at 10 and increasing the other until the point at which the numerical solution becomes unstable for the mesh described above. The two pairs chosen are reported below

$$Pe^1 = 100 \quad Pe^2 = 10 \tag{6.30}$$

$$Pe^1 = 10 \quad Pe^2 = 500 \tag{6.31}$$

In both cases the time step is taken to be equal to 0.001, and a constant shape parameter equal to 0.03 is chosen. The solutions and their residuals at the instant $t = 0.3$, $t = 0.5$, $t = 0.7$ and $t = 1.0$, for the two pairs of Peclet number (6.30) and (6.31) are reported in Figure 6.1 and Figure 6.16 respectively.

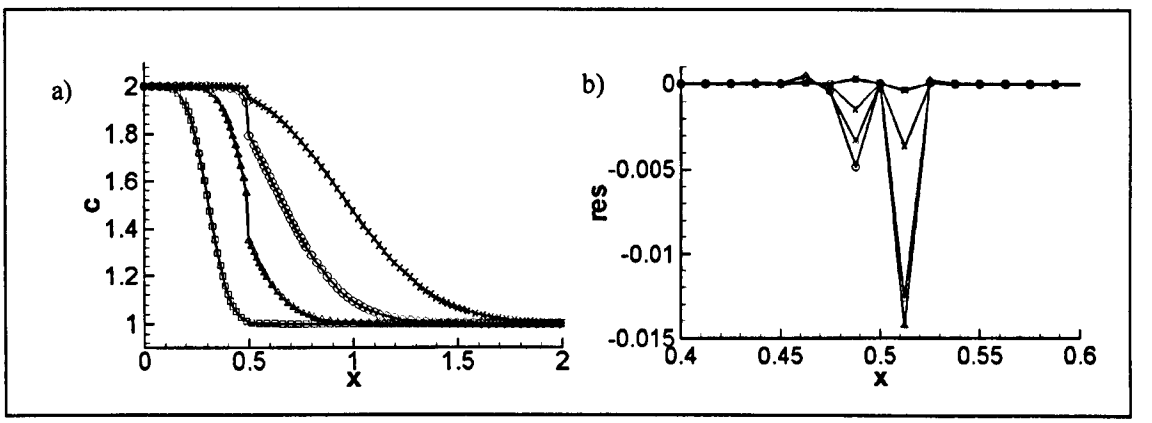

Figure 6.15 - Péclet number pair (6.30). a), CV-HRBF solution; b), Residual, zoom in the interface region. Square symbols, *t*=0.3; Delta symbols, *t*=0.5; Round symbols, *t*=0.7; Cross symbols, *t*=1.0

The Péclet number limit for the upstream region is five times smaller than that one achievable for the downstream zone. Having a higher advection in the upstream region causes a very large gradient in the upstream side of zone interface, Figure 6.15-a), requiring an extra refinement of the mesh in this area. In fact the solution forms an advective front under the high Péclet number conditions of the upstream zone, and a diffusive front in the low Péclet zone. The discontinuity itself acts as a barrier to the propagation of the advective front.

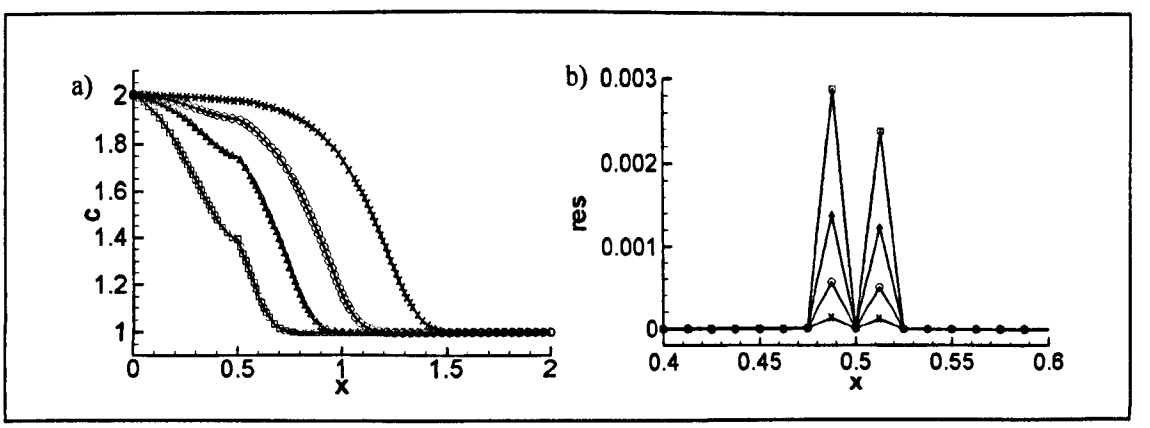

Figure 6.16 - Péclet number pair (6.31). a), CV-HRBF solution; b), Residual, zoom in the interface region. Square symbols, *t*=0.3; Delta symbols, *t*=0.5; Round symbols, *t*=0.7; Cross symbols, *t*=1.0

In both cases, the residuals grow around the zone interface, Figure 6.15-b) and Figure 6.16-b), although their values are small, and the solution could be improved by using a non-uniform mesh denser at the zone boundary. The value of the residual is not computed in the zone boundary, $x = \ell$, in fact in this location neither the left nor the right PDE operators are defined, and an estimation of their numerical residual would not add any useful indication to the accuracy of the solution. Note that in Figure 6.15-b) and Figure 6.16-b) the residual is equal to zero; this is only a post-processing flag used for points of the domain where the residual is not computed.

6.4 Conclusion

In this chapter, a non-overlapping non-iterative multi-domain formulation for the CV-HRBF scheme has been presented. The method exploits the robustness of the Hermite interpolation to satisfy locally physical matching conditions, i.e. imposing the continuity of the function and flux at the sub-domain interface. A double collocation technique has been implemented to impose the two conditions in the same set of points as done in Hernandez and Power (2007). In addition the Hermite interpolation is exploited even further to apply multiple flux continuities for those cases where more than two sub-domains converge in the same point.

The robustness of the CV-HRBF approach in dealing with multizone problems, has been assessed using one-dimensional advection-diffusion problems for which an analytical solution is known. The solution of more general two and three-dimensional engineering problems has also shown the capability of the method to capture the C^1 discontinuities at the zone boundary that feature abrupt variations of the material properties. This has been possible also in those points where more that two sub-domains converge due to the multiple flux condition that can be applied with the CV-HRBF discretisation.

7 CONCLUSION

7.1 Summary and conclusion

A new numerical scheme has been developed, with the main objective being to exploit the possible advantages of coupling the meshless RBF collocation approach and the CV methods. The proposed method can be considered meshless only at the local level of the interpolation stencils, where an auxiliary initial/boundary value problem is solved for every cell, in order to define the cell shape functions from which the evaluation of the flux across the cell faces is obtained. This circumstance increases the accuracy of the flux computation, whilst providing an analytical upwind scheme, as the local interpolation satisfies the PDE operator and therefore contains information about the physics of the problem. In the hybrid control volume/meshless method proposed in this thesis, approximate solutions of the governing equation based on RBF collocation approaches are used as interpolation functions to improve the performance of a CV method for the first time.

The method has been tested in a number of boundary value problems, for which an analytical solution is known, by testing different RBF collocation approaches, i.e. both the Kansas's (KRBF, unsymmetric) and Hermitian's (HRBF, symmetric) techniques. Having found the same level of accuracy between the CV-KRBF and CV-HRBF the second is preferred due to its robustness and the possibility of applying more than one linearly independent operators in the same location (e.g. 'double collocation technique').

A transient formulation of the CV-HRBF has been successively developed, in order to investigate the capability of the technique in the solution of reactive transport problems. The validation shows that the implicit upwinding intrinsic to the method leads to significant improvements in the stabilisation of the numerical solution, in particular in those cases where advection is dominant. In addition to the fully implicit time stepping scheme, the weighted Crank-Nicholson scheme has been tested, obtaining significant improvements in some of the problems considered.

The main CV-HRBF idea of having flux reconstruction functions that locally satisfy the governing equation has also been applied in the case of weakly non-linear problems. The fully

kinetic formulation presented in chapter 3 for the solution of multispecies reactive transport problems is an example of how the non-linearity can be handled at local level.

Although the CV-HRBF method it is independent from cell shape and mesh type, the use of unstructured meshes leads to a loss of accuracy (up to one order of magnitude in the experiments reported in this thesis). To improve the convergence of the CV-HRBF for unstructured meshes a *second order* integration scheme and the vertex centred (VC) discretisation have been implemented and tested in chapter 4. The *numerical solutions of one* and three-dimensional advection diffusion problems suggested that both approaches lead to good improvements, and that the VC is strongly recommended when the mass conservation is a crucial parameter of the problem being solved.

The CV-HRBF has been used to model the saturated zone of the unconfined aquifer, showing the capabilities of the method in dealing with porous media flows. A mesh adapting algorithm, which performs a local re-meshing as the phreatic surface moves in a vertical direction, has been presented. It has been found that the local meshless character of the CV-HRBF introduces several flexibilities in the groundwater numerical modelling. In fact using this numerical approach, the dynamic boundary condition can be applied in an arbitrary number of points on the phreatic surface, independently from the mesh element.

Finally a non-overlapping non-iterative multi-domain formulation for the CV-HRBF scheme has been presented in chapter 6. The method exploits the robustness of the Hermite interpolation to satisfy locally physical matching conditions, i.e. imposing the continuity of the function and flux at the sub-domain interface. A double collocation technique has been implemented to impose the two conditions in the same set of points. In addition, the Hermite interpolation is exploited even further to apply multiple flux continuities for cases where more than two sub-domains converge in the same point. The robustness of the CV-HRBF approach in dealing with multizone problems has been assessed using one-dimensional advection-diffusion problems for which an analytical solution is known. The solution of more general two and three-dimensional engineering problems has also shown the capability of the method to capture the C^1 discontinuities at the zone boundary that feature abrupt variations of the material properties. This characteristic is preserved in those points where more that two sub-domains converge, due to the multiple flux condition that can be applied with the CV-HRBF discretisation.

The flexibility and the accuracy gained by using a RBF meshless collocation method in the control volume reconstruction step, have been shown from a theoretical point of view, as well as in a number of numerical examples. The results reported in this thesis encourage the authors to

progress with development of the proposed approach, in particular when dealing with advective dominant problems and complex boundary conditions.

7.2 Future work

In this thesis the CV-HRBF has been used to solve a one-dimensional multispecies reactive transport problem. Work to enhance the capabilities of the software to handle multidimensional problem and the dispersivity terms is ongoing. The author expects to present the solution to more complex problems in the near future.

Although in this work only quasi-linear problems have been considered, the technique can be applied in principle to more complex applications characterised by high non-linearity such as the Navier-Stokes system of equations, i.e. viscous flow problems. The task of obtaining a local approximation that satisfies the Navier-Stokes equations within the interpolation, is a topic of ongoing research by several groups. In particular, it is not clear how the non-linearity is to be considered at the local level. From previous experience, it is expected that a robust non-linear solver needs to be implemented at the global level, but most likely a simple Picard iteration can be used at the local level. Further research is needed to understand if using a local interpolation that satisfies the governing equation can reduce the overall number of non-linear iteration, and if so, by how much.

Bibliography

Abgrall R. (1994): On essentially Non-Oscillatory Schemes on Unstructured Meshes: Analysis and Implementation, *Journal of Computational Physics,* **114**, 45-98.

Ahmed S. (2005): Mathematical Formulation and Validation of a Mixed Finite Element-Finite Difference Model for simulating Phreatic surface *Journal of Hydraulic Engineering,* **131**(12), 1098-1105.

Azaroual M.; Kerve3van C.; Durance M. V.; Brochot S.; Durst P. (2003). *SCALE2000 user's manual.* BRGM. Orle'ans, France: 57.

Baliga B. R.; Patankar S. V. (1980): A new finite-element formulation for convection-diffusion problems, *Numerical Heat Transfer,* **3**, 393-409.

Bear J. (1987). *Modeling Groundwater Flow and Pollution.* Dordercht, Reidel.

Ben Salah M.; Askri F.; Ben Nasrallah S. (2005): Unstructured Control-Volume Finite-Element Method for Radiative Heat Transfer in a Complex 2-D Geometry, *Numerical Heat Transfer, Part B: Fundamentals,* **48**(5), 459-475.

Brown D. (2005): On Approximate Cardinal Preconditioning Methods for Solving PDEs with Radial Basis Functions, *Engineering Analysis with Boundary Elements,* **29**(4), 343-353.

Bui T. T.; Popov V. (2009): Domain decomposition boundary element method with overlapping sub-domains, *Engineering Analysis with Boundary Elements,* **33**(4), 456-466.

Cai Z.; Jones J. E.; McCormick S. F.; Russell T. F. (1997): Control-volume mixed finite element methods, *Computers & Geosciences,* **1**, 289-315.

Carlson R. E.; Foley T. A. (1991): The parameter R2 in multiquadric interpolation, *Computers & Mathematics with applications,* **21**(9), 29-42.

Carslaw H. S.; Jaeger J. C. (1959). *Conduction of Heat in Solids.* Oxford, Oxford University Press.

Cautres R.; Herbin R.; Hubert F. (2004): The Lions domain decomposition algorithm on non-matching cell-centred finite volume meshes, *IMA journal of numerical analysis,* **24**(3), 465-490.

Cecil T.; Qian J.; Osher S. (2004): Numerical methods for high dimensional Hamilton-Jacobi equations using radial basis functions, *Journal of Computational Physics,* **196**, 327-347.

Chilakapati A. (1995).

Date A. W. (2005): Solution of transport equations on unstructured meshes with cell-centered colocated variables. Part I: Discretization, *International Journal of Heat and Mass Transfer,* **48**, 1117-1127.

Dubal M. R.; Olivera S. R.; Matzner R. A. (1993). *Approaches to Numerical Relativity.* Cambridge UK, Cambridge University Press.

Dumbser M.; Kaser M. (2007): Arbitrary high order non-oscillatory finite volume schemes on unstructured meshes for linear hyperbolic systems, *Journal of Computational Physics,* **211**, 693-723.

Faille I.; Nataf F.; Saas L.; Willien F. (2004). Finite volume methods on non-matching grids with arbitrary interface conditions and highly heterogeneous media. *Domain Decomposition Methods in Science and Engineering Series.* **40**.

Fasshauer G. E. (1997). Solving partial differential equations by collocation with radial basis functions. *Surface Fitting and Multiresolution Methods.* A. Lé Mehauté, C. Rabut and L. L. Shumaker, University Press: 131-138.

Fedoseyev A. I.; Friedmann M. J.; Kansa E. J. (2002): Improved multiquadratic method for elliptic partial differential equation via PDE collocation on the boundary, *Computers & Mathematics with Applications,* **43**, 439-455.

Florez W. F.; Power H.; Chejne F. (2000): Conservative interpolation for the boundary integral solution of the Navier–Stokes equations, *Computational Mechanics,* **26**(6), 507-513.

Fornberg B.; Flyer N. (2005): Accuracy of radial basis function interpolation and derivative approximations on 1-D infinite grids, *Advances in Computational Mathematics,* **23**(1), 5-20.

Franke C.; Schaback R. (1998): Convergence order estimates of meshless collocation methods using radial basis functions, *Advances in Computational Mathematics,* **8**, 381-399.

Gao X.-W.; Guo L.; Zhang C. (2007): Three-step multi-domain BEM solver for nonhomogeneous material problems, *Engineering Analysis with Boundary Elements,* **31**(12), 965-973.

Grissa H.; Askri F.; Ben Salah M.; Ben Nasrallah S. (2007): Three-dimensional radiative transfer modeling using the control volume finite element method, *Journal of Quantitative Spectroscopy and Radiative Transfer,* **105**(3), 388-404.

Hardy R. L. (1971): Multiquadric Equations of Topography and Other Irregular Surfaces, *J. Geophys. Res.,* **76**.

Henk H.; Vic K.; Wim L. (2001): Selecting MODFLOW Cell Sizes for Accurate Flow Fields, *Ground Water,* **39**(6), 931-938.

Hernandez Rosales A.; Power H. (2007): Non-overlapping domain decomposition algorithm for the Hermite radial basis function meshless collocation approach: applications to convection diffusion problems, *Journal of Algorithms and Technology,* **(preprint)**.

Hirt C. W.; Amsden A. A.; Cook J. L. (1972): An Arbitrary Lagrangian-Eulerian Computing Method for All Flow Speeds, *Journal of Computational Physics,* **14**, 227-253.

Hirt C. W.; Nichols B. D. (1981): Volume of fluid (VOF) method for the dynamics of free boundaries, *Journal of Computational Physics,* **39**, 201-225.

Holger W. (2005): On the Convergence of a General Class of Finite Volume Methods, *SIAM J. Numer. Anal.,* **43**(3), 987-1002.

Hon Y. C.; Mao X. Z. (1998): An efficient numerical scheme for Burgers' equation, *Applied Mathematics and Computation,* **95**(1), 37-50.

Huebner K. (1975). *The Finite Element Method for Engineers*, John Wiley & Sons.

Iske A.; Sonar T. (1996): On the structure of function spaces in optimal recovery of point functionals for ENO-schemes by radial basis functions, *Numerische Mathematik,* **74**(2), 177-201.

Jayantha P. A.; Turner I. W. (2003): A second order finite volume technique for simulating transport in anisotropic media, *International Journal of Numerical Methods for Heat & Fluid Flow,* **13**(1), 31-56.

Jayantha P. A.; Turner I. W. (2005): A Second Order Control-Volume Finite-Element Least-Squares Strategy For Simulating Diffusion In Strongly Anisotropic Media, *Journal of Computational Mathematics,* **23**(1), 1-16.

Jiang G.-S.; Shu C.-W. (1996): Efficient Implementation of Weighted ENO Schemes, *Journal of Computational Physics,* **126**(1), 202-228.

Jichun L.; Chen C. S. (2003): Some observations on unsymmetric radial basis function collocation methods for convection-diffusion problems, *International Journal for Numerical Methods in Engineering,* **57**(8), 1085-1094.

Jinglian J. L.; Bharat K. S. (1998): 2D Groundwater Contaminant Transport Modeling by using the Finite Volume Method on an Unstructured Grid System, *Applied Mathematics and Computation,* **89**(1-3), 199-211.

Jumarhon B.; Amini S.; Chen K. (2000): The Hermite collocation method using radial basis functions, *Engineering Analysis with Boundary Elements,* **24**(7-8), 607-611.

Kansa E. J.; Hon Y. C. (2000): Circumventing the Ill-Conditioning Problem with Multiquadric Radial Basis Functions: Applications to Elliptic Partial Differential Equations, *Computers & Mathematics with applications,* **39**, 123-137.

KEE R. J.; PETZOLD L. R.; SMOOKE M. D.; GRCAR J. F. (1985). Implicit methods in combustion and chemical kinetics modeling. *Multiple Time Scales*. J. U. Brackbill and B. I. Cohen. New York, Academic Press: 113-144.

Kurganov A.; Lin C.-T. (2007): On the Reduction of Numerical Dissipation in Central-Upwind Schemes, *Communications in Computational Physics,* **2**(1), 141-163.

La Rocca A.; Hernandez Rosales A.; Power H. (2005): Radial basis function Hermite collocation approach for the solution of time dependent convection-diffusion problems, *Engineering Analysis with Boundary Elements,* **29**(4), 359-370.

La Rocca A.; Power H. (2008): A double boundary collocation Hermitian approach for the solution of steady state convection-diffusion problems, *Comput. Math. Appl.,* **55**(9), 1950-1960.

Lee C.; Liu X.; Fan S. (2003): Local multiquadric approximation for solving boundary value problems, *Computational Mechanics,* **30**, 396-409.

Ling L.; Hon Y. C. (2005): Improved numerical solver for Kansa's method based on affine space decomposition, *Engineering Analysis with Boundary Elements,* **29**(12), 1077-1085.

Ling L.; Opfer R.; Schaback R. (2006): Results on meshless collocation techniques, *Engineering Analysis with Boundary Elements,* **30**(4), 247-253.

Liu F.; Anh V.; Turner I.; Bajracharya K.; Huxley W. J.; Su N. (2005): A finite volume model for saturated-unsaturated flow and application to Gooburrum, Bundaberg, Queensland, Australia, *Applied Mathematical Modelling,* **30**, 352-366.

Liu F.; Turner I.; Anh V.; Su N. (2003): A two-dimensional finite volume method for transient simulation of time- and scale-dependent transport in heterogeneous aquifer systems, *The Korean Journal of Computational & Applied Mathematics,* **11**(1-2), 215-241.

Liu F.; Turner I. W.; Anh V. (2002): An unstructured mesh finite volume method for modelling saltwater intrusion into costal aquifers, *Journal of Applied Mathematics & Computing,* **9**, 391-407.

Liu Y.; Vinokur M.; Wang Z. J. (2006): Spectral (finite) volume method for conservation laws on unstructured grids V: Extension to three-dimensional systems, *Journal of Computational Physics,* **212**(2), 454-472.

Liu Y.; Vinokur M.; Wang Z. J. (2006): Spectral difference method for unstructured grids I: Basic formulation, *Journal of Computational Physics,* **216**(2), 780-801.

Lo D. C.; Young D. L. (2003): Arbitrary Lagrangian-Eulerian finite element analysis of free surface flow using a velocity-vorticity formulation, *Journal of Computational Physics,* **195**, 175-201.

Madych W. R. (1992): Miscellaneous error bounds for multiquadric and related interpolators, *Computers & Mathematics with applications,* **24**(12), 121-138.

Madych W. R.; Nelson S. A. (1990): Multivariate Interpolation and Conditionally Positive Definite Functions. II, *Mathematics of Computation,* **54**, 211-230.

Manzini G.; Putti M. (2007): Mesh locking effects in the finite volume solution of 2-D anisotropic diffusion equations, *Journal of Computational Physics,* **220**, 751-771.

May-Duy A. N.; Tran-Cong T.; Tanner R. I. (2006): New High-order Time-kernel BIEM for the Burgers Equation, *CMES: Computer Modeling in Engineering and Sciences,* **16**, 177-186.

Mayer S.; Garapon A.; Sorensen S. (1998): A fractional step method for unsteady free-surface flow with applications to non-linear wave dynamics, *International Journal for Numerical Methods in Fluids,* **28**, 293-315.

Micchelli C. A. (1986): Interpolation of scattered data: Distance matrices and conditionally positive definite functions, *Constructive Approximation,* **2**(1), 11-22.

Moroney T. J.; Turner I. W. (2006): A finite volume method based on radial basis functions for two-dimensional nonlinear diffusion equations, *Applied Mathematical Modelling,* **30**(10), 1118-1133.

Moroney T. J.; Turner I. W. (2007): A three-dimensional finite volume method based on radial basis functions for the accurate computational modelling of nonlinear diffusion equations, *Journal of Computational Physics,* **225**(2), 1409-1426.

Nessyahu H.; Tadmor E. (1990): Non-oscillatory central differencing for hyperbolic conservation laws, *Journal of Computational Physics,* **87**(2), 408-463.

Nguyen-Van H.; Mai Duy N.; Tran-Cong T. (2007): A simple and accurate four-node quadrilateral element using stabilized nodal integration for laminated plates, *CMC: Computers, Materials and Continua,* **6**, 159-176.

Ollivier-Gooch C.; Van Altena M. (2002): A High-Order-Accurate Unstructured Mesh Finite-Volume Scheme for the Advection-Diffusion Equation, *Journal of Computational Physics,* **181**, 729-752

Orsini P.; Power H.; Lees M.; Morvan H. (2009): A Control Volume Radial Basis Function Techniques for the Numerical Simulation of Saturated Flows in Semi-confined Aquifer, *Transport in Porous Media,* **79**(2), 171-196.

Orsini P.; Power H.; Lees M.; Morvan H. (2009). Improving the convergence of the Hermite CVRBF method for unstructured meshes. *Advances on the Meshless Local Petrov-Galerkin (MLPG) Method (To appear)*. S. N. Atluri.

Orsini P.; Power H.; Morvan H. (2008): Improving Volume Element Method by Meshless Radial Basis Function, *CMES: Computer Modeling in Engineering and Sciences,* **23**(3), 187-207.

Orsini P.; Power H.; Morvan H.; Lees M. (2009): An implicit upwinding volume element method based on meshless radial basis function techniques for modelling transport phenomena, *International Journal for Numerical Methods in Engineering.*

Paniconi C.; Putti M. (1994): A comparison of Picard and Newton iteration in the numerical solution of multidimensional variably saturated flow problems, *Water resources research,* **30**(12), 3357-3374.

Popov V.; Power H. (1999): The DRM-MD integral equation method: an efficient approach for the numerical solution of domain dominant problems, *International Journal for Numerical Methods in Engineering,* **44**(3), 327-353.

Powell M. J. D. (1994): The uniform convergence of thin plate spline interpolation in two dimensions, *Numerische Mathematik,* **68**, 107-128.

Power H.; Barraco V. (2002): A comparison analysis between unsymmetric and symmetric radial basis function collocation methods for the numerical solution of partial differential equations, *Computers and Mathematics with Application,* **43**, 551-583.

Quarteroni A.; Valli A. (1999). *Domain decomposition methods for partial differential equations*. Oxford, Oxford University Press.

Rippa S. (1999): An algorithm for selecting a good value for the parameter c in radial basis function interpolation, *Advances in Computational Mathematics,* **11**(2), 193-210.

Rousse D. R. (2000): Numerical predictions of two-dimensional conduction, convection, and radiation heat transfer. I. Formulation, *International Journal of Thermal Sciences,* **39**(3), 315-331.

Saad Y. (1988-2000). "SPARSKIT: A basic tool-kit for sparse matrix computations." from http://www-users.cs.umn.edu/~saad/software/SPARSKIT/sparskit.html.

Saad Y. (1996). *Iterative Methods for Sparse Linear System*. Boston, PWS Publishing Company.

Saaltink M. W.; Ayora C.; Carrera J. (1998): A Mathematical Formulation for Reactive Transport That Eliminates Mineral Concentrations, *Water Resour. Res.,* **34**.

Saaltink M. W.; Batlle F.; Ayora C.; Carrera J.; Olivella S. (2004). RETRASO, a code for modeling reactive transport in saturated and unsaturated porous media, Consejo Superior de Investigaciones CientÃ-ficas (CSIC) ; Universitat de Barcelona.

Saaltink M. W.; Carrera J.; Ayora C. (2001): On the behavior of approaches to simulate reactive transport, *Journal of Contaminant Hydrology,* **48**(3-4), 213-235.

Sanchez-Vila X.; Dentz M.; Donado L. D. (2007): Transport-controlled reaction rates under local non-equilibrium conditions, *Geophys. Res. Lett.,* **34**.

Sarler B.; Vertnik R. (2006): Meshfree explicit local radial basis function collocation method for diffusion problems, *Computers & Mathematics with applications,* **51**(8), 1269-1282.

Schaback R. (1995): Error estimates and condition numbers for radial basis function interpolation, *Advances in Computational Mathematics,* **3**(3), 251-264.

Schaback R. (1995). Multivariate interpolation and approximation by translates of a basis function, *Approximation Theory VIII*, World Scientific Publishing Co.

Shu C.-W.; Oshert S. (1989): Efficient implementation of essentially non-oscillatory shock-capturing schemes, II, *Journal of Computational Physics,* **83**(1), 32-78.

Shu C.; Ding H.; Yeo K. (2003): Local radial basis function-based differential quadrature method and its application to solve two-dimensional incompressible Navier-Stokes equations, *Computer methods in applied mechanics and engineering,* **192**, 941-954.

Sladek V.; Sladek J.; Tanaka M. (2005): Local Integral Equations and two Meshless Polynomial Interpolations with Application to Potential Problems in Non-homogeneous Media, *CMES: Computer Modeling in Engineering and Sciences,* 7(1), 69-84.

Sonar T. (1996): Optimal recovery using thin plate splines in finite volume methods for the numerical solution of hyperbolic conservation laws, *IMA J Numer Anal,* **16**(4), 549-581.

Souli M.; Zolesio J. P. (2001): Arbitrary Lagrangian-Eulerian and free surface methods in fluid mechanics *Computer methods in applied mechanics and engineering,* **191**, 451-466.

Srivastava R.; Yeh T.-C. J. (1992): A three-dimensional numerical model for water flow and transport of chemically reactive solute through porous media under variably saturated conditions, *Advances in Water Resources,* **15**, 275-287.

Steefel C. I.; Lasaga A. C. (1994): A coupled model for transport of multiple chemical species and kinetic precipitation/dissolution reactions with application to reactive flow in single phase hydrothermal systems, *Am J Sci,* **294**(5), 529-592.

Steefel C. I.; MacQuarrie K. T. B. (1996). Approaches to modeling reactive transport in porous media. *Reactive Transport in Porous Media.* P. C. S. Lichtner, C.I. and E. H. Oelkers. Washington, Mineralogical Society of America. **34**.

Stevens D.; Power H.; Lees M.; Morvan H. (2009): The use of PDE centres in the local RBF Hermitian method for 3D convective-diffusion problems, *J. Comput. Phys.,* **228**(12), 4606-4624.

Truscott S. L.; Turner I. W. (2004): An Investigation of the Accuracy of the Control-Volume Finite-Element Method Based on Triangular Prismatic Elements For Simulating Diffusion in Anisotropic Media, *Numerical Heat Transfer, Part B: Fundamentals,* **46**, 243-268

Turner I. W.; Ferguson W. J. (1995): An unstructured mesh cell-centered control volume method for simulating heat and mass transfer in porous media: Application to softwood drying, Part I: The isotropic model, *Applied Mathematical Modelling,* **19**(11), 654-667.

US-Geological-Survey. (05-June-2009). from http://water.usgs.gov/nrp/gwsoftware/modflow.html.

Van Genuchten M.; Alves W. (1982): Analytical Solutions of the One-Dimensional Convective-Dispersive Solute Transport Equation, *United States Department of Agriculture, Agricultural research service,*(Technical bulletin number 1661).

Versteeg H. K.; Malalasekera W. (2007). *The Finite Volume Method,* Pearson Education Limited.

Versteeg H. K.; Malalasekera W. (2007). *The Finite Volume Method* Pearson Education Limited.

Vertnik R.; Zaloznik M.; Sarler B. (2006): Solution of transient direct-chill aluminium billet casting problem with simultaneous material and interphase moving boundaries by a meshless method, *Engineering Analysis with Boundary Elements,* **30**, 847-855.

Viecelli J. A. (1969): A Method Including Arbitrary External Boundaries In the MAC Incompressible Fluid Computing Technique, *Journal of Computational Physics,* **4**, 543-551.

Warren B.; Martin E. D. (1997): Modeling Axially Symmetric and Nonsymmetric Flow to a Well with MODFLOW, and Application to Goddard2 Well Test, Boise, Idaho, *Ground Water,* **35**(4), 602-611.

Welch J. E.; Harlow F. H.; Shannon J. P.; Daly B. J. (1966).

Wendland H. (1995): Piecewise polynomial, positive definite and compactly supported radial functions of minimal degree, *Advances in Computational Mathematics,* **4**(1), 389-396.

Wong A. S. M.; Hon Y. C.; Li T. S.; Chung S. L.; Kansa E. J. (1999): Multizone decomposition for simulation of time-dependent problems using the multiquadric scheme, *Computers & Mathematics with applications,* **37**(8), 23-43.

Wright G.; Fornberg B. (2006): Scattered node compact finite difference-type formulas generated from radial basis functions, *Journal of Computational Physics,* **212**(1), 99-123.

Wu Z. (1992): Hermite-Birkhoff interpolation of scattered data by radial basis functions, *Approximation Theory,* **8**(2), 1-11.

Wu Z. (1998). Solving PDEs with radial basis functions and the error estimation; , *Advances in Computational Mathematics.*

Yeh G. T. (1987).

Yeh T.-C. J.; Srivastava R.; Guzman A.; Harter T. (1993): A numerical model for water flow and chemical transport in variably saturated porous media, Ground Water, *Ground Water,* **31**(4), 634-644.

Zhou X.; Hon Y. C.; Li J. (2003): Overlapping domain decomposition method by radial basis functions, *Applied Numerical Mathematics,* **44**(1-2), 241-255.

Appendix

$$
A=\begin{pmatrix}
[\Psi] & L_{\xi}^{1}[\Psi] & [P_{M-1}] & [\Psi] & F_{\xi}^{1}[\Psi] & [\Psi] & F_{\xi}^{1}[\Psi] & [0] & [0] & [0] & [0] & [0] & [0] \\
L_{x}^{1}[\Psi] & L_{x}^{1}L_{\xi}^{1}[\Psi] & L_{x}^{1}[P_{M-1}] & L_{x}^{1}[\Psi] & L_{x}^{1}F_{\xi}^{1}[\Psi] & L_{x}^{1}[\Psi] & L_{x}^{1}F_{\xi}^{1}[\Psi] & [0] & [0] & [0] & [0] & [0] & [0] \\
\left[P_{M-1}^{T}\right] & L_{x}^{1}\left[P_{M-1}^{T}\right] & [0] & \left[P_{M-1}^{T}\right] & F_{x}^{1}\left[P_{M-1}^{T}\right] & \left[P_{M-1}^{T}\right] & F_{x}^{1}\left[P_{M-1}^{T}\right] & [0] & [0] & [0] & [0] & [0] & [0] \\
[\Psi] & L_{\xi}^{1}[\Psi] & [P_{M-1}] & [0] & F_{\xi}^{1}[\Psi]-F_{\xi}^{2}[\Psi] & [\Psi] & F_{\xi}^{1}[\Psi] & -[\Psi] & -L_{\xi}^{2}[\Psi] & -[P_{M-1}] & [0] & [0] & [0] \\
F_{x}^{1}[\Psi] & F_{x}^{1}L_{\xi}^{1}[\Psi] & F_{x}^{1}[P_{M-1}] & F_{x}^{1}[\Psi]-F_{x}^{2}[\Psi] & F_{x}^{1}F_{\xi}^{1}[\Psi]-F_{x}^{2}F_{\xi}^{2}[\Psi] & F_{x}^{1}[\Psi] & F_{x}^{1}F_{\xi}^{1}[\Psi] & -F_{x}^{2}[\Psi] & -F_{x}^{2}L_{\xi}^{2}[\Psi] & -F_{x}^{2}[P_{M-1}] & [0] & [0] & [0] \\
[\Psi] & L_{\xi}^{1}[\Psi] & [P_{M-1}] & [\Psi] & F_{\xi}^{1}[\Psi] & [0] & F_{\xi}^{1}[\Psi]-F_{\xi}^{3}[\Psi] & [0] & [0] & [0] & -[\Psi] & -L_{\xi}^{3}[\Psi] & -[P_{M-1}] \\
F_{x}^{1}[\Psi] & F_{x}^{1}L_{\xi}^{1}[\Psi] & F_{x}^{1}[P_{M-1}] & F_{x}^{1}[\Psi] & F_{x}^{1}F_{\xi}^{1}[\Psi] & F_{x}^{1}[\Psi]-F_{x}^{3}[\Psi] & F_{x}^{1}F_{\xi}^{1}[\Psi]-F_{x}^{3}F_{\xi}^{3}[\Psi] & [0] & [0] & [0] & -F_{x}^{3}[\Psi] & -F_{x}^{3}L_{\xi}^{3}[\Psi] & -F_{x}^{3}[P_{M-1}] \\
[0] & [0] & [0] & [\Psi] & F_{\xi}^{2}[\Psi] & [0] & [0] & [\Psi] & L_{\xi}^{2}[\Psi] & [P_{M-1}] & [0] & [0] & [0] \\
[0] & [0] & [0] & L_{x}^{2}[\Psi] & L_{x}^{2}F_{\xi}^{2}[\Psi] & [0] & [0] & L_{x}^{2}[\Psi] & L_{x}^{2}L_{\xi}^{2}[\Psi] & L_{x}^{2}[P_{M-1}] & [0] & [0] & [0] \\
[0] & [0] & [0] & \left[P_{M-1}^{T}\right] & F_{x}^{2}\left[P_{M-1}^{T}\right] & [0] & [0] & \left[P_{M-1}^{T}\right] & L_{x}^{2}\left[P_{M-1}^{T}\right] & [0] & [0] & [0] & [0] \\
[0] & [0] & [0] & [0] & [0] & [\Psi] & F_{\xi}^{3}[\Psi] & [0] & [0] & [0] & [\Psi] & L_{\xi}^{3}[\Psi] & [P_{M-1}] \\
[0] & [0] & [0] & [0] & [0] & L_{x}^{3}[\Psi] & L_{x}^{3}F_{\xi}^{3}[\Psi] & [0] & [0] & [0] & L_{x}^{3}[\Psi] & L_{x}^{3}L_{\xi}^{3}[\Psi] & L_{x}^{3}[P_{M-1}] \\
[0] & [0] & [0] & [0] & [0] & \left[P_{M-1}^{T}\right] & F_{x}^{3}\left[P_{M-1}^{T}\right] & [0] & [0] & [0] & \left[P_{M-1}^{T}\right] & L_{x}^{3}\left[P_{M-1}^{T}\right] & [0]
\end{pmatrix}
$$

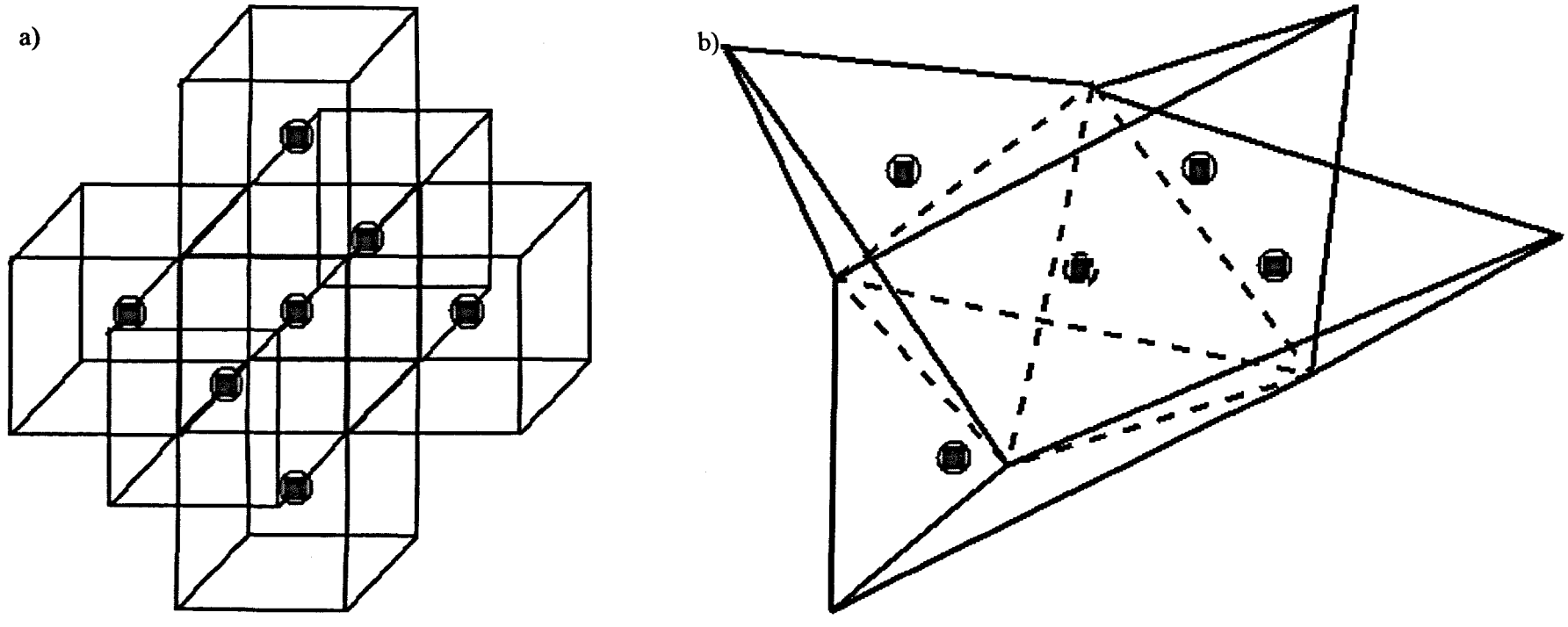

Figure App1 – Three-dimensional interpolation stencils stopped at the first level of neighbouring elements used for the unsteady simulations described in chapter 3. The square symbols indicate the locations where the Dirichlet operator is applied, the circles indicate the locations where the PDE operator is applied. Note that Dirichlet and the PDE operators are applied in the same location (i.e. double collocation)

a) Interpolation stencils used for structured meshes made of hexahedron elements, 7 Dirichlet points + 7 PDE point (total of 14 points)

b) Interpolation stencils used for unstructured meshes made of tetrahedron elements, 5 Dirichlet points + 5 PDE point (total of 10 points)